Cranfield University

Michail C. Kazilas

Acquisition and Interpretation of Dielectric Data For Thermoset Cure Monitoring

School of Industrial and Manufacturing Science

PhD Thesis

Cranfield University
School of Industrial and Manufacturing Science
Advanced Materials Department

PhD Thesis
Academic years: 2000 – 2002

Michail C. Kazilas

Acquisition and Interpretation of Dielectric Data For Thermoset Cure Monitoring

Supervisor: Dr Ivana K. Partridge

September 2003

ABSTRACT

The interpretation and modelling of the dielectric response of thermosetting materials during cure was the main focus of this study. The equivalence of complex permittivity and complex impedance in terms of information content was outlined in a series of case studies covering the separate effects of dipolar movements and charge migration as well as the combined effect of the two polarisation mechanisms. Equivalent electrical circuits were used in order to model the evolution of the complex impedance during cure. A numerical method that can model consecutive spectra throughout the cure was developed. The method is based on Genetic Algorithms and requires only input from the modelling of the initial spectra.

Complex impedance spectra were collected during the cure of a commercial epoxy resin formulation under isothermal and dynamic heating conditions. The spectra were analysed and modelled. The modelling was successful over the whole frequency range of the measurements (1 Hz – 1 MHz). The analysis of the estimated model parameters showed that charge migration dominates the dielectric response in a wide frequency range. In addition, the modelling algorithm also distinguished between the effects of electrode polarisation and dipolar movements in the signal. A new equivalent circuit was used in order to map the frequency regions where the each one of the three phenomena that together comprise the dielectric signal can be monitored most effectively.

A chemical cure kinetics model was developed for the studied system. A correlation between the maximum point of the imaginary impedance spectrum and the reaction conversion was established. A mathematical model, based on a simple linear dependence of the dielectric signal on conversion and temperature, was built. The model predictions agreed well with the experimental data.

The aim of simplifying the interpretation of the dielectric signals led to the development of a new experimental technique. Temperature Modulated Dielectric Analysis employs temperature modulations superimposed on an underlying thermal profile in order to separate the influence on the signal of the temperature alone from that of the cure reaction. The early study carried out here shows that such measurements are feasible and reveals important issues for its further development.

"Science is our century's art…"

Horace Freeland Judson[*]

[*] "The search for solutions", published by Hutchinson, 1980 (ISBN: 0091417007)

ACKNOWLEDGEMENTS

I am indebted to my supervisor Dr Ivana K. Partridge for her constant guidance, support and effort to improve the present work.
I would like to thank Dr Alexandros A. Skordos for his crucial help on various aspects of the work and for all the thought – provoking discussions through innumerable cups of coffee.
I would also like to thank Dr George M. Maistros for his help on the data acquisition setup and for useful discussions.

Finally, I would like to thank Christos and Dionyssia Kazilas for their continuous moral support during the period of this study.

This work was funded by EPSRC (GR/M89454).

TABLE OF CONTENTS

LIST OF FIGURES

LIST OF TABLES

NOMENCLATURE

The symbols used in the text are listed in alphabetical order

Symbol	Description	Unit
a	Absorptivity	1/(m.mol)
A	Absorbance	
a_1	Parameter used for the deconvolution of MDSC signal	°C
A_{CPE}	Parameter of Constant Phase Element	Ohm/s^n
A_I	Amplitude of the current response to a sinusoidal excitation	A
A_Q	Amplitude of the modulation component of heat flow	J/s
A_T	Amplitude of the modulated component of temperature profile	°C
A_V	Amplitude of the voltage excitation	Volt
a_x	Parameter used in the parametric description of Lissajous curves	
a_y	Parameter used in the parametric description of Lissajous curves	
$A_{Z''}$	Amplitude of the TMDA signal	log(Ohm)/min
$A_{\Delta T}$	Amplitude of the modulated component of the heat flow measured by MDSC™	°C
b	Sample thickness	M
b_1	Parameter used for the deconvolution of MDSC signal	°C
c	Velocity of ultrasound wave	m/s
C	Molar concentration	M
c_0	Cubic equation Parameter	
C_1	Fitting parameter	
c_1	Cubic equation parameter	
C_2	Fitting parameter	°C
c_2	Cubic equation Parameter	
C_{dip}	Dipolar capacitance	F
C_{ind}	Induced dipoles capacitance	F
c_{light}	Speed of light	m/s
c_p	Specific heat capacity	J/(g.°C)
$c_{p,R}$	Specific heat capacity of the reference	J/(g.°C)
C_{RS}	Absolute heat capacity of the reference side	J/°C

C_S	Absolute heat capacity of the sample	J/°C
C_{SS}	Absolute heat capacity of the sample side	J/°C
D	Interelectrode distance	m
d_b	Blocking electrode distance	m
D_f	Fractal dimension	
dα/dt	Reaction rate	1/min
D_ω	Discriminant of the cubic equation	
f	Frequency of the electric field	Hz
F	Fitness function	
f_0	Pre-exponential factor of the KWW relaxation function	
f_1	Constant used for latent heat analysis	J/s
f_2	Constant used for latent heat analysis	J/°C
f_{max}	Frequency of optimum point in the real or imaginary impedance spectrum	Hz
f_{min}	Frequency of minimum point in the real or imaginary impedance spectrum	Hz
f_T	Frequency of temperature modulation	Hz
G	Number of generations	
G^*	Shear modulus	Pa
H	Heat measured by the DSC/MDSC	J
H_{flow}	Heat flow measured by the DSC/MDSC™	J/s
H_{flow}	Modulated component of the heat flow measured by MDSC™	J/s
I_{DC}	DC component of the current response	A
J	Intensity transmitted by the sample	Cd
J_0	Intensity entering the sample	Cd
k	Reaction rate	1/min
K^*	Bulk modulus	Pa
k_1	constant	J/s
k_2	constant	J/(s.°C)
L^*	Mechanical modulus	Pa
L′	Real part of mechanical modulus	Pa
L″	Imaginary part of mechanical modulus	Pa
m	mass	g
M^*	Complex electric modulus	
N	Number of individuals in one generation	

n	Exponent of Constant Phase Element	
n_1	Exponent of the cure kinetic model	
n_2	Exponent of the cure kinetic model	
n_3	Exponent of the cure kinetic model	
N_e	Number of individual who advance directly to the next generation through elitism	
N_r	Number of individual who advance to the next generation through reproduction (crossover and mutation operations)	
N_S	Number of individual charged species	
N_μ	Concentration of dipoles	
P	Period of temperature modulation	min
p_e	Exchange probability	
p_i	Modelling parameters (equivalent circuit elements)	
$p_{i,est}$	Modelling parameters estimation values	
p_m	Mutation probability	
p_r	Percentage defining the range of the solution space	
Q	Total heat	J
q	charge	C
Q_{latent}	Heat from latent processes	J
Q_{losses}	Heat losses	J
r	Rate of linear increase/decrease of temperature	min/°C
R^2	Linear regression correlation coefficient	
R_{dip}	Dipolar resistance	Ohm
R_{ion}	Migrating charges (or ionic) resistance	Ohm
S	Objective function	
T	Temperature	°C
t	Time	min, s
T_0	Initial temperature	°C
T_{cure}	Cure temperature	°C
T_g	Glass transition temperature	°C
$T_{g,0}$	Glass transition temperature of the unreacted glass	°C
$T_{g,\infty}$	Ultimate glass transition temperature	°C
t_{gel}	Gelation time	min
T_{int}	Intercept temperature	K
T_m	Mean temperature over on cycle	°C

T_{mod}	Modulated component of temperature profile used in MDSC™	°C
T_R	Reference temperature	°C
T_S	Sample temperature	°C
T_U	Mean temperature	°C
u_m	Mobility of charged species	m/s
v_2	Volume fraction of the dispersed phase in a thermoset blend	
V_{DC}	DC bias voltage	Volt
w^{im}	Weight factor of the imaginary impedance data	1/Ohm
$w_{p,i}$	Weight factor of the modelling parameters	
w^{re}	Weight factor of the real impedance data	1/Ohm
Y^*	Complex admittance	1/Ohm
Z^*	Complex impedance	Ohm
Z^*_{CPE}	Constant Phase Element Impedance	Ohm
Z^*_{dip}	Dipolar Impedance	Ohm
Z^*_{ion}	Migrating charges impedance	Ohm
Z'	Real part of complex impedance	Ohm
Z''	Imaginary part of complex impedance	Ohm
Z''_{max}	Imaginary impedance maximum	Ohm
$Z''_{\alpha=0}$	Imaginary impedance before the reaction commencement	Ohm
$Z''_{\alpha=1}$	Imaginary impedance after the reaction has finished	Ohm
α	Fractional conversion	
α_{CC}	Exponent of the Cole – Cole relaxation function	
α_{DC}	Exponent of the Davidson – Cole relaxation function	
α_{gel}	Fractional conversion where gelation occurs (gelation conversion)	
α_{HN}	Exponent of the Havriliak – Negami relaxation function	
α_{max}	Maximum conversion at a specific temperature	
α_u	Attenuation of ultrasound wave	1/m
β	Fitting exponent	
β_{HN}	Exponent of the Havriliak – Negami relaxation function	
δ	Phase difference between excitation and response	rad
ΔH_{total}	Total heat of reaction	J/g
δ_x	Phase angle used in the parametric description of Lissajous curves	rad
δ_y	Phase angle used in the parametric description of Lissajous	rad

	curves	
$\delta_{Z''}$	Phase of the TMDA signal	rad
$\delta_{\Delta T}$	Phase of the modulated component of the measured heat flow on a MDSC™	rad
ε'	Real part of complex dielectric permittivity	
ε''	Imaginary part of complex dielectric permittivity	
ε^*	Complex dielectric permittivity	
ε_0	Permittivity of free space (8.854×10^{-12} F/m)	F/m
ε_1	Real permittivity of the bulk	
ε_2	Real permittivity of the dispersed phase	
ε'_{dip}	Real part of complex impedance due to dipolar relaxation	
ε''_{dip}	Imaginary part of complex dielectric permittivity due to dipolar relaxation	
ε'_{el}	Real part of complex impedance due to blocking electrodes	
ε''_{el}	Apparent imaginary part of complex dielectric permittivity due to blocking electrodes	
ε''_{ion}	Imaginary part of complex dielectric permittivity due to the presence of migrating charges	
ε_r	Relaxed dipolar permittivity	
$\varepsilon_{r,i}$	Relaxed permittivity of interfacial polarisation	
ε_u	Unrelaxed dipolar permittivity	
$\varepsilon_{u,i}$	Unrelaxed permittivity of interfacial polarisation	
η	Viscosity	Pa.s
η_g	Viscosity at glass transition	Pa.s
κ	Constant	
κ_1	Fitting parameter	log(Ohm)
κ'_1	Fitting parameter	log(Ohm)
κ_2	Fitting parameter	log(Ohm)/°C
κ'_2	Fitting parameter	log(Ohm)/°C
κ_3	Intercept of the IIM dependence on conversion	log(Ohm)
κ'_3	Fitting parameter	1/°C
κ'_4	Fitting parameter	1/°C
κ'_5	Fitting parameter	log(Ohm)
λ	Overall heat transfer coefficient	J/(s.°C)
λ_{Cp}	Ratio of the heat capacity of the fully cured material to the heat capacity of the uncured material	

λ_D	Parameter in the Di Benedetto equation	
λ_T	Tikhonov regularisation parameter	
μ	Dipole moment	A.s.m
ν	Wavenumber	1/m
ρ	Density	Kg/m^2
ρ	Ionic resistivity	Ohm/m
ρ_0	Ionic resistivity of the unreacted resin	Ohm/m
ρ_{max}	Ionic resistivity at the end of cure	Ohm/m
σ	Conductivity of the migrating charges	S/m
σ_1	Conductivity of the bulk	S/m
σ_2	Conductivity of the dispersed phase	S/m
τ	Dipolar relaxation time	s
$\tau_{,i}$	Relaxation time of interfacial polarisation	s
τ_0	Relaxation time at the beginning of cure	s
τ_1	Time constant	s
τ_2	Time constant	s
τ_3	Time constant	s
τ_∞	Relaxation time at the end of cure	s
τ_Π	Product of two time constants ($\tau_\Pi = \tau_1\tau_3$)	s^2
τ_Σ	Time constant ($\tau_\Sigma = \tau_1 + \tau_2 + \tau_3$)	s
Φ	Entanglement factor	
ω	Angular frequency	rad/s
ω_{IIM}	Frequency of the maximum point of the imaginary impedance spectrum	rad/s
ω_{max}	Frequency of maximum point in the real or imaginary impedance spectrum	rad/s
ω_{min}	Frequency of minimum point in the real or imaginary impedance spectrum	rad/s
ω_{opt}	Frequency of optimum point in the real or imaginary impedance spectrum	rad/s
ω_T	Angular frequency of temperature modulation	rad/s
ω_x	Angular frequency used in the parametric description of Lissajous curves	
ω_y	Angular frequency used in the parametric description of Lissajous curves	

MATHEMATICAL OPERATORS, SYMBOLS AND PHYSICAL CONSTANTS

Δ	Difference
$\bar{}$	Non – modulated part
$\tilde{}$	Modulated part
$\langle\ \rangle$	Average
π	3.141592...
j	Imaginary unit, $j^2 = -1$
c_{light}	Speed of light in vacuum, 2.9979×10^{8} m/s
k	Boltzmann constant, 1.3807×10^{-23} J/K

ABBREVIATIONS

The abbreviations are given in alphabetical order

Abbreviation	Explanation
CPE	Constant Phase Element
CTT	Conversion – Temperature – Transformation
DDM	4.4' – Diamino Diphenyl Methane
DDS	4.4' – Diamino Diphenyl Sulfone
DEA	Dielectric Analysis
DGEBA	Diglycidyl Ether of Bisphenol A
DMA	Dynamic Mechanical Analysis
DS	Dielectric Spectroscopy
DSC	Differential Scanning Calorimetry
DTA	Differential Thermal Analysis
FTIR	Fourier Transform Infra-Red
GA	Genetic Algorithms
IIM	Imaginary Impedance Maximum
MDA	4-4' Methylene Dianiline
MDSC™	Modulated Differential Scanning Calorimetry
MUT	Material Under Test
MWS	Maxwell – Wagner – Sillars
PGE	Phenyl Glycidyl Ether
RS	Raman Spectroscopy
TBA	Torsional Braid Analysis

TGDDM	Tetra – Glycidyl – 4-4’ – Diamino Diphenyl Methane
TMDA	Temperature Modulated Dielectric Analysis
TTT	Time – Temperature – Transformation
WLF	Williams – Landel – Ferry

1 Overview of Cure Monitoring and Thesis Structure

1.1 Scope and objectives

The cure of thermosetting systems is the main topic of this study. Cure monitoring aims to follow the physicochemical changes in thermosetting systems from the moment the cure cycle starts to the moment the component is fully cured.

In this introductory chapter the need for monitoring is outlined and the various monitoring techniques are briefly reviewed. In the last section, a roadmap of the thesis structure is given.

1.2 Why monitor

The cure of thermosets is a complex physicochemical phenomenon. The curing system passes through various stages, primarily defined by the imposed temperature profile (cure cycle). Thermoset monomers or pre – polymers are usually kept in freezers, at temperatures below the uncured glass transition temperature. This means that the system is kept as an unreacted glass. Typical glass transition temperatures of curing thermosets are well below 0 °C (1, 2). Therefore, when the material processing begins

at ambient temperature, the system is in the liquid phase. As the polymerisation reaction advances, the average molecular weight of the material increases. A backbone structure forms and a three dimensional molecular network builds up from that structure. When the molecular network size is of the same magnitude as the extent of the bulk material, the system transforms from the liquid phase to the rubber phase (3). This is the gelation "point". After gelation the polymerisation reaction continues to evolve and the molecular network becomes more tight and complex (1, 3).

The glass transition temperature (T_g) of the system increases as the polymerisation conversion increases. When the T_g reaches the curing temperature, the system transforms from the rubber phase to the vitreous state. This is the vitrification point. After vitrification the polymerisation reaction rate slows down, even if the temperature is increased further and in many cases essentially stops (1).

Apart from these two main events, other physicochemical phenomena may also appear during the polymerisation reaction, depending on the nature of the curing system and the cure cycle. An indicative list is given in Table 1-I.

Table 1-I: *Critical events during the curing of thermosets*

Event	**Description**	**Notes**
Gelation	A 3D molecular network is formed at a specific conversion α_{gel}. Gelation is an irreversible process (1, 3).	Gelation occurs when the conversion exceeds α_{gel}. Gelation usually precedes vitrification but can also take place after it (4).
Vitrification	The T_g of the system exceeds the curing temperature T_{cure}. The material becomes a glass.	The glass transition temperature depends on conversion. There is a maximum in T_g, $T_{g\infty}$, which corresponds to a fully cured material ($\alpha=1$).
Devitrification	The curing temperature T_{cure} exceeds the T_g of the vitrified system. The material returns to the rubber or liquid state.	Devitrification also occurs when the unreacted material is exposed to ambient temperature conditions.
Cure induced Phase separation	In the curing of polymer blends, a second phase appears at a specific conversion.	The final material exhibits two glass transition temperatures, one for each phase.

Some of these events are also shown in Figure 1-1, where the temperature and T_g changes of a thermosetting material are plotted from the time it is in the freezer to the time it is a final product.

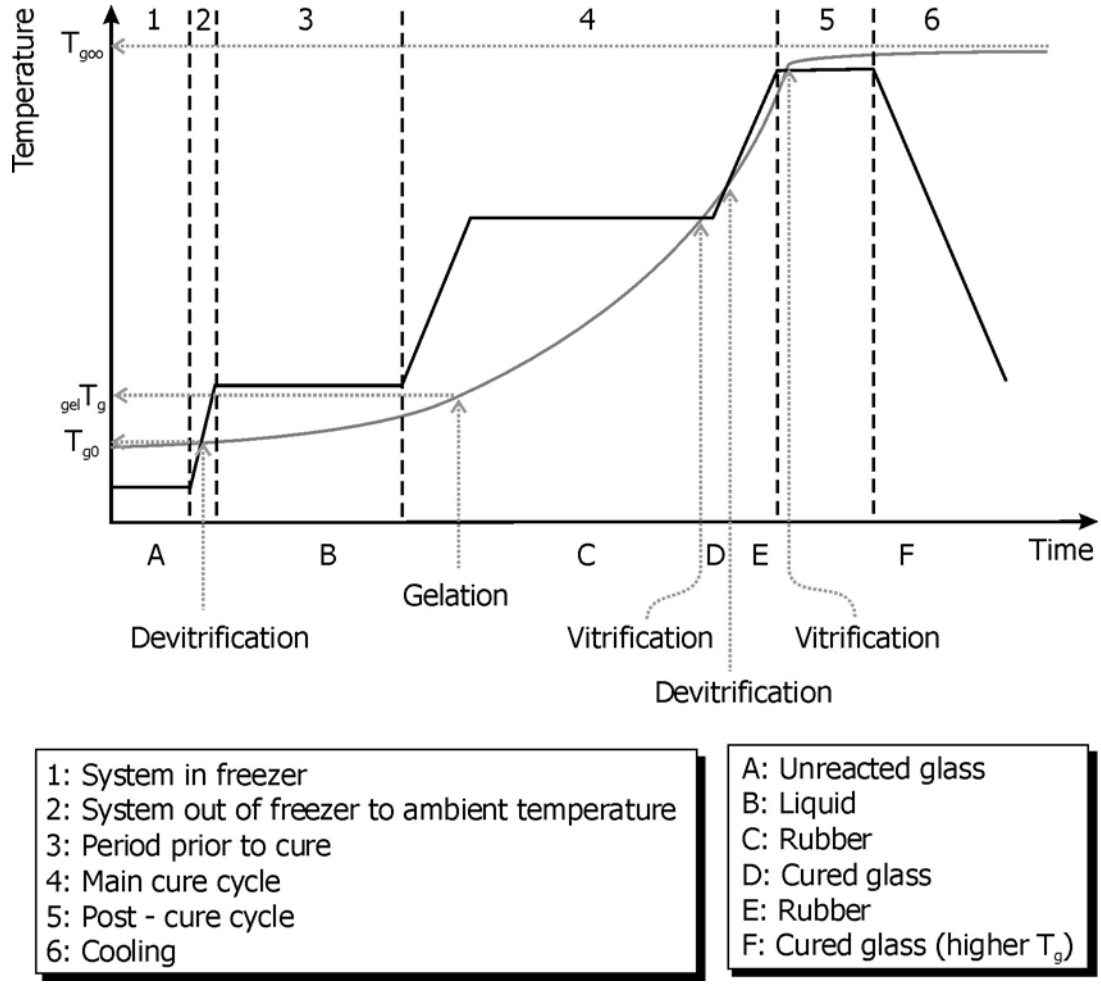

Figure 1-1 *Glass transition temperature advancement (grey line) and temperature experienced (black line) by a thermoset material from the time it is taken out of the freezer to the end of cure. The two text boxes show the temperature segments (numbers defined by the black dotted lines) and the physicochemical changes (letters defined by the grey dotted arrows). Critical values of the T_g and regions of gelation, vitrification and devitrification are also shown.*

Despite the fact that several stages of the cure process have been described and modelled adequately, there is no accepted theory that could predict the final properties of a curing system (5). Deviations from analytical models occur due to the nature of the polymerisation reaction in thermosets. In typical cases, there are several reaction mechanisms involved and different reaction paths can evolve in parallel. This complexity means that phenomenological models have to be employed for the characterisation of the curing reaction (1).

The final properties of thermosetting materials depend strongly on the curing conditions. As the demand for complex geometries and structures leads to complicated processes, accurate knowledge of the state of a curing thermoset is very important. Thermoset cure is an irreversible process. If the final material properties fail to meet some predefined standards, then the material becomes scrap and all the resources used for the process are lost without any benefit for the manufacturer and the consumer.

1.3 Modelling the cure process

The need for accurate prediction and optimisation of the cure process is the incentive for the abundance of publications on modelling the cure process. Key issue in most of the studies is the polymerisation reaction since critical phenomena such as gelation and vitrification are reaction induced.

1.3.1 Polymerisation reaction kinetics

Thermosetting polymers may be formed in two ways (1):

- Polymerisation of monomers
  A mixture of monomers reacts by a polymerisation mechanism. At least one of the monomers functionality has to be higher than 2.
- Crosslinking macromolecules
  Previously created macromolecules are chemically crosslinked. The original macromolecules may be linear or branched.

In either way, the polymerisation reaction depends on the concentration and the availability of the reacting species involved. Cure kinetics experiments measure the concentration of the reacting centres indirectly (i.e. by measuring a correlated parameter such as the exothermic heat produced by the reaction or the acoustic wave propagation).

There are two main ways of modelling the reaction of thermosetting systems:

the mechanistic approach and

the phenomenological approach.

Both analyses result in mathematical expressions in the general form:

$$\frac{da}{dt} = f\left(a, T\right) \tag{1.1}$$

In the above equation a is the fractional conversion, T is the temperature and t is the time. Eq. (1.1) implies that the reaction rate da/dt is a unique function of conversion and temperature.

Mechanistic kinetic models assume certain paths for the reaction which involve a number of steps. The initial reactants transform to a final product through these reaction steps. In the case of an epoxy – amine system, the reactions usually considered are the opening of the epoxy ring by primary, secondary and tertiary amines (10). Other reactions, such as etherification, are also considered (1). The concentrations of the reactants and the conversion are related through rate coefficients (1, 10 - 12). Conversion is defined as the ratio between the concentration change (concentration at a particular time minus the initial concentration) of one of the reacting species to the initial concentration of the same species. The rate coefficients are temperature dependent. The dependence is usually exponential (1, 10, 11). The incorporation of diffusion driven kinetics in the late stages of the reaction is dealt with in two ways: either by modifying the kinetic equation (13) or by assuming that thermoset cure is a kinetic process where diffusion and reaction act in series (14, 15). In the latter case, the overall reaction rate coefficient will be:

$$\frac{1}{k_{overall}} = \frac{1}{k_{reaction}} + \frac{1}{k_{diffusion}} \tag{1.2}$$

At initial cure stages, the diffusion of molecular species is easy because of the small size of the molecules contained in the system. The reaction is the slower process and defines the value of the overall rate coefficient, $k_{overall}$. At later stages though, the presence of macromolecules decreases the diffusion rate and diffusion limitations begin to influence the overall rate coefficient. Finally, when the system vitrifies, the overall reaction rate depends solely on diffusion.

Mechanistic models have certain advantages. They offer a more rigorous description of the chemical process, compared to the phenomenological models. Mechanistic models can also be used to study the effect of different initial concentrations of the reactants on the curing reaction. On the other hand, the nature of the polymerisation reaction makes it difficult to find the correct, or more influential, reaction paths. Furthermore, the complexity of the reaction means that the fitting of mechanistic models to experimental data can become very time consuming. Finally, the modification of the

models in order to incorporate diffusion limitation renders them similar to the phenomenological models.

The phenomenological approach uses kinetic equations that describe the reaction in a broader manner. The equations are formed after some experimental data have been gathered and analysed. According to the experimental results, an assessment of whether the reaction is of n^{th} order or has a catalytic or autocatalytic behaviour is performed. Based on such general observations, model equations are fitted to the experimental data. One of the most successful phenomenological models is Kamal's model (16 - 18):

$$\frac{da}{dt} = \left(k_0(T) + k_1(T)a^{n_1(T)}\right)(1-a)^{n_2(T)} \tag{1.3}$$

The model is a summation of n^{th} order kinetics and autocatalytic behaviour. Here the conversion is defined as the ratio between the value of a monitored variable and the initial or final value of the same variable. In Differential Scanning Calorimetry (DSC) for example, this variable is the exothermic heat of the reaction. Several variations of the model have described successfully the reaction of epoxy – amine systems (19-21), polyesters (22, 23), bismaleimide (24, 25) resins and thermoset/thermoplastic blends (26).

Karkanas et al used a modified version of Kamal's model to describe the reaction of epoxy – amine systems, (19, 27):

$$\frac{da}{dt} = k_o(T)(1-a)^{n_1(T)} + k_1(T)a^{n_2(T)}(1-a)^{n_3(T)} \tag{1.4}$$

The description included the later stages of the reaction where diffusion limitations become apparent.

Phenomenological models have a limited envelope of application compared to mechanistic models and no straightforward physical meaning in chemistry terms. Nevertheless, their simplicity, compared to the mechanistic models, makes them attractive for describing complex commercial systems, especially when prior knowledge of the chemical composition of such systems is not available.

An alternative modelling approach was recently introduced by Skordos and Partridge (28). In this approach no analytical equation is developed for the modelling of experimental data obtained by DSC. Direct interpolation is used instead for the prediction of conversion from reaction rate and temperature data. The method is purely numerical and provides no information on the chemistry of the system. The

quality of experimental data is more critical compared to the other two approaches since no fitting is performed, which means no averaging of errors. On the other hand, it gives predictions of similar quality and it is much easier to implement compared to the other two approaches.

1.3.2 Gelation

Gelation is a critical transition in the curing of thermosets. Before gelation the system behaves as a liquid. After gelation, solid like behaviour is observed. An example of such change is shown in Figure 1-2. Before gelation, the viscosity of the system can be monitored while after gelation the elastic modulus can be measured.

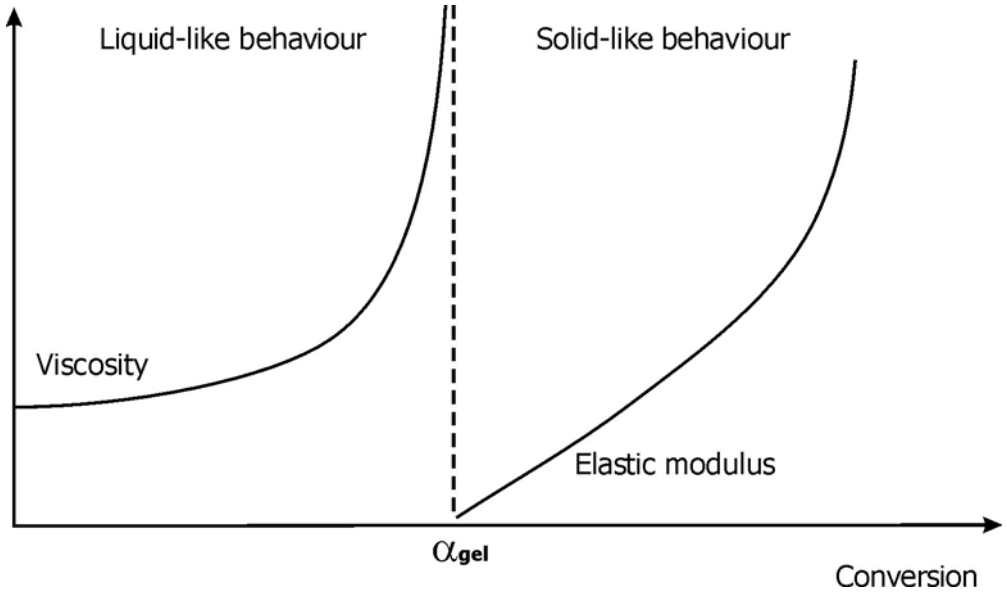

Figure 1-2 *Curing system liquid-like behaviour ($\alpha<\alpha_{gel}$) and solid-like behaviour ($\alpha>\alpha_{gel}$) as a function of the polymerisation reaction. At α_{gel} the viscosity diverges and solid material properties like the elastic modulus can be measured.*

Gelation occurs at a specific conversion, α_{gel} (4, 29). This means that a cure kinetics model is needed alongside rheological measurements for the determination of α_{gel} under specific temperature conditions.

The gelation time, t_{gel}, can be measured directly by monitoring the viscosity advancement of a curing system. As gelation approaches, viscosity increases abruptly and reaches values that cannot be measured. Measurements of the elastic modulus in the gelation region reveal that storage modulus is frequency independent in that region and can be used for identifying gelation (30, 31). Matejka (31) defined gelation

as the point of crossover between the values of storage and loss modulus. However, elastic moduli in the gelation region are very low and contain considerable noise. Therefore, an "operational" definition of gelation is usually employed in order to assign a specific value to t_{gel}. Stephan et al (32) set the value of 20 kPa.s as the gelation time, where Karkanas et al (33) used the value of 10 kPa.s. Typical experimental data of viscosity evolution during cure are shown in Figure 1-3.

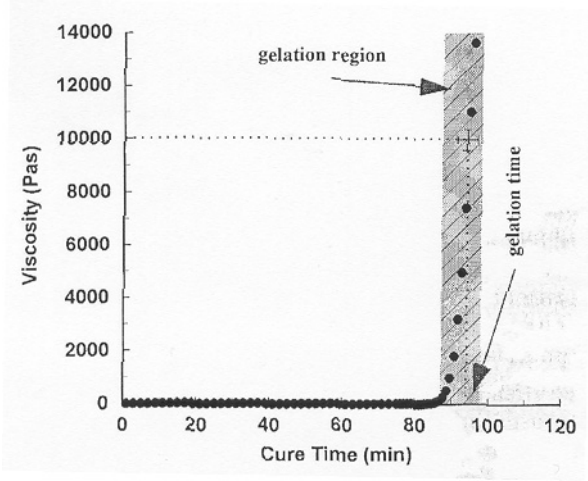

Figure 1-3 *Viscosity advancement of a curing epoxy. The gelation region is highlighted. The gelation point is identified at η = 10 kPas. Results after Karkanas and Partridge (33)*

Viscosity measurements have been correlated with the cure advancement through the glass transition temperature (33-35). One equation that has been used extensively in viscosity modelling is the Williams – Landel – Ferry (WLF) equation:

$$\ln\frac{\eta(T,\alpha)}{\eta_g} = -\frac{C_1(T)\left(T - T_g(T,\alpha)\right)}{C_2(T) + T - T_g(T,\alpha)} \tag{1.5}$$

where η is the viscosity, η_g is the viscosity at T_g and C_1, C_2 are temperature dependent fitting parameters. The value of η_g is considered constant, 10^{12} Pa.s (36).

Viscosity measurements have also been correlated with dielectric measurements (35, 37, 38) and used in identifying phase separation in thermoset/thermoplastic blends (39-41).

1.3.3 Vitrification

The glass transition phenomenon, or vitrification, signifies the passing from an equilibrium liquid or rubber state to a dynamic non–equilibrium vitreous state. Glass transition has been observed in a wide range of materials, including metals (42). A comprehensive review by Hödge (43) covers many of the proposed theories for glass transition. The glass transition temperature, T_g of non–reacting materials depends on the experimental conditions, namely the rate of temperature change and the frequency of observation (1, 8, 42, 43, 44). In thermosetting systems, vitrification can be either temperature or reaction induced. This can be pictured in a conversion – temperature – transformation (CTT) diagram:

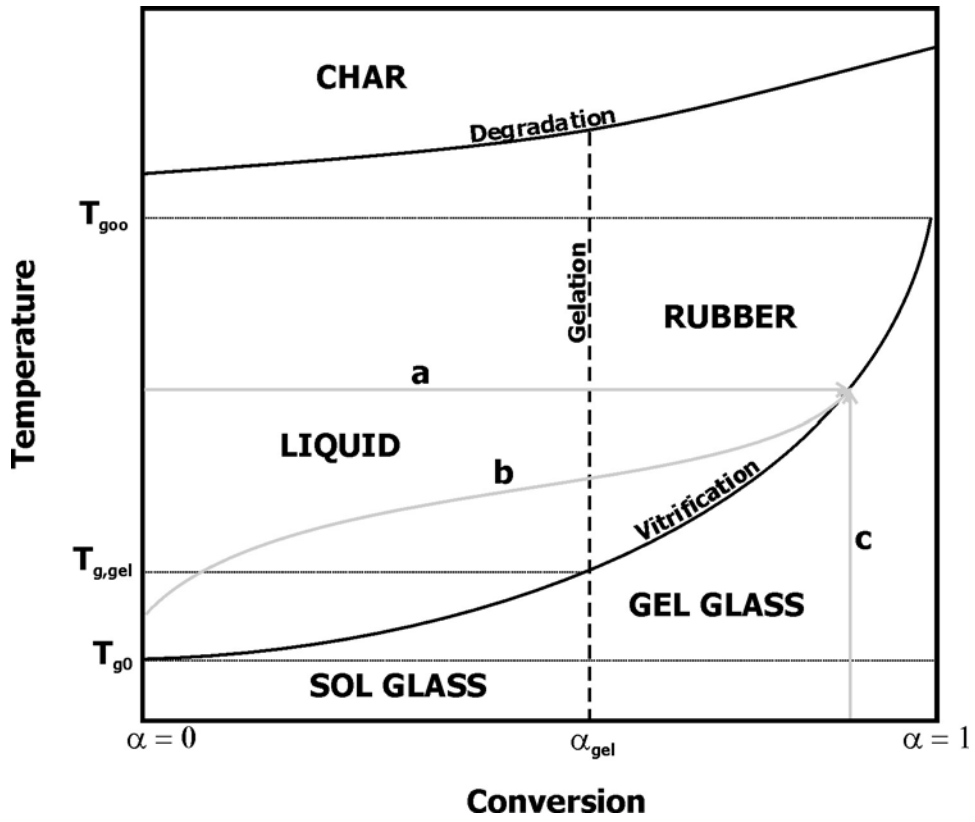

Figure 1-4 *CTT diagram for thermoset cure. The gelation, vitrification and degradation lines define the material state. The grey lines are trajectories leading to vitrification at the same glass transition temperature: (a) reaction induced, (b) temperature and reaction induced and (c) temperature induced.*

The use of such diagrams in thermoset cure was introduced by Gillham, who was the first to produce a Time – Temperature – Transformation (TTT) diagram for an epoxy system (4, 45). Many researchers have studied the dynamics of vitrification in

thermosets using dielectric measurements. The relaxation times of dipoles and other molecular groups (side chains for example) change several orders of magnitude when vitrification occurs. Molecular relaxations are usually termed α-, β-, γ-… relaxations. The α – relaxation is observed at the higher temperature (at constant frequency) and is related to the glass transition. All the other relaxations are also referred to as "secondary relaxations".

The glass transition temperature advancement during cure is frequently described by the Di Benedetto equation (1):

$$\frac{T_g(\alpha) - T_{g,0}}{T_{g,\infty} - T_{g,0}} = \frac{\lambda_D \alpha}{1 - (1 - \lambda_D)\alpha} \tag{1.6}$$

where the subscripts *0* and *∞* denote the beginning and end of cure respectively. The parameter λ_D is usually determined by curve fitting (33). T_g is usually found by measuring the heat capacity changes of the curing material using calorimetric methods such as Modulated Differential Scanning Calorimetry (MDSC) which is described in Chapter 2.

In dielectric cure monitoring, the dipolar relaxation time, discussed in § 4.2.3, is used for identifying vitrification. Mangion and Johari (46) studied the glass transition and the secondary relaxations in partially and fully cured epoxy/amine systems at very low temperatures. Fitz et al (48, 49) studied the molecular dynamics of several thermosetting systems. The systems were allowed to react up to a predefined level and then studied at temperatures which did not induce further reaction. They proposed that the orientation of molecules in a thermoset during cure is affected by the local structure of the network (molecular architecture) and by the type and concentration of electrically charged species (dielectric architecture). The same group also studied the effect of solvents on vitrification (50, 51). In the above studies, the conductivity of the thermosetting systems was low enough so that the dipolar relaxation features in the complex permittivity signal could be clearly identified and analysed (see § 4.2 for more details on the information contained in complex permittivity). In commercial systems however, dipolar effects are usually masked by the high conductivity levels. Therefore, in these systems, the complex permittivity cannot be used for a rigorous analysis in the molecular level. Fitz and Mijovic (52) used dielectric measurements in conjunction with light scattering measurements in order to study the vitrification process. The two methods produced similar values for the dipolar relaxation time.

1.4 Brief account of cure monitoring techniques

Cure monitoring is performed by measuring some physical quantity which corresponds directly or indirectly to the material state. The many techniques that fall under this general definition can be arranged in three categories, according to the nature of the measurement. Table 1-II lists some of the main cure monitoring techniques.

In thermal monitoring techniques, a physical quantity is measured as a function of time or temperature and compared with a reference value. Examples of such quantities are heat flow (DSC) and temperature (DTA). Thermal analysis techniques are well established in cure monitoring studies. Data analysis is relatively easy. They are often used as standard techniques for the validation of new experimental processes. One disadvantage of thermal techniques is that they cannot be used in-situ in industrial environments since they require use of small samples. In some cases, the cure of small coupons emulating the bigger part is being monitored at the same time as the bigger part is being cured. The main problem with the above approach is that the coupon is physically separated from the part being manufactured. Thus the temperature profiles experienced by the coupon and the part are not identical. Another problem is that the small dimensions reduce the scale of heat transfer effects that may alter the actual temperature of the curing part (53, 54).

Table 1-II: *Classification of various cure monitoring techniques*

Method	**Main Techniques**
Thermal Monitoring	Differential Scanning Calorimetry (DSC) Differential Thermal Analysis (DTA)
Optical methods	Fourier Transform Infrared Spectroscopy (FTIR) Raman Spectroscopy (RS) Fluorescence
Response to small external field	Acoustic cure monitoring (Ultrasound) Dielectric cure monitoring (DEA) Nuclear Magnetic Resonance (NMR) Torsional Braid Analysis (TBA)

The use of optical methods in cure monitoring is based on the absorption of radiation by molecular groups. Optical fibres drive high energy radiation (usually produced by a laser) into the curing material and carry out the response. In a way, optical methods also use an external field to get information about the system. The difference with the

last category is in the magnitude of the external field (much lower in the last category) and the duration over which the field is imposed (much longer in the last category compared to optical methods). The excess of energy provided to the molecular groups gives rise to several phenomena such us oscillatory movements (FTIR), radiation emission (RS) or excitation to a higher electronic state (Fluorescence). All these techniques use optical fibres as guiding media. Sophisticated software that usually comes with the instrument is used for the identification of molecular groups in the spectra. The great advantage of such optical techniques is that they can provide information about specific molecular groups that take part in the polymerisation reaction. Therefore, different reaction mechanisms can be identified and mechanistic kinetic models can be built. Furthermore, improvements concerning the cost and robustness of the optical fibres that carry the signal could render optical techniques applicable in industrial environment. This issue, which has already been tackled by some researchers, is discussed in more detail in the next section (55). One drawback is that data analysis is not straightforward since the responses from different molecular groups can overlap. Another problem in the analysis of experimental curves is the definition of a baseline needed for the calculation of conversion (see eq. 1.10 below).

The last category in Table 1-II exploits the response of the system when a small external excitation is applied. The excitation field can be acoustic (ultrasound), electric (DEA), magnetic (NMR) or mechanical (TBA). The different molecular species respond to this excitation in different time scales (relaxation times). The obtained signal encompasses the responses of all the molecular species present in the material. Therefore, the measurement provides macroscopic information about the system.

Out of the methods mentioned on Table 1-II, dielectric cure monitoring is the main subject of the present study and is presented separately (§ 1.5). The principles of DSC are presented in Chapter 3 as a part of the description of the calorimeter used for cure kinetics experiments (§ 3.4.3). In the two following sections, a brief overview of the FTIR and ultrasound cure monitoring techniques is given. These two techniques are the most popular in terms of published studies, after dielectric cure monitoring.

1.4.1 FTIR

Infrared Spectroscopy exploits the oscillatory movements of molecules when they absorb radiation. The molecules remain in the electronic ground state. Different oscillation modes are observed, namely vibration, rotation and bending. The oscillation

frequency is unique for every molecule or molecular group. Each frequency corresponds to a wavenumber, *v*, which is defined as:

$$v = \frac{f}{c_{light}} \tag{1.7}$$

where c_{light} is the speed of light (~ 3×10^8 m/s)

The infrared spectrum covers a frequency range that extends from about 300 GHz up to about 300 THz (56). The corresponding wavenumbers are about 10 – 14000 cm^{-1}. There are three regions in the infrared spectrum: the near infrared region (14000 cm^{-1} to 4000 cm^{-1}), the mid infrared region (4000 cm^{-1} to 400 cm^{-1}) and the far infrared region (400 cm^{-1} to 10 cm^{-1}).

The components of a typical FTIR experimental assembly are shown in Figure 1-5. The radiation source generates the high energy pulse that excites the sample. Thermal radiators provide continuum radiation, covering a broad wavenumber range, while laser sources are used when narrow spectral regions are studied (56).

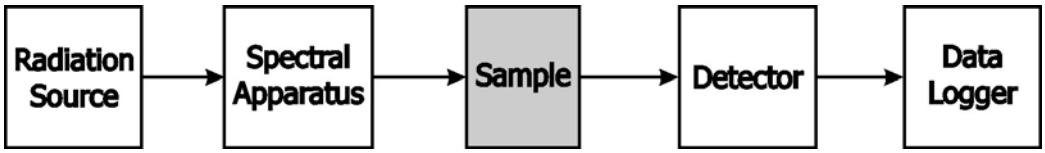

Figure 1-5 *Basic components of an FTIR spectrometer*

The spectral apparatus consists of an interferometer which splits the radiation beam into partial beams with different phases. The splitting is performed with the use of adjustable mirrors and beam-splitters. The beams recombine and are sent to the sample. The sample is usually held between transparent glass plates which do not alter the beam characteristics. The detector collects the optical signal and converts it to an electric signal, which is then recorded and analysed further.

The absorbance of the sample at a specific frequency, *A*, is defined as the logarithm of the ratio of the intensity of the beam that enters the sample to the beam intensity picked up by the detector. The absorbance follows Beer's law (56, 57):

$$A = \log\left(\frac{J_o}{J}\right) = abC \tag{1.8}$$

where *a* is the absorptivity of the molecular species at the particular frequency, *b* is the sample thickness and *C* is the concentration of the absorbing component. Beer's law is

considered to be additive (56). If there are more than one species that absorb energy at an individual frequency, then:

$$A = \sum_i a_i b C_i \tag{1.9}$$

The epoxy group absorbs energy at 910 – 916 cm^{-1} (58-60). These wavenumbers lie in the mid infrared region, which contains most of the fundamental absorptions and provides, in general, better information about the curing system. A typical set of infrared spectra during epoxy cure is shown in Figure 1-6. The magnitude of the absorbance peaks changes, indicating the concentration increase or decrease of the molecular species, as appropriate.

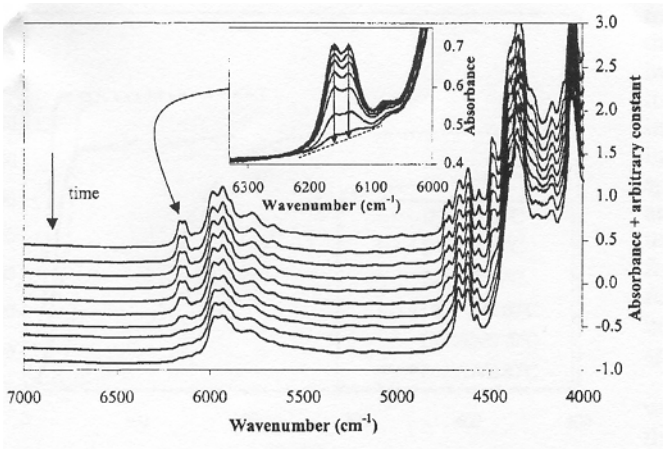

Figure 1-6 *Absorbance spectra in the near infrared region. Starting from above, each spectrum corresponds to a different time in cure. Results after Rey and Galy (61)*

The reaction extent is calculated by comparing the signal changes in the epoxy group band to the changes of a reference peak during the cure:

$$\alpha = 1 - \left(\frac{A_{epoxy}(t)}{A_{epoxy,0}} \right) \left(\frac{A_{reference,0}}{A_{reference}(t)} \right) \tag{1.10}$$

The subscript *0* denotes the signal prior to cure. Different peaks have been used as reference. Mijovic and Andjelic (58) have used the peak at 2920 cm^{-1} which is caused by the $–CH_2$ stretching vibration and stays unchanged during the cure. Fraga et al (60) used the peak at 830 cm^{-1} caused by phenylene. They also demonstrated that the peak due to the –OH stretching at 3450 cm^{-1} can be used instead of the epoxy peak. Rey et al (61) who studied dimethacrylate – vinylester blends, used the equation:

$$\alpha = \frac{a_{vinyl} A_{meth}(t) + a_{meth} A_{vinyl}(t)}{a_{vinyl} A_{meth,0} + a_{meth} A_{vinyl,0}} \quad (1.11)$$

They used the peaks at 6166 cm^{-1} (methacrylate) and 6135 cm^{-1} (vinyl double bonds).

One of the problems in acquiring spectra in the mid infrared region is that special fibres have to be employed for transmitting the optical signal. These fibres are sensitive to handling, have limited frequency interval and add considerably to the cost of the measurement (55). This difficulty led some researchers to the near infrared region (55, 62). In this region, commercial silica type optical fibres can be used for transmitting the signal. These fibres are inexpensive and come in a variety of types and forms. One the other hand, the near infrared region contains only overtones of the fundamental absorption and the analysis of the spectra is more difficult. Mijovic et al (55) used the peak at 4530 cm^{-1} for the epoxy group absorption and the peak at 4673 cm^{-1} (C-H stretching vibration of the benzene ring combined with C = C stretch). Musto et al (62), who compared results obtained from both the mid and the near infrared regions, used the peaks at 4524 cm^{-1} – essentially the same peak used in (55) – and at 6064 cm^{-1} for the epoxy group absorption. The conversion profiles calculated from the two peaks were significantly different. The authors attributed the differences to the catalytic effect of the holder substrate. Similar differences were reported by Mijovic and Andjelic (58). They explained the discrepancy as a result of the emergence of another peak at 905 cm^{-1} which overlaps with the epoxy peak at 915 cm^{-1}. In any case, such incongruities in translating the signal into cure kinetics profiles outline a difficulty in the interpretation of the experimental curves.

The application of FTIR in the near infrared region for in situ monitoring has already been demonstrated by various research groups (63, 64). The use of silica fibres enables the successful transport of the optical signal over large distances. Mijovic and Andjelic (63) constructed a novel test cell and monitored the cure of an epoxy/amine formulation in situ. The test cell was disposable. They collected spectra in the near infrared region and used eq. (1.10) and the same peaks as in (55) for the interpretation of data. The results showed that it is possible to use FTIR for in – situ cure monitoring.

1.4.2 Ultrasound

Ultrasound techniques can be applied to monitor the cure of thermosetting materials. Acoustic waves are transmitted and received by appropriate probes. The waves travel through the curing material and their characteristics change as the material mechanical properties change. A typical experimental configuration of the technique is pictured in Figure 1-7. Two transducers are used to transmit and receive the acoustic wave. The transducers are in contact with the curing thermoset or the tool.

The use of ultrasonic waves in measuring the elastic modulus in polymers and, in particular, in thermosetting systems, was reported as early as 1974 (65, 66).

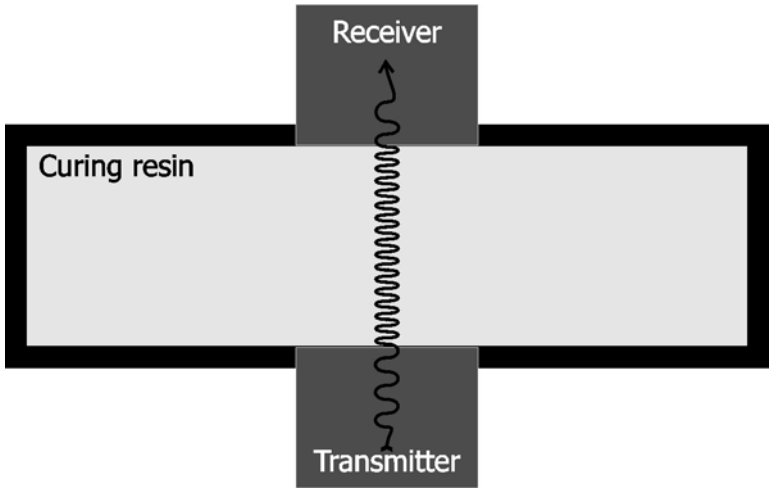

Figure 1-7 *Typical experimental setup for acoustic cure monitoring*

The real and imaginary components of the mechanical modulus of the material are given by the following relationships (67-69):

$$L' = \rho c^2 \frac{1 - \frac{a_u^2 c^2}{\omega^2}}{\left(1 + \frac{a_u^2 c^2}{\omega^2}\right)^2} \tag{1.12}$$

$$L'' = 2\rho c^2 \frac{\frac{a_u c}{\omega}}{\left(1 + \frac{a_u^2 c^2}{\omega^2}\right)^2} \tag{1.13}$$

In the above equations, L' and L'' refer to the real (storage) and imaginary (loss) modulus in the direction of the propagating wave, ρ is the material density, c is the

ultrasound velocity, a_u is the attenuation or absorption coefficient and ω is the frequency. For an isotropic material, the modulus L^* is related to the shear modulus G^* and the bulk modulus K^* according to the equation (70):

$$L^* = K^* + \frac{4}{3}G^* \tag{1.14}$$

For shear waves $L^* \approx G^*$ (71) whereas for resin in the liquid phase $K^* >> G^*$ (72).
In cure monitoring experiments the ultrasound velocity and attenuation measurements are such that (71, 72):

$$\frac{a_u^2 c^2}{\omega^2} << 1 \tag{1.15}$$

Therefore, eqs. 1.12 and 1.13 can be simplified:

$$M' = \rho c^2 \Leftrightarrow c = \sqrt{\frac{M'}{\rho}} \tag{1.16}$$

$$M'' = \frac{2\rho a_u c^3}{\omega} \Leftrightarrow a_u = \frac{\omega M''}{2\rho c^3} \tag{1.17}$$

The above relationships are used for calculating the mechanical modulus from ultrasound measurement and for comparing DMA and ultrasonic experiments (73).
Figure 1-8 shows typical ultrasound velocity and attenuation profiles during epoxy cure. The ultrasound velocity increases in a stepwise fashion, following the increase of the real modulus during cure (67, 68, 71, 74) as indicated by eq. (1.16).

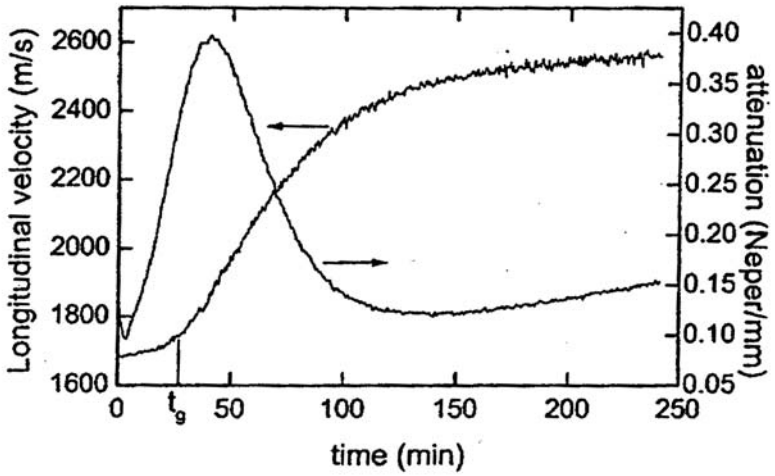

Figure 1-8 *Ultrasound velocity and attenuation development during epoxy cure (Epon 828-HY 961 system cured isothermally at 48 °C). Results after Maffezzoli et al (67).*

White et al (73) normalised the ultrasound velocity data of a curing epoxy and established correlations with data obtained by DSC and DMA. Some authors have linked the inflection point of the velocity curve with gelation (75-77). In the attenuation curve a peak is observed (67, 68, 71, 74). This peak has been attributed to vitrification (67) as in the DMA loss modulus curves, although there are experimental data which do not support this correlation (68, 74).

In recent publications, novel experimental configurations where compression and shear waves could be produced and analysed simultaneously have been reported (71, 79). The use of ultrasound for Resin Transfer Moulding (RTM) process monitoring has also been described. Sheppard and Smith (80) used a commercial system and monitored the cure of a carbon fibre epoxy prepreg. They found an inverse relationship between the sound velocity and the ionic conductivity of the curing material, which was obtained by dielectric measurements. This relationship however is purely phenomenological and no information about its general validity is given in the paper. Apart from the ultrasound velocity and attenuation, other features of the acoustic wave have also been used to monitor thermoset cure, such as the reflection coefficient (65) and the resonance frequency peak (81). Although it has been demonstrated that these parameters follow the structural changes in a curing thermoset, the high noise levels and the difficult interpretation of results set limits to their use.

1.5 Dielectric cure monitoring

The response of polymeric materials to external electric fields has been used for many years as a technique for studying a range of physicochemical processes. The large frequency range (10^{-6} Hz – 10^{12} Hz) accessible by Dielectric Spectroscopy (DS) has enabled researchers to study a broad range of phenomena with very different characteristic times, such as the slow molecular processes in vitrified polymers or the fast movements of small ions in liquid polymers. Recently, two books have been published (44, 82), reviewing the use of DS in polymers. Although several kinds of external fields have been used successfully in DS studies, alternating electric fields are the most commonly employed since the system can be studied at specific frequencies (i.e. characteristic times).

1.5.1 Principle of measurement

The response of a system to an external electric field depends on the ability of the system to either store or to dissipate the excess energy. When the external perturbation is small, so that no physicochemical changes alter the state of the system, the response of the system is given by the macroscopic relaxation function $\Phi(t)$ in the time domain or the complex permittivity ε^* in the frequency domain (2, 43, 82). The two quantities contain the same amount of information and are connected through a Laplace transform:

$$\frac{\varepsilon^*(\omega)-\varepsilon_u}{\varepsilon_r-\varepsilon_u}=1-\int_0^\infty \frac{d\Phi(t)}{dt}\exp(-j\omega t)\,dt \qquad (1.18)$$

In the above equation ε_u is the unrelaxed permittivity, ε_r is the fully relaxed permittivity, ω is the frequency of the applied field and j is the square root of -1, also termed "imaginary unit".

The complex permittivity sums the contributions from electrons, atoms, molecules and molecular groups that react to the applied field (2, 83). In the case of cure monitoring the main contributions come from migrating charges, blocking electrode and interfaces, and dipolar relaxations. These phenomena are analysed extensively in Chapter 4, where a theoretical connection between the complex permittivity representation and the complex impedance representation is established. Complex permittivity is normally used to describe dipolar relaxations whereas complex impedance is typically used to describe conductive systems (82, 84).

1.5.2 Cure monitoring studies in thermosetting systems

The first comprehensive review of cure monitoring in its modern state was given by Senturia and Sheppard in 1986 (85), while another review by Pethrick and Hayward was published recently (86). In the same year (1986), Lane et al studied the cure of commercial epoxy systems (87). They used parallel plate sensors and produced permittivity spectra. From the maximum of the dielectric loss curves, they calculated the relaxation time τ of the dipolar species and established a correlation with the viscosity during cure. Nass and Seferis (88) also used parallel plate sensors and studied the cure of an epoxy – amine system under isothermal and non – isothermal conditions. They separated the cure cycle into three regions: (i) prior to cure, (ii) during the polymerisation reaction and (iii) after the end of cure. A similar study on a

different system was performed by Koike (89). Lairez et al (90) produced a time – temperature – transformation (TTT) diagram, which was initially introduced by Enns and Gillham (4), from dielectric and rheological measurements. Bidstrup and Senturia (91) used a commercial instrument* and comb electrodes to study the cure of commercial epoxy systems. The same apparatus was used by Bidstrup et al (92) and Day (93), who studied dynamic cure cycles. They calculated the ionic conductivity from dielectric loss measurements and used it as a cure index. Bruckman and De Goeje (94) published the relationships used for translating the admittance measurements into material permittivity and dielectric loss, for a comb sensor:

$$\varepsilon'_{sample} = \frac{Y''_2}{Y''_1}\left(1 + \varepsilon'_{substrate}\right) - \varepsilon'_{substrate} \tag{1.19}$$

$$\varepsilon''_{sample} = \frac{Y'_2}{Y''_1}\left(1 + \varepsilon'_{substrate}\right) \tag{1.20}$$

The subscripts *1* and *2* denote the admittance measurements in air and in the curing material respectively. The above equations show that knowledge of the sensor substrate properties is required in order to calculate the material properties from the signal obtained by a comb sensor. The derivation of these relationships, which also appear in a recent publication by Challis et al (71), is presented in § 3.3.1.

Livi et al (95-97) studied the α- and β- relaxations during the cure of epoxy resins at frequencies up to 10 GHz. Complex permittivity data were described using two Havriliak – Negami equations (§ 4.2.3). King et al (98) developed and tested a microwave sensor and used it for in – situ cure monitoring. Mangion and Johari (99) studied the effects of different amine combinations on the curing of an epoxy resin. The same group studied the effect of different epoxy/amine ratios on the cure (100). For the studied system (DGEBA + DDM, see Table 1-III for definitions) the increase of the DGEBA:DDM ratio caused the cure to slow down and stop at lower conversions. When the ratio exceeded 4:1, no vitrification was observed. Parthun and Johari (101) gave a general formalism for the complex permittivity evolution under non-isothermal conditions starting from the complete differential of the complex permittivity ε^* with respect to time and temperature:

* Micromet Eumetric System II Dielectrometer, by Micromet Instrumets, Inc.

$$d\varepsilon^*(\omega,t,T) = \left.\frac{\partial\varepsilon^*(\omega,t,T)}{\partial T}\right|_t dT + \left.\frac{\partial\varepsilon^*(\omega,t,T)}{\partial t}\right|_T dt \qquad (1.21)$$

where ω is the angular frequency. The above derivative does not contain the effect of pressure on ε^*, which has been studied by the same group (102) and proved to be insignificant compared to the effects of temperature and reaction.

Table 1-III: *Some of the most popular epoxy/amine compounds found in literature*

Epoxy systems

Full name	Abbreviation	Commercial name(s)	Provider	Ref.
Diglycidyl Ether of Bisphenol A	DGEBA DGEBA BADGE	Epon 828 Epon 825 DER 332	Shell[1] Shell[1] Dow[2]	86, 89, 90, 92, 93, 95, 99, 111
Tetra – Glycidyl – 4-4′ – Diamino Diphenyl Methane	TGDDM	MY720	Ciba-Geigy[3]	86, 88, 91
Phenyl Glycidyl Ether	PGE	-	Aldrich[4]	104, 105

Amines

Full name	Abbreviation	Commercial name(s)	Provider	Ref.
4.4′ – Diamino Diphenyl Sulfone	DDS	HT976	Ciba-Geigy[3] Aldrich[4]	86, 88, 90, 91, 92, 93, 99, 111
4,4′ – Methylene Dianiline	MDA	-	Aldrich[4]	104, 105, 108
4,4′ – Diamino Diphenyl Methane	DDM	-	Aldrich[4]	89, 99

Mijovic and co-workers utilised the complex impedance and analysed cure monitoring data by using equivalent circuits (103-108). They calculated the apparent resistivity from the maximum of the imaginary impedance plot and correlated the material state with the imaginary impedance signal (103, 104). Vitrification was also identified as a

[1] full name: Shell Chemicals (URL: www.shellchemicals.com)
[2] full name: Dow Chemical Company (URL: www.dow.com)
[3] full name: Ciba Specialty Chemical inc. (URL: www.cibasc.com)
[4] full name: Sigma – Aldrich co. (URL: www.sigmaaldrich.com)

shoulder in the imaginary impedance curves (106, 108). Complex impedance appears to be more appropriate than complex permittivity in describing materials with high concentrations of charged species. Most commercial epoxy systems fall into that category. Williams et al used both complex permittivity and complex impedance (109) to study an epoxy/boroxine mixture. From complex permittivity they derived information about the vitrification of the system while from complex impedance they calculated the conductivity of the system. Bartolomeo et al (110) used a modified WLF equation and produced models for isothermal and non-isothermal cure cycles. Eloundou (111) used a normalised version of the Di Benedetto equation to correlate dielectric spectra with conversion. Both models are discussed in the following section.

Dielectric cure monitoring studies on phase separating thermoset/thermoplastic blends have also been published. Maistros and co-workers (83, 112) used models based on the Maxwell – Wagner – Sillars (MWS) polarisation mechanism to study rubber modified thermoset systems (§ 4.2.4). The MWS model was also applied by Poncet et al (113) and Bonnet et al (114) in cure monitoring studies of thermoset/thermoplastic systems. In both publications the formation of the second phase was identified by the increase in the real permittivity curve. In (114) a comparison of the detected times of phase separation between the dielectric measurement and other standard techniques, like rheology is also presented. The results from all techniques are in agreement. Alig and Jenninger (115) studied a thermoset/thermoplastic blend. They disentangled the contributions from the two phases on the permittivity curves and predicted the T_g advancement of each phase by fitting the complex permittivity curves with a combination of Havriliak – Negami elements (§ 4.2.3). The obtained results were in close agreement with calorimetric measurements of T_g. However the complex permittivity model consisted of 25 parameters in total and the information on the fitting procedure is limited.

The cure monitoring of glass fibre reinforced composites illustrated the negligible influence glass fibres have on the dielectric signal. Nixdorf and Busse (116) studied glass fibre composites using parallel plate sensors, while Bang et al (117) performed experiments in an autoclave. On the other hand, carbon fibre composites are more difficult to monitor since the highly conductive carbon fibres can short-circuit the dielectric sensor. This problem is usually overcome by placing a protecting film or cloth on the sensor so that only the resin and not the fibres contact the sensor surface. Kenny et al (118) produced full chemorheological and dielectric models of a carbon

fibre prepreg. Maistros and Partridge (119) also produced analytical models for the cure of carbon fibre composites and successfully monitored autoclave cure cycles (120). McIlhagger et al (121) monitored the cure of carbon fibre composites using parallel plate sensors. A polyimide film was used to insulate the plates from the carbon fibres.

1.5.3 Modelling the cure process using dielectric signals

The main goal of all dielectric cure monitoring studies is to connect the obtained signals with the cure process. This is performed by correlating a measurement parameter with a material state parameter, such as the reaction conversion.

Sheppard and Senturia (122) used a modified version of the Onsager equation (6) and correlated the relaxed permittivity ε_r with the degree of cure for isothermal conditions:

$$\frac{(\varepsilon_r - \varepsilon_u)(2\varepsilon_r + \varepsilon_u)}{\varepsilon_r(\varepsilon_u + 2)^2} = \frac{N_\mu(\alpha)\langle\mu\rangle^2}{9\varepsilon_0 k}\left(\frac{1}{T} - \frac{1}{T_{\text{int}}(\alpha)}\right) \tag{1.22}$$

where ε_0 is the permittivity of free space (8.854×10^{-12} F/m), N_μ is the concentration of the dipoles, $\langle\mu\rangle$ is the average dipole moment, k is Boltzmann 's constant (1.4×10^{-23} J/K) and T_{int} an adjustable parameter which has a linear dependence on the degree of cure.

Nass and Seferis (88) used the relaxation time τ as the dielectric parameter and derived the following equation:

$$\frac{1}{\tau} = \frac{1}{\tau_\infty} + \left(\frac{1}{\tau_0} - \frac{1}{\tau_\infty}\right)(1-\alpha)^\Phi \tag{1.23}$$

where τ_0 and τ_∞ are the relaxation times at the beginning and at the end of cure and Φ is a constant termed "entanglement" factor. A modified version of the above equation was used to describe non isothermal cure.

Day (93) used the normalised conductivity as a cure index for both isothermal and dynamic cure profiles. Maffezzoli et al (35) used the normalised resistivity signal and proposed the following relationship for isothermal cure:

$$\alpha(t) = \alpha_{\max}\frac{\log\rho(t) - \log\rho_0}{\log\rho_{\max} - \log\rho_0}\left(\frac{\log\rho_{\max}}{\log\rho(t)}\right)^\beta \tag{1.24}$$

where α_{max} is the maximum conversion for a particular temperature, ρ is the ionic resistivity calculated from the dielectric signal and β is an empirical parameter. The subscripts *0* and *max* correspond to the beginning and end of the cure respectively.

Pascault and Williams used a modified version of the Di Benedetto equation (123) and related the ionic conductivity σ with conversion α:

$$\frac{\log\sigma(t)-\log\sigma_0}{\log\sigma_{\max}-\log\sigma_0}=\frac{\lambda_{Cp}\alpha(t)}{1-(1-\lambda_{Cp})\alpha(t)} \tag{1.25}$$

In the above equation, the subscripts have the same meaning as in eq. (1.24). λ_{Cp} is the ratio of the heat capacity of the fully cured material to the heat capacity of the uncured material. Eq. (1.25) was employed by Eloundou (111) who used the relaxation time instead of ionic conductivity.

Eq. (1.24) was successfully extended to non-isothermal conditions by modelling the temperature dependence of resistivity using a WLF - like equation:

$$\rho(T)=\rho_0\exp\left(\frac{C_1(T-T_{g,0})}{C_2+T-T_{g,0}}\right) \tag{1.26}$$

where C_1 and C_2 are fitting parameters. Bartolomeo et al (110) used similar equations, replacing ionic resistivity with ionic conductivity.

Recently, Skordos and Partridge proposed a non – parametric method for relating the dielectric signal to the reaction conversion (124). The method treats the derivative of the maximum point of the imaginary impedance spectrum in the same way as the heat flow in a calorimetric experiment. It has been applied successfully in isothermal and non – isothermal cure conditions.

1.5.4 Dielectric cure monitoring studies on industrial environment

The use of dielectric cure monitoring in industrial processes has been documented since the late 80s. Most of the published studies refer to quality assurance and on – line monitoring of the cure process. The ultimate aim is the active control of the cure process using state – based models. Table 1-IV shows the different monitoring levels, with the techniques known to have been applied in the particular situation, to date.

Off – line cure monitoring measurements are used for building cure kinetic models and associating the monitoring signal to these models. They are mainly performed in laboratories and thus are capable of exhibiting high accuracy. Small material quantities are used for the experiments. On – line monitoring gives information about the state of

the actual curing part. When applied on the production line, it has the potential to detect possible discrepancies in the curing component. Therefore, on – line monitoring offers the chance of manually adjusting the cure process. In state based control monitoring, material state models are used in order to translate the dielectric signal into a cure index (5). The cure index is fed to a control algorithm which acts on the process accordingly, altering one or many parameters (for example, temperature or pressure). State based control systems are the ultimate aim for any cure monitoring technique. Up to the present time, state based control systems are more in the state of feasibility studies.

Table 1-IV: *Different levels of dielectric cure monitoring*

Monitoring level	Application environment	Purpose	Applicable techniques
Off – line	Laboratory	Research	All
On – line	Production	Process monitoring	Dielectric Ultrasound FTIR
State based control	Production	Process control	Dielectric, Ultrasound or FTIR in conjunction with heat transfer and material state models

Kranbuehl et al (125) monitored the autoclave cure of a 192 ply carbon fibre epoxy composite part using 4 sensors. The same group presented a state based control system for RTM cure (126). A series of dielectric sensors were placed underneath the bottom plate of the mould, as shown in Figure 1-9.

Small holes allowed the resin to reach the sensors. The control system target was to keep the resin viscosity at low values until the fabric impregnation had finished by slowly increasing the temperature. A further condition ensured that the curing system had to pass through a specific temperature – conversion point. This point (35% conversion at 121°C) was chosen, based on a heat transfer model.

Melotik et al (127) mounted dielectric sensors on the RTM tool. They performed on – line measurements focusing on the point of minimum viscosity and the vitrification point.

Methven et al (128) monitored a pultrusion line, using dielectric measurements at microwave frequencies. The measurements were conducted after the resin had left the die. They investigated the feasibility of a control system, based on the electric power supplied to the die.

Maguire et al (129) described in detail the architecture of a state based control system for thermoset processing. The algorithm breaks the cure cycle in phases and applies several criteria for the passing from one phase to the next. Light scattering measurements were taken in conjunction with the dielectric monitoring. The developed system was tailored to the cure of polyimide resins.

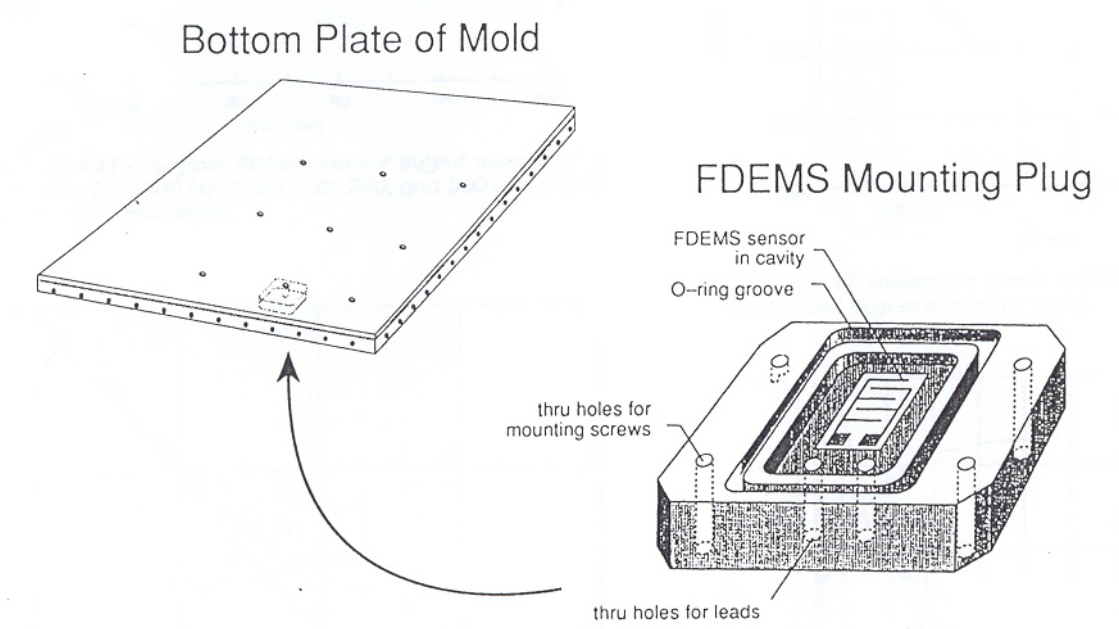

Figure 1-9 *Configuration for monitoring RTM. Reproduced after Kranbuehl (126)*

Chailleux et al (130) placed dielectric, piezoelectric and fibre – optic sensors in a model mould and compared the difference responses. The dielectric sensor gave information about the cure advancement, the ultrasonic signal correlated well with the mechanical properties of the component and the fibre – optic sensor could monitor the density changes in the material.

Finally, Shtrauss et al (131) described an on – line indirect cure monitoring system. He tested the system by curing two epoxy/amine thermosets in a small cylindrical mould. In a recent publication (132) the same author considers the use of neural networks in cure monitoring studies.

1.6 Thesis structure

The main body of this study consists of seven chapters:

- After the present chapter, where an overview of thermoset cure monitoring is presented, chapter 2 reviews the experimental techniques which use temperature modulated temperature profiles, focusing on Modulated Differential Scanning Calorimetry (MDSC).
- Chapter 3 gives information about the materials, sensors and apparatuses that were used in this study.
- Chapter 4 is divided in three parts: First, a brief review of the polarisation phenomena that affect the dielectric response of thermosetting systems is given. Then, simulated complex permittivity signals are translated in complex impedance curves and the equivalent circuit modelling of the impedance spectra is presented. Finally, in the third part, the building of a numerical procedure, based on genetic algorithms, that automatically models consecutive experimental spectra is outlined.
- In Chapter 5 the results from calorimetric and dielectric experiments are presented. A cure kinetics model is constructed and the vitrification point during cure is measured by MDSC. The trends observed in the impedance curves at the time and the frequency domain are discussed.
- Chapter 6 present the results from the modelling of the impedance curves. A correlation between the Imaginary Impedance Maximum (IIM) and the reaction conversion is established and an explanation is proposed.
- Chapter 7 introduces a new experimental technique. Temperature Modulated Dielectric Analysis (TMDA) is based on the theory and methodology used in MDSC. A new experimental cell is designed and built. Modulated dielectric signals are deconvoluted into an underlying and a modulated component. The correlation of the amplitude of the modulated component with the reaction conversion is investigated.

Several issues concerning the further development of TMDA as well as an overall discussion of the results of this study are presented in chapter 8. Chapter 9 summarises the suggestions for further investigation arising from the overall discussion of the results. Finally, the main conclusions of the work are listed in Chapter 10.

2 The use of Temperature Modulation in Experimental Techniques

2.1 Scope and objectives

The chapter outlines currently developed experimental techniques which employ temperature oscillations. Main emphasis is placed upon Modulated Differential Scanning Calorimetry™ (MDSC), which provides the basis of the signal analysis procedure of Temperature Modulated Dielectric Analysis (TMDA) presented in Chapter 8.

2.2 Historical background of temperature modulation techniques

Temperature modulation techniques were first reported in 1910 by Corbino (133). He used resistive wires and produced temperature oscillations by passing an AC current of small amplitude superimposed on a DC current. Using the modulated component of temperature exhibited by the wires he managed to measure accurately the heat capacity of metals at high temperatures. An improvement of experimental equipment widened the measuring capabilities of temperature modulated techniques to non-conducting materials as well.

Modulated dilatometry first appeared in 1965 (134). Temperature modulations enabled the accurate measurement of the thermal expansion coefficient in cases where other physicochemical events also alter the dimensions of the material. Other measurements, such us resistivity or radiation absorbance have also been reported (134).
Recent reviews by Kraftmakher (134) and Gmelin (135) describe the wide variety of relevant techniques developed throughout the years for calorimetric and dilatometric studies.

2.2.1 Original idea for temperature modulation techniques

In all the experimental techniques that involve temperature modulations the temperature experienced by a sample under test can be described by the following equation:

$$T(t) = T_0 + rt + T_{\mathrm{mod}}(t) \tag{2.1}$$

where T is the temperature, t is the time, T_0 is some initial temperature, r is the linear rate of temperature change and T_{mod} is a periodic function of time. It usually describes a sinusoidal change of temperature but it can also take other forms, like a sawtooth modulation (136-137). For sinusoidal modulation T_{mod} has the following form:

$$T_{\mathrm{mod}}(t) = A_T \sin\left(\frac{2\pi}{P}t\right) \tag{2.2}$$

where A_T is the amplitude of the modulation and P is the period.
The frequency of the temperature modulation will be:

$$f_T = \frac{\omega_T}{2\pi} = \frac{1}{60P} \tag{2.3}$$

where f_T is the frequency and ω_T is the angular frequency. In the last equation P is measured in minutes.

The heat flow balance of an inert material with constant heat capacity will be:

$$\frac{dQ}{dt} = mc_p\frac{dT}{dt} + \frac{dQ_{losses}}{dt} \tag{2.4}$$

where Q is the total heat input, m is the material mass, c_p is the specific heat capacity and Q_{losses} represent the heat losses. If the temperature change is relatively small, Q_{losses} can be written as a Taylor expansion series:

$$\frac{dQ_{losses}}{dt} = \left.\frac{dQ_{losses}}{dt}\right|_{T=T_u} + \frac{d}{dT}\left(\left.\frac{dQ_{losses}}{dt}\right|_{T=T_u}\right)(T - T_u) + \cdots \Rightarrow$$
$$\frac{dQ_{losses}}{dt} = k_1 + k_2 (T - T_u) \tag{2.5}$$

where T_u is a mean temperature very close to T_0 and k_1, k_2 are constants: k_1 represents the heat losses at a specific temperature T_u and k_2 can be interpreted as a heat transfer coefficient (134).

When a temperature profile of eq. (2.1) is imposed on the material, the heat flow balance becomes:

$$\frac{dQ}{dt} = mc_p\left(r + \frac{dT_{\text{mod}}}{dt}\right) + k_1 + k_2\left(rt + T_{\text{mod}}\right) \tag{2.6}$$

In the last equation the underlying temperature T_u is considered to be equal to T_0. This assumption is valid when the amplitude A_T is small.

When T_{mod} has a simple sinusoidal form (eq. (2.2)) the heat balance can be written in the following way:

$$\frac{dQ}{dt} = \underbrace{mc_p r + k_1 + k_2 rt}_{\text{underlying heat flow}} + \underbrace{A_T\sqrt{\left(mc_p\omega_T\right)^2 + k_2^2}\sin\left(\omega_T t - \varphi\right)}_{\text{modulating heat flow}} \tag{2.7}$$

where:

$$\tan\varphi = -\frac{mc_p\omega_T}{k_2} \tag{2.8}$$

The heat flow has an underlying component and a modulated one.

The basic equation of temperature modulation techniques is taken from the amplitude A_Q of heat flow modulation (134):

$$A_Q = A_T\sqrt{1 + \left(\frac{mc_p\omega_T}{k_2}\right)^2} \tag{2.9}$$

When the heat losses are negligible compared with the heat absorbed by the material the above equation is simplified:

$$mc_p\omega_T >> k_2 \Rightarrow c_p = \frac{k_2 A_Q}{m\omega_T A_T} \tag{2.10}$$

From the last equation the specific heat capacity of the material is calculated.

The above analysis is based on three main assumptions:

- There is no temperature gradient within the material
- Temperature changes slowly during the experiment (low r and A_T values)
- Heat losses are negligible compared to heat absorbed by the material or have a known constant value

The first assumption ensures that the temperature in the material is uniform. Simon (138) reported the maximum acceptable dimensions of several materials required in order for the measured heat capacity to have an error of 1%, if none of the other error factors are taken into account. These dimensions usually translate to sample masses in the range of 5 – 20 mg for polymers (138-140).

The slow temperature changes put restrictions on the underlying heating rate and the modulation amplitude that can be used. The changes due to r and A_T need to be small compared with the overall material temperature so that no higher terms of the Taylor expansion of Q_{losses} become important (as expressed in eq. (2.5)). Furthermore, steady state has to be reached for the analysis to be valid (139-143). The important issue of linearity is discussed in a separate section (§ 2.3.2).

The third assumption concerns the heat losses. It usually refers to the experimental apparatus used for measurements and is affected by the experimental cell design (138-141).

2.3 Modulated Differential Scanning Calorimetry™

The best known application of temperature modulation experimental techniques in the characterisation of thermosetting materials is Modulated Differential Scanning Calorimetry™ (MDSC). In MDSC, a temperature profile described by eq. (2.1) is employed (141). The aim is to separate the measured heat flow into a non-modulated component and a modulated one as was demonstrated previously. The difference compared with the previous analysis (§ 2.2.1) is that thermosets undergo chemical and physical changes during cure. This introduces another term in the heat flow balance equation and adds the complexity of a continuously changing heat capacity.

The following analysis refers to a heat flux calorimeter where the temperature difference between the sample and the reference side is being measured and used to determine the heat flow. An analytical description of the apparatus is given in § 3.4.3.

The cell of a heat flux DSC is shown in Figure 2-1.

2.3.1 Theory

In general the heat flow balance for a material in a heat flux DSC is similar to eq. (2.4) with the addition of an extra term accounting for the heat flow due to latent processes:

$$\frac{dQ}{dt}(t,T) = mc_p(t,T)\frac{dT}{dt} + \frac{dQ_{losses}}{dt}(t,T) + \frac{dQ_{latent}}{dt}(t,T) \qquad (2.11)$$

where Q_{latent} is the heat arising from physicochemical events like a transition or a reaction. The dependence on time and temperature has been denoted in the above equation.

The heat from latent processes like chemical reaction and vitrification is usually a complex function of time and temperature. Such behaviour is expected for thermosets. During a polymerisation reaction the material is in a continuously changing state (1) and heat is released. During vitrification the material enters the glassy state and moves away from equilibrium (8, 43).

From the assumptions stated previously (§ 2.2.1), the most critical requirement for the MDSC analysis is that all the processes under investigation need to be slow enough so that the material will not change significantly during a specific measuring time interval (139-144). The modulation frequency f_T is a measure of how slow the changes in the material should be in order to satisfy this requirement. Processes should normally have a characteristic frequency much lower than f_T. If this requirement is met by the material, the temporal dependence of the heat flow balance will be contained in the temperature equation:

$$\frac{dQ}{dt}(T(t)) = mc_p(T(t))\frac{dT}{dt} + \cancel{\frac{dQ_{losses}}{dt}(T(t))} + \frac{dQ_{latent}}{dt}(T(t)) \qquad (2.12)$$

The heat losses term will be neglected in the following analysis. This does not compromise the generality of the theory, since all the heat losses will be incorporated in a single coefficient relating the temperature and the sample heat flow. It is implied though that heat losses are linearly related with the heat flow (i.e. eq. (2.5) holds).

In a heat flux DSC the temperature difference between the sample under test and a reference sample is being measured. The measured heat flow will be proportional to that difference:

$$H_{flow}(t) = \lambda\left(T_S(t) - T_R(t)\right) = \lambda\Delta T \qquad (2.13)$$

where T_R is the temperature of the reference and T_S the temperature of the sample. In eq. (2.13) λ is an overall heat transfer coefficient accounting for all the heat losses. Its

value depends on the experimental cell material and design. It also encompasses the influence of other parameters such as the material of the sample holder or any cell asymmetry.

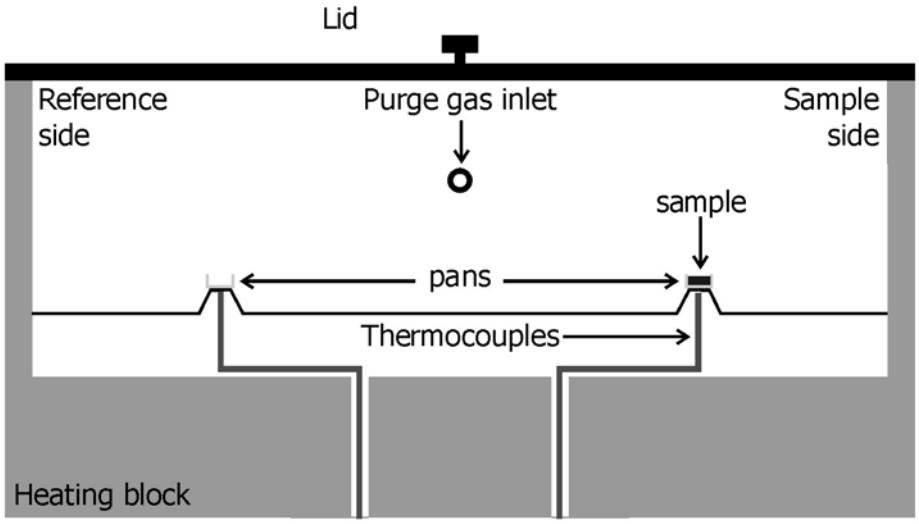

Figure 2-1 *Heat flux DSC cell*

Eq. (2.12) is applied to both reference and sample sides. Combination with eq. (2.13) and use of absolute heat capacities C_{RS} and C_{SS} values, for the reference and sample sides respectively, yields (145):

$$C_{RS}\frac{d\Delta T(t)}{dt} - \lambda\Delta T(t) = (C_{SS} - C_{RS})\frac{dT_S(t)}{dt} + \frac{dQ_{latent}}{dt}(T_S(t)) \qquad (2.14)$$

The above differential equation is the basic equation of MDSC. In general it cannot be solved analytically. Numerical solutions have been reported for various cases (142-145).

If Q_{latent} can be treated the same way as Q_{losses} in the previous section (see eq. (2.5)) then:

$$\frac{dQ_{latent}}{dt} = f_1 + f_2\left[rt + A_T\sin(\omega_T t)\right] \qquad (2.15)$$

where f_1 is the average latent heat flow at the temperature range of interest and f_2 is the rate of change of Q_{latent} in that temperature range.

When T_S follows the temperature profile described by eqs. (2.1) and (2.2) the differential eq. (2.14) accepts the following steady state* solution:

$$\Delta T(t) = \frac{(C_{SS} - C_{RS})r + f_1}{\lambda} + \frac{rf_2}{\lambda}\left(t - \frac{C_{RS}}{\lambda}\right) + A_{\Delta T}\sin(\omega_T t + \delta_{\Delta T}) \qquad (2.16)$$

where

$$A_{\Delta T} = \frac{\omega_T A_T}{\lambda}\frac{\sqrt{(C_{SS} - C_{RS})^2 + \left(\frac{f_2}{\omega_T}\right)^2}}{\sqrt{1 + \left(\frac{\omega_T C_{RS}}{\lambda}\right)^2}} \qquad (2.17)$$

and

$$\tan\delta_{\Delta T} = \frac{\lambda}{\omega_T C_{RS}}\frac{\omega_T(C_{SS} - C_{RS}) - \frac{\omega_T C_{RS}}{\lambda}f_2}{\omega_T(C_{SS} - C_{RS}) + \frac{\lambda}{\omega_T C_{RS}}f_2} \qquad (2.18)$$

If the reference side contains an empty pan and the sample side contains the material under test inside an identical pan, the above equations are simplified:

$$\Delta T(t) = \frac{C_S r + f_1}{\lambda} + \frac{rf_2}{\lambda}\left(t - \frac{C_{RS}}{\lambda}\right) + A_{\Delta T}\sin(\omega_T t + \delta_{\Delta T}) \qquad (2.19)$$

$$A_{\Delta T} = \frac{\omega_T A_T}{\lambda}\frac{\sqrt{C_S^2 + \left(\frac{f_2}{\omega_T}\right)^2}}{\sqrt{1 + K^2}} \qquad (2.20)$$

$$\tan\delta_{\Delta T} = \frac{1}{K}\frac{\omega_T C_S - Kf_2}{\omega_T C_S + \frac{f_2}{K}} \qquad (2.21)$$

Here C_s is the heat capacity of the sample and K is a dimensionless constant characterising the calorimeter:

$$K = \frac{\omega_T C_{RS}}{\lambda} \qquad (2.22)$$

K can be seen as a ratio of two heat transfer coefficients. The nominator gives a measure of the heat that could be transferred to a material during one cycle. The

* The transient terms are not included in the solution. The general solution can be found in (142) and (145).

denominator describes the ability of the instrument to transfer heat to the material. *K* is usually thought of as a measure of how far from "ideal" the calorimeter is (145).
Eq. (2.19) has an underlying (the first two terms) and a modulating part (last term):

$$\overline{\Delta T} = \frac{C_S r + f_1}{\lambda} + \frac{r f_2}{\lambda}\left(t - \frac{C_{RS}}{\lambda}\right) \tag{2.23}$$

$$\widetilde{\Delta T} = A_{\Delta T}\sin\left(\omega_T t + \delta_{\Delta T}\right) \tag{2.24}$$

From these two terms, an underlying and a modulated heat capacity can be calculated for the material under test. Table 3.1 lists the resulting heat capacity values for various conditions.

Table 2-I : *Mathematical expressions for the heat capacity calculation using MDSC*

Case	Underlying component	Modulated component
General case	$\overline{C_S} = \frac{\lambda\overline{\Delta T}}{r} - \frac{f_1}{r} - f_2\left(t - \frac{C_{RS}}{\lambda}\right)$	$\widetilde{C_S} = \sqrt{\left(\frac{\lambda A_{\Delta T}}{\omega_T A_T}\right)^2\left(1-K^2\right) - \left(\frac{f_2}{\omega_T}\right)^2}$
"Ideal" calorimeter $\lambda \gg \omega_T C_{RS} \Leftrightarrow K \to 0$	$\overline{C_S} = \frac{\lambda\overline{\Delta T}}{r} - \frac{f_1}{r} - f_2\left(t - \frac{C_{RS}}{\lambda}\right)$	$\widetilde{C_S} = \sqrt{\left(\frac{\lambda A_{\Delta T}}{\omega_T A_T}\right)^2 - \left(\frac{f_2}{\omega_T}\right)^2}$
Inert material $\frac{dQ_{latent}}{dt} = 0$	$\overline{C_S} = \frac{\lambda\overline{\Delta T}}{r}$	$\widetilde{C_S} = \frac{\lambda A_{\Delta T}}{\omega_T A_T}\sqrt{1-K^2}$
Inert material in an "ideal" calorimeter $\frac{dQ_{latent}}{dt} = 0, K \to 0$	$\overline{C_S} = \frac{\lambda\overline{\Delta T}}{r}$	$\widetilde{C_S} = \frac{\lambda A_{\Delta T}}{\omega_T A_T}$
Constant heat flow from latent processes $\frac{dQ_{latent}}{dt} = f_1$	$\overline{C_S} = \frac{\lambda\overline{\Delta T}}{r} - \frac{f_1}{r}$	$\widetilde{C_S} = \frac{\lambda A_{\Delta T}}{\omega_T A_T}\sqrt{1-K^2}$
Constant heat flow from latent processes and "ideal" calorimeter $\frac{dQ_{latent}}{dt} = f_1, K \to 0$	$\overline{C_S} = \frac{\lambda\overline{\Delta T}}{r} - \frac{f_1}{r}$	$\widetilde{C_S} = \frac{\lambda A_{\Delta T}}{\omega_T A_T}$

The most useful cases are when *K* is either known or taken as zero. This is usually not difficult since the material of the pan is a well characterised metal (for example Al, Cu

or Au) and λ is determined through calibration. Furthermore the heat flow from latent processes is usually considered constant during one cycle. The latter is true for thermosets when the rate of reaction is not too high and the temperature modulation amplitude has a low value compared to the underlying temperature. In such cases the heat flow coming from latent processes does not affect the modulating part of ΔT and the heat capacity of the material can be resolved. This enables the separation of the heat flow signal to the two components described in eq. (2.12) to be made.

Typical MDSC experimental values have been used in order to investigate which of the expressions listed in Table 2-I is valid for thermoset cure. An analytic cure kinetics model developed for RTM6 resin was used for the simulation of the reaction heat flow (19). A typical value for λ is taken from (145). All parameters are listed in Table 2-II.

Table 2-II : *Typical parameter values for an MDSC experiment on an epoxy*

λ (W/°C)	**r (°C/min)**	**A_T (°C)**	**P (min)**	**C_{pan} (J/°C)**
850	1	1	1	0.9
C_S (J/°C)	**C_R (J/°C)**	**f_1 (J/min)**	**f_2 (J/min.°C)**	**ΔH_{total} (J/g)**
2.2	0	0.391	4.65×10^{-5}	440

The K constant has a value of 1.1×10^{-4}. Since the square of K is subtracted from one (general case on Table 2-I) the influence on the heat capacity calculation is negligible. This means that the calorimeter can be considered ideal. The corresponding heat capacities are:

$$\overline{C_S} = \frac{\lambda \overline{\Delta T}}{r} - \frac{f_1}{r} - f_2\left(t - \frac{C_{RS}}{\lambda}\right) = 2.59 - 0.39 - 5 \times 10^{-5} = 2.20 \text{ J/°C}$$

$$\widetilde{C_S} = \sqrt{\left(\frac{\lambda A_{\Delta T}}{\omega_T A_T}\right)^2 \left(1 - K^2\right) + \left(\frac{f_2}{\omega_T}\right)^2} = \sqrt{\left(2.20\right)^2 1 + \left(7.4 \times 10^{-6}\right)} = 2.20 \text{ J/°C}$$

Both values are equal to the value set in Table 2-II. From the first calculation the influence of the reaction on the underlying C_S is evident. If the heat of reaction was not taken into account a C_S value of 2.59 J/°C would have been calculated. The error in that estimation is about 18 %. On the other hand, the modulated C_S is much less

sensitive to the effect of the reaction since only f_2 is involved in the calculation. Provided that K is very small and that the heat from the reaction does not change significantly over one temperature cycle, the modulated C_S gives a straightforward estimation of the sample heat capacity. The reaction effect can then be extracted from the underlying signal by a simple subtraction.

2.3.2 Linearity of MDSC experiments

The linearity of MDSC has already been implied by eq. (2.13). The physical meaning of this equation is that the signal from MDSC is proportional to the applied perturbation. This is generally true for cases where no transitions occur (147). In transition areas, the nature of the transition designates the thermal response of the material (147 - 149). In the case of thermosets, the polymerisation reaction is essentially a nonlinear transformation (1). Vitrification is also a nonlinear process (150). On the other hand both chemical reaction and vitrification are slow enough processes that can be linearised successfully in time intervals sufficient for accurate MDSC analysis (144, 145, 147, 151).

The demand for a linear response sets constraints on the modulation amplitude A_T and linear heating rate r. The modulated heat flow must be independent of A_T (144).

A simple way of visual inspection of the linear or nonlinear response of any technique that uses temperature modulations is the use of Lissajous plots (152). A Lissajous curve is defined by the following equations (153):

$$\begin{aligned} x(t) &= a_x \sin(\omega_x t + \delta_x) \\ y(t) &= a_y \sin(\omega_y t + \delta_y) \end{aligned} \tag{2.25}$$

Here a_x and a_y are constants, ω_x and ω_y are angular frequencies and δ_x and δ_Y are phase shifts.

In the MDSC case, the temperature evolution in the sample can be written as follows:

$$\begin{aligned} T_S(t) &= T_0 + rt + A_T \sin(\omega_T t) \Rightarrow \\ T_S(t) - T_m(t) &= A_T \sin(\omega_T t) \end{aligned} \tag{2.26}$$

where T_m is the average temperature over one cycle.

For linear behaviour, the heat flow will follow eq. (2.13):

$$H_{flow}(t) = \lambda \Delta T \Rightarrow$$
$$H_{flow}(t) = \lambda\left(\overline{\Delta T}(t) + A_{\Delta T}\sin\left(\omega_T t + \delta_{\Delta T}\right)\right) \Rightarrow \quad (2.27)$$
$$H_{flow}(t) - \lambda\overline{\Delta T}(t) = \lambda A_{\Delta T}\sin\left(\omega_T t + \delta_{\Delta T}\right)$$

Eq. (2.26) and (2.27) are the parametric form of a Lissajous curve. In the general form, the curve will be a skewed ellipse, like the one shown in Figure 2-2a. If the calorimeter is "ideal" (i.e. if $K \rightarrow 0$) then the figure will be an ellipse with the two axes giving the temperature and the heat flow modulation. If there is a nonlinear component in the signal the elliptical shape becomes distorted. An example of a Lissajous curve of a nonlinear signal is given in Figure 2-2b.

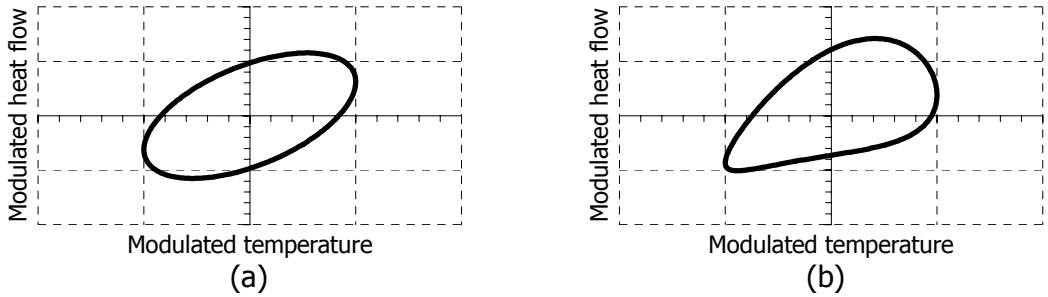

Figure 2-2 *Lissajous curve for linear (a) and nonlinear (b) response. In the nonlinear case a second term with twice the modulated frequency and ¼ of the amplitude of the 1st harmonic is added to the response.*

For the case considered previously (Table 2-II) the calorimeter is "ideal" (K = 1.1×10^{-4} which gives $\delta_{\Delta T}$ = 89.98°). The corresponding Lissajous curve, given in Figure 2-3, is an ellipse.

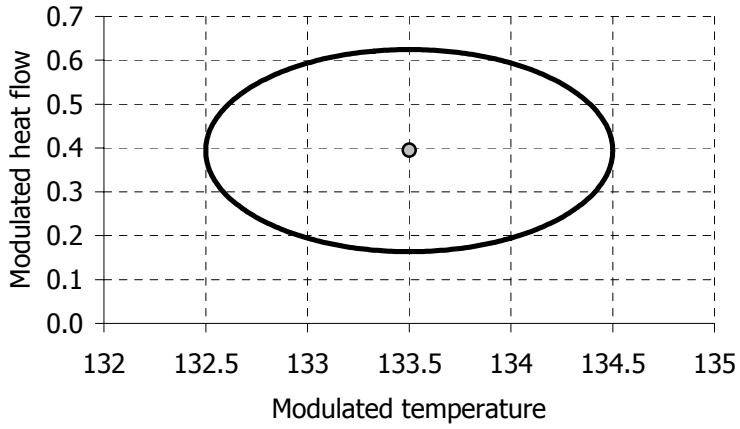

Figure 2-3 *Lissajous curve for the case described in Table 2-II.*

2.3.3 Signal deconvolution techniques

Before any analysis is performed on the MDSC signal, a Fourier transformation on the acquired data should be performed in order to ensure the absence of any nonlinear terms (higher order harmonics).

In general, the heat flow can be written as a Fourier series (146):

$$H_{flow}(t) = \overline{H_{flow}}(t) + \sum_{n=1}^{\infty}\left(a_n \sin(n\omega_T t) + b_n \cos(n\omega_T t)\right) \tag{2.28}$$

where the amplitudes a_n and b_n are given by the relations:

$$a_n = \frac{1}{2P}\int_{-\frac{P}{2}}^{\frac{P}{2}} H_{flow}(t)\sin(n\omega_T t)\,dt \tag{2.29}$$

$$b_n = \frac{1}{2P}\int_{-\frac{P}{2}}^{\frac{P}{2}} H_{flow}(t)\cos(n\omega_T t)\,dt \tag{2.30}$$

When linearity is assured only the first terms of the infinite series of eq. (2.28) are considered (n = 1). The heat flow will be expressed by eqs. (2.13) and (2.19) as a sum of a modulated and a non – modulated component. Following the previous analysis:

$$H_{flow}(t) = \lambda\left(\overline{\Delta T}(t) + \widetilde{\Delta T}(t)\right) \tag{2.31}$$

A more convenient way to express the above equation is:

$$H_{flow}(t) = \lambda\left(\overline{\Delta T}(t) + a_1 \sin(\omega_T t) + b_1 \cos(\omega_T t)\right) \tag{2.32}$$

Direct comparison between the last two equations yields the values of parameters a_1 and b_1:

$$a_1 = A_{\Delta T}\cos\delta_{\Delta T} \tag{2.33}$$

$$b_1 = A_{\Delta T}\sin\delta_{\Delta T} \tag{2.34}$$

If n_p is the number of points per temperature cycle the non – modulating component can be calculated by averaging the signal:

$$\overline{H_{flow}}(t) = \lambda\overline{\Delta T}(t) = \frac{1}{n_p}\sum_{i=1}^{n_p} H_{flow}(t_i) \tag{2.35}$$

Here $H_{flow,i}$ are the experimental points. In every average calculation, all the experimental points within one cure cycle are needed. This means that the first calculated average will refer to the time t = *0.5*Period*.

The non – modulating part can then be subtracted from the total heat flow:

$$\widetilde{H_{flow}}(t) = H_{flow}(t) - \overline{H_{flow}}(t) \tag{2.36}$$

Using this modulated heat flow signal and the eqs. (2.29) and (2.30) the mean values of the parameters a_1 and b_1 can be evaluated (the integrals become sums):

$$\langle a_1 \rangle = \frac{1}{2n_p} \sum_{i=1}^{n_p} \widetilde{H_{flow}}(t_i) \sin(\omega_T t_i) \tag{2.37}$$

$$\langle b_1 \rangle = \frac{1}{2n_p} \sum_{i=1}^{n_p} \widetilde{H_{flow}}(t_i) \cos(\omega_T t_i) \tag{2.38}$$

From a_1 and b_1 the amplitude and the phase shift can be calculated from eqs. (2.33) and (2.34).

In Figure 2-4 the heat flow produced by the parameters given in Table 2-II is analysed using the above procedure.

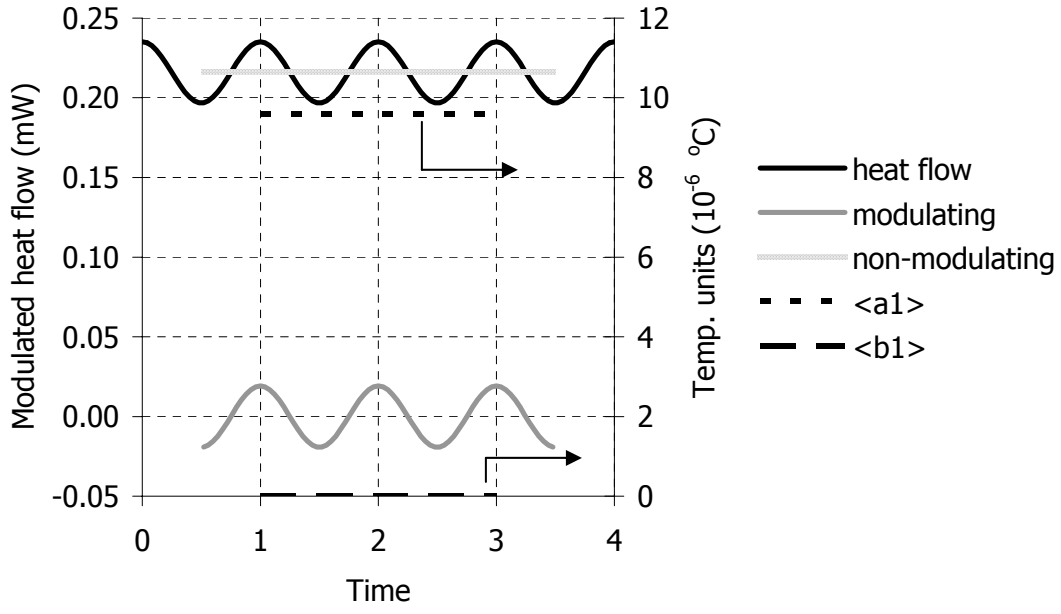

Figure 2-4 *Fourier analysis of the MDSC signal. The simulation parameters are given in Table 2-II*

The parameters a_1 and b_1 calculation starts after the first cycle, at t = 1 min. Their values, and the corresponding $A_{\Delta T}$ and $\delta_{\Delta T}$ values are:

$$\left.\begin{array}{l} \langle a_1 \rangle = 3.0 \times 10^{-9} \ ^oC \\ \langle b_1 \rangle = 9.6 \times 10^{-6} \ ^oC \end{array}\right\} \xrightarrow[\text{equation (3.33)}]{\text{equation (3.32)}} \begin{array}{l} A_{\Delta T} = 2.71 \times 10^{-4} \ ^oC \\ \delta_{\Delta T} = 89.98^o \end{array}$$

In many cases, the above calculations extend for more than one cycle. This action smoothes the experimental data and reduces the influence of erroneous points (146). In most calorimetric instruments dedicated software provides all the necessary analysis tools for signal deconvolution.

2.3.4 Application to thermoset cure

The main application of MDSC in thermoset cure is identification of vitrification. Vitrification is a very critical point in the processing of curing thermosets (§ 1.2). At vitrification the material heat capacity undergoes a step decrease (43, 152, 154). This is usually hidden by the undergoing chemical reaction. The MDSC capability of discerning heat capacity changes from other thermal events makes it ideal for identifying the vitrification point. Montserrat and co – workers have studied the vitrification of a curing thermoset under isothermal cure conditions (155). They compared the vitrification time found by MDSC with dielectric measurements. Van Assche and co – workers have also measured the vitrification time under isothermal and non isothermal conditions (156). They also studied the devitrification process where the heat capacity undergoes another step change (it increases).

MDSC has also been used for the study of polymer blends (157 - 159). Cure induced phase separation results in two phase systems with different vitrification times. These times can be monitored and separated in the obtained signal as long as they are not close to one another.

The polymerisation reaction is usually studied by simple DSC and not MDSC. Despite the fact that – in principle – the non modulated component of the heat flow gives exactly the same information as the conventional DSC experiment, most of the studies appearing in literature present cure kinetics models based on DSC data. One possible explanation of this trend may lie in the fact that conventional DSC experiments have been the standard in cure kinetics modelling for over two decades. Other possible reasons are the unconditionally linear behaviour of the DSC and the straightforward analysis of the obtained signal (149, 160).

3 Materials and Methods

3.1 Scope and objectives

In this chapter the materials and the instruments that were used in this study are reported. Different experimental cells were constructed, depending on the nature of the resin. A commercial dielectric sensor was used for the monitoring experiments. The response of the sensor in a wide temperature range is examined using standard liquids and epoxy resin. It is concluded that the sensor is suitable for monitoring resin cure.

3.2 Resins

The main material used in the study is RTM6 (161, 162). RTM6 is an epoxy resin specially developed for Resin Transfer Moulding (RTM) processes. The chemical components of RTM6 are premixed (mono – component product). The processing temperature window for its cure is 160 °C – 180 °C. Upon curing RTM6 transforms from a high viscosity paste to a translucent vitrified glass. The cured resin can be used in a wide temperature window spanning from – 60 °C to 180 °C. The batch used in this studied was supplied by Hexcel® Composites (161).

Two more resin systems were employed in order to test the general applicability of equivalent circuits in characterising epoxy cure: Fibredux® 913 provided by Ciba – Geigy® (the same resin is also provided by Hexcel® Composites (163)) and AY105 + HY2958 provided by Ciba – Geigy® (the system is now available by Vantico*). Fibredux® 913 is a mono – component thermoplastic modified epoxy used in autoclave applications. The unreacted material exhibits high viscosity and cannot be poured into containers or moulds. Due to the thixotropic behaviour, a special experimental cell was constructed for the cure monitoring experiments. The cell is described in § 3.4.1.
AY105 is an Araldite® structural adhesive. The stoichiometric mixing ratio is 4:1 w/w resin to hardener. The system cures at room temperature.

3.3 Dielectric sensors

The dielectric sensors used in this study were the commercially available GIA sensors provided by Pearson Panke Ltd. Figure 3-1 shows the geometric features of the sensor.

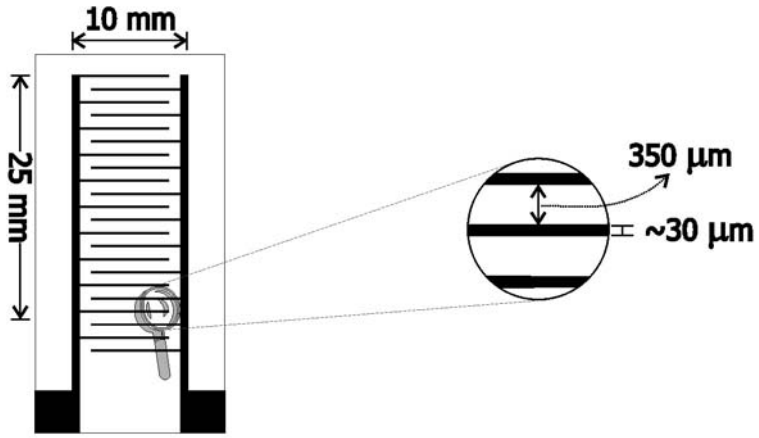

Figure 3-1 *GIA dielectric sensor*

The sensor comprises of two comb electrodes. The electrodes material is copper. The prong width is about 30 – 35 µm and the interelectrode space is about 350 µm. The sensor substrate is a soft, porous polymer film.

* http://www.huntsman.com/pu/ShowPage.cfm?PageID=3596

In order to ensure the similar behaviour of all the sensors, the capacitance and the resistance in air were recorded prior to every run. Table 3-I lists the averaged results from 25 sensors.

Table 3-I: *Air capacitance and resistance of GIA sensor at different frequencies*

Test frequency	***C (pF)***	***R (Ohm)***
1 Hz	9.82 ± 3.68	$3.72\times10^{10} \pm 0.93\times10^{10}$
10 Hz	7.33 ± 0.34	$3.58\times10^{10} \pm 0.11\times10^{10}$
100 Hz	7.37 ± 0.21	$2.07\times10^{10} \pm 0.41\times10^{10}$
1 kHz	7.23 ± 0.17	$1.59\times10^{9} \pm 0.21\times10^{9}$
10 kHz	7.05 ± 0.18	$1.42\times10^{8} \pm 0.13\times10^{8}$
100 kHz	6.88 ± 0.18	$8.68\times10^{6} \pm 0.24\times10^{6}$
1 MHz	6.67 ± 0.18	$1.94\times10^{5} \pm 0.03\times10^{5}$

We can see that the capacitance values remain relatively constant (~ 7 pF) at all frequencies, except for 1 Hz. At that frequency the dielectric bridge is at its measuring limits in terms of the resistance. When the sensor is measured in air, resistance values at low frequencies can include errors in the order of 10%. This is owed to the fact that the measured resistances are extremely high (in the GOhm region) due to the capacitive nature of the substrate material. One way to improve the accuracy of the measurement is by increasing the measuring time. In thermosets though, measurements have to be made as quickly as possible because of the continuously changing state of the material. In § 3.4.2, the capabilities and limitations of the dielectric bridge used in this study are discussed.

3.3.1 Modelling the GIA sensor dielectric response*

The dielectric sensor can be modelled by the simple equivalent circuit shown in Figure 3-2. The sample and the substrate side are considered to be materials modelled by a capacitance and a resistance connected in parallel.

The complex admittance Y^*_2 of the equivalent circuit will be the sum of the sample and substrate admittance, Y^*_{sample} and $Y^*_{substrate}$ respectively:

* Discussions with prof. R.A. Challis in the model development presented here are gratefully acknowledged.

$$Y_2^* = Y_{sample}^* + Y_{substrate}^* = \left(\frac{1}{R_{sa}} + \frac{1}{R_{su}}\right) + j\omega\left(C_{sa} + C_{su}\right) \tag{3.1}$$

When the sensor is measuring air, the admittance Y^*_1 will be:

$$Y_1^* = Y_{air}^* + Y_{substrate}^* = \left(\frac{1}{R_{air}} + \frac{1}{R_{su}}\right) + j\omega\left(C_{air} + C_{su}\right) \tag{3.2}$$

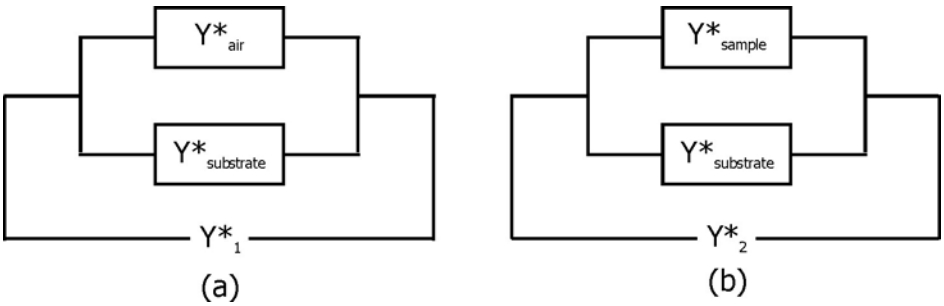

Figure 3-2 *Equivalent circuit for sensor response when it is left on air (a) and when it is immersed on a material (b).*

The complex permittivity of the sample and the substrate will be, by definition:

$$\varepsilon_{substrate}^* = \frac{Y_{substrate}^*}{Y_{air}^*} \Rightarrow Y_{substrate}^* = \varepsilon_{substrate}^* Y_{air}^* \tag{3.3}$$

$$\varepsilon_{sample}^* = \frac{Y_{sample}^*}{Y_{air}^*} \Rightarrow Y_{sample}^* = \varepsilon_{sample}^* Y_{air}^* \tag{3.4}$$

Substituting the last two eqs. into eqs. (3.1) and (3.2) yields:

$$Y_2^* = \left(\varepsilon_{sample}^* + \varepsilon_{substrate}^*\right) Y_{air}^* \tag{3.5}$$

$$Y_1^* = \left(1 + \varepsilon_{substrate}^*\right) Y_{air}^* \tag{3.6}$$

Taking the quotient of the last two equations we get:

$$\frac{Y_1^*}{Y_2^*} = \frac{1 + \varepsilon_{substrate}^*}{\varepsilon_{sample}^* + \varepsilon_{substrate}^*} \Rightarrow \varepsilon_{sample}^* = \frac{Y_2^*}{Y_1^*}\left(1 + \varepsilon_{substrate}^*\right) - \varepsilon_{substrate}^* \tag{3.7}$$

Analysis of the last equation into real and imaginary parts gives the real permittivity and the dielectric loss of the sample as function of the measured admittances and the substrate properties:

$$\varepsilon'_{sample} = \frac{\left(Y_2'Y_1' + Y_2''Y_1''\right)\left(1 + \varepsilon'_{substrate}\right) + \left(Y_2''Y_1' - Y_2'Y_1''\right)\varepsilon''_{substrate}}{Y_1'^2 + Y_1''^2} - \varepsilon'_{substrate} \tag{3.8}$$

$$\varepsilon''_{sample} = \frac{\left(Y'_2 Y''_1 - Y''_2 Y'_1\right)\left(1 + \varepsilon'_{substrate}\right) - \left(Y'_2 Y'_1 + Y''_2 Y''_1\right)\varepsilon''_{substrate}}{Y'^2_1 + Y''^2_1} - \varepsilon''_{substrate} \quad (3.9)$$

The above expressions are simplified when we consider the substrate to exhibit a purely capacitive response ($Y'_1 \to 0$ and $\varepsilon''_{substrate} \to 0$):

$$\varepsilon'_{sample} = \frac{Y''_2}{Y''_1}\left(1 + \varepsilon'_{substrate}\right) - \varepsilon'_{substrate} \quad (3.10)$$

$$\varepsilon''_{sample} = \frac{Y'_2}{Y''_1}\left(1 + \varepsilon'_{substrate}\right) \quad (3.11)$$

The substrate properties are usually given by the sensor manufacturer as parameters independent of temperature and frequency.

The substrate behaviour in the case of thermoset cure is very important for the quality of the measurement. Curing thermosets usually exhibit very large electrical resistance values. The substrate resistance has to be even higher so that most of the current passes through the material under test and not through the substrate.

The GIA sensor substrate is a polymeric film with unknown dielectric properties. The polymeric film allows the resin to permeate and thus the substrate properties are close to the materials in which the sensor is immersed. On the other hand, the permeability of the substrate means that it will behave differently in different environments. In this case the mathematical model based in Figure 3-2 is not entirely appropriate, since it implies that the substrate side exhibits the same response in the air and in the material under test. In the two following sections, the applicability of the above model is investigated using standard liquids and epoxy resin.

3.3.2 GIA sensor response in liquids

In order to assess the sensor response and the influence of the substrate on the measurement, the sensor was tested using standard liquids with known dielectric properties. Three pure (>99.9%) liquids were used: Acetone, Water and Dichloromethane. All experiments were conducted at 20 °C. The permittivity values for the three liquids were obtained from the Landolt – Börnstein database (164). The measurements were performed at 25 frequencies ranging from 1 Hz to 1 MHz. Before the sensor had been immersed in the liquid, a measurement in air was performed in order to determine the air admittance (equivalent circuit on Figure 3-2). The air admittance spectra are shown in Figure 3-3.

We can see that *Y″* values are more than one order of magnitude higher than *Y′* values at all frequencies. This implies that ionic losses due to the substrate are very small. The sensor exhibits a purely capacitive behaviour in air ($\varepsilon''_{substate} \rightarrow 0$). The log-linear frequency dependence means that the substrate dielectric properties are constant in the frequency window of measurement. No polarisation phenomena are observed.

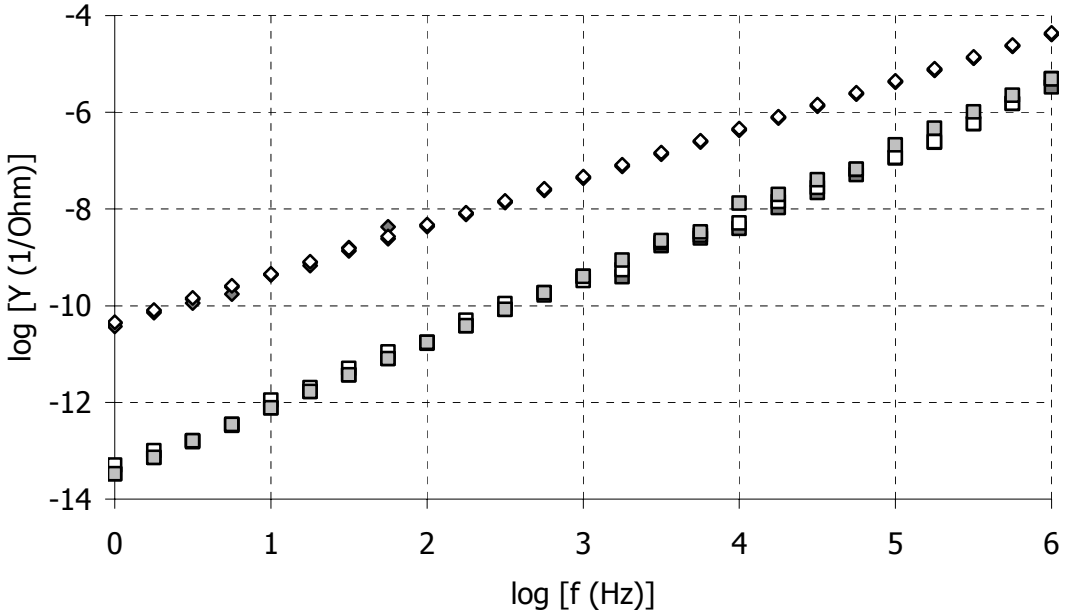

Figure 3-3 *Real (rectangular points) and imaginary (diamond points) admittance of the three GIA sensors used with the standard liquids at 20°C.*

The obtained admittance spectra for the three liquids are shown in Figures 3-4 (real admittance) and 3-5 (imaginary admittance). The real admittance for the three liquids is much higher than the real admittance of the sensor in air. According to Figure 3-2 this indicates that the resistance of the liquids is much lower compared to the substrate resistance. Real admittance does not change significantly with frequency. In the dichloromethane spectrum there is a slight increase at high frequencies where the admittance of the system is comparable with the admittance of the sensor in air. The imaginary admittance plot is similar for the three liquids at high frequencies (*log f > 4)*, where purely capacitive behaviour is observed (slope in the log-log plot of Figure 3-5 very close to 1, as in Figure 3-3). At lower frequencies polarisation effects become apparent in the signal. Therefore, only data obtained at frequencies above 10 kHz were used for the calculation of the parameters in eqs. (3.8) and (3.10). At these frequencies, the resulting permittivity will be frequency independent.

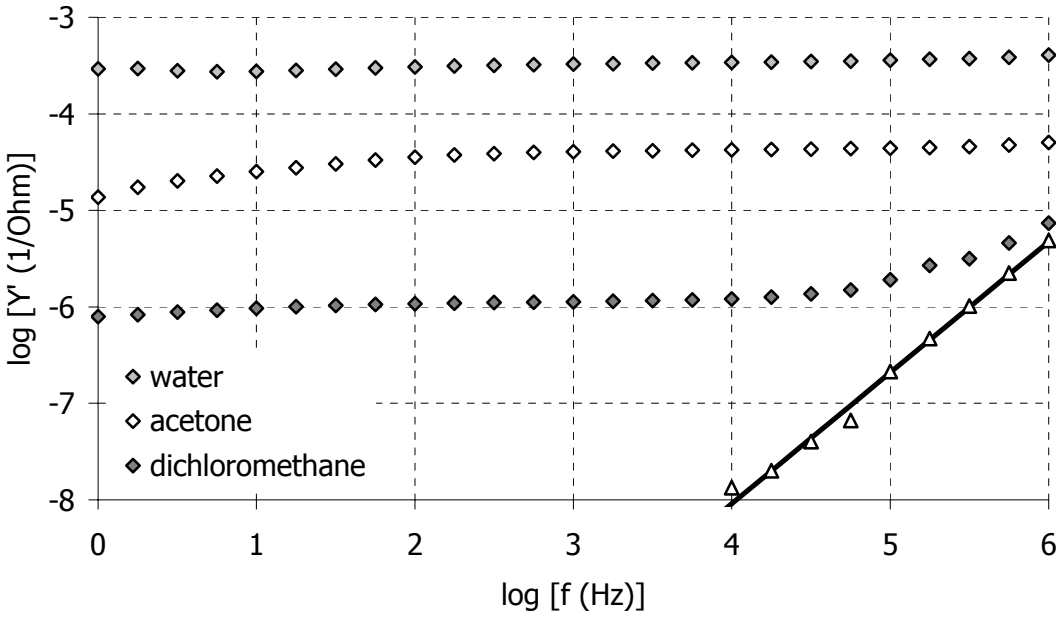

Figure 3-4 *Real admittance spectra of standard liquids. The black line denotes the sensor response in air.*

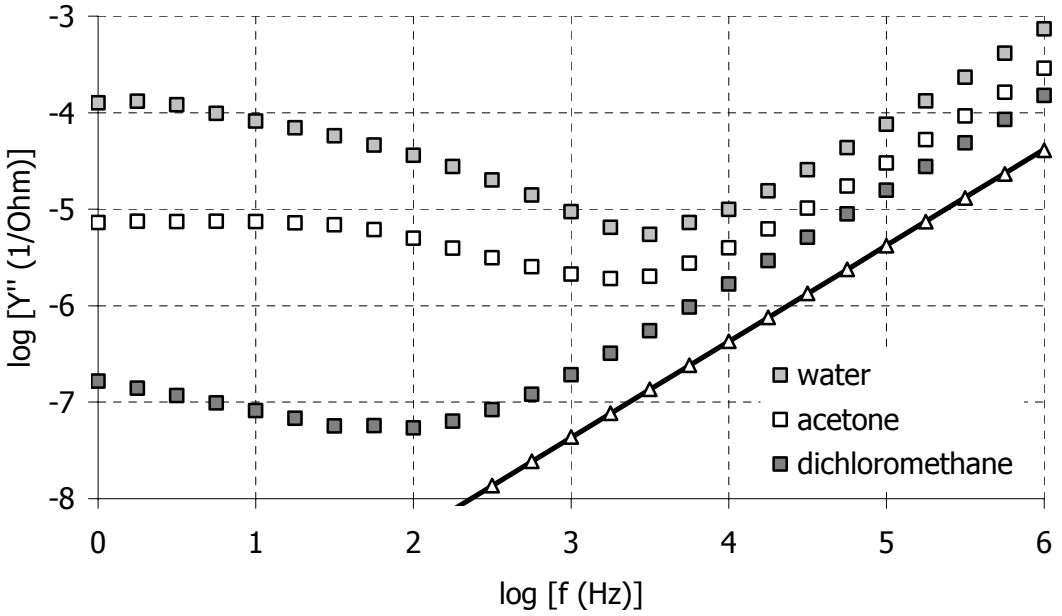

Figure 3-5 *Imaginary admittance spectra of standard liquids. The black line denotes the sensor response in air.*

The average values of the substrate properties were calculated for each standard liquid. The results are shown in Table 3-II and Figure 3-6. The permittivity values are

close to the values reported in literature. The highest error is around 3%, in the case of water. The calculated substrate permittivity value varies considerably. The variation seems to follow the permittivity of the liquids.

Table 3-II : *Determination of the calibration function parameters of the GIA sensor*

	$\varepsilon'_{substrate}$	$\varepsilon'_{literature}$	$\varepsilon'_{eq.\ 3.10}$
Acetone	2.58 ± 0.12	21.4	20.24
Water	3.29 ± 0.26	80.1	76.73
Dichloromethane	2.02 ± 0.06	8.9	8.89
Average :	2.63 ± 0.44		

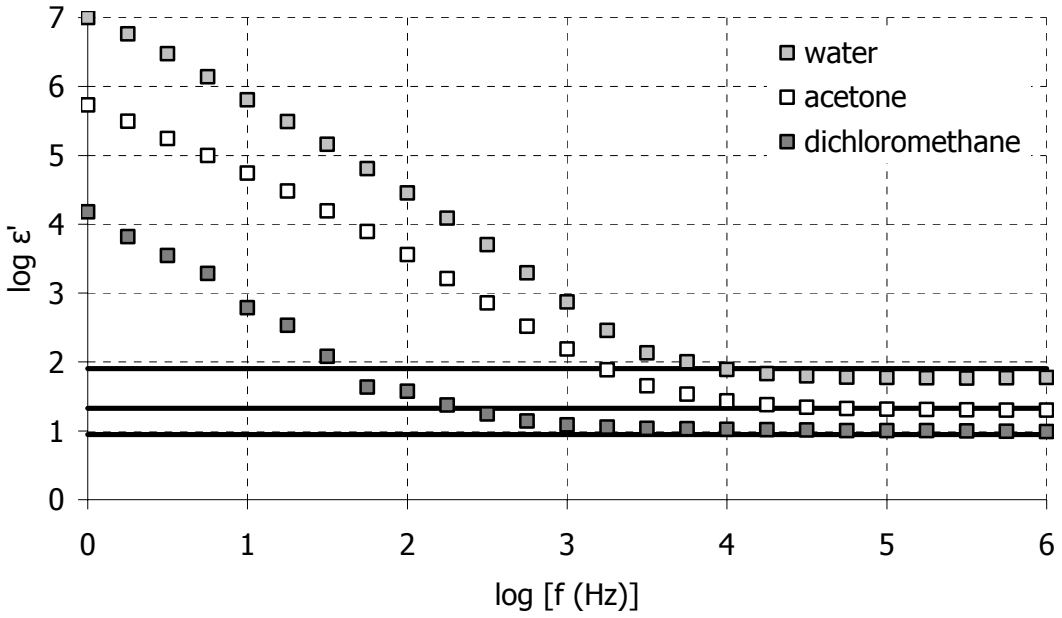

Figure 3-6 *Permittivity calculated using eq. (3.10) for the three standard liquids. The black lines represent the permittivity values found in literature (164)*

3.3.3 GIA sensor response at elevated temperatures

The sensor response at elevated temperatures was also studied. The sensor was heated up to 210°C at a rate of 0.2°C/min. After the end of the experiment the sensor substrate had blackened; indication of the onset of a degradation process. The degradation became visible at around 210°C.

The resulting experimental curves are shown in Figure 3-7 where the modulus of the complex admittance is plotted against temperature. We can see that the admittance curves do not change up to about 120°C. This shows the capacitive behaviour of the sensor up to that temperature. At higher temperatures, admittance increases. The sensor starts to exhibit conductive behaviour. The superposition of the curves designates a frequency region where purely resistive behaviour is observed.

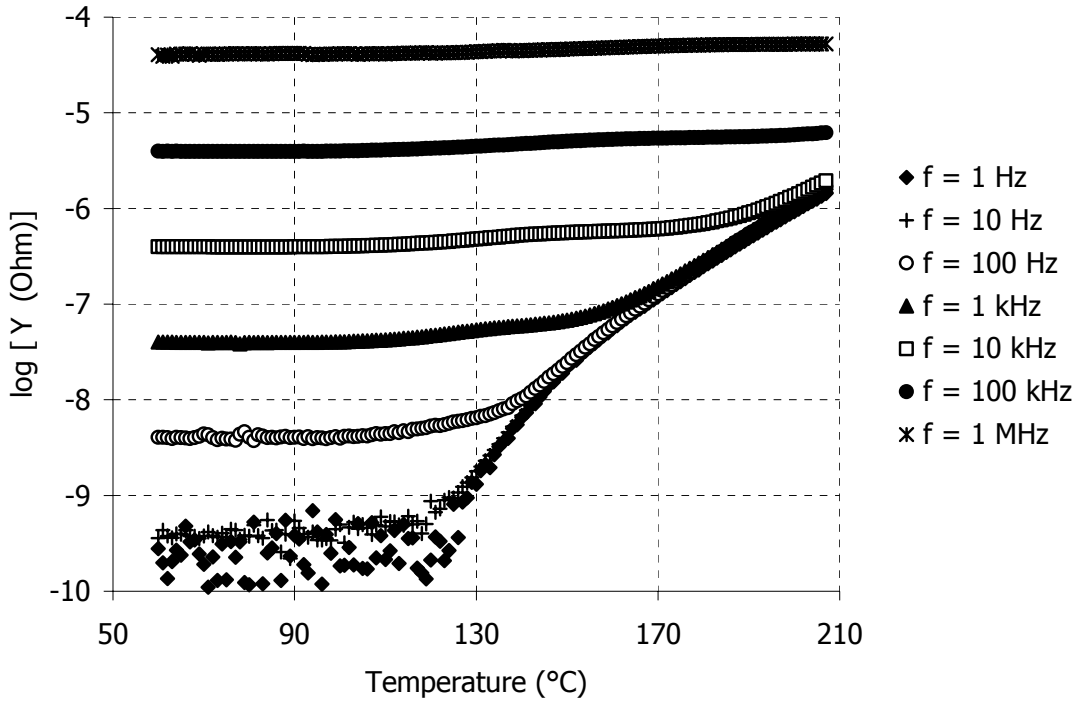

Figure 3-7 *GIA sensor response as a function of temperature*

When the sensor was immersed in epoxy resin a different response was observed. Figure 3-8 compares the response in air and in the resin at two frequencies (1 Hz and 1 kHz). The real admittance is plotted, since it reflects the resistance changes (see real part of eq. (3.1)). The epoxy (RTM6) was cured at 0.2°C/min. Initially the sensor response in the resin produces higher admittance values compared to the air measurement. At higher temperatures, however, the admittance of the curing resin decreases and becomes lower than the admittance recorded in air. The crossover happens at around 140°C. If the substrate behaved the same in the air and in the resin, the signal would be limited by the substrate response and admittance could not be measured at a level lower than that of the substrate admittance (see real part of

eq. (3.1)). The lower admittance in the resin implies that the substrate properties have changed.

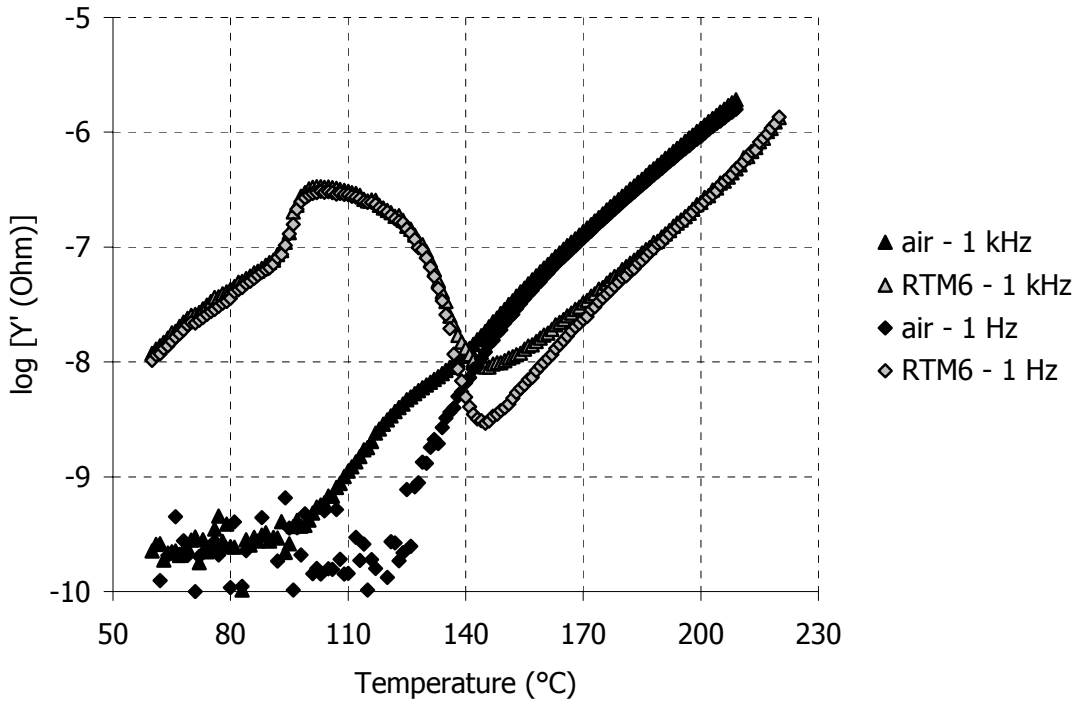

Figure 3-8 *Comparison of the GIA sensor response when it is measuring on air (black points) and when it is immersed on curing epoxy (grey points)*

The reason for the different behaviour is probably the permeation of resin in the substrate. Migrating charges from the substrate seem to interact with the curing resin, altering the conductivity levels of the material. The interaction leads to either reduced mobility (the growing molecular network hinders the movements of the charges) or reduced concentration (charges become part of the molecular network) of the substrate ionic species. In both cases, the state of the resin determines the sensor response. Therefore the dielectric signal reflects the changes in the material state throughout the cure. The effect of the substrate material on the polymerisation reaction was also studied. In Figure 3-9 the heat flow of the curing reaction when the substrate is present is compared to the heat flow obtained by RTM6 alone. We can see that the influence of the substrate on the kinetics is negligible.

An interesting observation is that when the sensor is immersed in the resin, no degradation of the substrate is observed (in Figure 3-8 data up to 220°C are shown for the resin cure; in dielectric experiments under dynamic conditions temperature was

allowed to reach 240°C). This is possibly due to the lack of oxygen when the sensor is engulfed by resin.

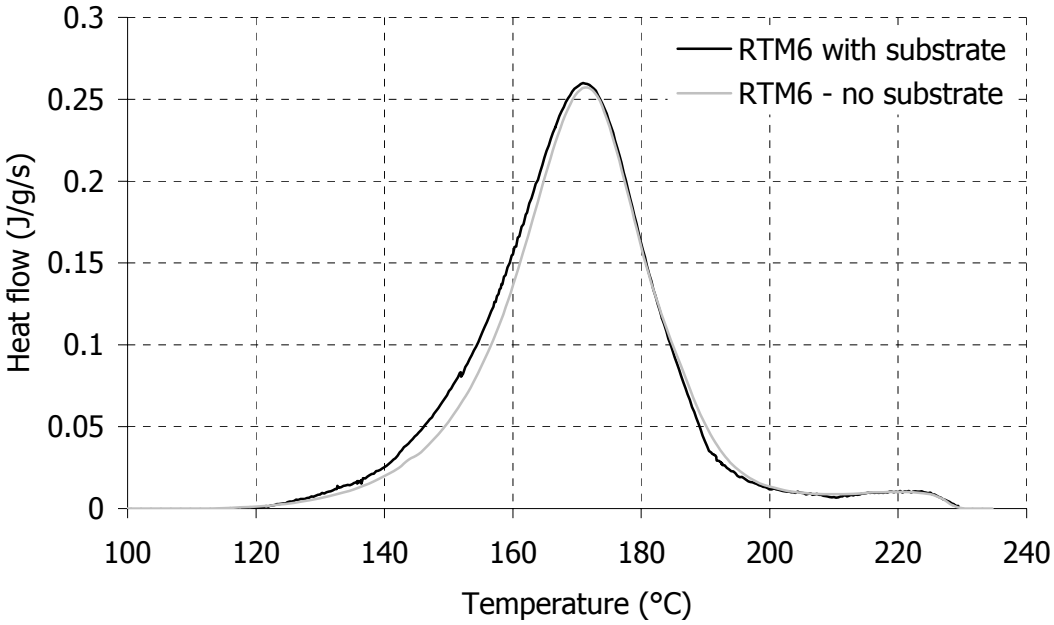

Figure 3-9 *Heat flow evolution of the cure of RTM6 with and without the sensor substrate. The heating rate is 1°C/min.*

The conclusion from the above analysis is that the GIA sensor is suitable for thermoset cure monitoring. The substrate material does not contribute to any losses ($\varepsilon''_{substate} \rightarrow 0$) at low temperatures, up to 120°C. At higher temperatures, the substrate interacts with the curing resin but the signal still reflects the material state changes. The sensor does not alter the reaction kinetics. Consequently, in the analysis of equivalent circuit modelling (presented in § 4.4) the substrate material influence on the signal is considered negligible.

3.4 Apparatus used

The dielectric measurements were carried out on a Solartron Analytical 1260 Gain – Phase Analyser. A Eurotherm 2204e PID temperature controller was utilised for temperature programming and control (165). A DAS-TC board was used for the acquisition of temperature readings via K-type thermocouples. A computer code was developed for the simultaneous tuning and control of the two instruments and the DAS-TC board.

3.4.1 Experimental cells

Two different container configurations were used for the placement of the resin samples and the dielectric sensor pictured in Figures 3-10 and 3-11.

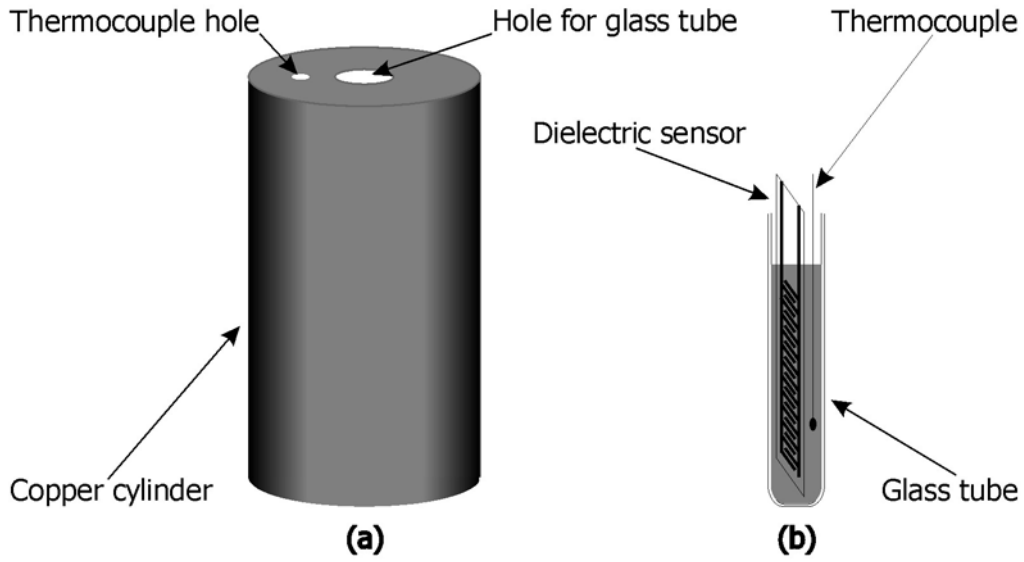

Figure 3-10 *Experimental cell for RTM6 and AY105+HY2958 experiments, (a) copper cylinder, (b) glass tube.*

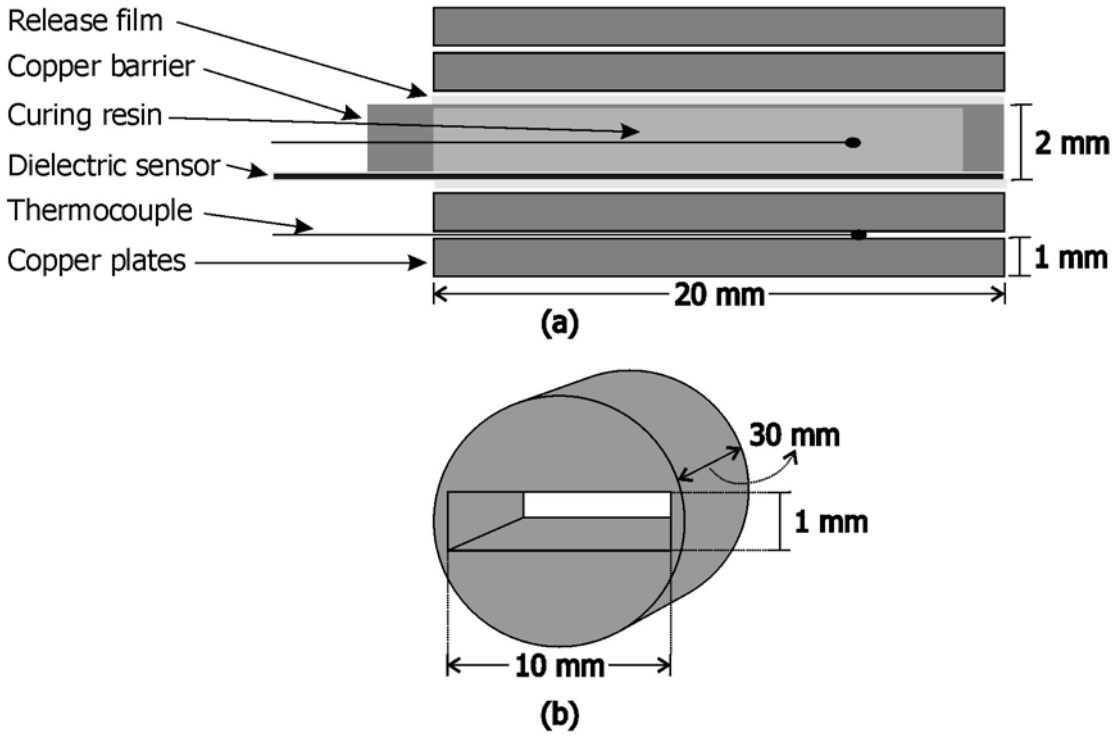

Figure 3-11 *Experimental cell for the Fibredux® 913 experiments, (a) "sandwich" structure, (b) copper cylinder*

A vertical glass tube placed on a hollow copper cylinder was used for RTM6 and AY105 + HY2958 resins. Heating elements surrounded the cylinder. A control and a monitoring thermocouple were placed in appropriate holes on the copper cylinder. A third thermocouple was immersed in the resin in order to record the actual temperature experienced by the sample.

For the Fibredux® 913 resin a horizontal configuration had to be used because of the viscous nature of the resin. A "sandwich" structure comprised of copper plates was fitted into a copper cylinder. Again, three thermocouples were used, for monitoring and controlling the temperature in the experimental cell and the resin.

In both configurations the amount of resin used was about 1 g. The temperature difference between the copper cylinder and the resin sample was about 0.5°C in isothermal runs. Under dynamic conditions this difference varied according to the heating rate but never exceeded 2°C.

3.4.2 Solartron Analytical 1260 Gain – Phase Analyser

The 1260 Gain – Phase Analyzer provides a comprehensive range of impedance and frequency response facilities. The ranges for frequency, capacitance and resistance cover 10 orders of magnitude and are listed in Table 3-III. The instrument is also capable of measuring inductance.

Table 3-III: *Ranges of the Solartron Analytical 1260 Gain – Phase Analyser (166)*

	frequency (Hz)	***resistance (Ohm)***	***capacitance (F)***
Lower limit	10^{-3}	10^{-2}	10^{-12}
Upper limit	3.2×10^{6}	10^{8}	10^{-2}

The analyser sends a sinusoidal voltage to the material under test (MUT). The voltage is defined by three variables:

$$V = V_{DC} + A_V \sin\left(2\pi ft\right) \tag{3.12}$$

In the above equation, V_{DC} is the dc bias voltage, A_V is the amplitude of the excitation and f is the frequency. These three variables are set prior to each measurement. The response from the MUT is an out of phase current:

$$I = I_{DC} + A_I \sin\left(2\pi ft + \delta\right) \tag{3.13}$$

where I_{DC}, A_I have definitions similar to V_{DC}, A_V and δ is the phase difference between excitation and response. The experimental parameters values used in the dielectric experiments are given in Table 3-IV.

Table 3-IV: *Experimental parameter values used in dielectric experiments*

dc bias V_{DC}	Excitation amplitude A_V	Frequency range f
0 Volts	3 Volts	1 Hz – 1 MHz

The impedance of the MUT can be determined by the ratio of the different amplitudes of the excitation and the response, and by the phase δ *(82)*.

The measurement error varies according to the impedance that is being measured. Figure 3-12 shows the different error levels at different measurement conditions. The usual values of the capacitance and the resistance that are being measured during thermoset cure are also shown in the graph (heavy grey).

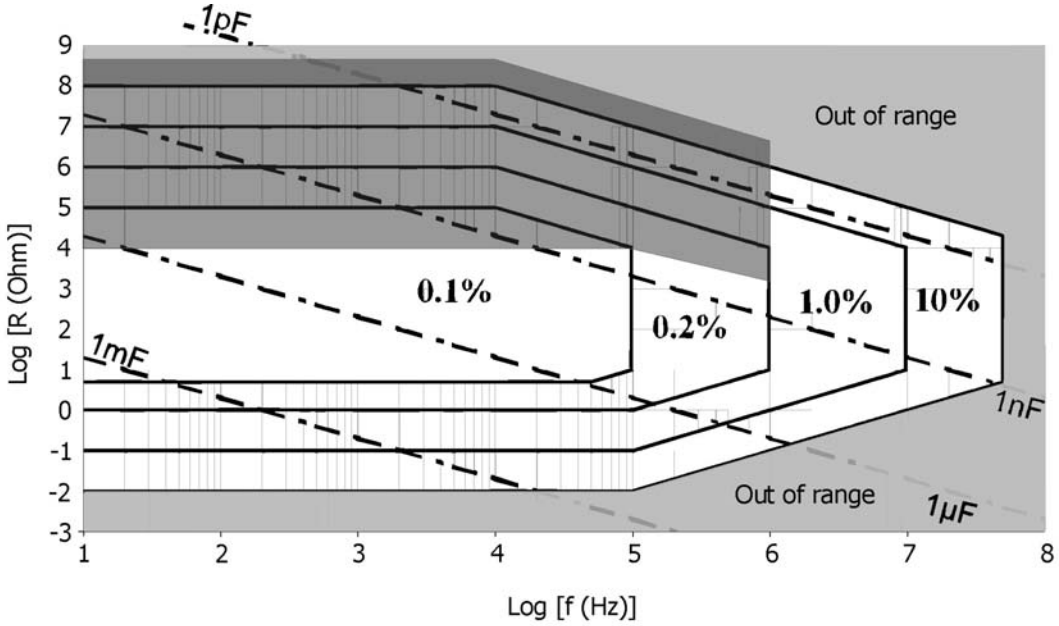

Figure 3-12 *Error limits of the 1260 Analyser (166). The dotted lines show the capacitance levels. Light grey denotes the areas where the analyser is out of range. The heavier grey area shows the ranges of measured capacitance and resistance during thermoset cure.*

The capacitance values of the sensors impregnated with thermosetting materials never fall below 10 pF at all frequencies. At low frequencies, they may exceed 10 nF or go even higher due to electrode polarisation phenomena. Resistance values can be as high as 10^9 Ohm, which is over the measuring limits of the instrument. This is a general problem in thermosetting systems. Resistance during cure can be as low as 10^3 Ohm, although for the resins used in this study never measured below 10^4 Ohm.

3.4.3 TA Instruments 2920 Differential Scanning Calorimeter

The 2920 Differential Scanning Calorimeter is a heat flux DSC. A schematic representation of the experimental cell is given in Figure 2-1. For convenience, it is reproduced here in Figure 3-13.

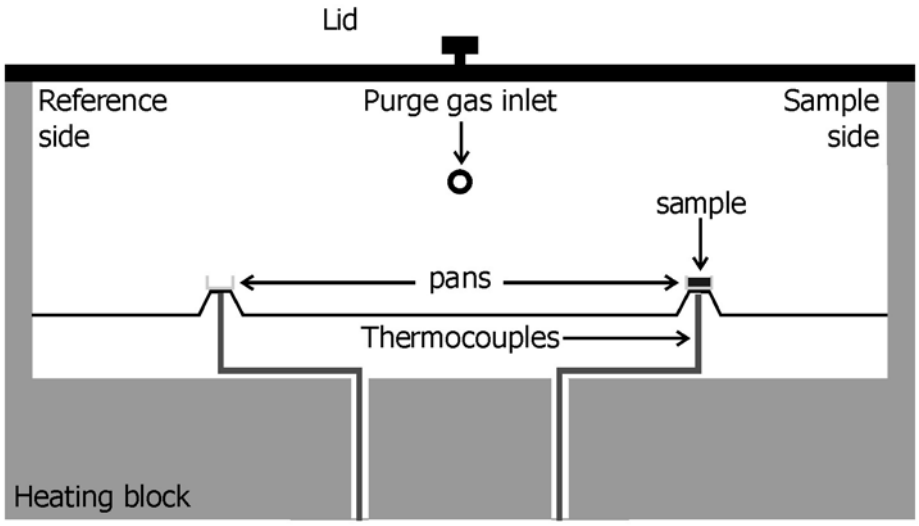

Figure 3-13 *TA Instruments 2920 DSC experimental cell (same as in Figure 2-1)*

The cell comprises of a constantan disk with two symmetrical positions slightly elevated. The sample and the reference are placed inside special pans, supplied by the manufacturer. The pans are sealed and then placed on the elevated positions. Thermocouples are placed underneath these positions. The whole chamber is surrounded by a heater. Nitrogen gas is supplied to the cell through an inlet, ensuring uniform atmosphere.

During an experiment, the temperature difference between the reference and the sample is being recorded through the two thermocouples. Since the reference and the sample experience the same temperature profile, any temperature differences will

correspond to thermal events occurring in the sample or reference. The operation of the DSC is based on the three assumptions discussed in § 2.2.1, (page 30).
Prior to conducting the experiments, a three stage calibration of the instrument was performed:

- Temperature calibration

In this type of calibration, the temperature of melting of well characterised substances is recorded and compared to the accepted value. The difference between the measured melting temperature and the correct one is stored in the instrument. Raw experimental values are corrected automatically. In this study, indium was used as the standard material.

- Cell calibration

In cell calibration, the cell constant of the apparatus is determined. The latent heat of melting of a standard material is recorded and compared with the accepted value. The ratio between the two constitutes the cell constant of the instrument. The cell constant is then used for translating the temperature difference to heat flow.

- Symmetry calibration

The sample and reference positions on the constantan disk are symmetrical in order to ensure identical thermal profiles in the two points. Continuous usage of the instrument however, aggravates any minor asymmetries. In order to compensate for these asymmetries, a temperature program identical to that of the actual experiment is imposed to an empty cell. The measured signal is stored in the instrument and automatically subtracted by the raw data. Symmetry calibration is essential in dynamic experiments.

In all the experiments, aluminium pans were used. On the reference side the pan was empty. Resin quantities of no more than 7 mg were cured and the exothermic heat of reaction monitored. The reaction rate will be proportional to the exothermic heat:

$$\frac{da}{dt} = \frac{H_{flow}}{\Delta H_{total}} = \frac{1}{\Delta H_{total}} \frac{dH}{dt} \tag{3.14}$$

The exothermic heat was calculated from the thermogram by using an appropriate baseline. The baseline, which reflects the heat capacity changes during the cure, was calculated using an iterative procedure initially proposed by Bandara (167) and

successfully implemented by Skordos (28, 168). In house software, built and supplied by Dr A.A. Skordos, was used for the analysis of the experimental curves.

4 Interpretation of Dielectric Data

4.1 Scope and objectives

In this chapter the theoretical relationship between complex permittivity and complex impedance is established. The advantage of complex impedance is in its direct connection with electric circuitry. Equivalent circuit modelling of the complex impedance provides straightforward means of interpretation of the dielectric signal. The build up of a robust fitting algorithm, based on genetic algorithms, reveals the specific challenges posed by cure monitoring signals. The algorithm is validated using real and artificial data.

4.2 Related dielectric theory

The response of thermosets to a perturbing electric field is a superposition of three phenomena: Electrode polarisation, charge migration and dipolar relaxation. These phenomena are traditionally analysed in terms of complex permittivity ε^*. In this section the dielectric theory related to these three phenomena is reviewed. A brief account of interfacial phenomena is also presented.

4.2.1 Electrode polarisation

Electrode polarisation is a phenomenon mentioned in many cure monitoring studies (84, 85, 103). Adamec and Calderwood described the phenomenon as the result of different transfer rates of charges across the electrode interface (slower) and the bulk (faster) when an electric field is present (170, 171). Due to that difference, charges accumulate in the vicinity of the sensor electrodes.

A three layer capacitor (blocking electrodes model) has been used for the description of electrode polarisation. The two layers adjacent to the electrodes are identical. The model is shown in Figure 4-1.

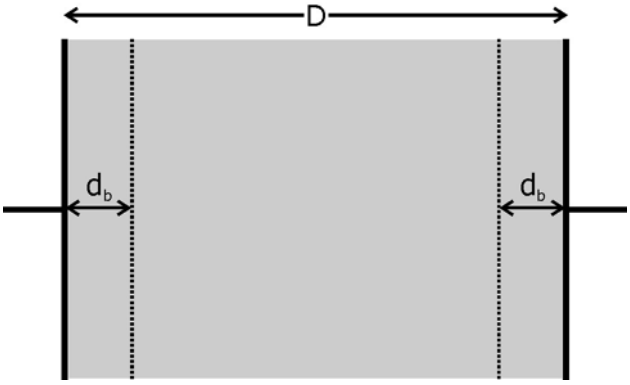

Figure 4-1 *Blocking electrodes model for electrode polarisation*

Using this model, Day and co – workers calculated the effect of electrode polarisation on complex permittivity (172):

$$\varepsilon'_{el} = \varepsilon' \frac{D}{2d_b} \frac{\frac{\varepsilon''}{\varepsilon'} + \frac{D}{2d_b}}{\left(\frac{\varepsilon''}{\varepsilon'}\right)^2 + \left(\frac{D}{2d_b}\right)^2} \tag{4.1}$$

$$\varepsilon''_{el} = \varepsilon'' \frac{D}{2d_b} \frac{\frac{D}{2d_b} - 1}{\left(\frac{\varepsilon''}{\varepsilon'}\right)^2 + \left(\frac{D}{2d_b}\right)^2} \tag{4.2}$$

where ε'_{el} and ε''_{el} are the measured complex permittivity values, D is the interelectrode distance and d_b is the blocking electrode width. The complex permittivity of the bulk material is given by ε' and ε''.

From the above equations the effect of electrode polarisation on the measured complex permittivity can be assessed. Figure 4-2 shows the dependence of the measured permittivity on $D/2d_b$ for a material with constant complex permittivity. When electrode polarisation is low ($d_b \rightarrow 0$) the measured complex permittivity is equal to the actual complex permittivity of the bulk. When electrode polarisation is high ($d_b \rightarrow D$) the measured real permittivity diverges slightly compared to the permittivity of the bulk material (~ 9% change in the extreme case where $2d_b = D$). The dielectric loss divergence, however, is much more pronounced. The measured value decreases. As will be depicted in the subsequent section, low dielectric loss translates to high measured resistance.

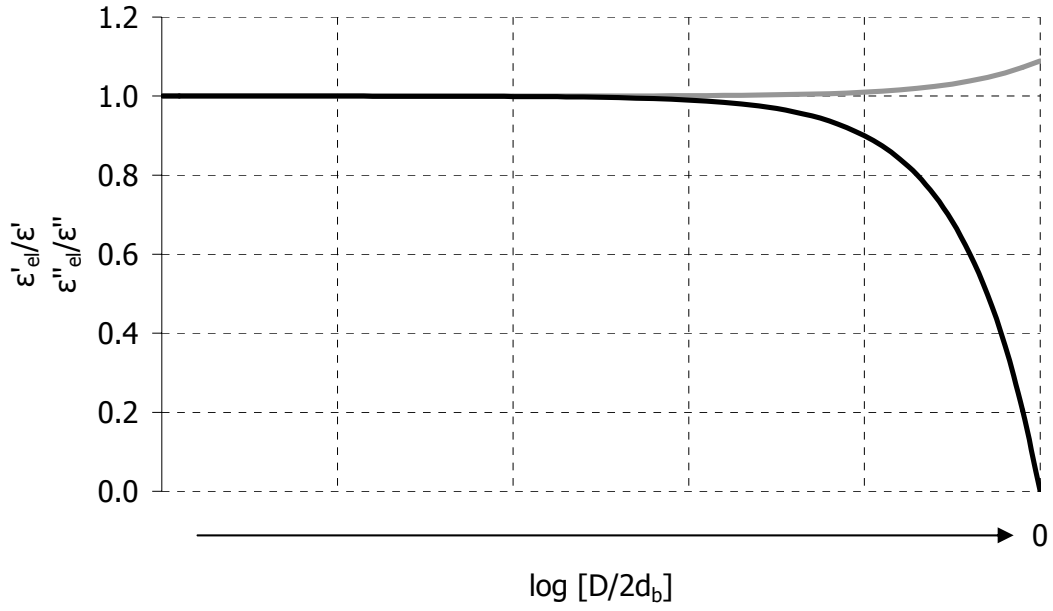

Figure 4-2 *Electrode polarisation effect on complex permittivity values as a function of the width ratio $D/2d_b$. The normalised real permittivity (grey line) diverges slightly from unity as $D/2d_b \rightarrow 0$. The dielectric loss (black line) is more affected. Note that the x – axis is in reverse order.*

Since electrode polarisation is a charge induced phenomenon, the concentration and mobility of charged species on the curing system will affect its magnitude. During epoxy resin cure the concentration and mobility of charged species changes by several orders of magnitude (2, 85). Electrode polarisation is usually present at initial stages of cure, where the system is liquid and the reaction rate is low. Under such conditions, ionic transport in the bulk is not hindered by macromolecular growth. In literature, values of $D/2d_b$ in the range of 10^2 have been reported for relatively clean (i.e. low

concentration of ions) epoxy resin systems (85, 83). For thermosetting blends, the value increases to ~10^3 (83).

An important implication of the blocking electrode model is that the electrode properties – namely geometry and manufacturing material – influence the manifestation and magnitude of electrode polarisation. This stems from the initial point that the charge transfer rate at the interface is the key factor for the formation of the blocking layers in the vicinity of the electrodes.

4.2.2 Migrating charges

The term "migrating charges" encompasses all molecular entities that carry electrical charge and are mobile enough so that energy supplied by the electric field can dissipate through their movement.

The origin of migrating charges in thermosetting systems is manifold. One contribution comes from low molecular weight ions that are leftovers from the synthesis of the raw materials (85, 99, 104). Another source is the polymerisation reaction. Depending on the reaction mechanism, charged species form and/or are consumed in the course of polymerisation (1, 9, 173). Furthermore, in complex three dimensional networks, charges originating by the formation of hydrogen bonds also contribute to the overall conductivity of the system (101, 173).

The overall conductivity due to migrating charges is considered to be a summation of the conductivities of all the charged species (9):

$$\sigma = \sum q_i N_{S,i} u_{m,i} \tag{4.3}$$

In the above equation σ is the measured conductivity, q is the charge, N_S is the number of charge carriers and u_m is the mobility.

The transport of charges is a purely dissipative process. In terms of complex permittivity, only the dielectric loss is influenced by the presence of migrating charges (85):

$$\varepsilon'_{ion} = 0 \tag{4.4}$$

$$\varepsilon''_{ion} = \frac{\sigma}{\omega \varepsilon_0} \tag{4.5}$$

where, ω is the angular frequency and ε_0 is the permittivity of free space (ε_0 = 8.854×10^{-12} F/m). Eq. (4.5) shows that whenever migrating charges dominate the dielectric signal, the product $\omega.\varepsilon_0.\varepsilon''$ will be frequency independent and equal to σ. A

lot of researchers have calculated $\omega.\varepsilon_0.\varepsilon''$ experimentally and used it as proof for signals dominated by conductivity (85, 86, 88, 93).

4.2.3 Dipolar relaxation

There are two classes of dipoles affecting the dielectric signal: Permanent dipoles and induced dipoles. Both classes are pictured schematically in Figure 4-3.

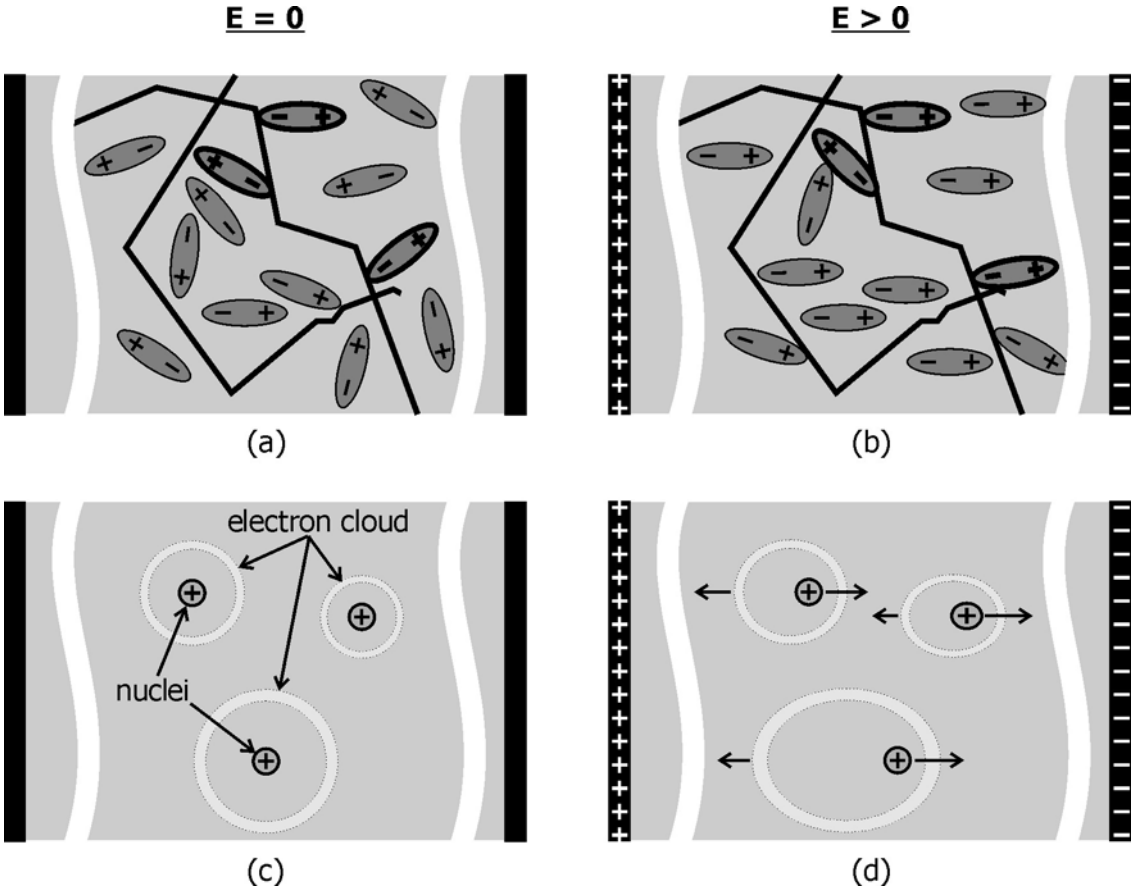

Figure 4-3 *Permanent and induced dipoles before and after the application of an electric field. In (a) permanent dipoles are randomly distributed in the material. Black lines denote macromolecules. Dipoles with bold outline are connected to the macromolecules and have limited mobility. In (b) dipoles re-orientate according to the electric field. The re-orientation is hindered by the presence of macromolecules and by the movement of other species. In (c) single molecules with zero dipole moment are polarised by the field (d).*

Permanent dipoles have a charge distribution due to asymmetries in their molecular structure (2). They can be individual molecules, molecular groups or part of a macromolecule. In an unperturbed system, permanent dipoles are randomly distributed and the total dipole moment is zero (Figure 4-3a). When an electric field is applied to

the system, permanent dipoles re-orientate according to the field direction (Figure 4-3b). When the field is removed the dipoles return to their original random state. Thus, an amount of energy is stored when permanent dipoles polarise and given back when they depolarise. Energy also dissipates due to local interactions with other molecular species (2, 6).

Induced dipoles have zero dipole moment when no field is applied to the system (Figure 4-3c). The application of an external field delocalises the positive and negative charge centres (Figure 4-3d). The response of induced dipoles to an external perturbation is very fast, compared with the permanent dipoles response (2).

The response of permanent dipoles under an oscillating electric field is described in complex permittivity terms by phenomelogical models originating by the Debye model for a spherical dipole having a single relaxation time (7):

$$\frac{\varepsilon^* - \varepsilon_u}{\varepsilon_r - \varepsilon_u} = \frac{1}{1 + j\omega\tau} \tag{4.6}$$

where ε_u is the unrelaxed permittivity exhibited at high frequencies, ε_r is the fully relaxed permittivity exhibited at low frequencies, ω is the frequency of the applied field and τ is the relaxation time. The real and imaginary components are:

$$\varepsilon' = \varepsilon_u + \frac{\varepsilon_r - \varepsilon_u}{1 + \omega^2\tau^2} \tag{4.7}$$

$$\varepsilon'' = \frac{\left(\varepsilon_r - \varepsilon_u\right)\omega\tau}{1 + \omega^2\tau^2} \tag{4.8}$$

A plot of the permittivity and dielectric loss is given in Figure 4-4. In the same figure other relaxation functions are plotted. A list of some of the various relaxation models is given in Table 4-I. All the models are generalisations of the Debye equations. The Kohlrausch – Williams – Watts function is expressed in the time domain. Recently, Hilfer derived analytical time and frequency domain expressions for all relaxation functions listed in Table 4-I (178).

The relaxation of dipoles is related to the glass transition or vitrification (2, 8, 85). A lot of researchers have used the peak of the dielectric loss spectrum for identification of the vitrification of the system. The frequency of the peak is inversely related to the relaxation time (7, 85). Vitrification is identified arbitrarily as the point where the peak frequency reaches a specific value. This value lies in the 0.01 Hz – 1 Hz region (43).

Table 4-I : *Relaxation functions for permanent dipoles*

	Reference	Relaxation function
Debye	(7)	$\frac{\varepsilon^* - \varepsilon_u}{\varepsilon_r - \varepsilon_u} = \frac{1}{1 + j\omega\tau}$
Cole – Cole	(174)	$\frac{\varepsilon^* - \varepsilon_u}{\varepsilon_r - \varepsilon_u} = \frac{1}{1 + (j\omega\tau)^{a_{CC}}} \quad 0 \le a_{CC} \le 1$
Davidson – Cole	(175)	$\frac{\varepsilon^* - \varepsilon_u}{\varepsilon_r - \varepsilon_u} = \frac{1}{(1 + j\omega\tau)^{a_{DC}}} \quad 0 \le a_{DC} \le 1$
Havriliak - Negami	(176)	$\frac{\varepsilon^* - \varepsilon_u}{\varepsilon_r - \varepsilon_u} = \frac{1}{\left(1 + (j\omega\tau)^{1-a_{HN}}\right)^{\beta_{HN}}} \quad 0 \le a_{HN} \le 1 \quad 0 \le \beta_{HN} \le 1$
Kohlrausch –Williams – Watts	(177)	$\frac{f(t)}{f_0} = \exp\left(-\left(\frac{t}{\tau}\right)^{\beta_{KWW}}\right) \quad 0 \le \beta_{KWW} \le 1$

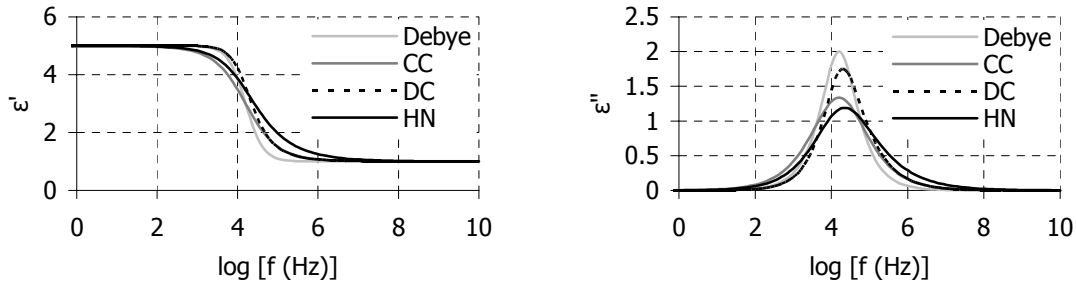

Figure 4-4 *Real permittivity (a) and dielectric loss (b) for various relaxation functions listed in Table 4-I. In both graphs $a_{CC} = a_{DC} = a_{HN} = \beta_{HN} = 0.75$, $\varepsilon_u = 1$, $\varepsilon_r = 5$ and $\tau = 10^{-5}$ s*

The relaxed permittivity and the relaxation time are temperature and conversion dependent (2, 6, 83). The relaxation time, especially, changes by several orders of magnitude as the system transforms from the liquid state ($\tau < 10^{-6}$ s) to the final glassy state ($\tau > 1$ s). This broad change has been used by many researchers as a cure index (see § 1.5.3). In commercial systems though, the domination of migrating charges means that dipolar effects are hidden in the signal. This renders the identification of the relaxation time a difficult task.

4.2.4 Other polarisation phenomena affecting the dielectric signal

Apart from the three main phenomena that contribute to the dielectric signal, polarisation phenomena due to the formation of interfaces can alter the dielectric response of a curing material. Interfaces can form in polymer blends (1, 179). The blend can be thermoset/rubber (180 - 182), thermoset/thermoplastic (114, 183) or thermoset with dispersed particles (184).

Interfaces in thermoset blends can either be present due to the initial immiscibility of the constituents of the blend, or induced by the polymerisation reaction.

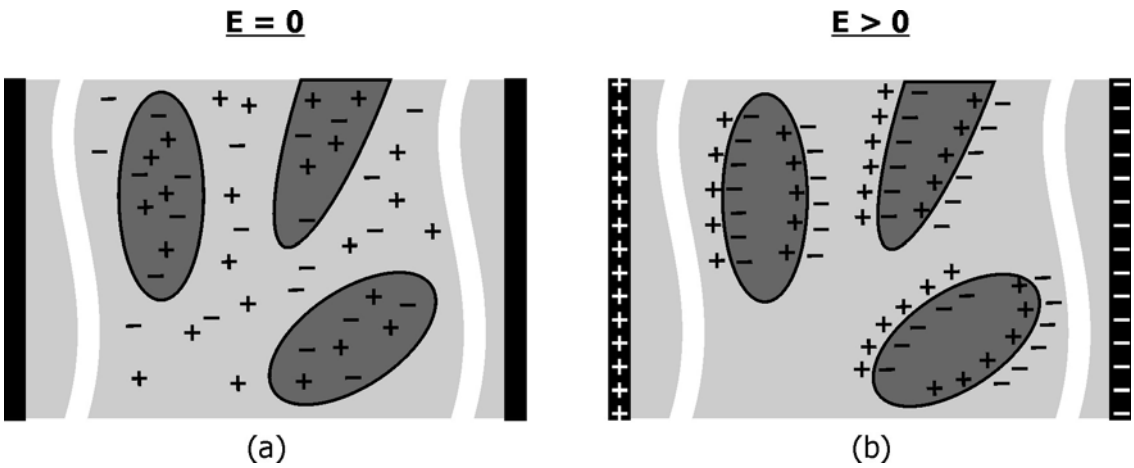

Figure 4-5 *Schematic representation of interfacial polarisation; (a) charges randomly distributed in the bulk and in the dispersed phase, (b) charges accumulate at the interfaces under the influence of the electric field*

The Maxwell – Wagner – Sillars (MWS) model (185 - 187) is usually utilised for the description of interfacial polarisation phenomena. For a two phase system, the relaxed and unrelaxed permittivity and the relaxation time of the interfacial polarisation are:

$$\varepsilon_{r,i} = \varepsilon_1 \left(\frac{2\sigma_1 + \sigma_2 + 2v_2\Delta\sigma}{2\sigma_1 + \sigma_2 - v_2\Delta\sigma} \right) + 3v_2\sigma_1 \left(\frac{(2\sigma_1 + \sigma_2)\Delta\varepsilon - (2\varepsilon_1 + \varepsilon_2)\Delta\sigma}{(2\sigma_1 + \sigma_2 - v_2\Delta\sigma)^2} \right)$$

$$\varepsilon_{u,i} = \varepsilon_1 \left(\frac{2\varepsilon_1 + \varepsilon_2 + 2v_2\Delta\varepsilon}{2\varepsilon_1 + \varepsilon_2 - v_2\Delta\varepsilon} \right) \qquad (4.9)$$

$$\tau_i = \varepsilon_0 \left(\frac{2\varepsilon_1 + \varepsilon_2 - v_2\Delta\varepsilon}{2\sigma_1 + \sigma_2 - v_2\Delta\sigma} \right)$$

In the above relationships, v_2 is the volume fraction of the dispersed phase, ε_1 and ε_2 are the real permittivities of the bulk and the dispersed phase, σ_1 and σ_2 are the

corresponding conductivities, $\Delta\varepsilon = \varepsilon_2 - \varepsilon_1$, $\Delta\sigma = \sigma_2 - \sigma_1$ and ε_0 is the permittivity of free space. The model is valid for $v_2 < 0.2$.

Interfacial polarisation spectra are similar to dipolar relaxation spectra and the relationships listed in Table 4-I can be used for modelling the phenomenon (83, 112).

4.3 Complex impedance representation of dielectric data

Apart from complex permittivity, the electrical response of a material can be described in any one of the functions presented in Table 4-II. These functions are generally termed immitances (84).

Table 4-II: *Major immitance functions and their relationships (reproduced from 84)*

	Modulus M^*	**Impedance** Z^*	**Admittance** Y^*	**Permittivity** ε^*
M^*	-	$j\omega C_O Z^*$	$\frac{j\omega C_O}{Y^*}$	$\frac{1}{\varepsilon^*}$
Z^*	$\frac{M^*}{j\omega C_O}$	-	$\frac{1}{Y^*}$	$\frac{1}{j\omega C_O \varepsilon^*}$
Y^*	$\frac{j\omega C_O}{M^*}$	$\frac{1}{Z^*}$	-	$j\omega C_O \varepsilon^*$
ε^*	$\frac{1}{M^*}$	$\frac{1}{j\omega C_O Z^*}$	$\frac{Y^*}{j\omega C_O}$	-

In Table 4-II j is the imaginary unit ($j^2 = -1$), ω is the angular frequency of the applied field and C_O is the air capacitance which is a function of the geometrical features of the dielectric sensor. M^* is the electric modulus, Z^* is the complex impedance and Y^* is the complex admittance.

All the above functions are equivalent in terms of the information carried on them. The main difference lies in their frequency dependence.

The complex impedance Z^* of a dielectric material is inversely related to the complex dielectric permittivity ε^*:

$$Z^* = \frac{1}{j\omega C_O \varepsilon^*} \tag{4.10}$$

where

$$Z^* = Z' - jZ'' \tag{4.11}$$

Using eq. (4.10) and analysing into real and imaginary components, eq. (4.11) gives:

$$Z' = \frac{1}{\omega C_O} \frac{\varepsilon''}{\varepsilon'^2 + \varepsilon''^2} \tag{4.12}$$

$$Z'' = \frac{1}{\omega C_O} \frac{\varepsilon'}{\varepsilon'^2 + \varepsilon''^2} \tag{4.13}$$

In general, the real and imaginary dielectric permittivity will sum up the contributions of the blocking electrodes phenomenon, the dipolar relaxation and the influence from migrating charges. For a system without any electrode polarisation ε' and ε'' will be given by the following equations:

$$\varepsilon' = \varepsilon'_{dip} \tag{4.14}$$

$$\varepsilon'' = \varepsilon''_{dip} + \varepsilon''_{ion} \tag{4.15}$$

Substitution of eqs. (4.14) – (4.15) into eqs. (4.12) – (4.13) yields general expressions for the real and imaginary impedance:

$$Z' = \frac{1}{\omega C_O} \frac{\varepsilon''_{dip} + \varepsilon''_{ion}}{\varepsilon'^2_{dip} + \left(\varepsilon''_{dip} + \varepsilon''_{ion}\right)^2} \tag{4.16}$$

$$Z'' = \frac{1}{\omega C_O} \frac{\varepsilon'_{dip}}{\varepsilon'^2_{dip} + \left(\varepsilon''_{dip} + \varepsilon''_{ion}\right)^2} \tag{4.17}$$

Further substitution from eqs. (4.5) – (4.8) gives the real and imaginary impedance in terms of ε_r, ε_u, τ and σ:

$$Z' = \frac{\varepsilon_0}{C_O} \frac{\left(2\sigma\tau + \left(\varepsilon_r - \varepsilon_u\right)\varepsilon_0\right)\tau\omega^2 + 2\sigma}{\left(2\sigma\tau + \varepsilon_r\varepsilon_0\right)^2 \omega^2 + \left(\omega^2\tau\varepsilon_u\varepsilon_0 - 2\sigma\right)^2} \tag{4.18}$$

$$Z'' = \frac{\omega\varepsilon_0}{C_O} \frac{\varepsilon_u\varepsilon_0\tau^2\omega^2 + \varepsilon_r\varepsilon_0}{\left(2\sigma\tau + \varepsilon_r\varepsilon_0\right)^2 \omega^2 + \left(\omega^2\tau\varepsilon_u\varepsilon_0 - 2\sigma\right)^2} \tag{4.19}$$

The shapes of Z' and Z'' frequency dependencies are shown in Figure 4-6.

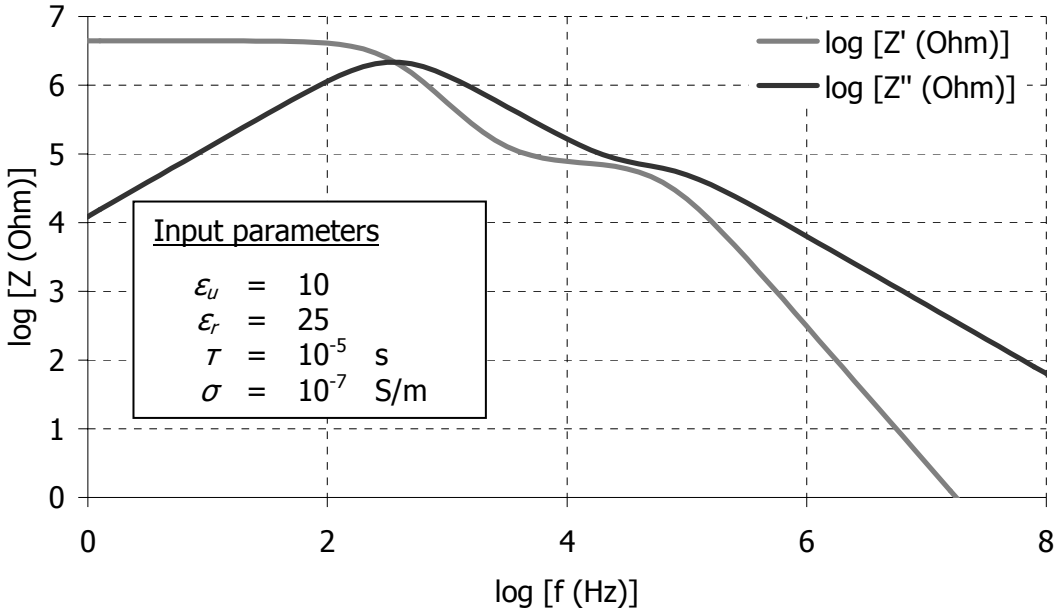

Figure 4-6 *Real and imaginary impedance spectra. The curves are constructed using equations 4.18 - 4.19. The input parameters are also given.*

Representative values for ε_r, ε_u, τ and σ were used. In the real impedance plot, we observe two plateau regions where the Z' values remain relatively constant and two regions where there is a logarithmic decrease. The imaginary impedance curve exhibits a maximum and a shoulder. In Appendix A complex permittivity spectra are constructed using the same input parameters.

An investigation of the possible number of optimum points in eqs. (4.18) and (4.19) is presented in Appendix B. It is proved that Z' has no optimum and that Z'' exhibits one maximum or two maxima and a minimum point, depending on the input parameters. Figure 4-7 shows detail of how the *log* Z'' – *log* f dependence varies as ε_r is allowed to change from 14 to 22.

In the following sections (4.3.1 and 4.3.2) the simpler cases where either dipoles or migrating charges dominate the material response are studied.

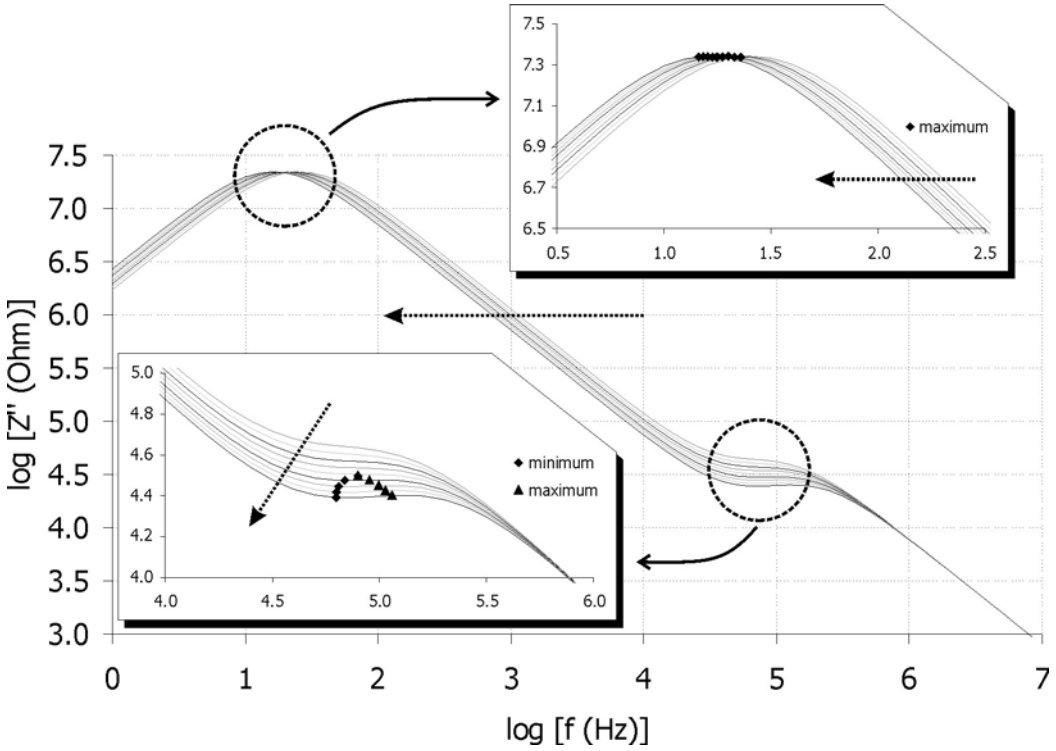

Figure 4-7 *Optima points in the imaginary impedance spectrum. For the spectra construction σ, τ and ε_u were kept constant with values 10^{-8} S/m, 10^{-5} s and 2. Relaxed permittivity ε_r varied from 14 to 22. The dotted arrows show the movement of the spectrum as ε_r increases. The encircled areas are shown enlarged in the inset graphs, where the axes have the same units as in the main plot. The optimum points for each spectrum are shown in the inset graphs.*

4.3.1 Case 1: Dipoles dominate the signal

When there are no migrating charges affecting the dielectric signal eqs. (4.18) and (4.19) become:

$$Z' = \frac{1}{\omega C_O \varepsilon_u} \frac{\left(\frac{\varepsilon_r}{\varepsilon_u} - 1\right)\omega\tau}{\left(\frac{\varepsilon_r}{\varepsilon_u}\right)^2 + \omega^2\tau^2} \tag{4.20}$$

$$Z'' = \frac{1}{\omega C_O \varepsilon_u} \frac{\frac{\varepsilon_r}{\varepsilon_u} + \omega^2\tau^2}{\left(\frac{\varepsilon_r}{\varepsilon_u}\right)^2 + \omega^2\tau^2} \tag{4.21}$$

The real impedance plot is shown in Figure 4-8. Comparison with the spectrum where conductivity is non – zero (black thick line in the figure) reveals that dipoles dominate the impedance spectrum at high frequencies.

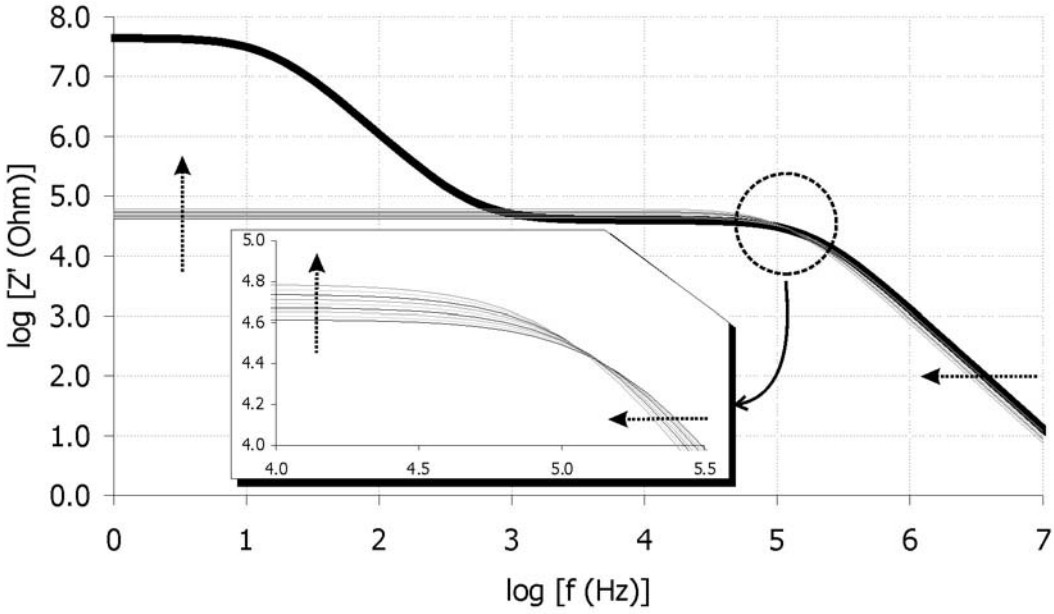

Figure 4-8 *Real impedance spectrum under conditions when dipoles dominate the signal. The black thick line is drawn for comparison and contains both dipoles and migrating charges contributions ($\sigma = 10^{-8}$ S/m). For the spectra construction τ and ε_u were kept constant with values 10^{-5} s and 2 respectively. Relaxed permittivity ε_r varied from 14 to 22. Dotted arrows show the spectrum movement as ε_r increases.*

The imaginary impedance dependence on frequency is shown in Figure 4-9. As in the real impedance case, comparison with the spectrum where conductivity is non – zero shows that dipoles dominate the signal at high frequencies.

The minimum and maximum points in the imaginary impedance spectrum are obtained by differentiating eq. (4.21). The mathematical expressions for the optima points are:

$$\omega_{opt} = \frac{\sqrt{2}}{2\tau}\sqrt{\frac{\varepsilon_r}{\varepsilon_u}\left(\frac{\varepsilon_r}{\varepsilon_u}-3\right) \pm \frac{\varepsilon_r}{\varepsilon_u}\sqrt{\left(\frac{\varepsilon_r}{\varepsilon_u}-1\right)\left(\frac{\varepsilon_r}{\varepsilon_u}-9\right)}} \qquad (4.22)$$

The solution for the optima points frequencies is real when $\varepsilon_r > 9\varepsilon_u$. When this inequality is satisfied the expressions for the minimum and maximum points are:

$$\omega_{\min} = \frac{1}{\tau}\left(\frac{\varepsilon_r}{\varepsilon_u}\right)^{\frac{3}{4}}$$
$$\omega_{\max} = \frac{2^{-\frac{1}{4}}}{\tau}\left(\frac{\varepsilon_r}{\varepsilon_u}\right)^{\frac{1}{2}}\left(\left(\frac{\varepsilon_r}{\varepsilon_u}-4+\sqrt{7}\right)\left(\frac{\varepsilon_r}{\varepsilon_u}-4-\sqrt{7}\right)\right)^{\frac{1}{4}} \quad (4.23)$$

Both optima points depend on the relaxation time and the relaxed and unrelaxed permittivity. Therefore they could provide information about the evolution of those parameters during cure. In thermosets, however, the features related to the relaxing dipoles (i.e. the minimum – maximum points or the shoulder in the case where there are no optima) are not often visible due to the high concentration of migrating charges or because the relaxation lies out of the frequency window of the experiment. Furthermore, the changes in the relaxation time, which are discussed in the next paragraph, are more influential in the case of thermoset cure.

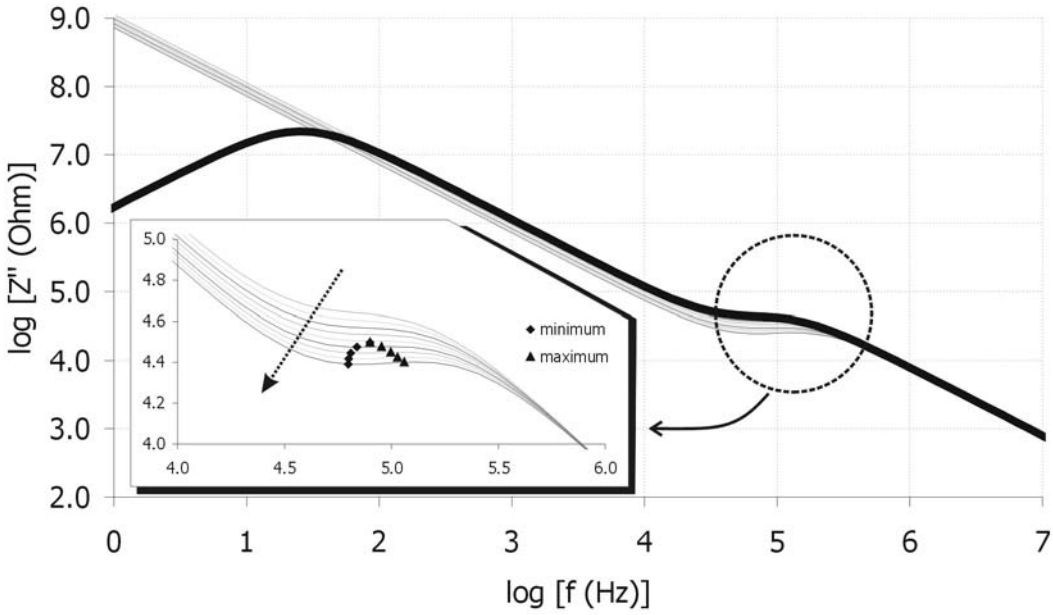

Figure 4-9 *Imaginary impedance spectrum for purely dipolar behaviour for different values of ε_r (from 14 to 22). The black thick line is taken from Figure 4-7 for comparison. For the spectra construction τ and ε_u were kept constant with values 10^{-5} s and 2 respectively. Relaxed permittivity ε_r varied from 14 to 22. Dotted arrows show the spectrum movement as ε_r increases. The encircled area, where the maximum and minimum points are denoted, is shown enlarged in the inset graph. The axes in the inset graph have the same units as the main plot.*

For given values of ε_r and ε_u the effect of the relaxation time on impedance can be studied. Similarly to the above analysis, Figure 4-10 shows the changes in the Z' spectrum and Figure 4-11 pictures the changes in the Z" spectra as τ increases.

In Figure 4-10 a crossover in the spectra is observed, similarly to Figure 4-8. The crossover area, enlarged in the inset graph, is much wider compared with Figure 4-8. This is expected, since the relaxation time changes exponentially while ε_r changes linearly, as has been observed in thermoset cure (83, 85).

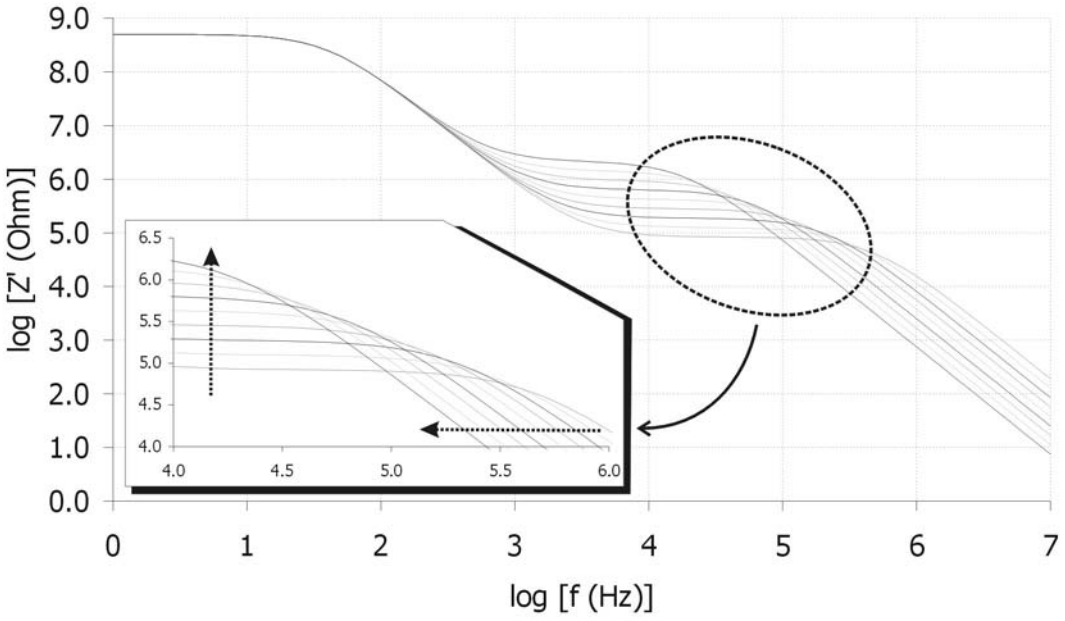

Figure 4-10 *Real impedance spectrum under conditions when dipoles dominate the signal. For the spectra construction σ, ε_r and ε_u were kept constant with values 10^{-8} S/m, 9 and 3 respectively. Relaxation time τ varied from 10^{-6} s to 5×10^{-5} s. Dotted arrows show the spectrum movement as τ increases. The axes in the inset graph have the same units as the main plot.*

In the imaginary impedance spectrum, a shoulder appears and shifts to lower frequencies as τ increases. The shoulder movements are confined between two parallel lines, unlike Figure 4-9. The distance between these two lines indicates the values of ε_r and ε_u. Since ε_r and ε_u remain constant the position of the lines will not change.

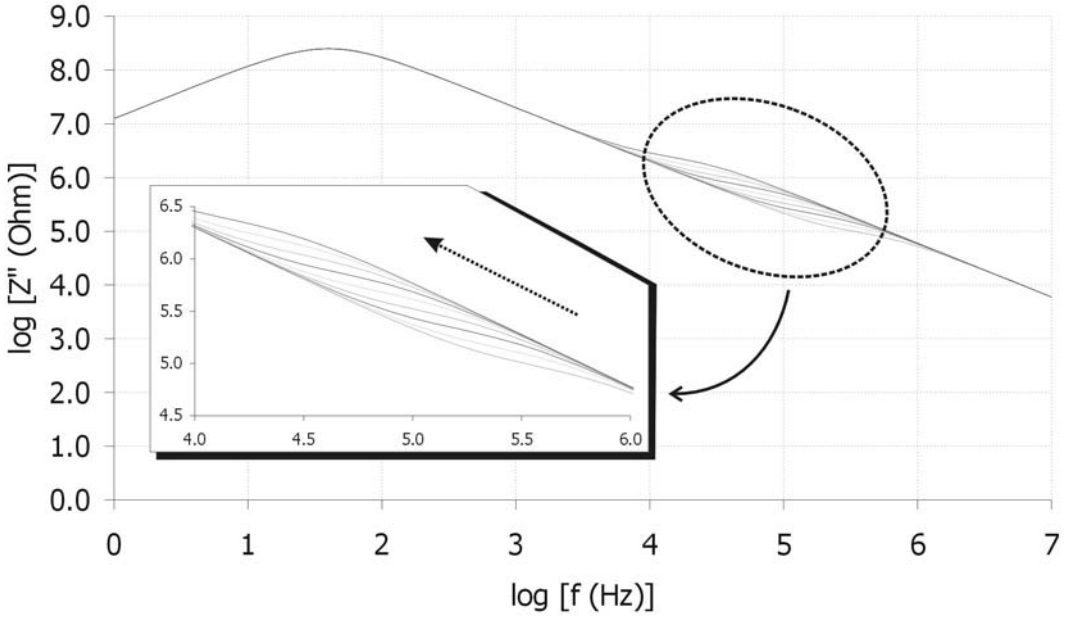

Figure 4-11 *Imaginary impedance spectrum for purely dipolar behaviour for different values of τ (from 10^{-6} s to 5×10^{-5} s). For the spectra construction σ, ε_r and ε_u were kept constant with values 10^{-8} S/m, 9 and 3 respectively. Dotted arrows show the spectrum movement as τ increases. The axes in the inset graph have the same units as the main plot.*

4.3.2 Case 2: Migrating charges dominate the signal

When migrating charges dominate the dielectric signal, the frequency dependence of dipolar relaxation is suppressed (2, 188). Taking $\langle\varepsilon\rangle$ as the relaxed, frequency independent, permittivity of the dipoles, eqs. (4.18) – (4.19) form as follows:

$$Z' = \frac{\sigma\varepsilon_0}{C_O}\frac{1}{\sigma^2 + \langle\varepsilon\rangle^2 \varepsilon_0^2\omega^2} \tag{4.24}$$

$$Z'' = \frac{\langle\varepsilon\rangle\varepsilon_0}{C_O}\frac{\varepsilon_0\omega}{\sigma^2 + \langle\varepsilon\rangle^2 \varepsilon_0^2\omega^2} \tag{4.25}$$

The real impedance plot is shown in Figure 4-12. The spectrum moves towards higher frequencies and lower impedance values as σ increases. There is a plateau at low frequencies and an exponential decrease at higher frequencies. These features are similar to the features exhibited in real impedance when dipoles dominate the signal (black thick line in Figure 4-12).

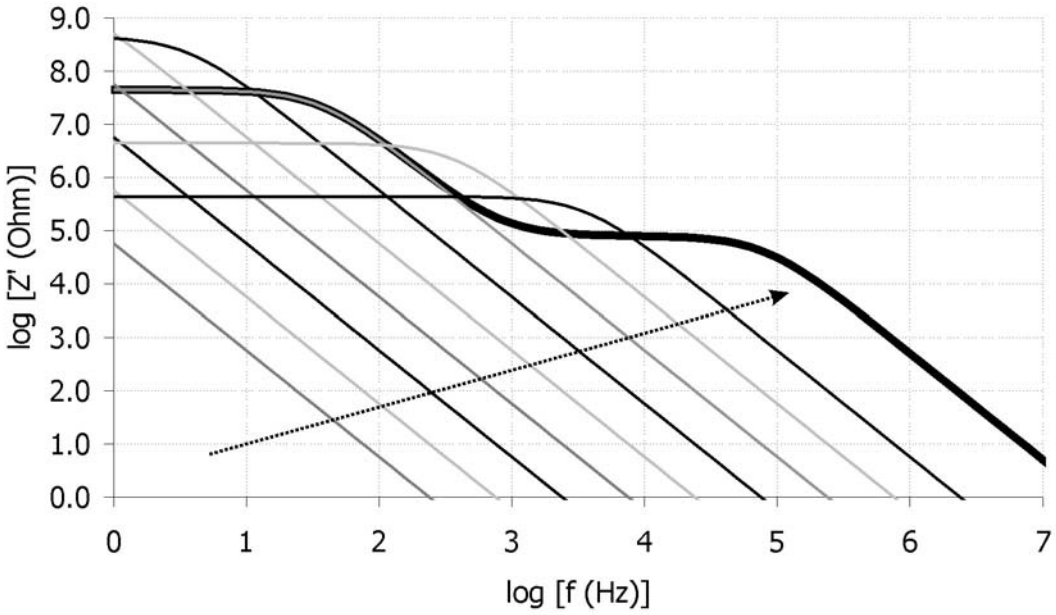

Figure 4-12 *Real impedance spectrum when migrating charges dominate the signal. The black thick line, drawn for comparison, is the same as in Figure 4-8. For the spectra construction $\tau = 10^{-5}$ s and $\langle\varepsilon\rangle = 10$. The dotted arrow shows the spectrum movement as σ increases from 10^{-14} to 10^{-6} S/m in decade increments.*

Analysis of eqs. (4.20) and (4.24) provides expressions for the two plateaus and the two exponentially decreasing regions of the real impedance spectrum when the influence of dipoles is well separated from the influence of migrating charges on a time and frequency scale. The analysis is pictured in Figure 4-13.

The imaginary impedance plot is shown in Figure 4-14. The spectrum moves along a curve which describes all the spectra at high frequencies. This line is defined by eq. (4.25) when the high frequency limit is considered:

$$\omega \to \infty \quad \Rightarrow \quad Z'' = \frac{1}{\langle\varepsilon\rangle C_O}\frac{1}{\omega} \tag{4.26}$$

Imaginary impedance spectrum exhibits a maximum point. The point is identified by differentiating eq. (4.25):

$$\omega_{\max} = \frac{\sigma}{\langle\varepsilon\rangle\varepsilon_0}$$
$$Z''_{\max} = \frac{\varepsilon_0}{2\sigma C_O} \tag{4.27}$$

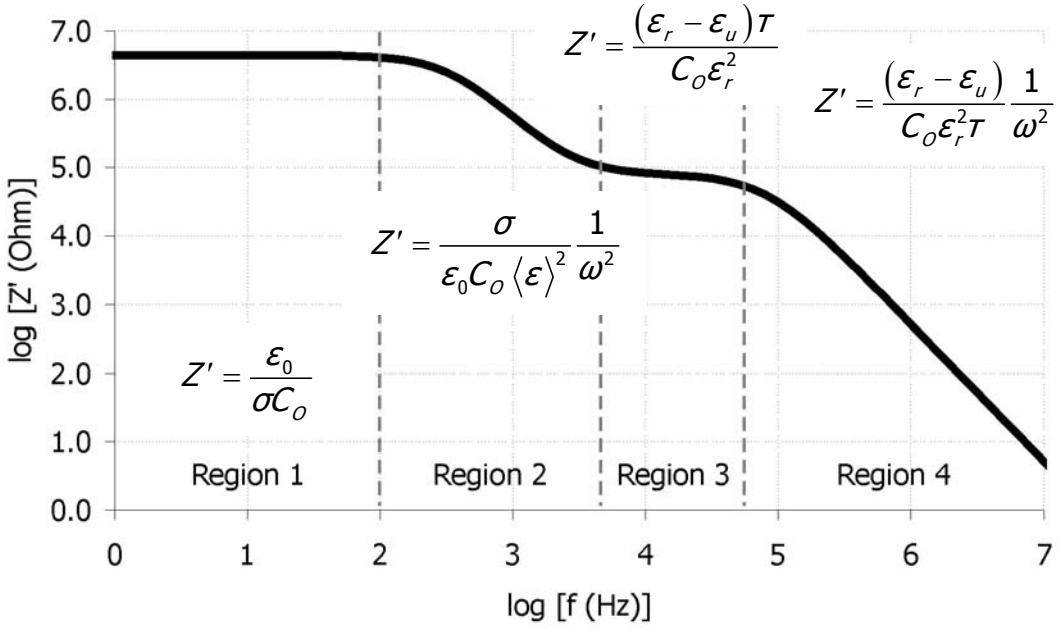

Figure 4-13 *Simplified equations describing the real impedance spectrum in different regions*

Eq. (4.27) demonstrates that there is a linear dependence between the frequency of the imaginary impedance maximum (which will be denoted as ω_{IIM} from this point onwards) and the conductivity of migrating charges. These relationships are extremely useful in the case of thermosets, where migrating charges are the dominant phenomenon (103).

An interesting remark on eq. (4.27) is that the product $\omega_{max}.Z''_{max}$ is independent of the conductivity:

$$\omega_{\max} Z''_{\max} = \frac{1}{2\langle\varepsilon\rangle C_O} \tag{4.28}$$

A plot of the above product should remain constant as long as dipoles do not influence the signal (i.e. $<\varepsilon>$ is constant). Therefore the product $\omega_{max}.Z''_{max}$ can be used for investigating whether the effect of dipoles is significant or not.

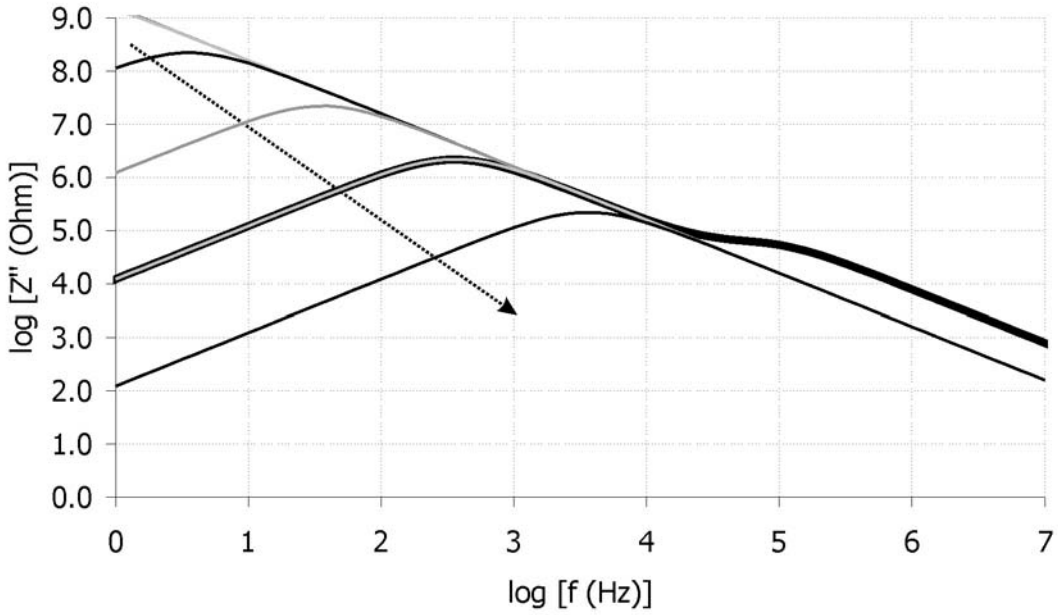

Figure 4-14 *Imaginary impedance spectrum when migrating charges dominate the signal. The black thick line, drawn for comparison, is the same as in Figure 4-9. For the spectra construction $\tau = 10^{-5}$ s and $\langle\varepsilon\rangle = 10$. The dotted arrow shows the spectrum movement as σ increases from 10^{-14} S/m to 10^{-6} S/m in decade increments.*

4.4 Equivalent electrical circuits

In many physicochemical processes there is a phenomenological connection between the behaviour of a system and that of an electrical circuit. This analogy has been exploited by scientists in many different fields.

Dissipative processes can be modelled by resistances. Capacitors can simulate phenomena where energy is stored. Inductors are also used in cases where magnetic fields are investigated. Apart from these elements, there is a number of distributed elements that can be used for effective description of various phenomena (84).

Mijovic and co-workers were the first to employ equivalent circuits for the characterisation of curing systems and reviewed the subject (105).

4.5 Modelling the dielectric behaviour using equivalent circuits

The three prominent phenomena that affect the dielectric signal in thermoset cure can be modelled in terms of circuit elements. Whilst the dipolar relaxation and the charge migration equivalent circuit representations are quite standard, the modelling of

electrode polarisation is still an open issue (84). Many different models and circuits have been proposed, based on different assumptions and case studies.

4.5.1 Circuit model for electrode polarisation

The effect of electrode polarisation in cure monitoring studies has been considered by some researchers as a parasitic phenomenon (103, 189) bearing no useful information about the curing system. On the other hand, as was outlined in § 4.2.1, electrode polarisation depends on both the condition of the electrodes and on the number and mobility of the charged species. It is therefore expected to reflect the decrease in the number and the mobility of the charges species during cure.

Feldman et al (189) reviewed some of the methods used to model electrode polarisation. One of the most common equations employed corresponds to the constant phase element (CPE):

$$Z^*_{CPE} = \frac{A_{CPE}}{(j\omega)^n} \tag{4.29}$$

The parameter A_{CPE} has units of Ohm/s^n which implies that its physical meaning will depend on the value of the exponent n (190). For $n = 1$, $(A_{CPE})^{-1}$ is regarded as a capacitor. For $n = 0$, A_{CPE} represents a resistor.

One physical explanation for the CPE is electrode roughness. The electrode surface is considered to be a fractal surface with dimension between 2 and 3. Mulder et al (191) showed that the exponent n is related with the fractal dimension D_f of the electrode surface:

$$n = \frac{1}{D_f - 1} \tag{4.30}$$

For a completely flat electrode, the above equation gives $n = 1$ whereas for a three dimensional porous electrode $n = 0.5$.

4.5.2 Circuit model for charge migration

The migration of charges is considered a purely dissipative process. A simple resistance, R_{ion}, is used for modelling the process.

$$Z^*_{ion} = R_{ion} \tag{4.31}$$

This, however, is not true for all cases. There are materials where charges do not move instantaneously with the application of the external field. A dispersion of the

ionic species response to the field is observed and the recorded impedance is adequately modelled by equations similar to those listed in Table 4-I for the dielectric response of different dipoles (84).

4.5.3 Circuit model for dipolar relaxation

The equivalent circuit model for dipolar relaxation accounts for the movements of both induced and permanent dipoles. The instantaneous response of induced dipoles means that minimum energy is lost during their movement, as they polarise. Therefore, only a capacitor, C_{ind}, is used for modelling this process. The polarisation of permanent dipoles, on the other hand, involves movements of large molecular segments. These movements are much slower compared to the induced dipoles and become hindered by other neighbouring molecular species resulting in some energy dissipation (see Figure 4-3). The overall response of permanent dipoles is modelled by a capacitor, C_{dip}, and a resistor, R_{dip}, connected in series. The equivalent circuit is shown in Figure 4-15a. The overall dipolar impedance will be:

$$Z^*_{dip} = \frac{\dfrac{R_{dip}C_{dip}^2}{\left(C_{dip}+C_{ind}\right)^2}}{1+\omega^2\dfrac{R_{dip}^2C_{dip}^2C_{ind}^2}{\left(C_{dip}+C_{ind}\right)^2}} - j\frac{\dfrac{1}{\omega\left(C_{dip}+C_{ind}\right)}+\omega\dfrac{R_{dip}^2C_{dip}^2C_{ind}}{\left(C_{dip}+C_{ind}\right)^2}}{1+\omega^2\dfrac{R_{dip}^2C_{dip}^2C_{ind}^2}{\left(C_{dip}+C_{ind}\right)^2}} \qquad (4.32)$$

Using the transformation relationships of Table 4-II one can easily prove* that the above impedance equation transforms to the simple Debye permittivity eqs. (4.7) – (4.8) with the identities (104):

$$\begin{aligned} \tau &= R_{dip}C_{dip} \\ \varepsilon_r &= \frac{C_{ind}}{\varepsilon_0} \\ \varepsilon_u &= \frac{C_{dip}+C_{ind}}{\varepsilon_0} \end{aligned} \qquad (4.33)$$

If there are more than one dipolar species in the material exhibiting different relaxation times, a series of parallel *RC* circuits has to be used, each one representing a dipolar relaxation. The resulting circuit is pictured in Figure 4-15b.

* The transformation is much easier in terms of algebraic calculation when admittance is used instead of impedance

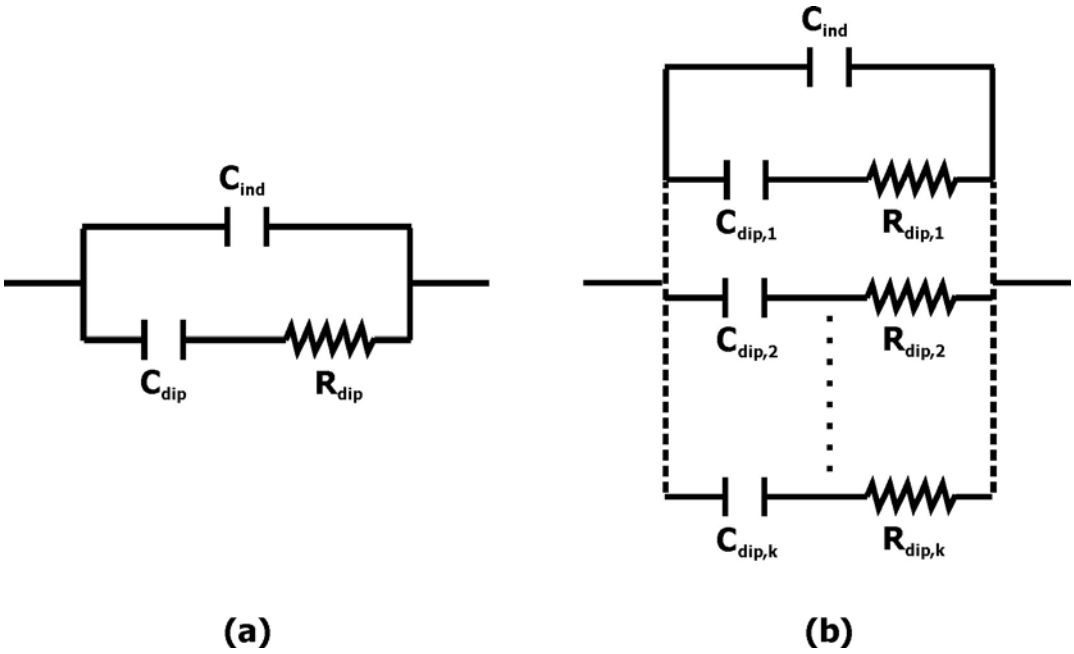

Figure 4-15 *Equivalent circuits for dipolar relaxation. (a) Dipoles with a single relaxation time (Debye model), (b) distribution of dipolar species with different relaxation times*

In this study, the single relaxation time equivalent circuit (Debye model) is used for the description of dipolar relaxations. The dominance of migrating charges in the signal renders the identification and quantification of any dipolar relaxations a difficult task. It is therefore assumed that all the relaxing dipoles give rise to a mean relaxation time.

4.5.4 Overall equivalent circuit

The final circuit for thermoset cure, accounting for all three phenomena present in the dielectric signal, is given in Figure 4-16. In the remaining of the text this circuit will be termed as the "standard circuit".

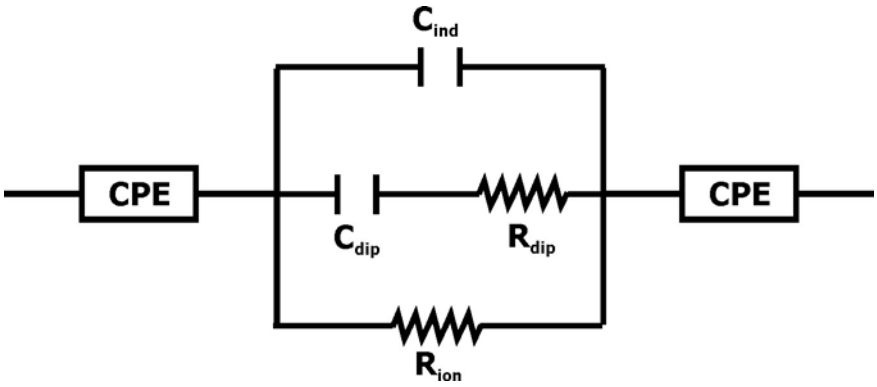

Figure 4-16 *Equivalent circuit for thermoset cure (standard circuit)*

The real and imaginary impedance of the circuit are:

$$Z' = \frac{R_{ion}\left(\omega^2 \tau_3 \left(\tau_3 + \tau_2\right) + 1\right)}{\omega^2 \left(\tau_1 + \tau_2 + \tau_3\right)^2 + \left(\omega^2 \tau_1 \tau_3 - 1\right)^2} + 2A_{CPE} \frac{\cos\left(\frac{n\pi}{2}\right)}{\omega^n} \tag{4.34}$$

$$Z'' = \frac{\omega R_{ion}\left(\omega^2 \tau_2 \tau_3^2 + \tau_1 + \tau_2\right)}{\omega^2 \left(\tau_1 + \tau_2 + \tau_3\right)^2 + \left(\omega^2 \tau_1 \tau_3 - 1\right)^2} + 2A_{CPE} \frac{\sin\left(\frac{n\pi}{2}\right)}{\omega^n} \tag{4.35}$$

where

$$\begin{aligned} \tau_1 &= R_{ion} C_{ind} \\ \tau_2 &= R_{ion} C_{dip} \\ \tau_3 &= R_{dip} C_{dip} \end{aligned} \tag{4.36}$$

are time constants. The first two time constants do not have a direct physical meaning. The third time constant, τ_3, is the mean dipolar relaxation time. A plot of the real and imaginary impedance spectrum is given in Figure 4-17. The circuit element values are given on Table 4-III.

The Z' spectrum decreases exponentially, linearly on the log-log plot, with increasing frequency at very low and very high frequencies. At intermediate frequencies the plot is similar to Figure 4-12 where migrating charges dominate the signal. Similarly, the Z'' spectrum decreases exponentially at very low and high frequencies. A peak, characteristic of the migrating charge domination, exists at intermediate frequencies.

Table 4-III: *Circuit element values for the construction of the spectra of Figure 4-17*

R_{ion} (Ohm)	R_{dip} (Ohm)	C_{dip} (F)	C_{ind} (F)	A_{CPE} (Ohm.s$^{-0.5}$)	n
10^6	10^4	2×10^{-12}	10^{-11}	5.00×10^5	0.5

A more clear understanding of the different features of the Z' and Z'' spectrum can be made if the circuit of Figure 4-16 is transformed into a simpler equivalent circuit, which is shown in Figure 4-18. The CPEs which model electrode polarisation remain the same. The circuit which models ionic conduction and dipolar relaxation is split into two simple parallel RC circuits. The inter-relationships between the elements of the two

circuits are given in Table 4-IV. The derivation of these relationships can be found in Appendix C.

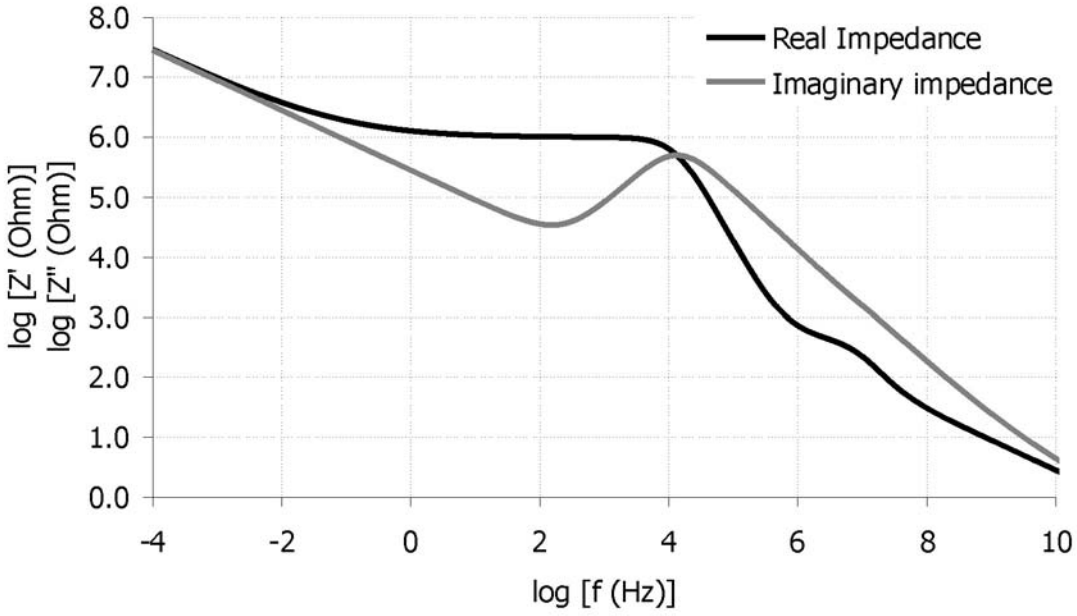

Figure 4-17 *Real and imaginary impedance spectrum of the standard circuit*

The real and imaginary impedance spectra of Figure 4-17 are analysed according to the new equivalent circuit in Figures 4-19 and 4-20 respectively. The influence of the three sub-circuits is seen clearly. The CPEs dominate the signal at very low and very high frequencies. Circuit A contribution dominates the signal at intermediate frequencies while circuit B is responsible for the shoulder in the *Z'* spectrum.

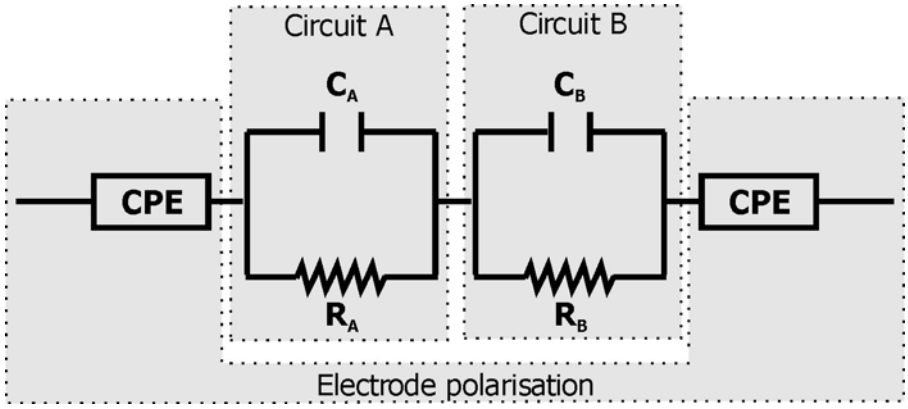

Figure 4-18 *Equivalent circuit yielding the same impedance as the standard circuit. The circuit is split in three simpler sub-circuits.*

In Chapter 6, this separation of the standard equivalent circuit into three sub-circuits will be used for the identification of frequency ranges where only one phenomenon dominates the signal (frequency mapping).

Table 4-IV: *Relationships between the elements of the two circuits*

Standard circuit → Figure 4-18	**Figure 4-18 → Standard circuit**
$R_A = \frac{R_{ion}}{2}(1+k)$	$R_{ion} = R_A + R_B$
$R_B = \frac{R_{ion}}{2}(1-k)$	$R_{dip} = \frac{R_A R_B (R_A + R_B)(C_A + C_B)^2}{(R_A C_A - R_B C_B)^2}$
$C_A = \frac{1}{k}\left(C_{ind} + C_{dip} - \frac{1-k}{1+k}\frac{R_{dip}C_{dip}}{R_{ion}}\right)$	$C_{ind} = \frac{C_A C_B}{C_A + C_B}$
$C_B = \frac{1}{k}\left(\frac{1+k}{1-k}\frac{R_{dip}C_{dip}}{R_{ion}} - C_{ind} - C_{dip}\right)$	$C_{dip} = \frac{(R_A C_A - R_B C_B)^2}{(R_A + R_B)^2 (C_A + C_B)}$
$k = \frac{\frac{R_{ion}}{R_{dip}}\left(\frac{C_{ind}}{C_{dip}} + 1\right) - 1}{\sqrt{\left(\frac{R_{ion}}{R_{dip}} + 1\right)^2 + \left(\frac{R_{ion}}{R_{dip}}\frac{C_{ind}}{C_{dip}} - 1\right)^2 + 2\left(\frac{R_{ion}}{R_{dip}}\right)^2 \frac{C_{ind}}{C_{dip}} - 1}}$	

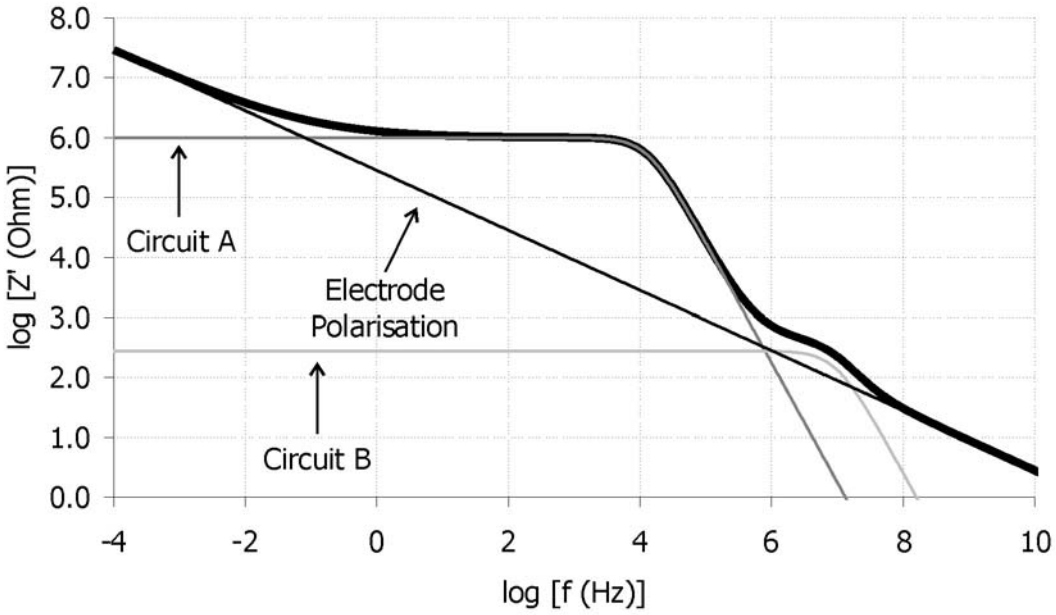

Figure 4-19 *Analysis of the real impedance (thick line) spectrum according to the equivalent circuit of Figure 4-18. The influence of Circuits A, B and the electrode polarisation contribution are shown.*

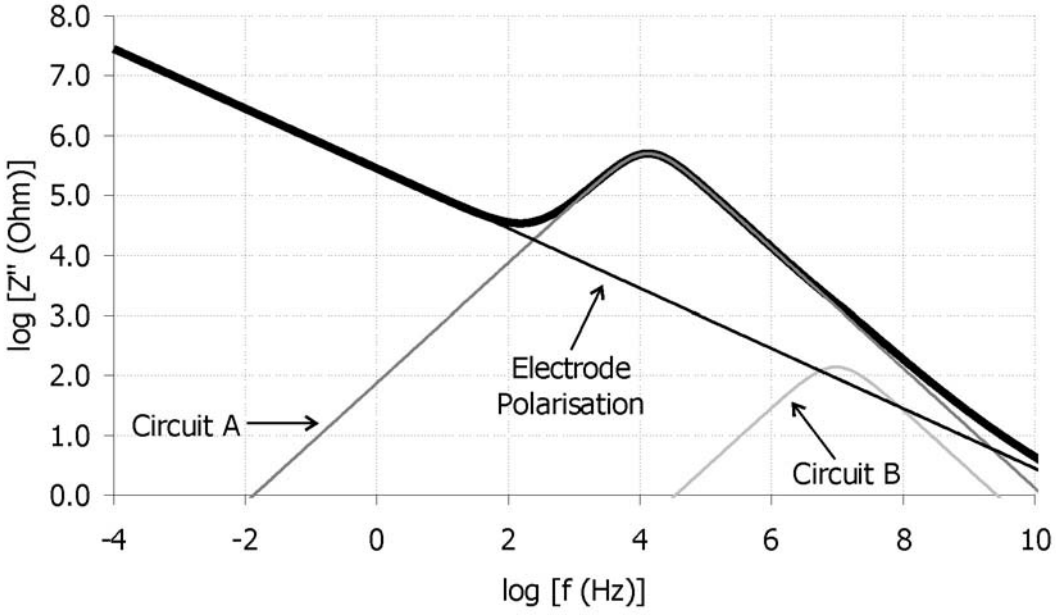

Figure 4-20 *Analysis of the imaginary impedance spectrum (thick line) according to the equivalent circuit of Figure 4-18. The influence of Circuits A, B and the electrode polarisation contribution are shown.*

4.5.5 Sensitivity of the circuit parameters on the impedance spectrum

The influence of each of the circuit parameters on the impedance spectrum has been studied numerically. The value of each parameter was altered by ± 10% while the rest of the parameters remained unchanged. The values of Table 4-III were used for the nominal spectrum. The average (over the whole frequency range) percentage differences are listed in Table 4-V and illustrated for real impedance in Figure 4-21. The most influential parameters are R_{ion} and C_{ind}. A 10% change in these values results in an average change of more than 5% in the impedance spectra. The change at individual frequencies could be as high as 20% as can be seen in Figure 4-21. On the other hand, the less influential parameters are R_{dip} and C_{dip}. A 10% change in R_{dip} causes an average change of 0.5% in the real impedance spectrum. The change in the imaginary impedance spectrum is less than 0.01%.

Table 4-V: *Average percentage change of the impedance spectrum when one of the circuit parameters is altered by ±10%*

Circuit parameters	Real Impedance		Imaginary Impedance	
	+10%	-10%	+10%	-10%
R_{ion}	8.42	7.10	8.00	7.56
R_{dip}	0.58	0.01	0.57	0.01
C_{ind}	6.14	5.36	4.95	4.96
C_{dip}	1.34	1.03	1.35	1.02
A_{CPE}	0.25	2.86	0.25	2.86
n	2.21	2.61	1.12	2.52

It is expected that the estimation accuracy will be higher in the most influential parameters. Parameters with less impact on the spectrum are estimated with less accuracy, as it will be shown in § 4.6.6. It has to be noted though, that the sensitivity of each parameter on the spectrum depends on the values of all the circuit parameters. The numbers in Table 4-V will be different if the initial values, taken from Table 4-III, are different. However, the values of Table 4-III are representative of the values obtained during resin cure and the remarks drawn from Table 4-V have been proved valid in the modelling of thermoset cure dielectric spectra.

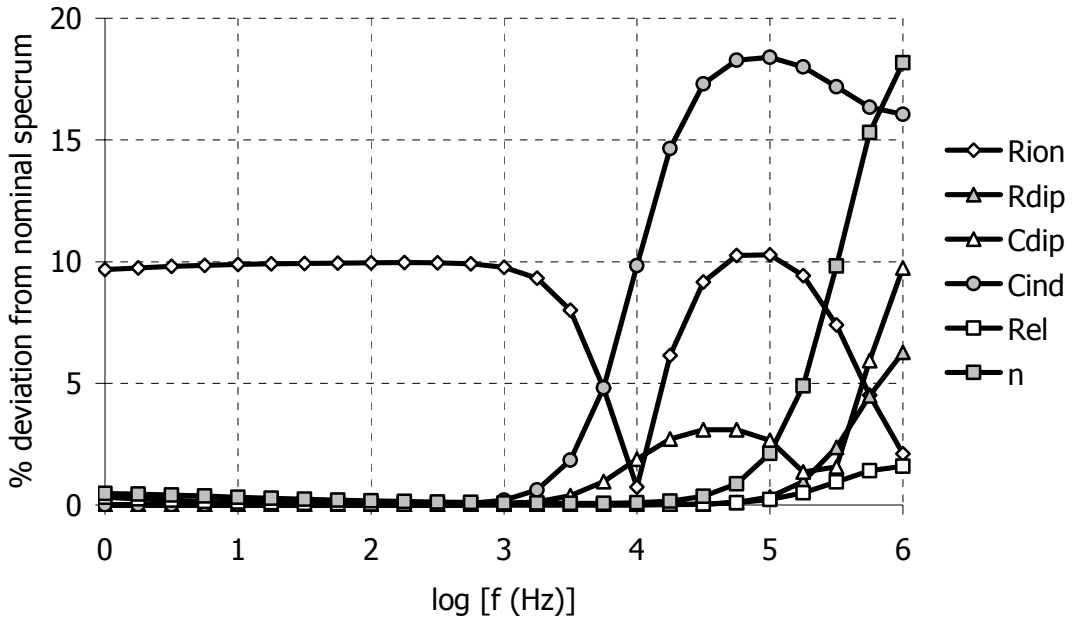

Figure 4-21 *Percentage changes in the real impedance spectrum when one of the circuit parameter is altered by +10% as function of frequency*

So far, the connection between complex permittivity and complex impedance has been demonstrated for the case of thermoset cure. Equivalent circuit analysis provides an excellent tool for the study and separation of the contributions of the different polarisation phenomena that together produce the dielectric response. In the remainder of this chapter, the numerical techniques used for the modelling of the dielectric data are presented.

4.6 Genetic algorithms (GA)

This second part of Chapter 4 deals with the numerical techniques used for modelling the cure monitoring impedance spectra.

Genetic algorithms are a family of optimisation methods that use appropriate operators with principles taken from biological processes (192, 193). The algorithm performs iterative exploration of a predefined solution space. Genetic algorithms are an excellent tool for finding global optima in multivariable systems (192).

4.6.1 Principles of Genetic algorithms

The basic biological processes that genetic algorithms emulate are the following:

- Survival of the fittest individuals
- Accidental mutation

In mathematical terms, the survival of the fittest individuals depend on some conditions expressed generally by a set of equations (192). In optimisation problems these conditions usually sum up to a single equation called the fitness function (192, 193).

Based on their "fitness function" value (or plain fitness) two individuals are selected and produce two new individuals called "offspring". Fitter individuals are more likely to be selected. The procedure is repeated until a new population is produced. The next generation of individuals will have a higher average fitness than the previous generation (192). Therefore, on average, the new individuals will be closer to the solution. This is the "crossover operation". Crossover exploits the given population of individuals and produces new, fitter individuals.

The "mutation operation" explores the whole solution space by randomly changing some individuals. These altered individuals are then exploited by the crossover operation based on their fitness value. Mutation ensures that new areas of the solution space are always included in the search.

Apart from these two basic operations, other operations exist and are used depending on the problem. One of the operations used in this study is "elitism" (193). In elitism, a number of individuals with the highest fitness pass directly to the next generation.

In general, there are seven major steps in a common genetic algorithm:

- Creation of a population of random individuals representing possible solutions of the problem under consideration.

- Evaluation of how close to the real solution each individual is. The evaluation is achieved by using an appropriate fitness function.
- Sorting of the individuals according to their fitness value.
- Selection of two individuals from the initial population. The selection probability of each individual is based on its fitness value.
- Application of crossover and mutation operations.
- Iteration of the two last steps until a new population is produced.
- Iteration of the whole procedure (apart from the initial step) until an individual with fitness higher than a predefined value has been obtained. That individual is set as the solution to the problem under consideration.

The fitness function has to possess some specific properties. It has to assign small values to individuals that are far from the solution and high values to individuals that are close to the solution.

The individuals are coded in binary format before the application of the crossover and mutation operations. Binary format simplifies the implementation of the two operations on the individuals. After the application of crossover and mutation the individuals are decoded for the calculation of their fitness value.

4.6.2 Genetic algorithm as a tool for data fitting

The use of genetic algorithms as a curve fitting technique is straightforward. In all fitting methods, the aim is to minimise the errors between the experimental values and the values obtained by a model. In the least squares methods, for example, the sum of squares of the differences between the experimental data and the model are minimised. The objective function has the following form:

$$S\left(p_1, p_2, \ldots, p_k\right) = \sum_{i=1}^{q}\left(y_i - f\left(p_1, p_2, \ldots, p_k, x_i\right)\right)^2 \qquad (4.37)$$

where p_i $i = 1,2,\ldots,k$ are the model parameters and (x_i, y_i) $i = 1,2,\ldots,q$ are the experimental points.

In linear problems, eq. (4.37) results in a linear system of k equations (as many as the model parameters) which can be solved easily. In non-linear problems, however, iterative methods have to be used. These methods require an initial estimate of the solution or a starting point. Depending on the initial estimate, iterative methods can get trapped in a local minimum. They are not guaranteed to find the global minimum.

Equations such as eq. (4.37) can be implemented easily on a GA as a part of a fitness function. Instead of using gradient methods, a solution space is constructed by setting high and low limits for each model parameter. Each individual is a vector of the model parameters. The GA performs a search on the whole solution space and calculates directly the sum of squares for each individual. Consequently, the search for a solution cannot get trapped in a local minimum.

GA algorithms have already been used in fitting impedance/admittance spectra in other scientific areas like electrochemistry (194, 195).

4.6.3 Use of a genetic algorithm for fitting dielectric data

The flow chart of the genetic algorithm used for the minimization of the objective function is illustrated in Figure 4-22. The fitness function F was:

$$F = \frac{100}{S + 1} \tag{4.38}$$

where S is the objective function. The fitness function takes the value of 100 when $S \rightarrow 0$ and approaches 0 when $S \rightarrow \infty$. Prior to the algorithm, the solution search space is defined by setting appropriate ranges for the circuit parameters. The algorithm terminates when an individual with fitness higher than some critical value $F_{critical}$ is found or when the number of generations G exceeds a predefined value G_{max}.

When an old generation is used for the production of a new generation, the individuals are sorted according to their fitness. When a new generation is produced, N_e individuals with the highest fitness pass directly to the next generation (elitism). The rest N - N_e individuals are the offspring of the previous generation individual which reproduce through crossover and mutation.

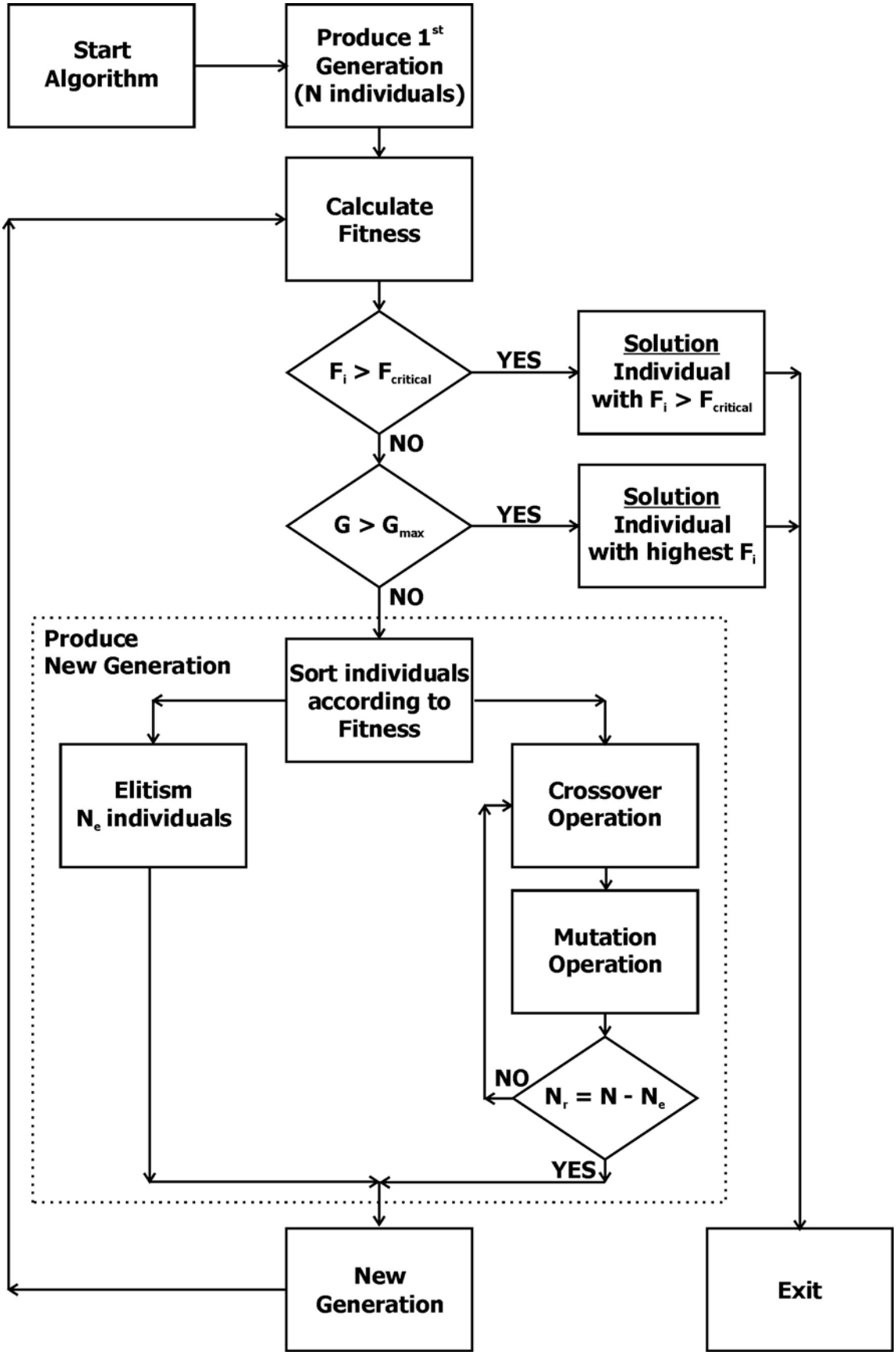

Figure 4-22 *Flow chart of the GA used for spectra modelling*

4.6.4 The significance of the objective function

Impedance spectra are usually fitted using weighted least squares methods introduced by Macdonald (84, 196-200) who has also developed an application for fitting equivalent circuits to impedance/admittance spectra (201). The weight factors are a measure of the variance of each experimental point (84, 202). As impedance is a complex variable, the real and imaginary components are fitted concurrently, taken as independent variables. Theoretically this is incorrect since the Kramers – Kronig transformation relates the real and imaginary part of such a variable (203, 204). In practice, however, one needs to cover a very large frequency spectrum for the transformation to give valid results (84).

The objective function for the weighted least squares has the following form:

$$S = \sum_{i=1}^{q} \left(\left(w_i^{re} \left(Z'_{\exp,i} - Z'_{\mathrm{mod},i} \right) \right)^2 + \left(w_i^{im} \left(Z''_{\exp,i} - Z''_{\mathrm{mod},i} \right) \right)^2 \right) \tag{4.39}$$

where S denotes the objective function, q is the number of measured frequencies and w_i are the weight factors for the real (superscript *re*) and imaginary (superscript *im*) impedance. The subscripts *exp* and *mod* denote the experimental and the model predicted impedance values respectively.

Instead of the sum of squares, one can use the sum of absolute differences as the objective function:

$$S = \sum_{i=1}^{q} \left(w_i^{re} \left| Z'_{\exp,i} - Z'_{\mathrm{mod},i} \right| + w_i^{im} \left| Z''_{\exp,i} - Z''_{\mathrm{mod},i} \right| \right) \tag{4.40}$$

Absolute differences are more robust than least squares (205). This robustness is very useful in cases where experimental data are noisy or when they contain outliers. In cure monitoring, the impedance values change several orders of magnitude (typically 10^3 – 10^9 Ohm) during the experiment and towards the end of cure they reach the limit of the apparatus measuring range (see § 3.4.2). Outliers could originate from interference with other electrical devices, especially in the 60 Hz region (206). Dygas and Breiter have proposed a method for detecting and eliminating outliers in impedance spectra by comparing each experimental point with its estimated standard deviation (207). However, this method is not suitable for analyzing consecutive dielectric spectra, as it demands replicate scans for the standard deviation calculation. In cure monitoring, the impedance spectrum changes as the cure progresses. As a

result it is not possible to repeat the measurement because the material state will change. Only the whole experiment can be repeated.

Instead of using weights, one can use logarithmic scaling of the experimental data. In the case of least squares, the objective function will be:

$$S = \sum_{i=1}^{q} \left(\left(\log Z'_{\text{exp},i} - \log Z'_{\text{mod},i} \right)^2 + \left(\log Z''_{\text{exp},i} - \log Z''_{\text{mod},i} \right)^2 \right) \tag{4.41}$$

An investigation on which of the above functions is more appropriate to model cure monitoring data has been carried out. Four objective functions were tested. They are listed in Table 4-VI.

Table 4-VI: *Objective functions tested for modelling cure monitoring data*

Weighted least squares	$S_1 = \sum_{k=1}^{q} \left(\left(\frac{Z'_{\text{exp},k} - Z'_{\text{mod},k}}{Z'_{\text{mod},k}} \right)^2 + \left(\frac{Z''_{\text{exp},k} - Z''_{\text{mod},k}}{Z''_{\text{mod},k}} \right)^2 \right)$
Weighted absolute differences	$S_2 = \sum_{i=1}^{q} \left(\left\| \frac{Z'_{\text{exp},i} - Z'_{\text{mod},i}}{Z'_{\text{mod},i}} \right\| + \left\| \frac{Z''_{\text{exp},i} - Z''_{\text{mod},i}}{Z''_{\text{mod},i}} \right\| \right)$
Logarithmic scaling Least squares	$S_3 = \sum_{i=1}^{q} \left(\left(\log Z'_{\text{exp},i} - \log Z'_{\text{mod},i} \right)^2 + \left(\log Z''_{\text{exp},i} - \log Z''_{\text{mod},i} \right)^2 \right)$
Logarithmic scaling Absolute differences	$S_4 = \sum_{i=1}^{q} \left(\left\| \log Z'_{\text{exp},i} - \log Z'_{\text{mod},i} \right\| + \left\| \log Z''_{\text{exp},i} - \log Z''_{\text{mod},i} \right\| \right)$

As can be seen in the above table, the inverse of each experimental point is taken as a measure of the variance of the particular point (84, 194) and used as a weight. Error free data are produced at 25 frequencies, using eqs. (4.34) - (4.35) and the parameter values listed in Table 4-III. The search space for each parameter is given in Table 4-VII. The estimation of the circuit parameters was repeated 10 times. The average results, the standard deviation and the percentage difference from the correct values are presented in Table 4-VIII. The corresponding imaginary impedance spectra are shown in Figure 4-23.

We can see that none of the four objective functions is significantly better or worse than the rest. Logarithmic scaling performs as well as using weights.

Table 4-VII : *Search space of the fitting parameters*

	R_{ion} (Ohm)	R_{dip} (Ohm)	C_{dip} (F)	C_{ind} (F)	A_{CPE} (Ohm)	n
Upper limit	1.25×10^{6}	4.95×10^{4}	1.90×10^{-12}	1.25×10^{-12}	1.95×10^{6}	0.625
Lower limit	7.50×10^{5}	5.00×10^{2}	1.00×10^{-13}	7.50×10^{-13}	5.00×10^{4}	0.375

The elements describing dipolar relaxation (R_{dip} and C_{dip}) are the least accurately estimated parameters because of their small influence on the overall spectrum. The objective functions based on absolute differences (S_2 and S_4) give better estimations for R_{dip} and C_{dip} compared to the objective functions employing least squares (S_1 and S_3).

Table 4-VIII: *Results from test runs for the determination of the objective function*

	R_{ion} (Ohm)	R_{dip} (Ohm)	C_{dip} (F)	C_{ind} (F)	A_{CPE} (Ohm/s^n)	n
S_1	1000391	23793	1.35×10^{-12}	1.02×10^{-11}	505406	0.503
S_2	1003824	14534	1.68×10^{-12}	1.02×10^{-11}	507548	0.505
S_3	1004254	16695	1.59×10^{-12}	1.03×10^{-11}	508711	0.506
S_4	1005266	15424	1.67×10^{-12}	1.02×10^{-11}	509733	0.507
% Percentage difference compared to the correct values						
S_1	0.04	137.93	32.55	2.28	1.08	0.69
S_2	0.38	45.34	15.94	2.23	1.51	0.90
S_3	0.43	66.95	20.69	2.78	1.74	1.13
S_4	0.53	54.24	16.00	2.10	1.95	1.41
Standard deviation						
S_1	1251	3984	9.18×10^{-14}	8.18×10^{-14}	4603	0.004
S_2	1029	1608	9.80×10^{-14}	8.33×10^{-14}	3011	0.003
S_3	1832	2075	1.03×10^{-13}	7.62×10^{-14}	4691	0.003
S_4	1285	2124	9.66×10^{-14}	8.12×10^{-14}	4697	0.003

In this study, the logarithmic scaling absolute differences objective function was used for the modelling of cure monitoring spectra.

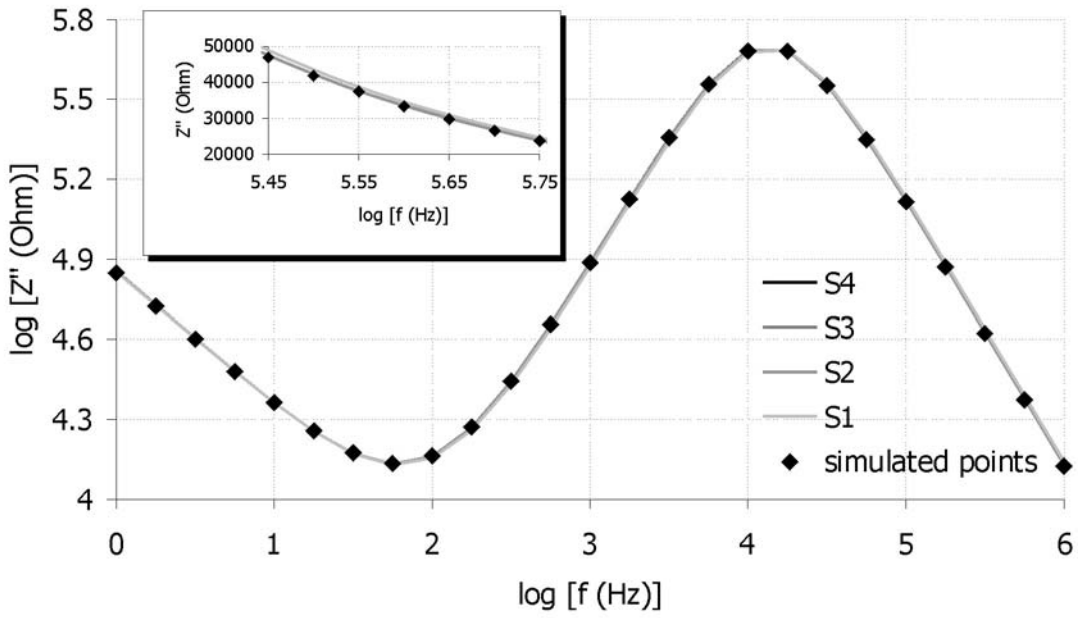

Figure 4-23 *Imaginary impedance spectrum fitting using the four objective functions. The differences between the objective functions are barely visible even on the non-logarithmic scale (inset graph).*

The performance of the objective function when error and outliers are present in the data was also assessed. The simulated data used for the determination of the objective function above were contaminated with 10% Gaussian noise. Four outliers were also added to the spectrum. These conditions are worse than the actual experimental cure monitoring spectra where the usual level of noise is around 1% (however, a 10% error could arise when very high impedance values are measured – see Figure 3-12) and only one or two outliers could be observed in just a few spectra per experiment. The fitting was repeated 10 times. Table 4-IX summarises the averaged results.

Table 4-IX: *Fitting results from spectra contaminated with noise and outliers*

	R_{ion} (Ohm)	R_{dip} (Ohm)	C_{dip} (F)	C_{ind} (F)	A_{CPE} (Ohm/s^n)	n
Correct values	1000000	10000	2.00×10^{-12}	1.00×10^{-11}	500000	0.500
Estimated values	982742	12044	2.13×10^{-12}	9.74×10^{-12}	533720	0.580
Standard deviation	1780	5076	6.37×10^{-13}	9.76×10^{-14}	7910	0.007

The circuit parameters are estimated with satisfactory accuracy. The parameters with the highest error are R_{dip} and n which differ from the correct values by about 20% and 16% respectively. Also, R_{dip} and C_{dip} estimation exhibits high standard deviation.

In order to further enhance the robustness of the objective function a regularisation term was added:

$$S = \sum_{i=1}^{q}\left(\left|\log Z'_{\exp,i} - \log Z'_{\mathrm{mod},i}\right| + \left|\log Z''_{\exp,i} - \log Z''_{\mathrm{mod},i}\right|\right) + \lambda_T \sum_{i=1}^{P_{no}}\left(\left|\frac{p_i - p_{i,est}}{p_{i,est}}\right|\right) \quad (4.42)$$

where q is the number of experimental points, λ_T is the Tikhonov regularisation parameter (208), $P_{no} = 6$ is the number of fitting parameters, p_i are the parameter values and $p_{i,est}$ is an estimation of the expected parameter values.

The presence of the regularisation term suppresses any irregular fluctuations imposed by errors or outliers on the estimated parameters (209, 210).

The same spectrum (10% Gaussian noise – 4 outliers) was used in order to test the effectiveness of eq. (4.42). The correct parameter values, given in Table 4-IX, were used as the expected estimates. In order to determine the optimum value of the regularisation parameter λ_T the algorithm was run for a range of values. Each run was repeated 10 times.

Figure 4-24 shows the dependence of λ_T on the estimated circuit parameters. The initial value ($\lambda_T = 0$) means that the fitting was performed without the regularisation term. The migrating charges resistance R_{ion} estimation is independent of the regularisation parameter. The estimated value has a 2% error compared with the correct value. Conversely, the estimation of the dipolar resistance R_{dip} shows some dependence on λ_T. For $\lambda_T < 0.2$ there is 20% error on the estimation. As the regularisation parameter increases the estimation error is reduced. This improvement on the estimation becomes less significant for $\lambda_T > 1$. Similar observations are made in the case of C_{dip}. The initial estimation error of about 7% is reduced to less than 2% when $\lambda \geq 1$. The estimation error on the induced capacitance C_{ind} is always less than 3%. However, C_{ind} estimation also improves as λ_T increases. The electrode polarization parameters exhibit a more significant dependence with λ_T. A_{CPE} shows an error of about 8% without regularisation. This error is reduced to less than 1% when $\lambda_T = 1$. The exponent n estimation error is over 15% without regularisation. This error is reduced to around 5% for $\lambda_T > 1$.

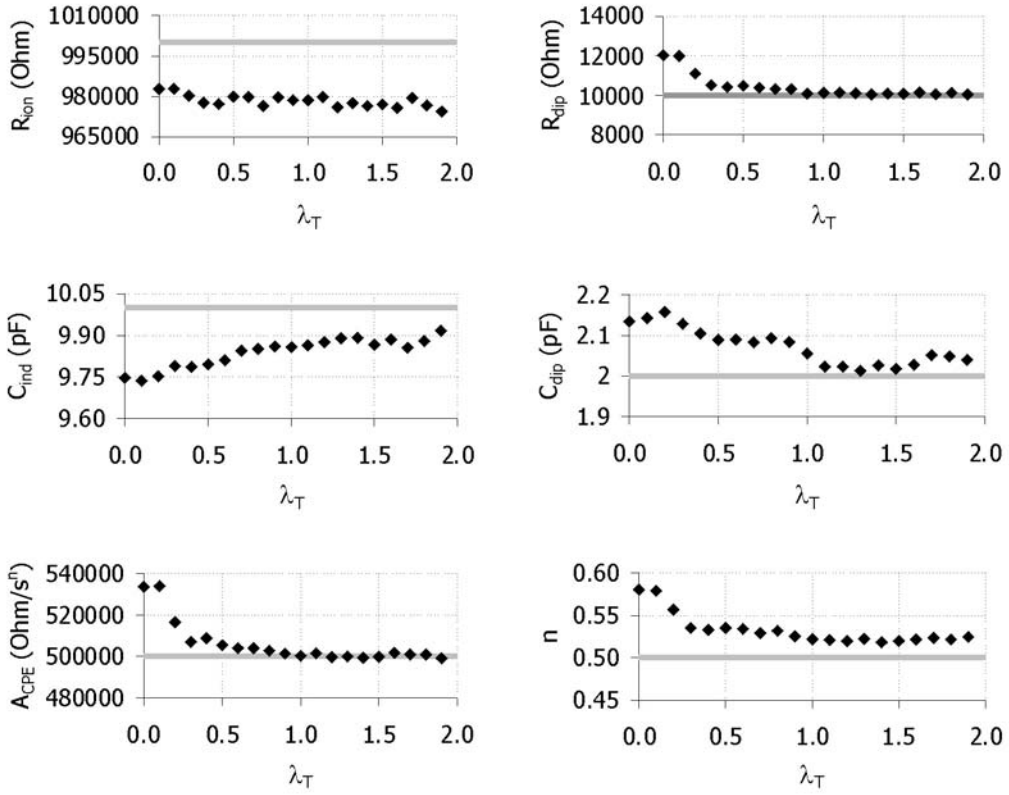

Figure 4-24 *Circuit parameter estimation as a function of the regularisation parameter λ_T. Grey lines indicate the correct values.*

From the above analysis we can see that the presence of the regularisation term improves the parameter estimation algorithm. One problem for the implementation of eq. (4.42) is the need for an adequate estimation of the circuit parameters. In cure monitoring experiments the impedance spectra "move" slowly as the cure progresses. It is expected that most of the circuit parameter values will not change significantly during two consecutive measurements. Thus, the modelling of the chronologically preceding spectra could be used for the calculation of the estimates $p_{i,est}$ for the modelling of the next spectrum. This issue is discussed in detail in § 4.6.6.

4.6.5 Evaluation of GA parameters

The GA main parameters are the number N of individuals per generation, the maximum number of generations G, the exchange probability p_e and the mutation probability p_m. Other parameters are the number of individuals N_e which pass directly to the next generation and the number of individuals N_r which reproduce. The solution vectors were encoded in binary format before the application of the crossover and

mutation operations. The crossover operation is performed by selecting two encoded individuals and exchanging their bits. The bits to be exchanged are selected with probability p_e.

The mutation operation is performed by selecting a bit of an individual with probability p_m and changing that bit from zero to one or reversely. The probability p_m changes for each successive generation according to the dispersion of the solution vectors (adaptive mutation).

Test runs of the genetic algorithm were performed using the spectra shown in Figure 4-17 without any error in order to tune the algorithm parameters. The search space for each parameter is given in Table 4-VII.

Eq. (4.42) was used as the objective function in these test runs. Eq. (4.38) was the fitness function. The maximum fitness of the final generation was used for comparing the different scenarios. For the number of generations G the fitness is divided by the final fitness value which is obtained after 200 generations. For each scenario the algorithm ran 10 times. The average values of the runs are reported in Table 4-X.

Table 4-X : *Fitting results for the tuning of the genetic algorithm parameters*

p_e	Maximum Fitness value	Standard Deviation
0.4	95.41	4.242
0.5	95.12	4.052
0.6	94.25	3.351
G	**Normalised Fitness**	**Standard deviation**
60	0.996	0.00245
80	0.998	0.00122
100	1.000	0.00051
120	1.000	0.00005
140	1.000	0.00002
N	**Maximum Fitness value**	**Standard deviation**
81	95.32	4.700
101	94.50	4.785
121	94.48	4.126

It can be observed that p_e values in the range of 0.4 – 0.6 do not affect the algorithm performance. The maximum fitness is obtained when the number of generations G is close to 100. Higher G values make the algorithm slower without improving its performance. The population number N does not affect the algorithm performance when its value is higher than 81.

The final algorithm parameter values are given in Table 4-XI. The number of individual that pass directly to the next generation (elitism) was 10% of the total population.

The chosen values were used for all the experimental fitting runs that will be presented in the subsequent chapters. The mutation probability value p_m shown in Table 4-XI is the initial value for the first generation.

Table 4-XI : *Genetic algorithm values used for modelling cure monitoring spectra*

G	N	p_e	p_m	N_e	N_r
100	101	0.5	0.025	10	90

4.6.6 Algorithm validation in monitoring consecutive spectra

One of the main aims of the modelling algorithm is the automatic fitting of all the spectra acquired during a single experiment, with the minimum human intervention. Since impedance spectra shift during thermoset cure, the solution space for the parameters has to be adjusted prior to the implementation of the genetic algorithm.

Another issue that has to be addressed is the calculation of the estimates of the parameter values, $p_{i,est}$, which appear in the regularisation term in eq. (4.42).

Figure 4-25 shows three consecutive imaginary impedance spectra from the cure of RTM6 at 1°C/min. The spectra are taken from a point in the cure where the temperature increase causes the signal to shift at the highest observable rate. We can see that the shift is relatively minor. This implies that the relative changes of the circuit parameter values are small between consecutive spectra.

Therefore we can assume that the circuit parameter values vary linearly during the acquisition of two consecutive spectra. The search space of the circuit parameters can then be adjusted by linear extrapolation:

$$p_{i,est}^{k} = \frac{p_i^{k-1}\left(t^k - t^{k-2}\right) - p_i^{k-2}\left(t^k - t^{k-1}\right)}{t^{k-1} - t^{k-2}} \qquad i = 1,2,\ldots,P_{no} \qquad (4.43)$$

In the above equation, the subscripts denote the parameter number (in accordance to eq. (4.42)) and the superscripts denote time steps. When the time step is constant, something common in dielectric experiments, the above equation is simplified:

$$p_{i,est}^{k} = 2p_i^{k-1} - p_i^{k-2} \tag{4.44}$$

This estimation is also used for the calculation of the regularisation term in eq. (4.42).

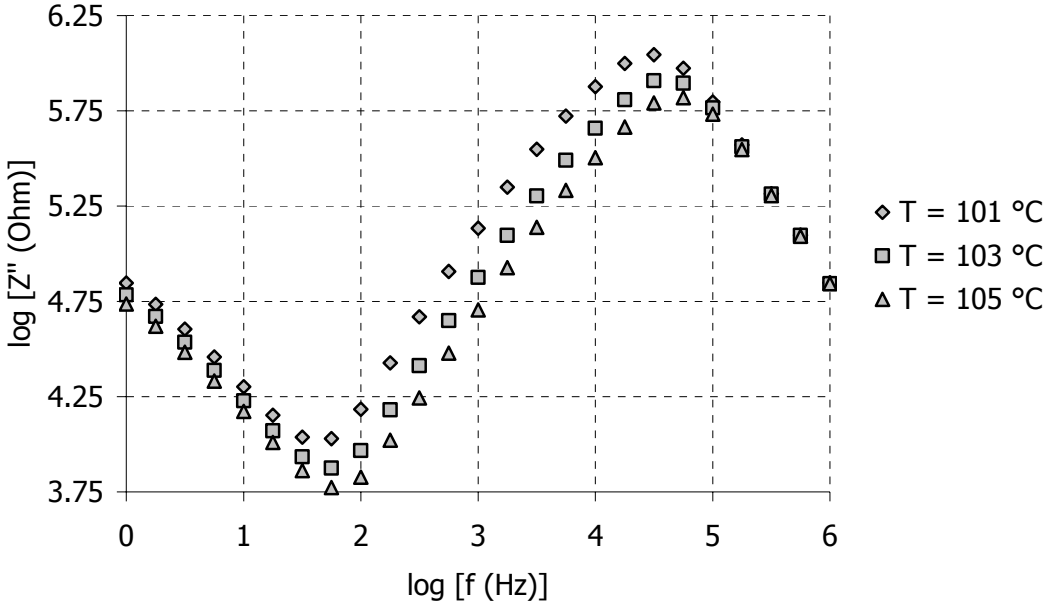

Figure 4-25 *Consecutive Imaginary Impedance spectra during the cure of RTM6 at 1°C/min. The shift rate of the spectra is the highest observed in all RTM6 dielectric experiments.*

The expected parameter values $p_{i,est}$ are used as the arithmetic means of the solution space. The range of the solution space is defined as a percentage p_r of the parameter estimations $p_{i,est}$.

$$\begin{aligned} &\text{Upper limit: } p_i = \left(1 + p_{r,i}\right) p_{i,est} \\ &\text{Lower limit: } p_i = \left(1 - p_{r,i}\right) p_{i,est} \end{aligned} \tag{4.45}$$

Different percentages are used for each parameter. They are listed in Table 4-XII. Parameters with greater uncertainty are given wider ranges.

Table 4-XII: *Adaptive solution space for the equivalent circuit parameters*

	R_{ion}	R_{dip}	C_{dip}	C_{ind}	A_{CPE}	n
Range (%)	99	99	50	10	99	20

The flow chart of the modelling procedure is shown in Figure 4-26.

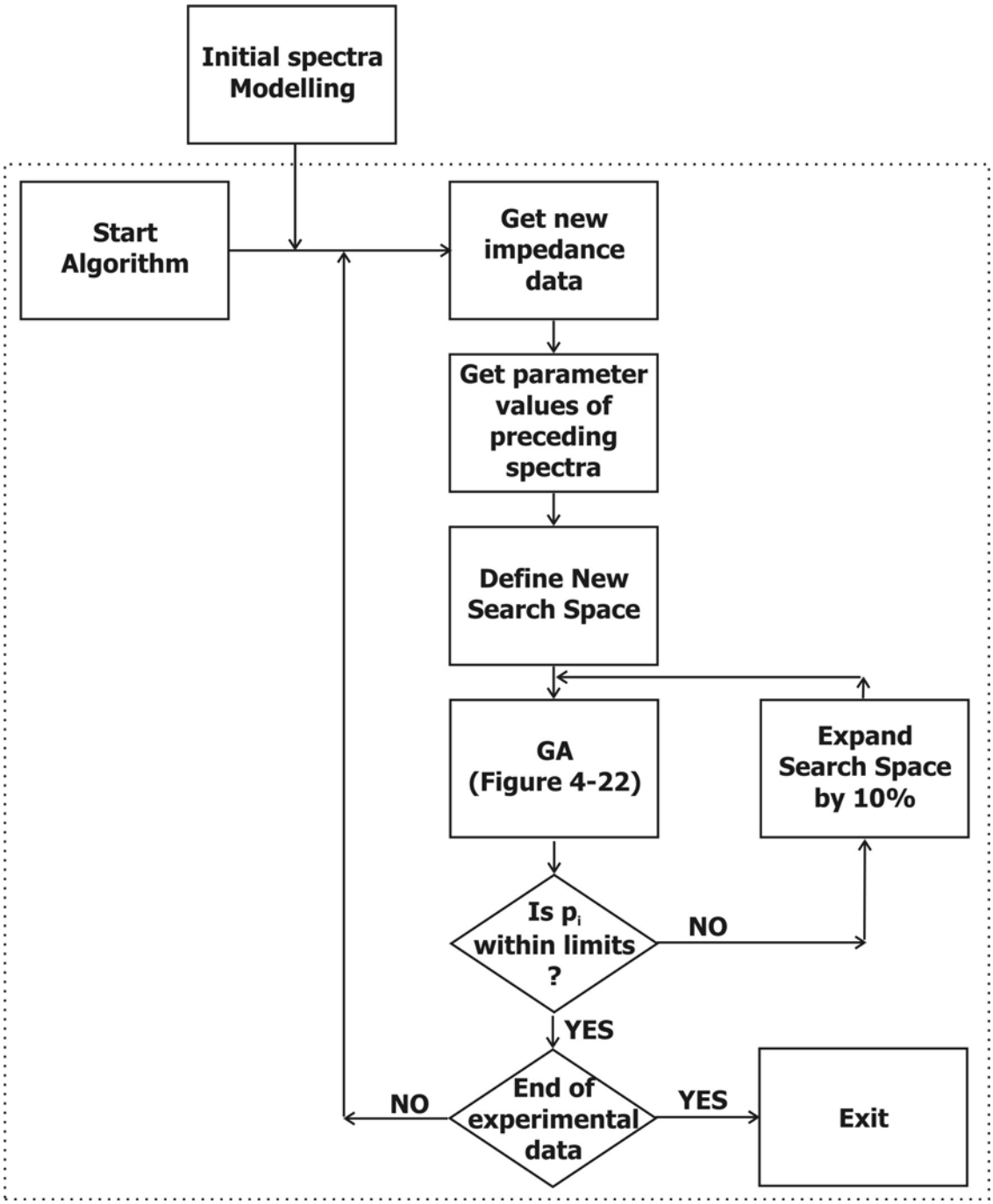

Figure 4-26 *Modelling algorithm for dielectric cure monitoring experiments*

The first two spectra are modelled separately and the results are inputs to the main algorithm. If any of the parameter estimations is within 5% of the upper or lower limit of the search space then the limits are widened by 10% and the modelling of the spectrum is repeated. The algorithm continues until all spectra have been modelled.

The validation of the modelling procedure was done by creating artificial impedance spectra which shift similarly to the experimental ones. The relationships listed below were used for constructing the spectra.

$$
\begin{aligned}
R_{ion} &= 10^5 e^{0.0871t} \quad Ohm \\
R_{dip} &= 10^4 e^{0.0951t} \quad Ohm \\
C_{ind} &= 1.5\times10^{-11} \quad F \\
C_{dip} &= 2\times10^{-12} + \frac{5\times10^{-12}}{1+\left(7\times10^{-10}e^{0.4055(t-30)}\right)^2} \quad F \qquad 35 < t < 73 \qquad (4.46) \\
A_{CPE} &= 10^5 e^{0.0599t} \quad Ohm.s^{0.5} \\
n &= 0.5
\end{aligned}
$$

where t is the time. 5 % Gaussian error was added to the data. Four outliers were also placed in random.

As Figure 4-26 suggests, the first two spectra were modelled separately. The resulting spectra and the modelling results are shown in Figure 4-27 for the imaginary impedance. We can see that the modelling curves describe the artificial data very well.

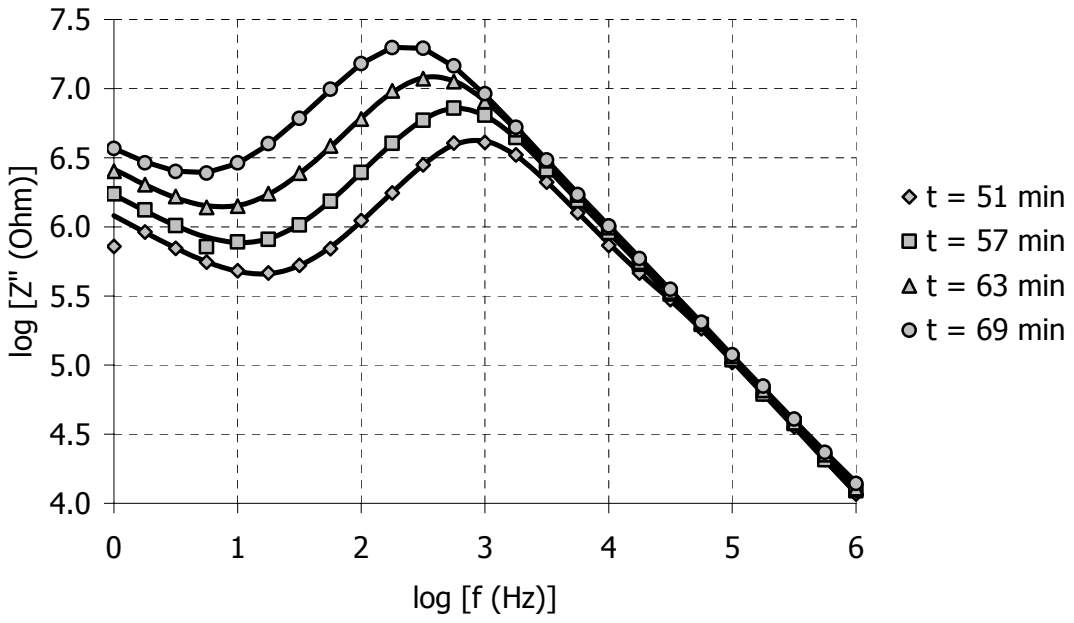

Figure 4-27 *Modelling artificial imaginary impedance spectra*

The algorithm performs well even when outliers are present, as is the case in the curve corresponding to 51 min (outlier at 1 Hz).

The equivalent circuit parameter values obtained by the GA are shown in Figure 5-25. In each plot, grey lines represent the correct values as they are calculated using the relationships in eq. (4.46). All parameters are accurately estimated. The maximum and average percentage errors from all the modelled spectra are given in Table 4-XIII.

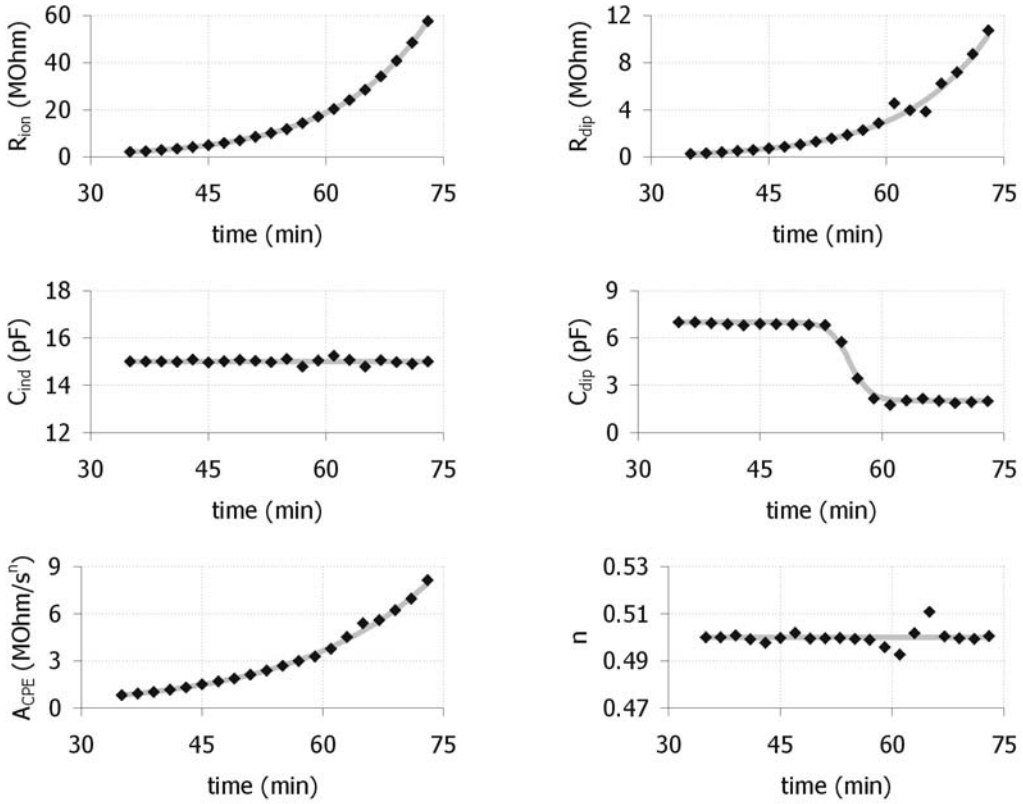

Figure 5-25 *Equivalent circuit parameters fitting. Grey lines denote the correct values*

R_{ion}, C_{ind} and n are determined with an average error less than 0.5%. On the other hand R_{dip} and C_{dip} errors are higher. This is due to the low sensitivity of these parameters on the modelled spectra (see § 4.5.5).

Table 4-XIII: *Equivalent circuit parameters percentage error*

	R_{ion} (Ohm)	R_{dip} (Ohm)	C_{dip} (F)	C_{ind} (F)	A_{CPE} (Ohm)	n
Maximum error	2.06	38.2	16.6	1.64	9.91	2.17
Average error	0.50	5.08	3.98	0.49	1.78	0.39

It is concluded that the algorithm shown in Figure 4-26 is suitable for modelling consecutive impedance spectra. The success of the estimation of each equivalent circuit parameter depends on its influence on the spectra. The combination of the least squares term and the regularisation term in the objective function (eq. (4.42)) ensures the global nature of the solution and enhances the correlation with the estimation of the preceding spectra.

5 Cure Characterisation: Measurement

5.1 Scope and objectives

In this chapter, the results from the experimental work are presented. A non parametric cure kinetics model for RTM6 is developed, based on DSC measurements and following the analysis of Skordos and Partridge (28). The glass transition temperature advancement is studied using MDSC. The main features of dielectric spectra taken under isothermal and non – isothermal conditions are identified and the combined influence of temperature and cure reaction is discussed.

5.2 Cure kinetics characterisation

DSC experiments were carried out on RTM6 resin under isothermal and non isothermal conditions. In all experiments the amount of resin cured did not exceed 7 mg. In the isothermal runs, a 20°C/min heating ramp was used in order to get to the dwell temperature. This is preferable to equilibrating the cell to the cure temperature and placing the sample in afterwards, since the resin will start to cure before its temperature reaches the dwell temperature. By increasing the temperature in a controlled manner, the cure of the resin prior to the isothermal segment can be

monitored and quantified (168). The non – isothermal conditions were heating ramps at constant rates. The heat flow was recorded as a function of time (isothermal experiments) and temperature (non – isothermal experiments). All experiments were repeated 2 – 4 times, depending on the reproducibility of the curves. The presented results are averages of the repeated runs.

5.2.1 Calorimetric experimental results

The reaction rate curves under isothermal conditions are shown in Figures 5-1 and 5-2. The autocatalytic nature of the polymerisation reaction is observed at all temperatures. The heat flow increases, reaches a maximum point and then decreases to a very low value as the resin approaches the vitrification point. The heat flow at "low" cure temperatures has very small values. The cure lasts up to 1000 minutes (at 100°C). At higher temperatures, the reaction commences before the cure temperature is reached and lasts less than 40 minutes (at 210°C).

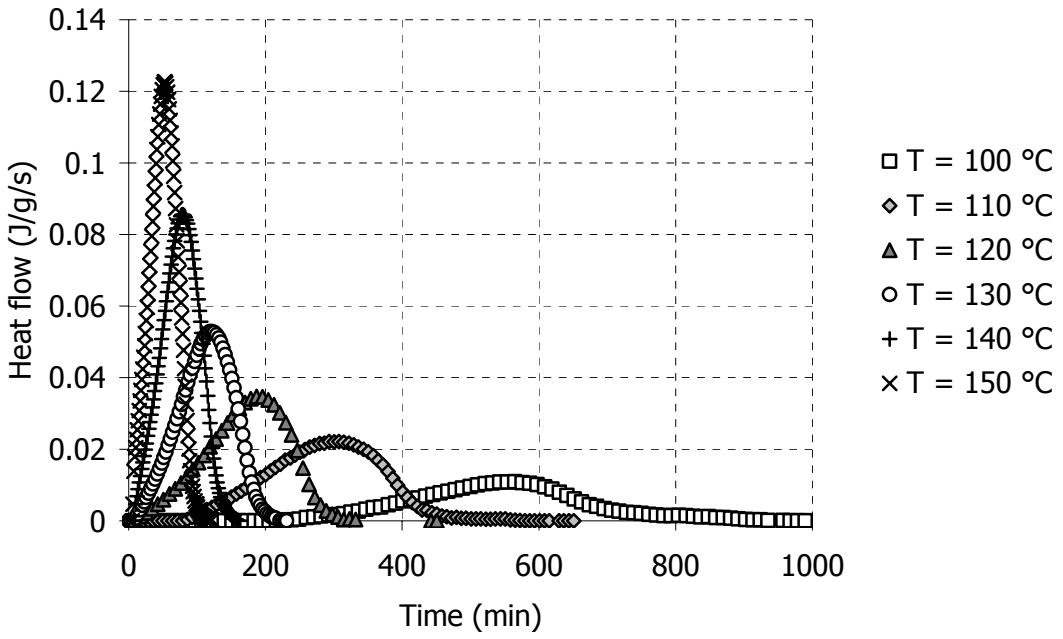

Figure 5-1 *Heat flow in the isothermal cure of RTM6 at "low" temperatures*

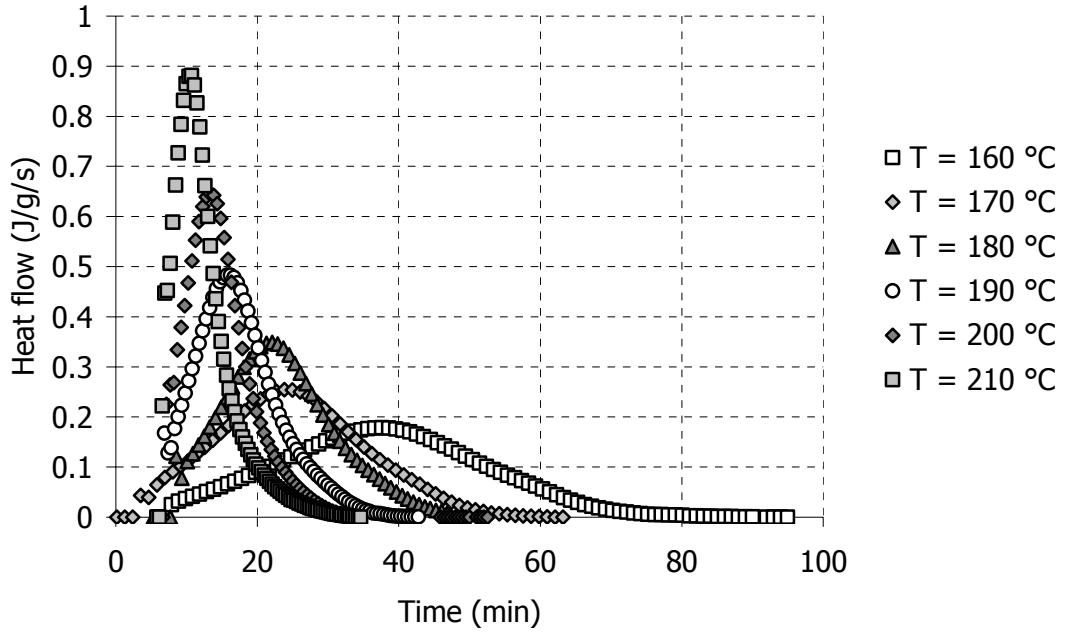

Figure 5-2 *Heat flow in the isothermal cure of RTM6 at "high" temperatures*

The reaction rate curves under dynamic conditions are shown in Figures 5-3 and 5-4. As in the isothermal experiments, the autocatalytic nature of the reaction is observed. At low reaction rates (Figure 5-3), the heat flow continues to exhibit measurable values well after the end of the reaction. A second peak in the heat flow is observed at temperatures above 200 °C. This peak is attributed to devitrification (156). The resin vitrifies before the reaction is complete as will be shown in the MDSC experiments (§ 5.2.3). Vitrification causes the reaction rate to decrease (cure reaction "slows down"). When the resin devitrifies the reaction resumes and the reaction rate increases causing the small peak to appear.

The slow increase of temperature allows the T_g of the resin to reach the cure temperature and causes the resin to vitrify. The curing temperature continues to increase and at some point exceeds the T_g of the resin. The resin devitrifies and the reaction rate increases (small peaks above 200°C in Figure 5-3). The increase of conversion causes the T_g to increase further. When the reaction is over (α = 1) the ultimate glass transition temperature, $T_{g\infty}$, is attained. At higher reaction rates, temperature increases too fast and the T_g does not exceed the curing temperature before the reaction is over.

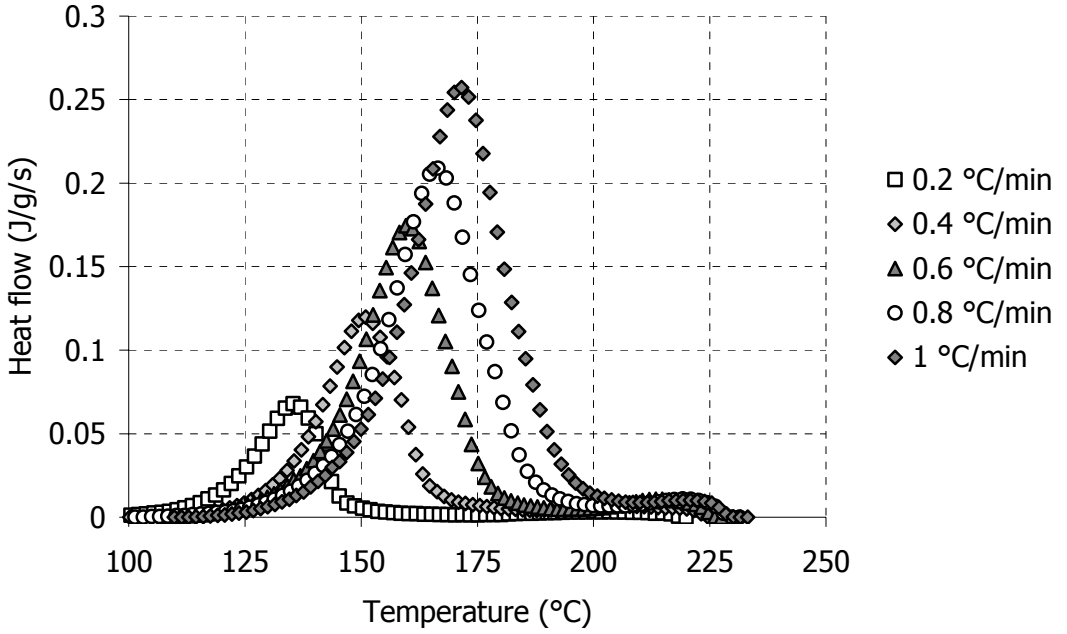

Figure 5-3 *Heat flow in the dynamic cure of RTM6 at low heating rates*

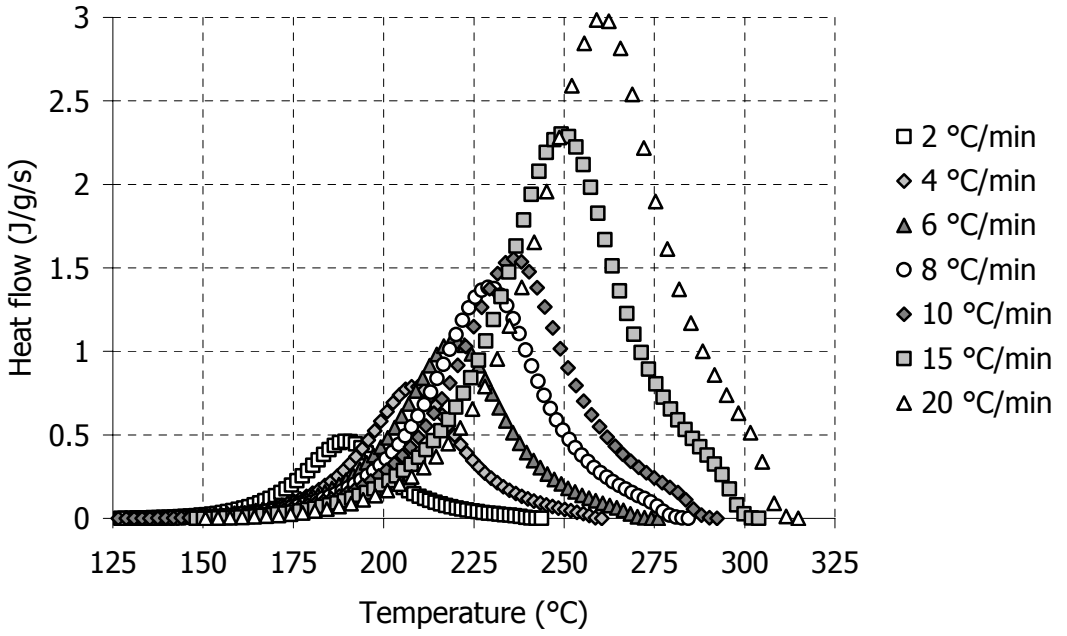

Figure 5-4 *Heat flow in the dynamic cure of RTM6 at high heating rates*

The total heat of the curing reaction is calculated by integrating the heat flow curves of the dynamic experiments. The baseline for the integration is calculated numerically using software provided by Dr A.A. Skordos (see § 3.4.3 for more information). The results are listed in Table 5-I.

Table 5-I: *Analysis of DSC experiments: Dynamic cure of RTM6*

Heating rate r (°C/min)	Total heat of reaction ΔH_{total} (J/g)	Conversion and temperature at maximum reaction rate	
		α^{max}	T^{max} (°C)
0.2	420	0.544	135.7
0.4	427	0.508	150.8
0.6	444	0.495	160.2
0.8	430	0.524	166.4
1	432	0.528	171.5
2	449	0.499	190.0
4	429	0.513	208.7
6	424	0.536	220.2
8	429	0.519	229.4
10	411	0.515	236.2
15	425	0.516	249.8
20	428	0.519	260.8
Average :	429.0 ± 9.9	0.518 ± 0.014	

The total heat of reaction is 429.0 ± 9.9 J/g. This value is in agreement with previous investigations on the same resin (19, 28). The total heat ΔH_{total} is independent of the heating rate. The reaction rate is calculated by the relationship:

$$\frac{d\alpha}{dt} = \frac{1}{\Delta H_{total}} \frac{dH}{dt} \tag{5.1}$$

where α is the conversion, $d\alpha/dt$ is the reaction rate, ΔH is the heat of the reaction and $d\Delta H/dt$ is the heat flow. Eq. 5.1 is valid when the reaction rate is proportional to the heat flow (§ 3.4.3). This is true in cases where the same molecular species are transformed throughout the reaction. In epoxy resin cure, the epoxy ring opens in the presence of hydrogen atoms taken from amines (1). Therefore the same species are involved in the curing reaction. Integration of eq. 5.1 gives the conversion α.

$$\alpha(t) = \frac{1}{\Delta H_{total}} \int_0^t \frac{dH}{dt} dt \tag{5.2}$$

The calculated reaction rates for all isothermal experiments are shown in Figure 5-5. The final conversion in all experiments is less than one. This indicates that the cure of RTM6 is not complete, due to vitrification.

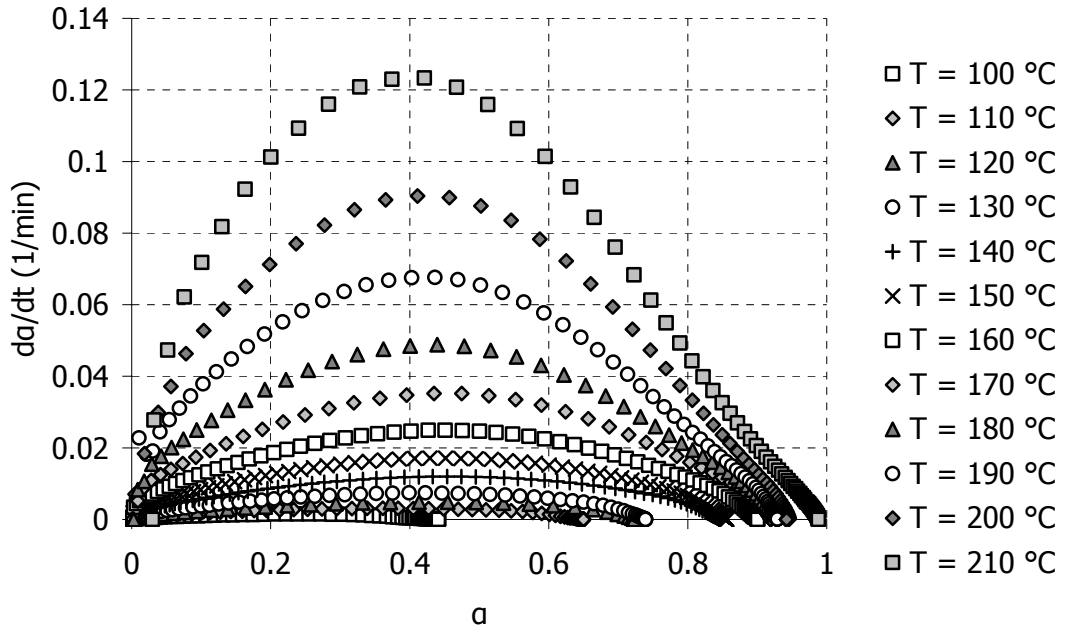

Figure 5-5 *Reaction rate versus fractional conversion in the isothermal cure of RTM6*

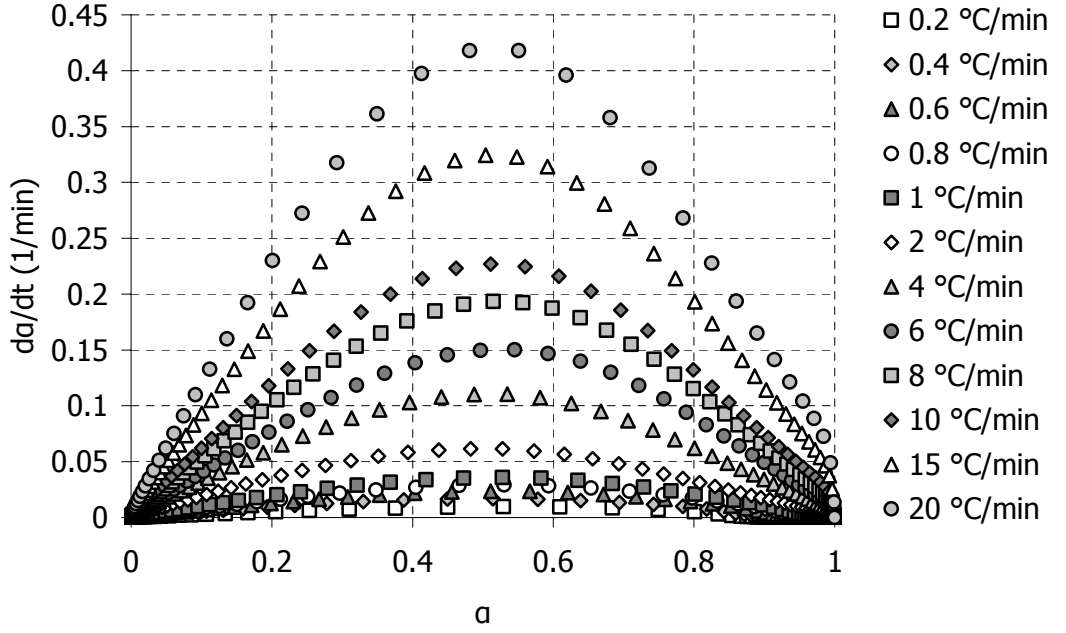

Figure 5-6 *Reaction rate versus fractional conversion in the dynamic cure of RTM6*

The reaction rate for the dynamic runs is shown in Figure 5-6. All the curves exhibit a maximum at a specific conversion, which is listed in Table 5-I. The similarity of the reaction rate curves is an indication that the reaction mechanism does not depend on the heating rate experienced by the resin.

The effect of thermal history on the reaction rate is illustrated in Figure 5-7 where reaction rate curves obtained by isothermal runs are compared with data obtained by dynamic runs having the same temperature and conversion values.

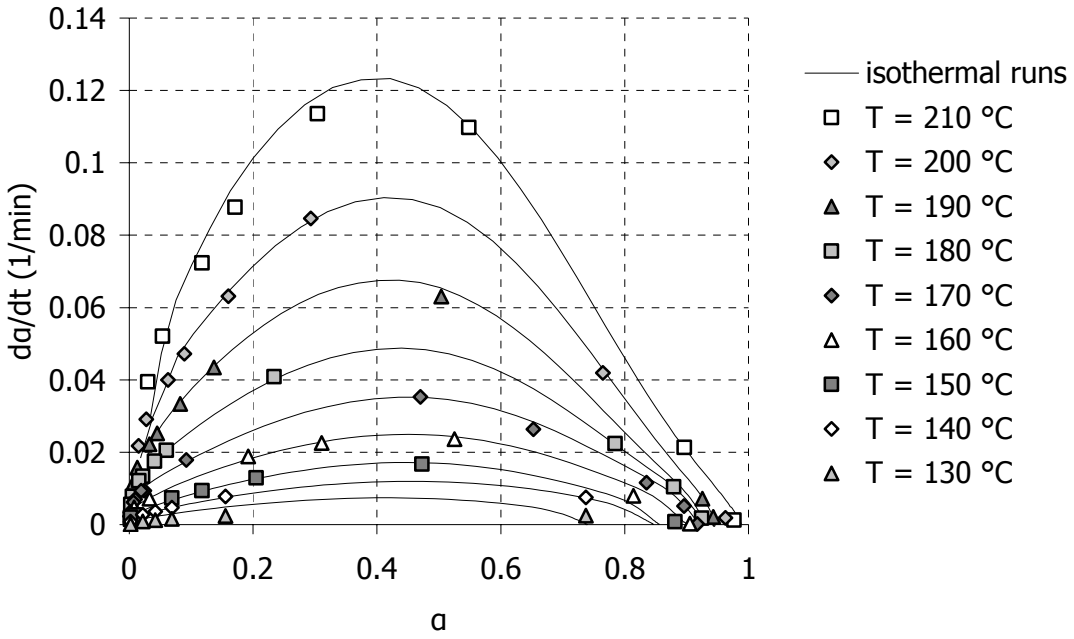

Figure 5-7 *Superposition of reaction rate – conversion data points obtained by dynamic DSC runs and reaction rate – conversion curves obtained by isothermal DSC runs for RTM6. Different markers are used for the dynamic data that correspond to different temperatures. The solid lines denote the isothermal curves.*

The reaction rate values obtained by dynamic experiments are very close to the values obtained by the isothermal experiments. Therefore, the reaction rate is uniquely defined at any stage by the temperature and the conversion (28):

$$\frac{d\alpha}{dt} = f\left(\alpha, T\right) \tag{5.3}$$

As already discussed in § 1.3.1, the existence of such a function *f(α,T)* is necessary for the application of any modelling technique to the DSC data.

5.2.2 Non – parametric cure kinetics modelling

Using all the DSC experimental curves, a map of the reaction rate in the temperature conversion space was built. Conversion steps of 0.01 and temperature steps of 4°C were used for the map construction. Linear interpolation was used for calculating the reaction rate at intermediate temperatures – conversions. The map is shown in Figure 5-8.

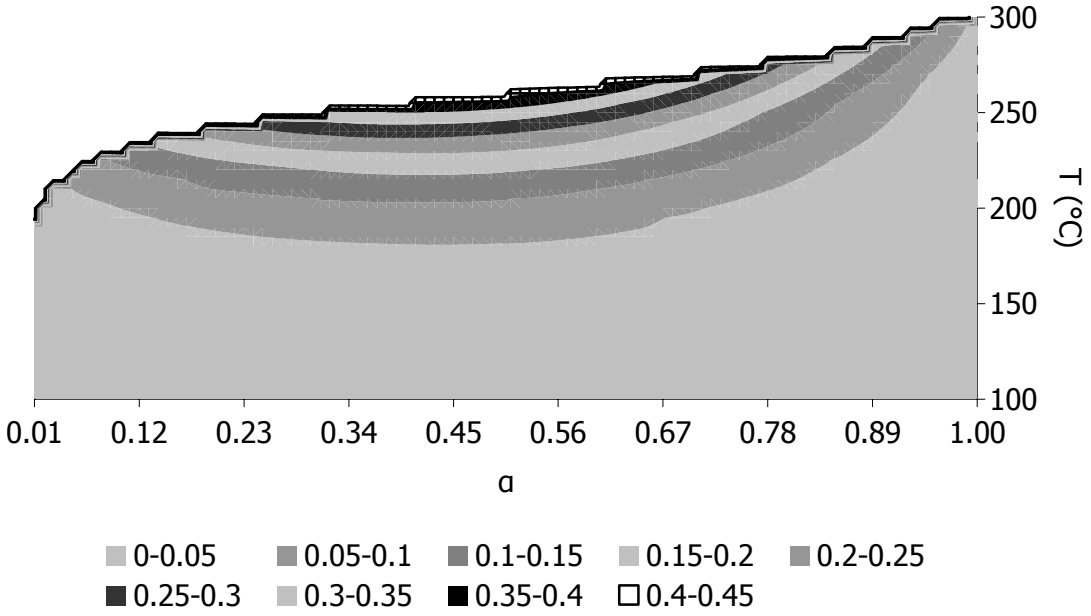

Figure 5-8 *Reaction rate map for RTM6 cure. Different shades correspond to different reaction rate ranges. The reaction rate unit is 1/min.*

The map can be used for modelling the cure kinetics of RTM6 (28). The inputs are the temperature and the conversion and the output is the reaction rate. Given the temperature profile and an initial conversion, the reaction rate can be calculated by linear interpolation. The reaction rate is then used for the calculation of the conversion at the next time step. The procedure continues until the end of the given temperature profile. The initial conversion is chosen to be arbitrarily small. In this study, the initial conversion was 0.01 in all cases. A correlation between the reaction rate and the temperature at which the conversion is 0.01 was established by the experimental curves. This correlation, which is shown in Figure 5-9, is used for assigning the first temperature – conversion point in the reaction rate map.

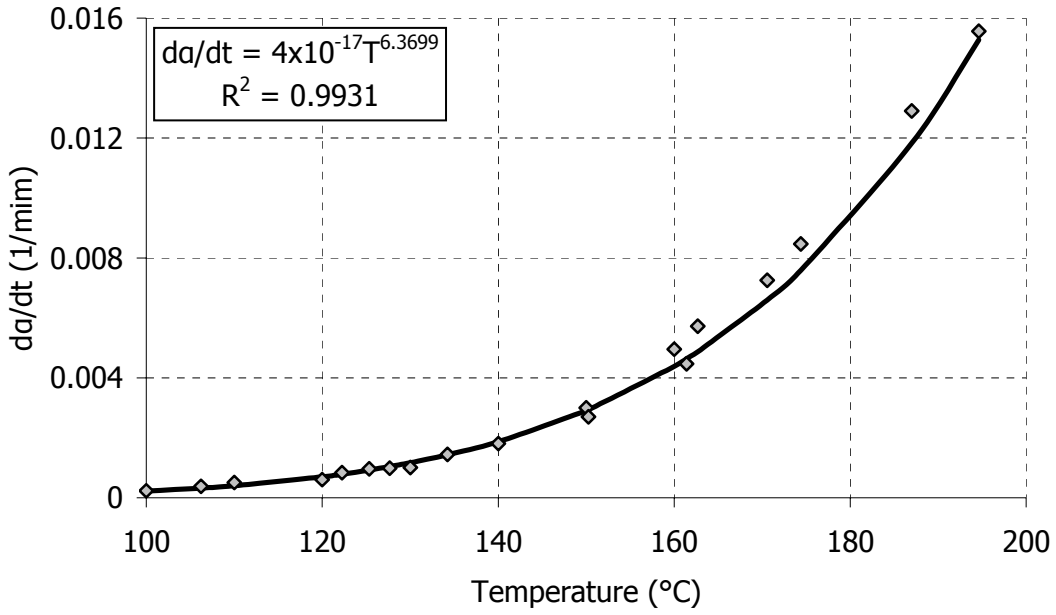

Figure 5-9 *Reaction rate versus temperature at α = 0.01. Experimental points taken from both isothermal and dynamic experiments*

The model is validated by simulating the DSC experiments. Prior to each simulation, the experimental data corresponding to the simulated temperature profile were removed and the reaction rate map was reconstructed.

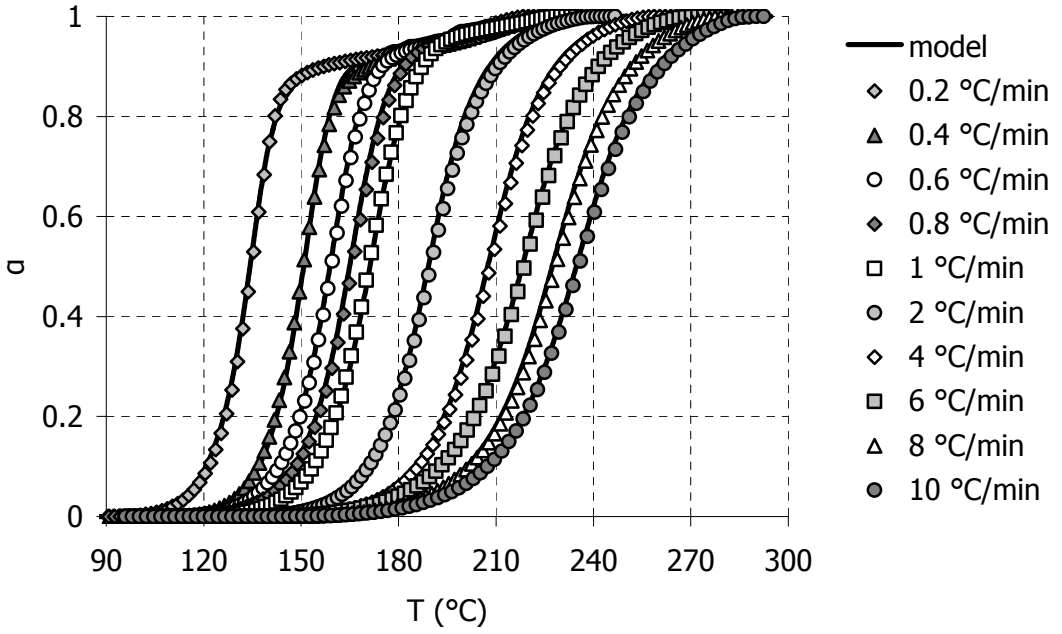

Figure 5-10 *Comparison of model prediction and experimental results for the dynamic cure of RTM6*

The modelling results are shown in Figure 5-10 for dynamic runs and in Figure 5-11 for isothermal runs. In all cases the agreement with the experimental data is very good. The non – parametric model is capable of following the kinetics of RTM6 throughout the cure, even in later stages where vitrification – devitrification phenomena are observed.

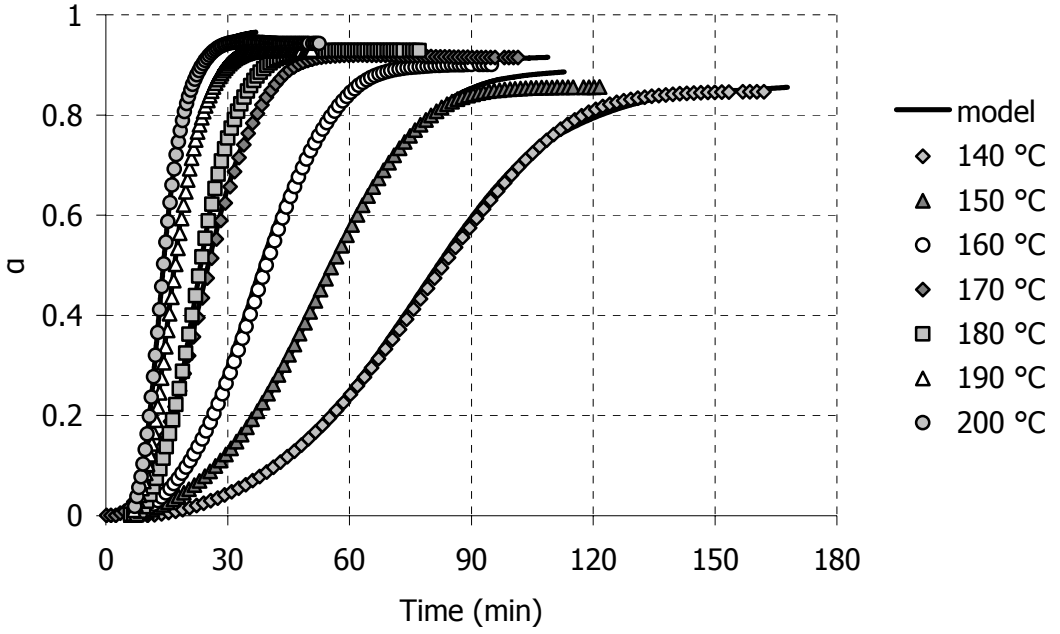

Figure 5-11 *Comparison of model prediction and experimental results for the isothermal cure of RTM6*

5.2.3 Vitrification measurements

The vitrification time of RTM6 under isothermal and dynamic cure conditions was measured using MDSC. Isothermal experiments were conducted at 120°C, 130°C, 140°C, 150°C, 160°C, 170°C, 180°C, 190°C and 200°C. The underlying heating rates in the dynamic experiments were 0.4°C/min, 0.6°C/min, 0.8°C/min and 1°C/min. The curing temperature was modulated around the underlying thermal profile. The modulation period was 1 min. The modulation amplitude was 1°C.

The experimental data are pictured in Figure 5-12 for the cure of RTM6 at 140°C and in Figure 5-13 for the cure of RTM6 at 0.6°C/min. In both cases the heat flow follows the modulated changes of temperature. In Figure 5-14 a Lissajous plot is constructed for both experiments. The signal in the isothermal experiment is much lower compared to the dynamic one because of the low exotherm in the isothermal cure. In both cases,

however, an ellipse is formed and retained throughout the experiment. This indicates a linear response from the resin reaction to the imposed temperature modulation.

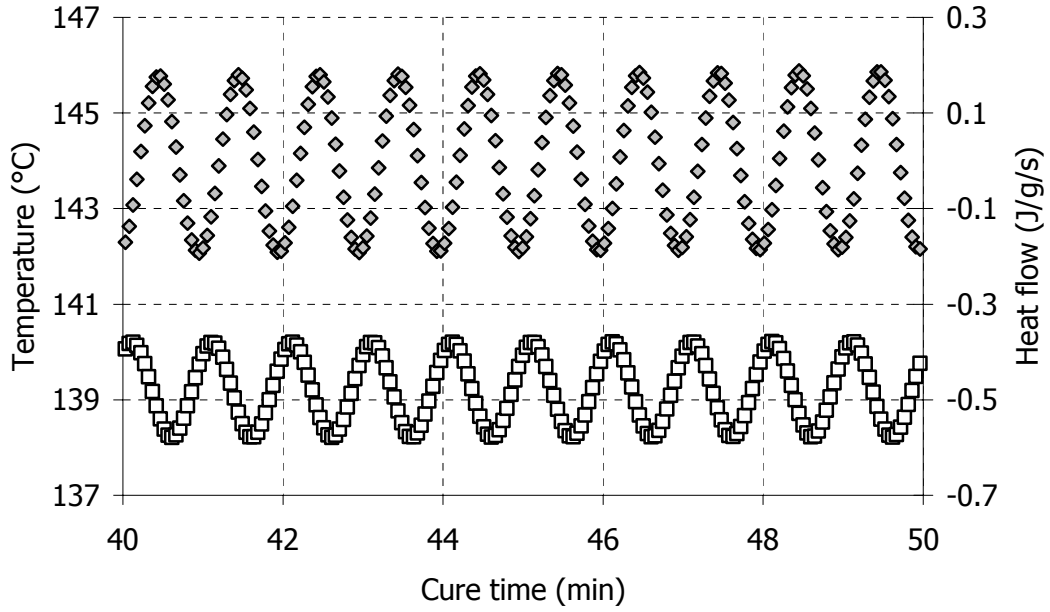

Figure 5-12 *Temperature (white squares) and heat flow (grey diamonds) raw MDSC data from the isothermal cure of RTM6 (140°C).*

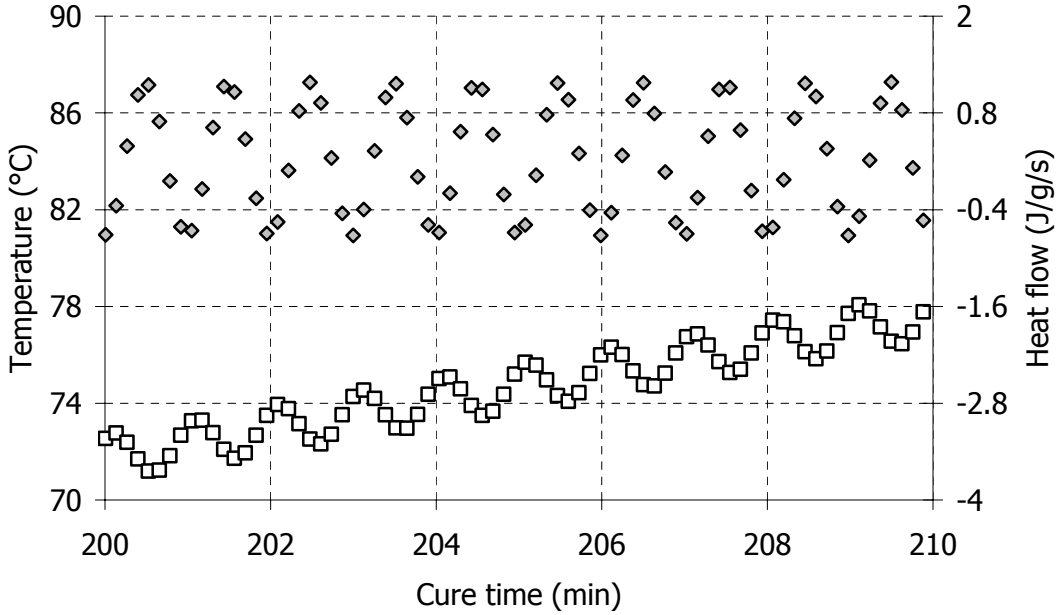

Figure 5-13 *Temperature (white squares) and heat flow (grey diamonds) raw MDSC data from the non – isothermal cure of RTM6 (0.6°C/min)*

The ellipse "moves" during the experiment. This movement reflects the changes in the heat flow due to the curing reaction. When the reaction is over, the ellipse assumes its final position and the movement stops. Similar trends were observed in all isothermal MDSC experiments.

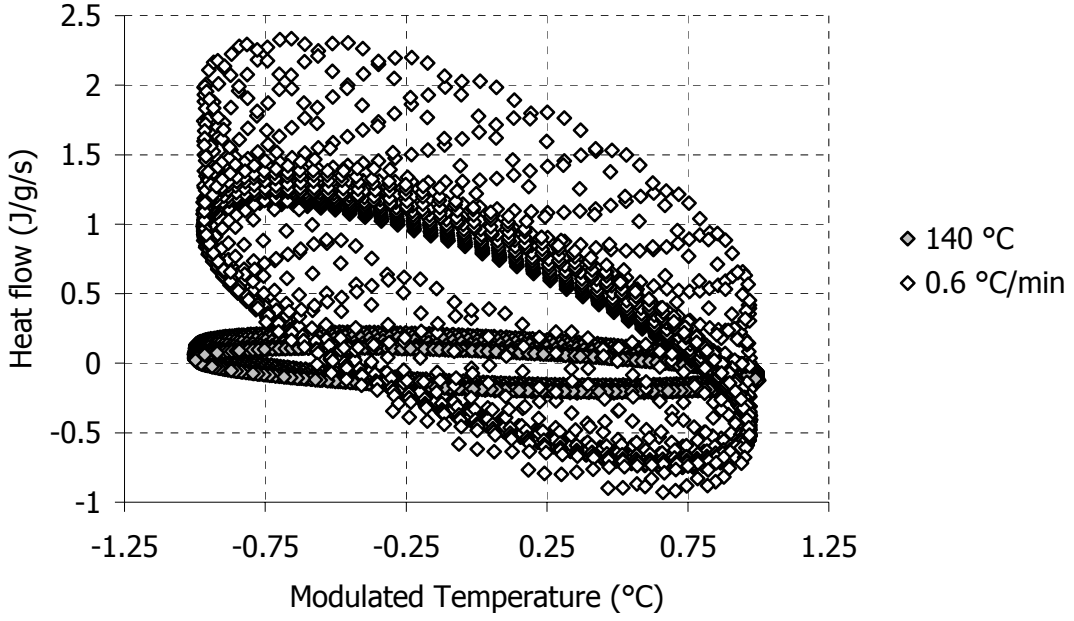

Figure 5-14 *Lissajous plot for the MDSC run at 140°C*

The heat capacity during the cure of RTM6 was calculated using the deconvolution technique described in § 2.3.3 and assuming ideal behaviour for the calorimeter. The same calculations were performed using the DSC manufacturer's software. The two calculations yielded the same results.

The specific heat capacity changes during isothermal cure are shown in Figure 5-15. We can see that c_P prior to vitrification has a value of 2.3 – 2.4 J/g/°C. After vitrification, c_p drops to 2.1 J/g/°C.

The heat capacity changes during non – isothermal cure are shown in Figure 5-16. Heat capacity increases linearly during the cure. When the resin vitrifies, heat capacity drops about 0.4 J/g/°C, as in the isothermal experiments. After vitrification, heat capacity starts increasing again. At around 220°C the increase becomes more rapid up to 230°C. This step – like increase denotes the devitrification of the resin. Since in all dynamic experiments the resin is fully cured at 220°C, devitrification occurs at the same temperature (experimental points in Figure 5-16 superimpose).

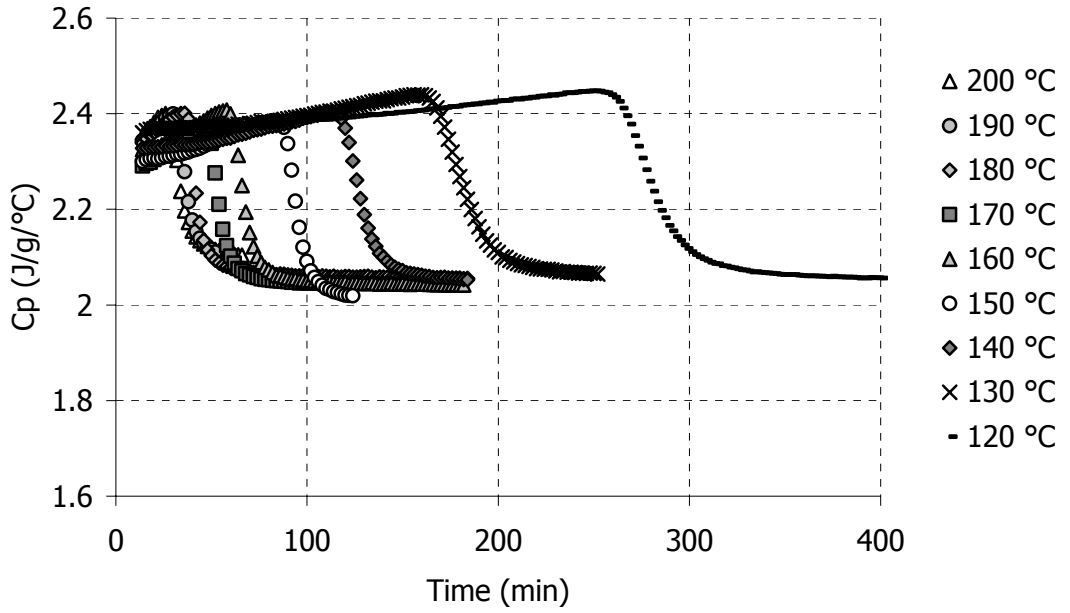

Figure 5-15 *Heat capacity changes during isothermal cure of RTM6*

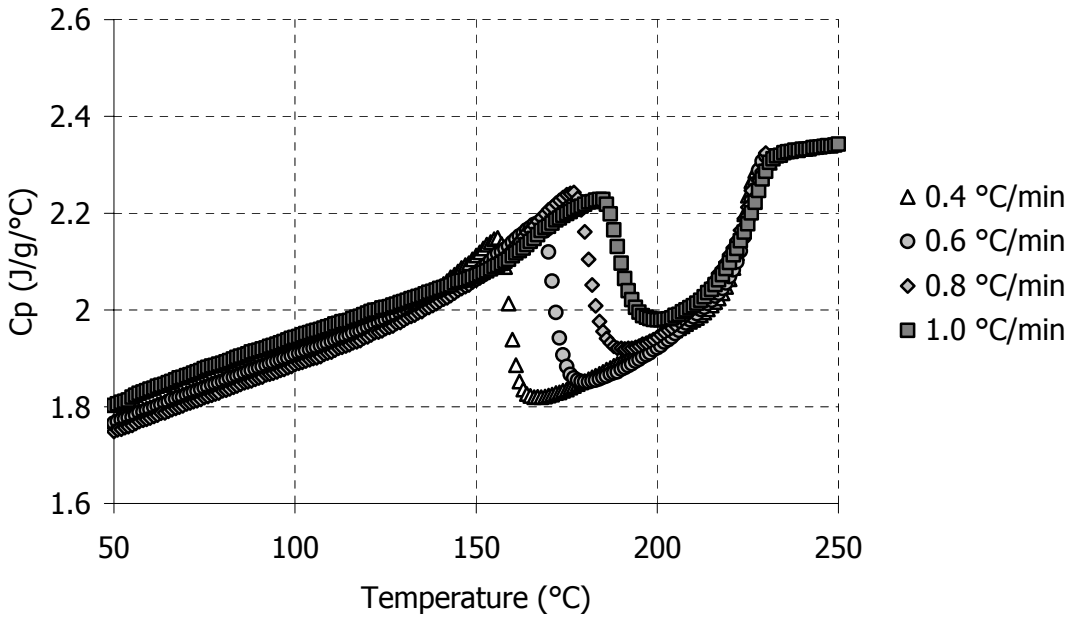

Figure 5-16 *Heat capacity changes during non - isothermal cure of RTM6*

The vitrification point and the corresponding conversion are given in Table 5-II for the isothermal experiments and in Table 5-III for the dynamic experiments. The vitrification point is identified as the mid – point of the step transition. The onset and

the end of the transition are also given. The conversion is calculated from the kinetic model.

Table 5-II: *Vitrification point and corresponding conversion for the isothermal cure of RTM6*

Cure Temperature	Vitrification point			Conversion			
	t_{onset}	$t_{mid\text{-}point}$	t_{end}	α_{onset}	α_{mid}	α_{end}	α_{max}
120 °C	258 min	277 min	315 min	0.69	0.71	0.72	0.72
130 °C	164 min	180 min	200 min	0.70	0.72	0.74	0.73
140 °C	116 min	128 min	146 min	0.78	0.82	0.84	0.85
150 °C	86 min	95 min	104 min	0.83	0.86	0.88	0.88
160 °C	60 min	67 min	76 min	0.84	0.87	0.89	0.90
170 °C	48 min	54 min	60 min	0.89	0.91	0.92	0.92
180 °C	38 min	42 min	48 min	0.89	0.91	0.93	0.93
190 °C	32 min	36 min	42 min	0.92	0.94	0.95	0.95
200 °C	28 min	33 min	37 min	0.94	0.96	0.97	0.97

Table 5-III: *Vitrification point and corresponding conversion for the dynamic cure of RTM6*

Cure profile	Vitrification point			Conversion		
	T_{onset}	$T_{mid\text{-}point}$	T_{end}	α_{onset}	α_{mid}	α_{end}
0.4 °C/min	157 °C	159 °C	164 °C	0.75	0.81	0.89
0.6 °C/min	168 °C	172 °C	177 °C	0.81	0.88	0.91
0.8 °C/min	178 °C	181 °C	189 °C	0.87	0.90	0.94
1 °C/min	185 °C	190 °C	199 °C	0.87	0.92	0.95

In the isothermal experiments, the vitrification region is quite wide at low temperatures (about 50 minutes at 120°C). At higher curing temperatures the vitrification region narrows (less than 10 minutes at 200°C). The conversion at the vitrification point is very close to the final conversion, α_{max}. This is evidence that when vitrification occurs in isothermal experiments the reaction essentially stops.

In all the dynamic experiments, the vitrification region is about 15 minutes*. During this period the continuous increase of temperature causes the reaction to advance more than in the isothermal experiments. The conversion changes are between 7% - 10%. The reaction continues to advance in the vitrified state, albeit at a very slow rate, as observed in the calorimetric results (Figure 5-3)

5.3 Dielectric measurements

Dielectric cure monitoring experiments were carried out on RTM6 under isothermal and dynamic conditions. Isothermal experiments were performed at 120°C, 130°C, 140°C, 150°C, 160°C, 170°C and 180°C. Dynamic experiments were performed at constant heating rates: 0.2°C/min, 0.4°C/min, 0.6°C/min, 0.8°C/min and 1°C/min from 50°C up to 220°C. Experiments at 2°C/min were also conducted, but not used in the analysis because of the exotherm that was observed during the cure (~ 5°C). About 2g of resin were used in each experiment. Prior to every run, the resin sample was taken out of the freezer, left at ambient temperature for about 10 minutes before it was inserted in the experimental cell (shown in Figure 3-10). In isothermal runs the experimental cell was preheated to the curing temperature. In dynamic runs the cell was preheated to 50°C. The monitoring experiment started as soon as the resin sample was placed on the cell. Measurements were taken at 25 frequencies ranging from 1 Hz to 1 MHz at logarithmic intervals.

In this section, a description of the experimental results as a function of cure time and frequency is given.

5.3.1 Isothermal cure

The real and imaginary impedance spectra of RTM6 cure at 160°C are shown in Figures 5-17 and 5-18 respectively. Both Z' and Z'' spectra move towards higher impedance values and low frequencies during cure. These movements slow down towards the end of cure.

Real impedance exhibits a plateau at the low frequency side of the spectrum. This plateau initially covers 4 frequency decades (1 Hz – 10 kHz). As the spectrum shifts to

* $vitrification\ region = \frac{T_{end} - T_{onset}}{heating\ \text{rate}}$

the left, the plateau moves out of the experimental frequency window. At higher frequencies, *Z'* values decrease as frequency increases.

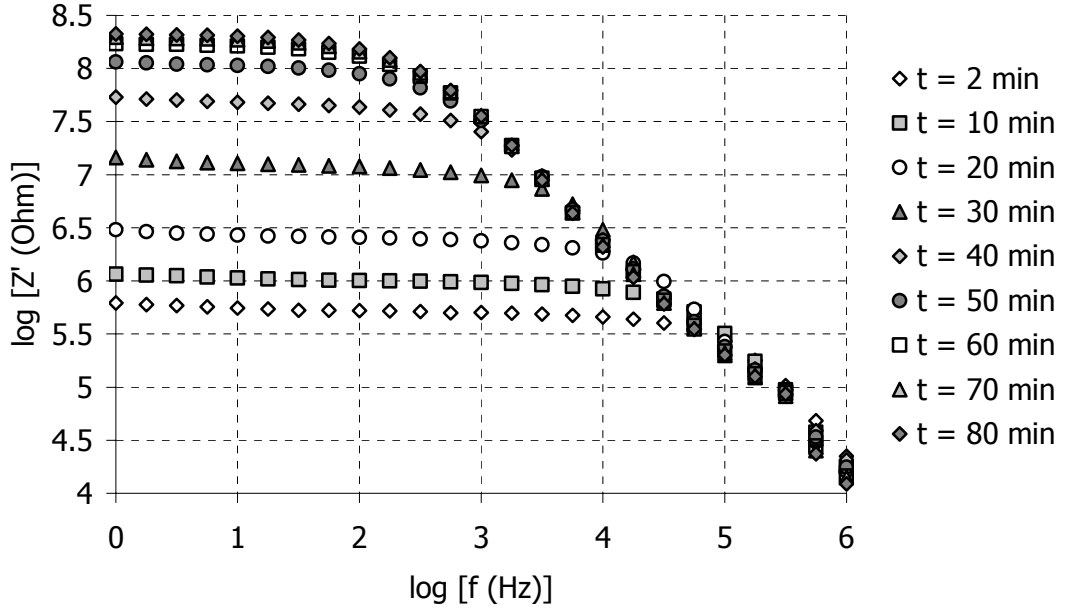

Figure 5-17 *Real Impedance spectrum during the isothermal cure of RTM6 at 160°C*

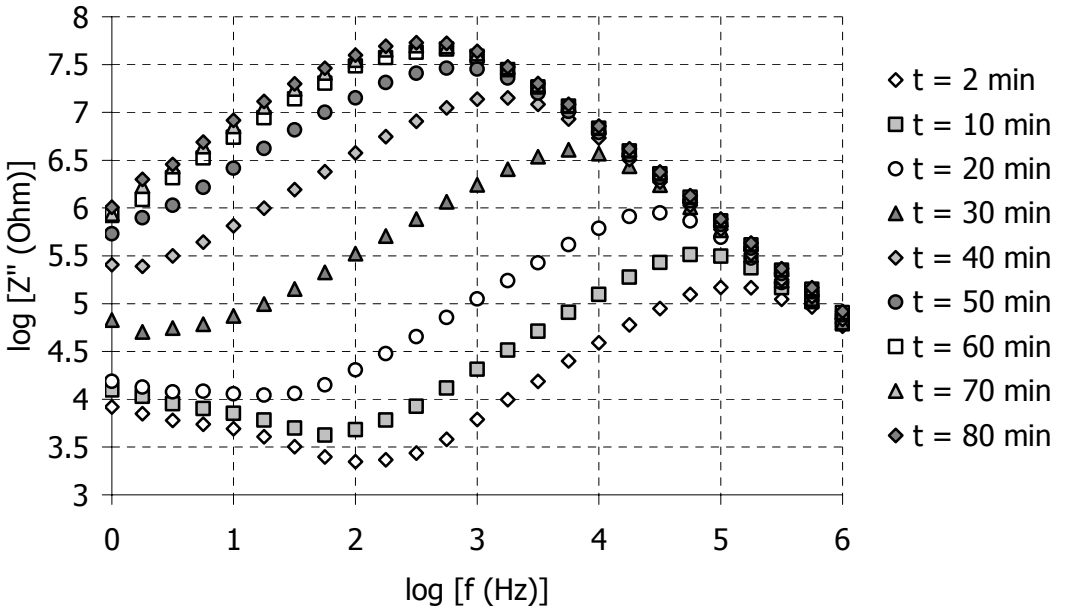

Figure 5-18 *Imaginary impedance spectrum during the isothermal cure of RTM6 at 160°C.*

Imaginary impedance spectrum exhibits a maximum and minimum point at initial cure stages. As the cure progresses and the spectrum shifts to lower frequencies, the minimum point goes out of the experimental frequency window. The maximum point, which will be referred to as IIM in accordance with the nomenclature adopted in Chapter 4, remains inside the experimental frequency window throughout the cure. After the IIM, *Z″* values decrease exponentially (straight line on the log – log plot of Figure 5-18) with increasing frequency. Imaginary impedance spectrum moves along this line as the cure progresses.

The same experimental points of *Z′* and *Z″* are plotted against cure time, in Figures 5-19 and 5-20 respectively. Real impedance curves superimpose at low frequencies and initial cure stages, reflecting the plateau region observed in the real impedance spectrum (Figure 5-17). As the cure progresses, and the plateau in Figure 5-17 moves to lower frequencies, the curves in Figure 5-19 start to break away. At higher frequencies (lines corresponding to 100 kHz and 1 MHz in Figure 5-19), a maximum is observed. This maximum is linked to the vitrification of the resin (211). A detailed analysis of this feature is given in § 5.4.3.

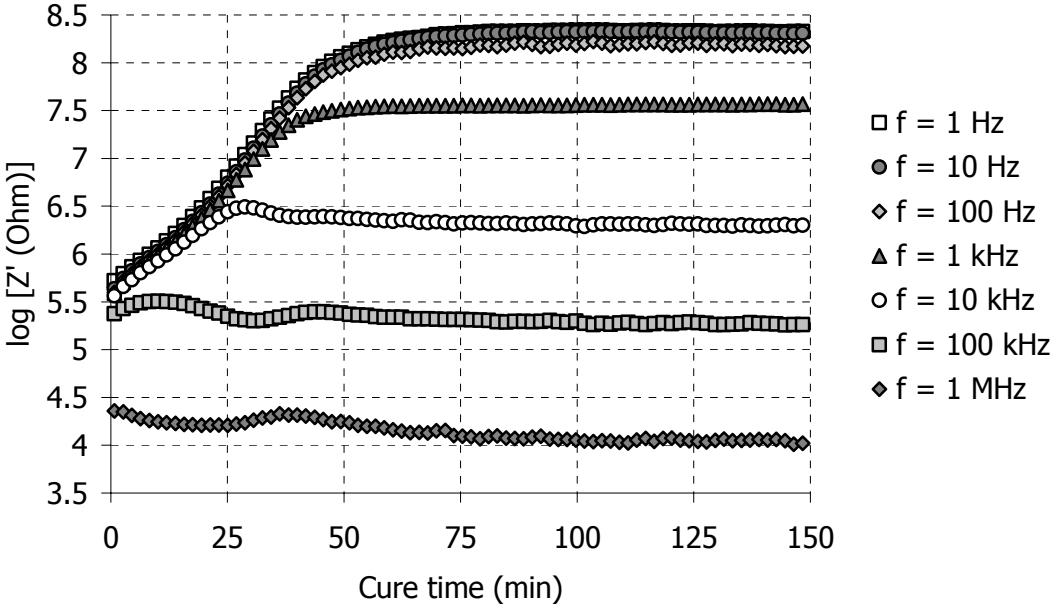

Figure 5-19 *Real impedance evolution during the isothermal cure of RTM6 at 160°C. The curves superimpose at initial stages and start to separate as the cure progresses.*

The imaginary impedance curves rise continuously during the cure, at all frequencies. The increase is more pronounced at frequencies closer to the IIM. In Figure 5-20 these frequencies are 1 kHz and 10 kHz. At higher frequencies, a shoulder is observed which also is related to the vitrification phenomenon (108, 211). The existence of the shoulder means that the straight line in the high frequency end of the imaginary impedance spectrum observed in Figure 5-18 does not remain constant but shifts in the y – axis direction.

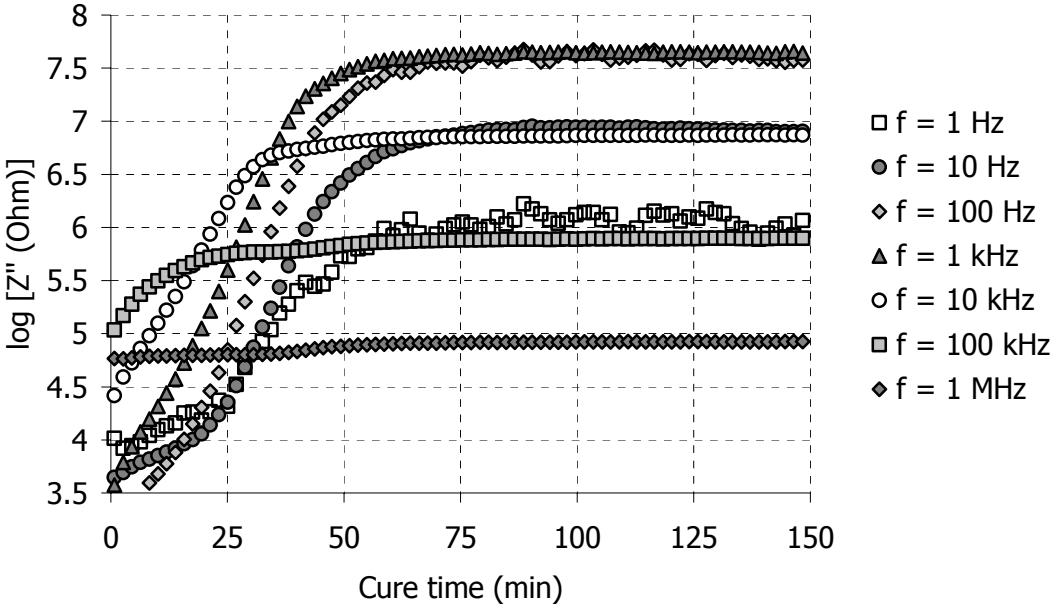

Figure 5-20 *Imaginary impedance evolution during the isothermal cure of RTM6 at 160°C. At all frequencies the Z″ values increase and reach a final plateau.*

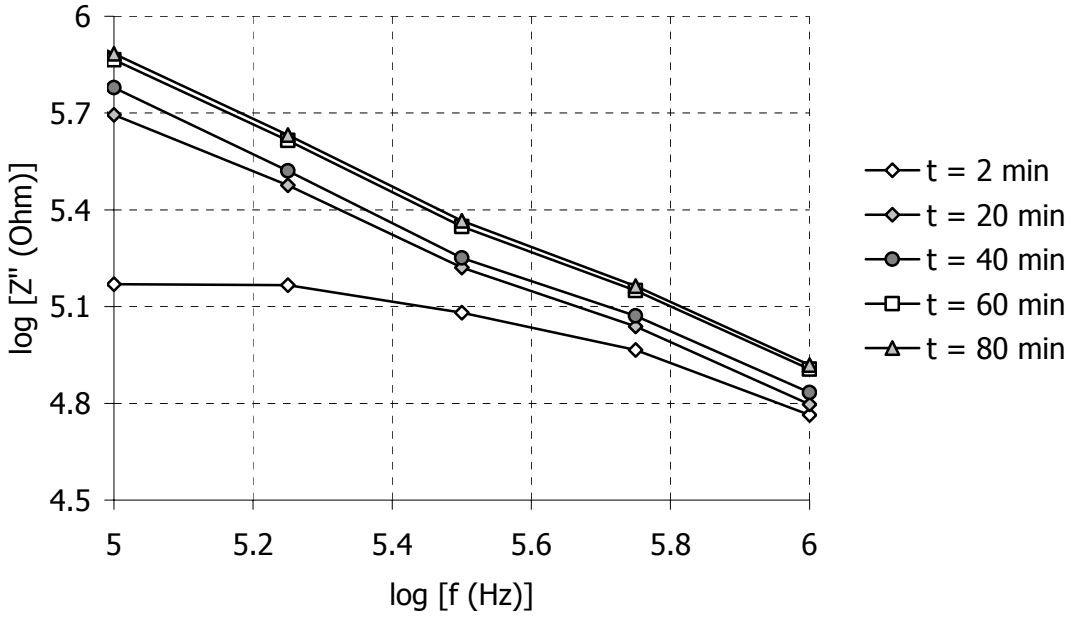

Figure 5-21 *Imaginary impedance spectrum of the cure of RTM6 at 160°C at high frequencies. This graph magnifies the high frequency area in Figure 5-18. The shift occurs between 40 min and 60 min.*

This can be observed better in Figure 5-21 where only the high frequency area of the imaginary impedance spectrum is shown. The shift occurs between the lines corresponding to 40 and 60 minutes.

The above trends are observed in all isothermal experiments. Figures 5-22 – 5-27 show the evolution of the real and imaginary impedance with cure time at three specific frequencies for all the isothermal experiments.

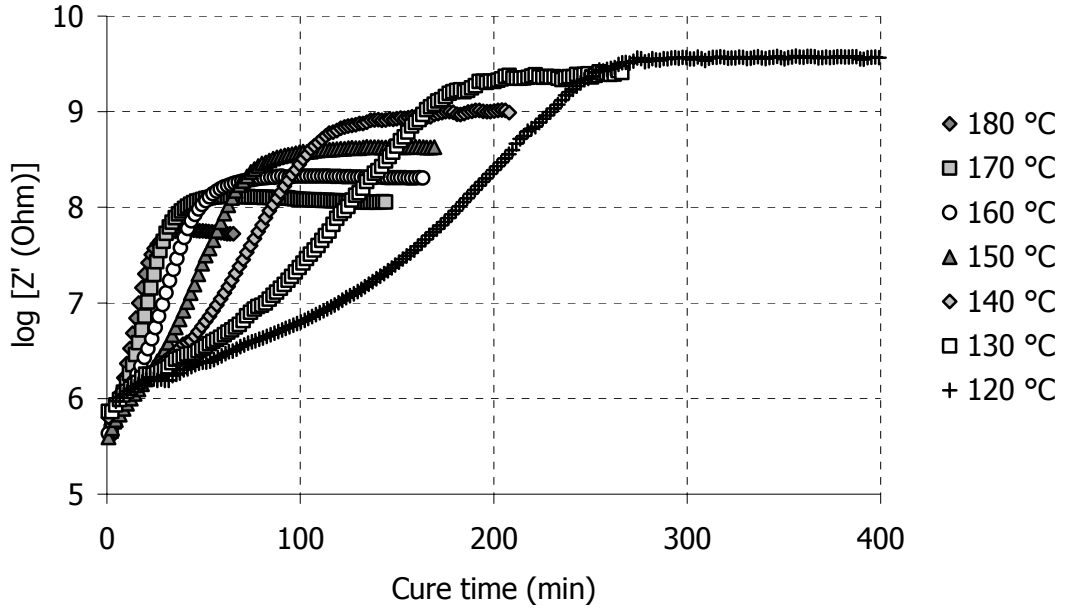

Figure 5-22 *Real impedance evolution at 10 Hz for all isothermal experiments*

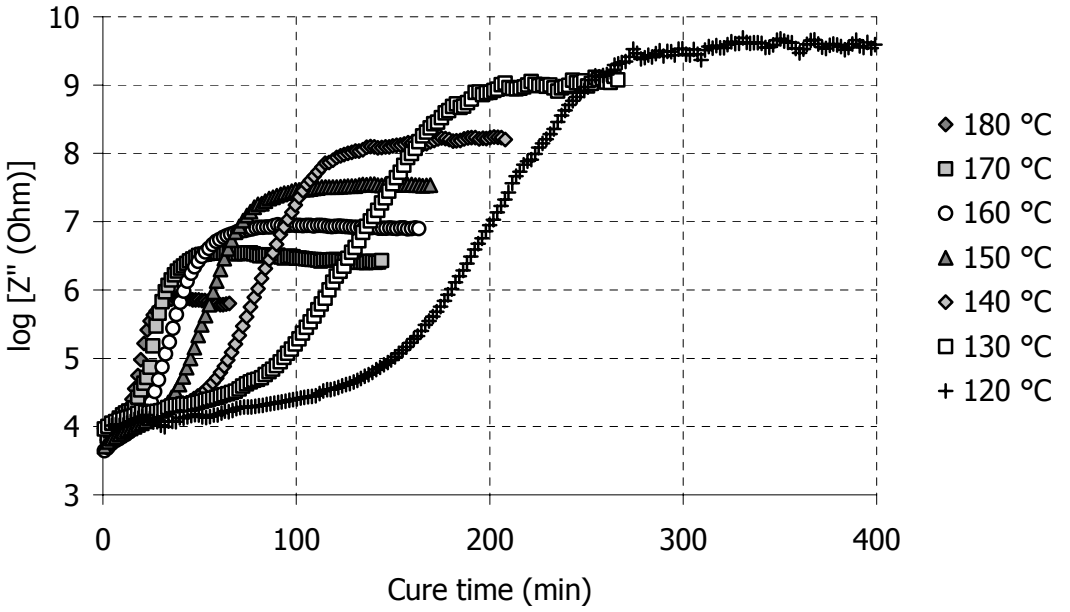

Figure 5-23 *Imaginary impedance evolution at 10 Hz for all isothermal experiments*

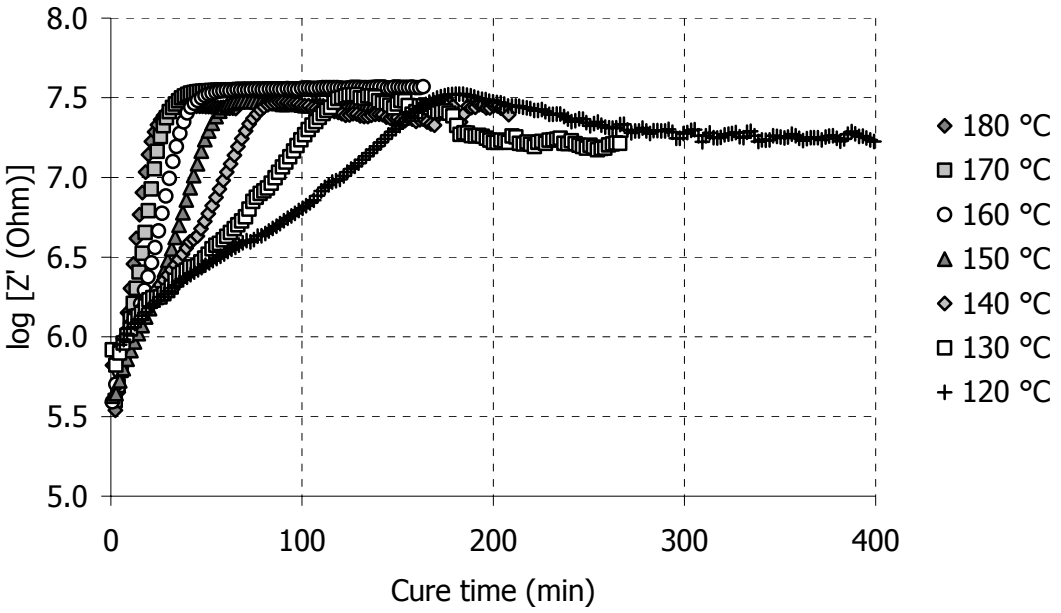

Figure 5-24 *Real impedance evolution at 1 kHz for all isothermal experiments*

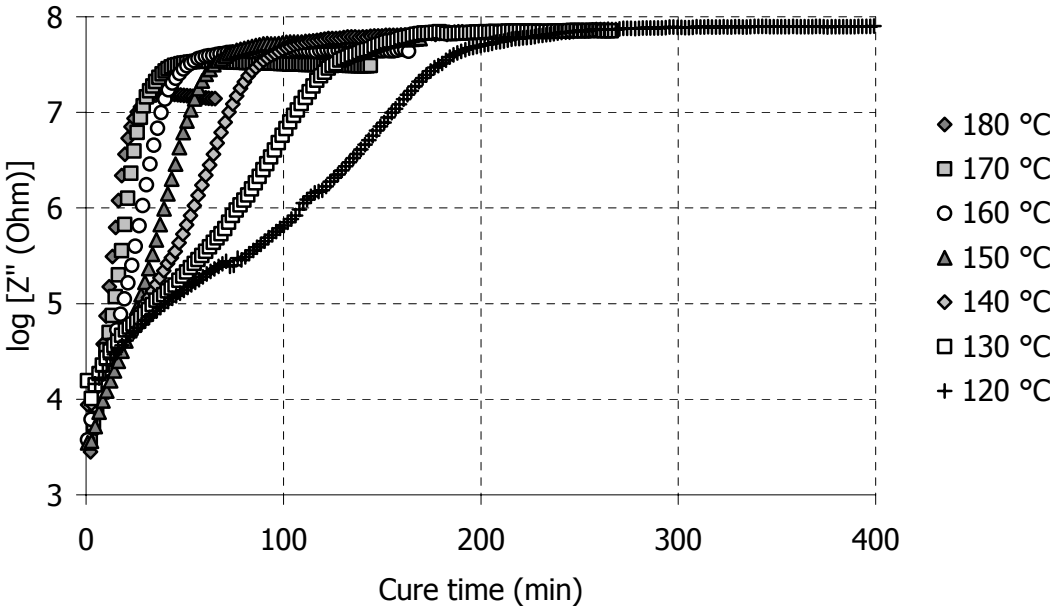

Figure 5-25 *Imaginary impedance evolution at 1 kHz for all isothermal experiments*

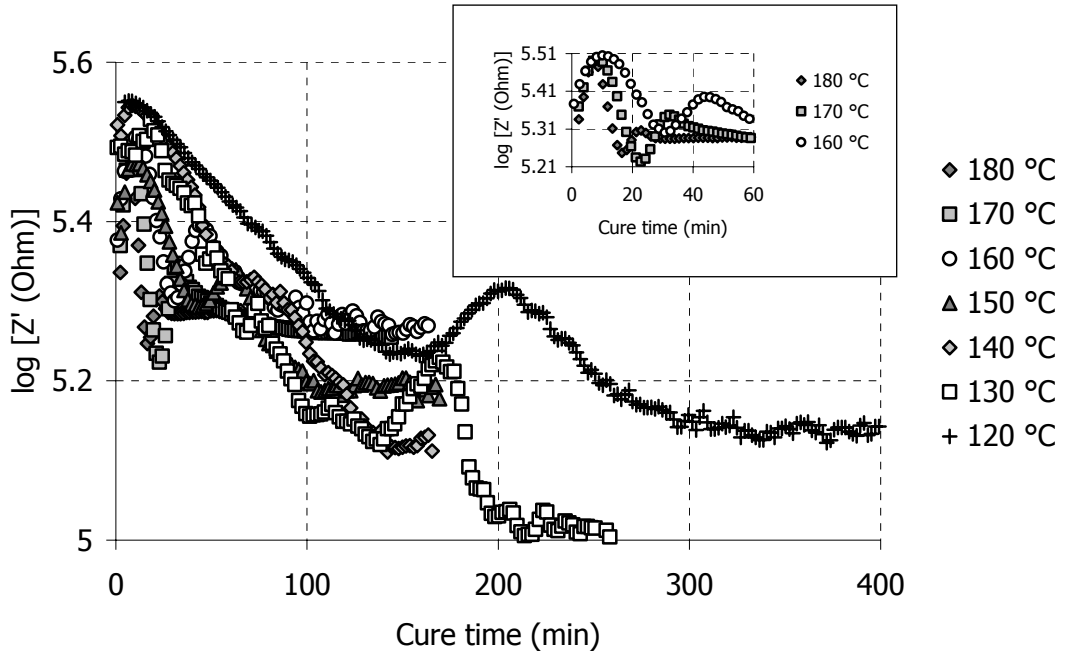

Figure 5-26 *Real impedance evolution at 100 kHz for all isothermal experiments. The inset graph shows the experimental points for the three higher dwell temperatures which are not clearly visible in the main graph.*

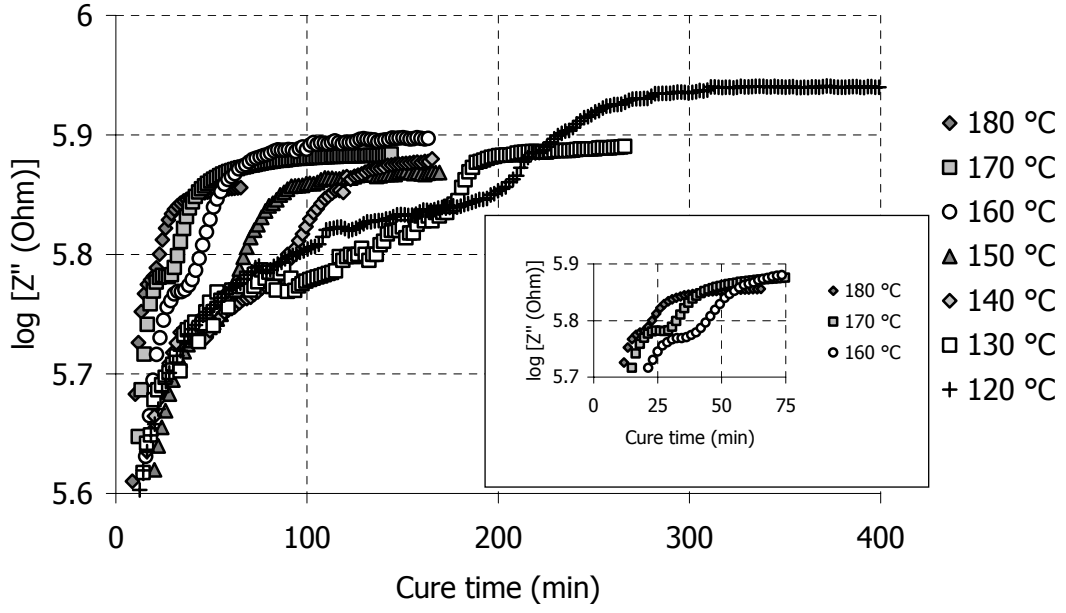

Figure 5-27 *Imaginary impedance evolution at 100 kHz for all isothermal runs. The inset graph shows the experimental points for the three higher dwell temperatures which are not clearly visible in the main graph.*

At 10 Hz (Figures 5-22 – 5-23) there is an "s – shape" increase in the real and imaginary impedance at all temperatures. We can also observe an inverse relationship between the curing temperature and the final *Z'* and *Z''* value. At 1 kHz (Figures 5-24 – 5-25) real impedance increases rapidly until it reaches a plateau value. A different behaviour is observed at the two low temperature experiments (120°C and 130°C). Real impedance reaches a maximum and then decreases. The reason for this trend at low temperatures is explained in Figure 5-28 where the Z' spectrum shift during the cure of the resin is plotted alongside the time evolution of the spectrum. Due to the spectrum movement towards higher impedance values and lower frequencies, the 1 kHz frequency goes out of the plateau region of the spectrum. This trend can also be traced in Figure 4-12 where the movement of the *Z'* spectrum is pictured in the case where migrating charges dominate the signal (the movement of the experimental spectrum is opposite to the arrow shown in the figure).

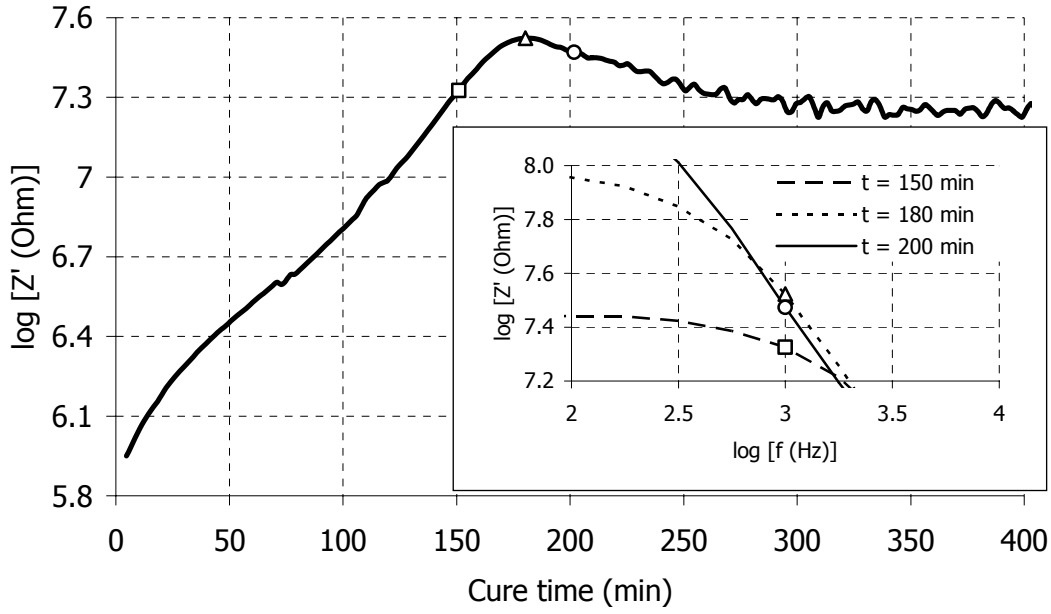

Figure 5-28 *Real impedance evolution at 1 kHz for the isothermal cure of RTM6 at 120°C. Three points have been highlighted in the graph before (rectangular), on (triangle) and after (circle) the maximum point. The inset graph shows the positions of the three points as the spectrum moves toward higher impedance values and lower frequencies.*

At 100 kHz the shoulder in the imaginary impedance values is observed in all experiments. Real impedance values exhibit a maximum which, as the shoulder in the imaginary impedance curves, corresponds to vitrification (see § 5.4.3). At high

temperatures another maximum is observed at earlier times (inset graph in Figure 5-26). The formation of this maximum is due to the movements of the spectrum, similar to the 1 kHz frequency case explained in Figure 5-28.

5.3.2 Non – isothermal cure

The real and imaginary impedance spectra evolution during the dynamic cure of RTM6 at 0.6°C/min is pictured in Figures 5-29 and 5-30 respectively. The overall features of the spectra are similar to the isothermal case. Real impedance exhibits a plateau region at low frequencies, followed by a decrease at higher frequencies. Imaginary impedance contains the maximum (IIM) and minimum point, which after a point goes out of the experimental window.

The significant difference between the spectra obtained under isothermal conditions and the spectra obtained under dynamic conditions is noted when the movements of the spectra during the cure are studied.

Under dynamic conditions, the impedance spectra initially shift to higher frequencies and lower values. At some point (spectrum at 110°C – white circles – in Figures 5-29 and 5-30) the trend reverses and the spectra begin to move towards lower frequencies and higher impedance values. The situation reverses once again at elevated temperatures (spectrum at 170 °C – dark grey circles – in Figures 5-29 and 5-30).

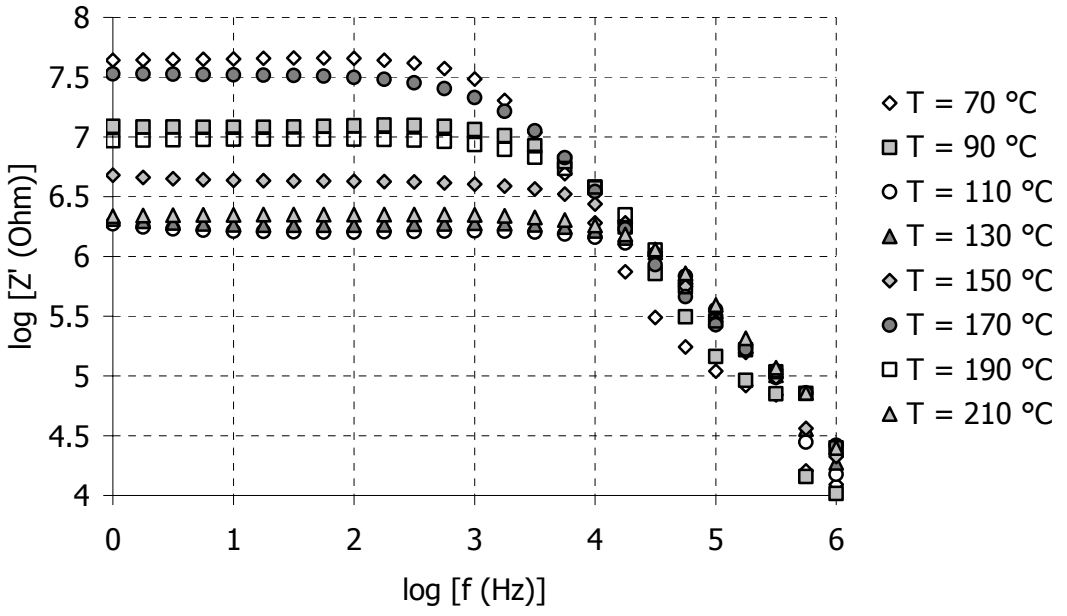

Figure 5-29 *Real impedance spectrum during the cure of RTM at 0.6°C/min*

In the imaginary impedance spectrum, these "up and down" movements cause the minimum point to reappear at high temperatures (spectrum at 210°C – light grey triangles).

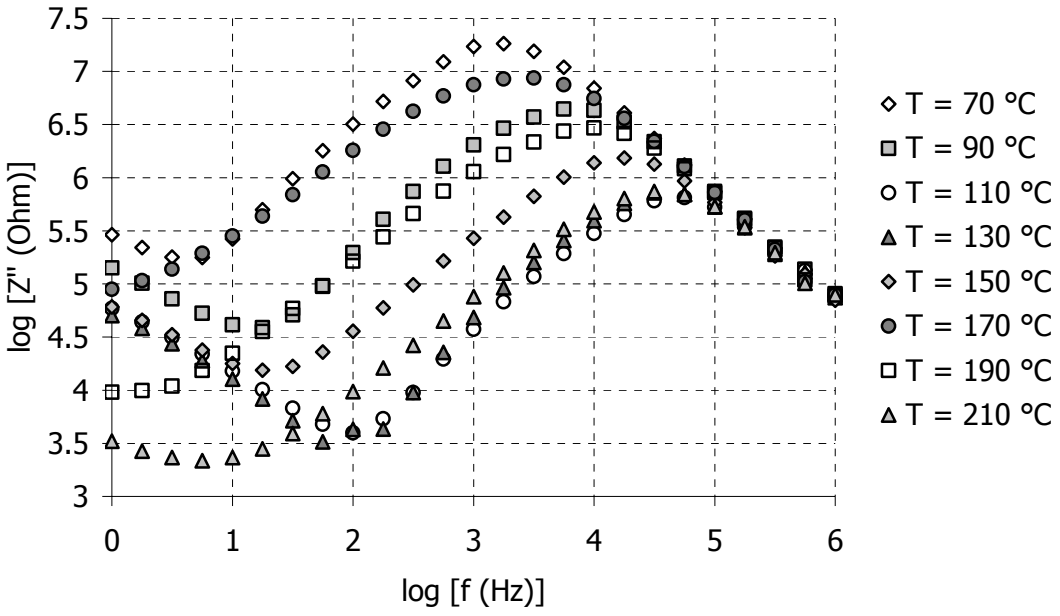

Figure 5-30 *Imaginary impedance spectrum during the cure of RTM at 0.6°C/min*

The time evolution of the real and imaginary impedance for cure of RTM6 at 0.6°C/min is given in Figures 5-31 and 5-32 respectively. Since the experiment is performed at a constant heating rate, the resin curing temperature is used as the x – axis in the graphs. In Figure 5-31, real impedance curves superimpose at low frequencies, as in the isothermal experiments. The superposition is due to the existence of the plateau region in the Z' spectrum. As the spectra move towards high frequencies and lower values, the Z' values decrease and the plateau region expands to higher frequencies, causing the curves corresponding to these frequencies to superimpose. An example of such trend in Figure 5-31 is the curve corresponding to 10 kHz (white circles). The situation reverses, when a minimum impedance value is obtained for the superimposed curves. This point is located at about 110°C in Figure 5-31. After the minimum point, the Z' spectrum shifts to higher values and the curves begin to separate up to about 170°C when a maximum is obtained and the situation reverses again. At very high frequencies the curves never superimpose because they lie out of the plateau region at all times. The movements at these frequencies will be analysed in § 5.4.3 where the

appearance of a small maximum is attributed to vitrification. This maximum is slightly visible in the 100 kHz and the 1 MHz curves in Figure 5-31 at about 160°C – 170°C.

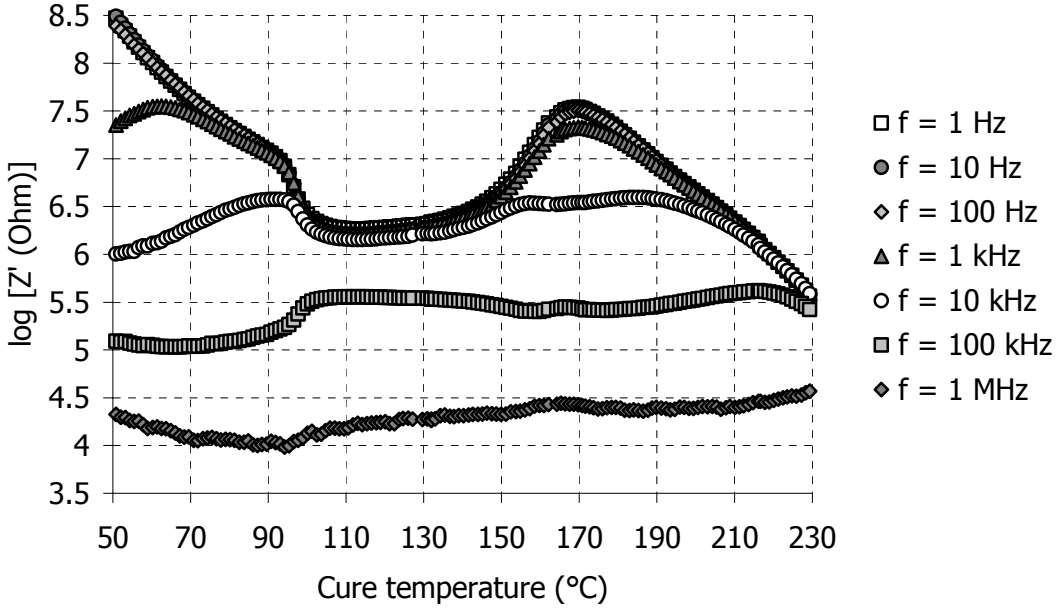

Figure 5-31 *Real impedance evolution during the cure of RTM6 at 0.6°C/min at specific frequencies*

The imaginary impedance curves follow more complicated paths. At low frequencies they initially decrease, reach a minimum and then increase up to a maximum. After the maximum point, *Z″* decreases again. The curve corresponding to 100 Hz (light grey diamonds) in Figure 5-32 exhibits such a trend. At intermediate frequencies (10 kHz – white circles – for example) the imaginary impedance stays constant during the initial cure stages. As the cure progresses, imaginary impedance at intermediate frequencies follows the trend described earlier for the low frequency curves: *Z″* decreases to a minimum, increases to a maximum and then decreases again. Finally, at very high frequencies no significant trends can be observed on the logarithmic scale of Figure 5-32. However, as will be illustrated in § 5.4.3, imaginary impedance curves at high frequencies exhibit a shoulder, similarly to the isothermal cases shown in Figure 5-27 (see also Figure 5-39).

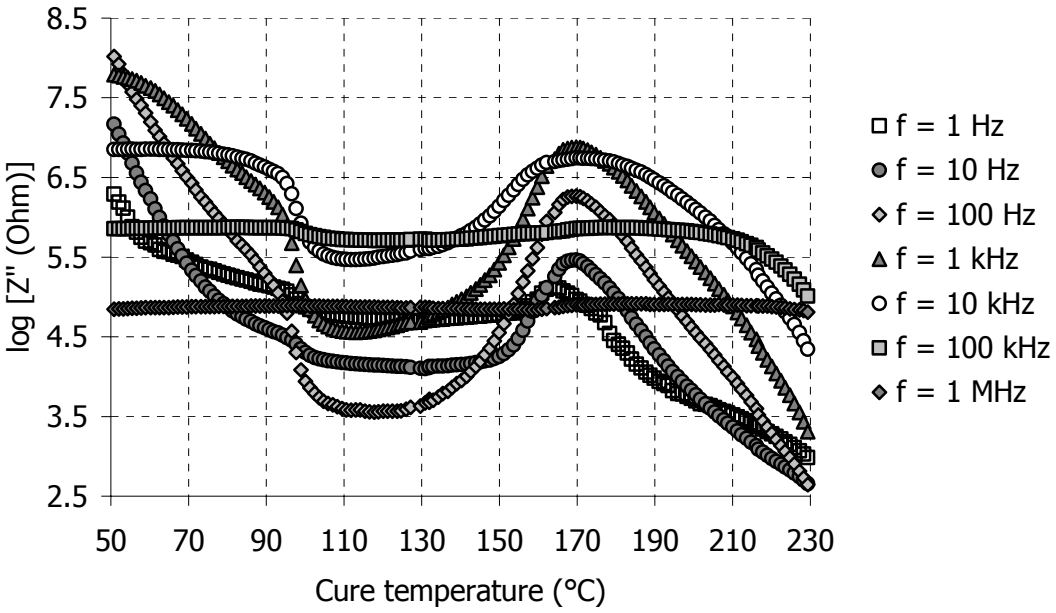

Figure 5-32 *Imaginary impedance during the cure of RTM6 at 0.6°C/min at specific frequencies*

A more comprehensive view of the imaginary impedance evolution at specific frequencies, as the Z" spectra move during the cure, is presented in Figure 5-33. The imaginary impedance at 100 Hz and 10 kHz is shown. Several points are picked up along the two curves and their positions in the Z" spectra are highlighted in the two plots below the main graph in Figure 5-33. The spectrum on the left covers temperatures up to 110°C where the spectrum shifts to higher frequencies and lower impedance values. In the 100 Hz curve, all the points lie before the Imaginary Impedance Maximum (IIM). As the spectrum shifts, Z" values at 100 Hz constantly decrease. On the other hand, the points drawn from the 10 kHz curve initially lie after the IIM and thus are not affected by the spectrum shift (see spectra corresponding to 60°C and 70°C in Figure 5-33). At about 90°C, the IIM passes through 10 kHz. After that point, the 10 kHz curve has the same trend as the 100 Hz curve. In the same figure we can see that at very high frequencies (black triangles at 1 MHz) the influence of the movements on the spectrum is very small (not visible in the logarithmic scale of the plots). This explains the featureless *Z"* curves at 100 kHz and 1 MHz in Figure 5-32.

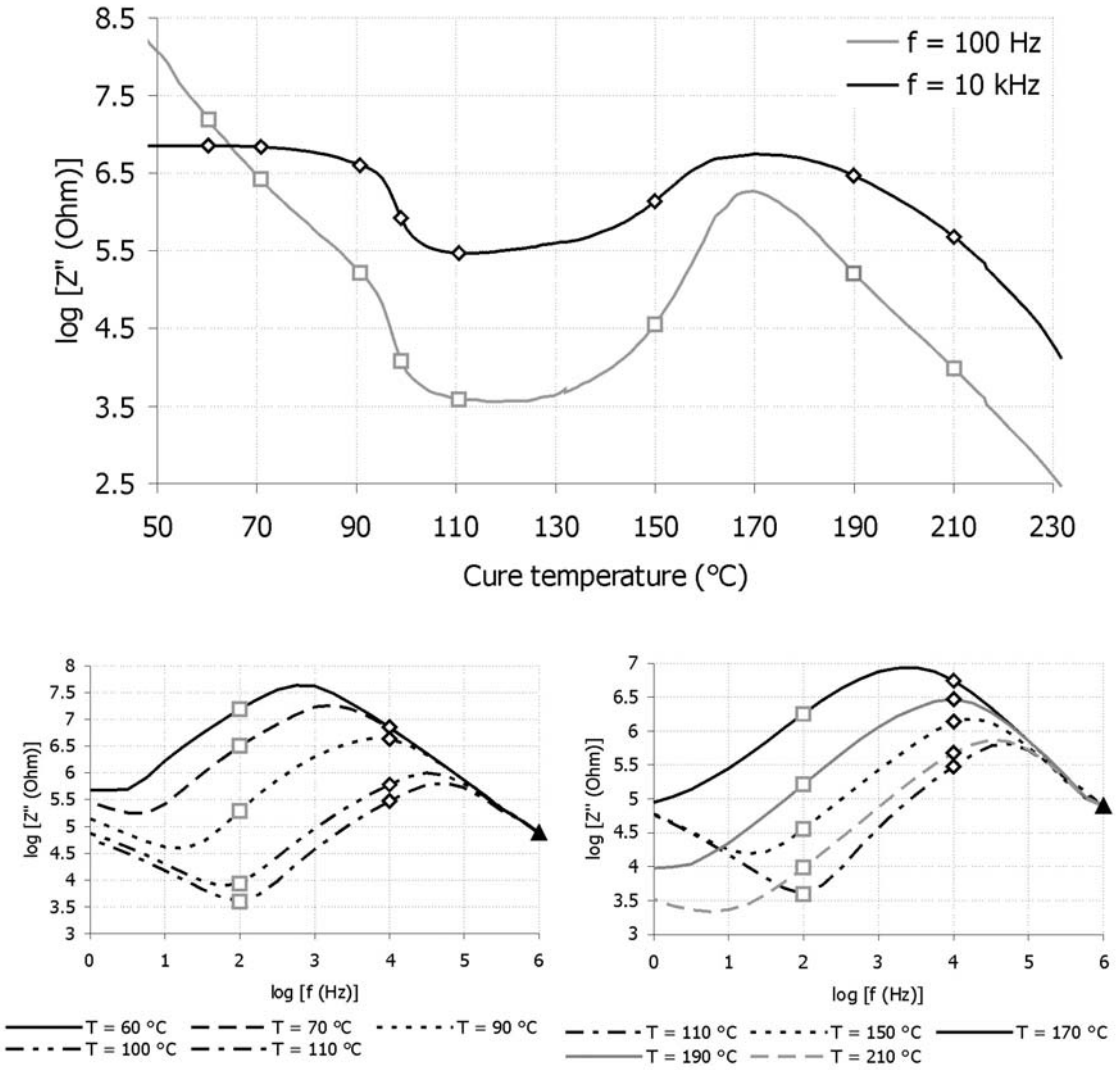

Figure 5-33 *Imaginary impedance evolution in the time (main graph) and frequency (two smaller graphs) domain. Several points have been highlighted and their positions in the two domains are shown. The data are from the dynamic cure of RTM6 at 0.6°C/min*

The above description of the *Z'* and *Z''* cure monitoring data covers all the dynamic experiments. Figures 5-34 – 5-39 show results from all the non – isothermal runs at 10 Hz, 1 kHz and 100 kHz respectively.

At 10 Hz we can see that the real and imaginary impedances start from the same values in all experiments. The curves continue to superimpose up to about 90°C for the *Z'* curves. At that point, a sudden drop in the *Z'* values is observed. After that rapid decrease, the curves start to separate and *Z'* increases as the cure progresses. The curves corresponding to lower heating rate separate first and reach the maximum impedance value first. At very high temperatures, towards the end of cure, the curves

start to superimpose again. As will be explained in § 5.4.2 the regions where the curves superimpose are areas where either no reaction takes places (superposition at low temperatures) or the curing reaction is over (superposition at high temperatures).

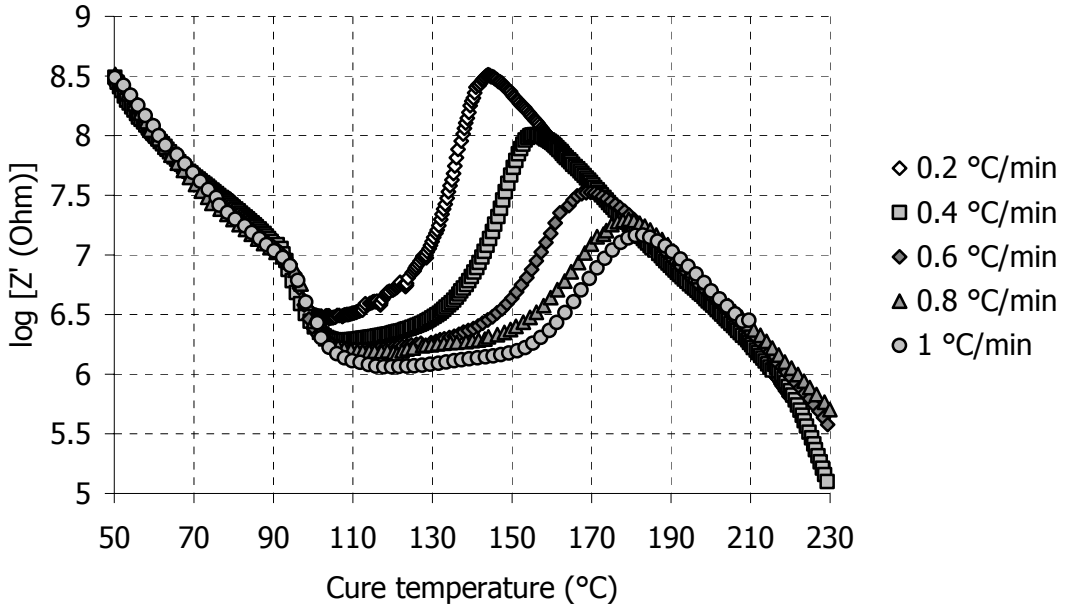

Figure 5-34 *Real impedance evolution at 10 Hz for all dynamic runs*

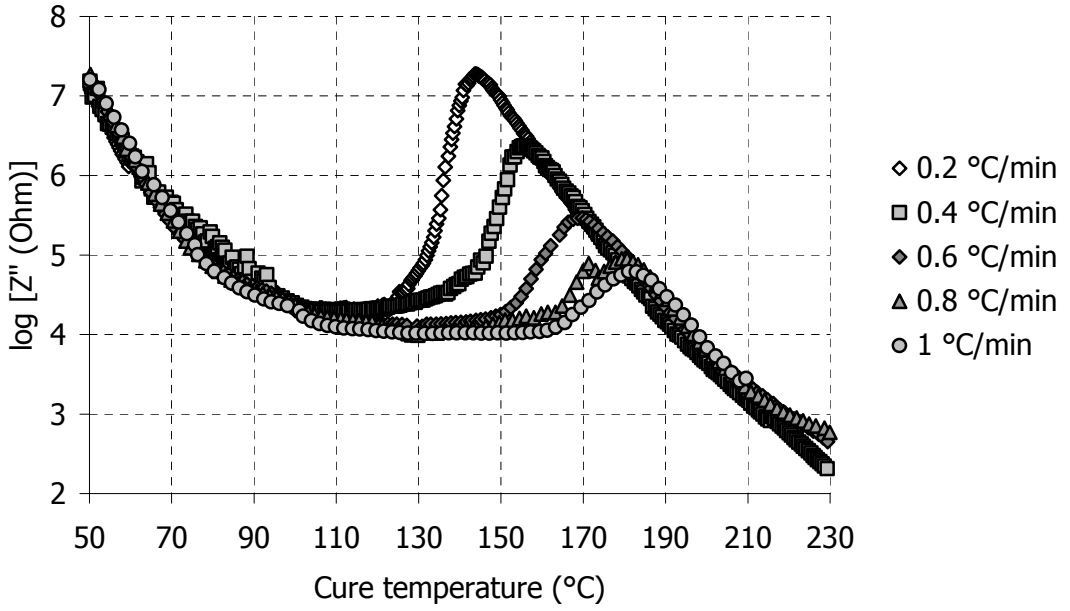

Figure 5-35 *Imaginary impedance evolution at 10 Hz for all dynamic runs*

Therefore, in those regions, only the temperature affects the signal. In the region where the curves separate, the effect of the curing reaction is coupled with the effect of temperature.

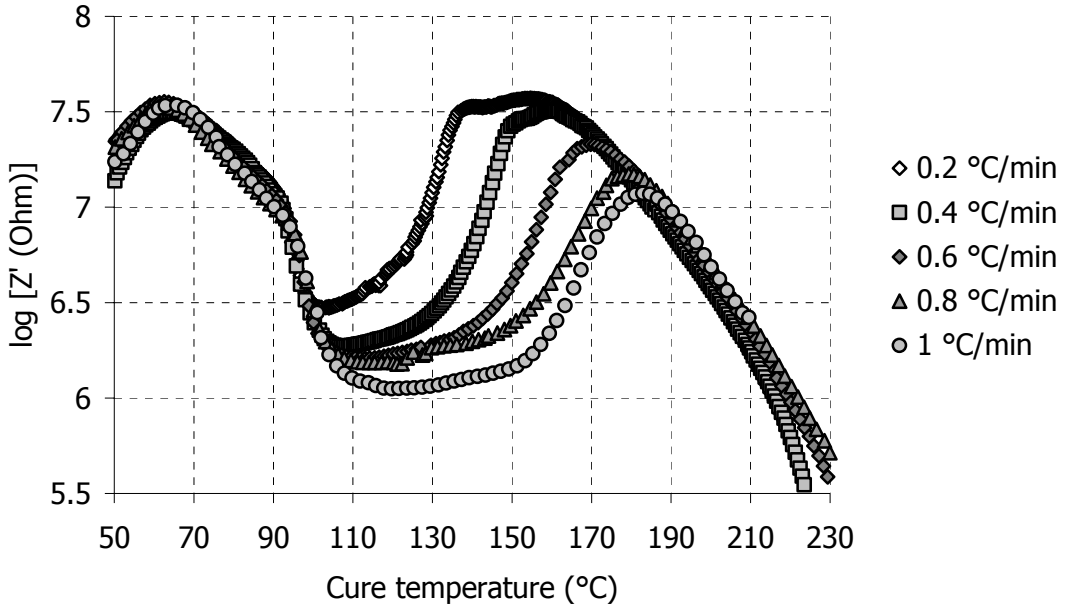

Figure 5-36 *Real impedance evolution at 1 kHz for all dynamic runs*

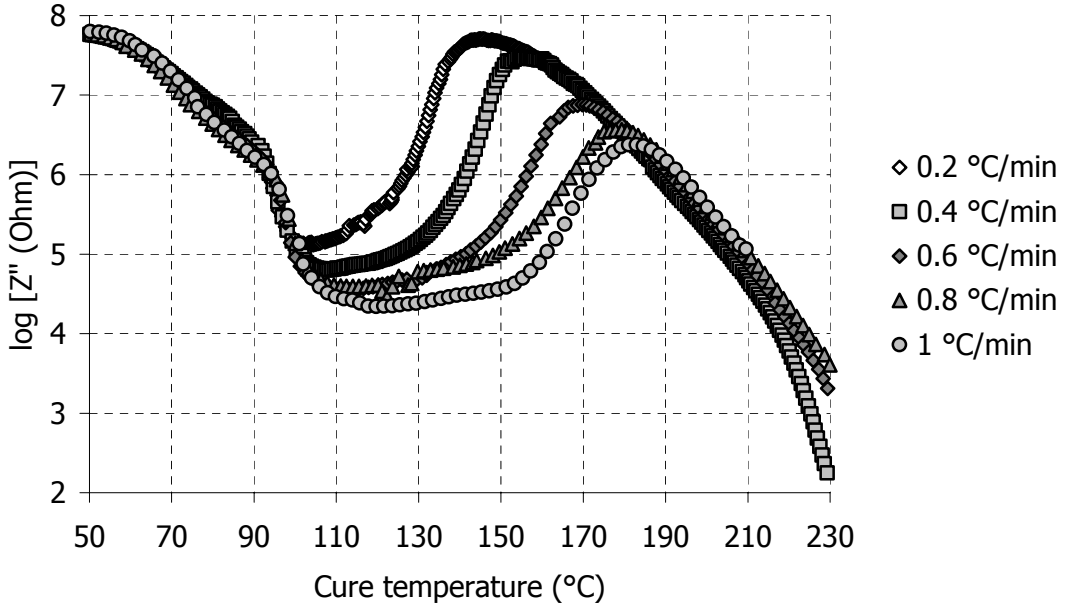

Figure 5-37 *Imaginary impedance evolution at 1 kHz for all dynamic runs*

The curves at 1 kHz also display the superposition at the initial and the final cure stages. The trends are similar to the 10 Hz curves described above.

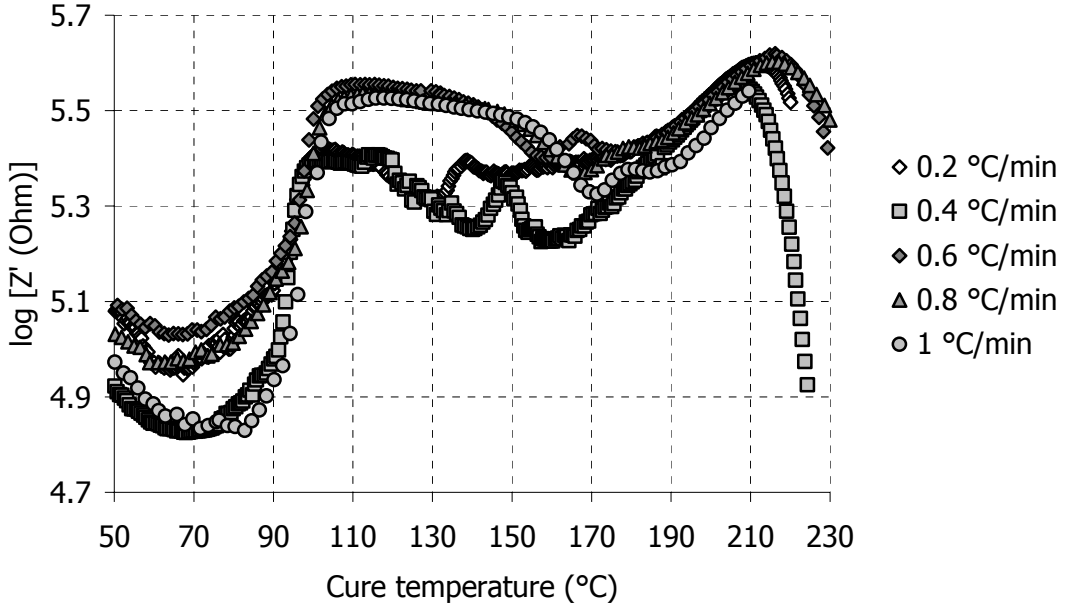

Figure 5-38 *Real impedance evolution at 100 kHz for all dynamic runs*

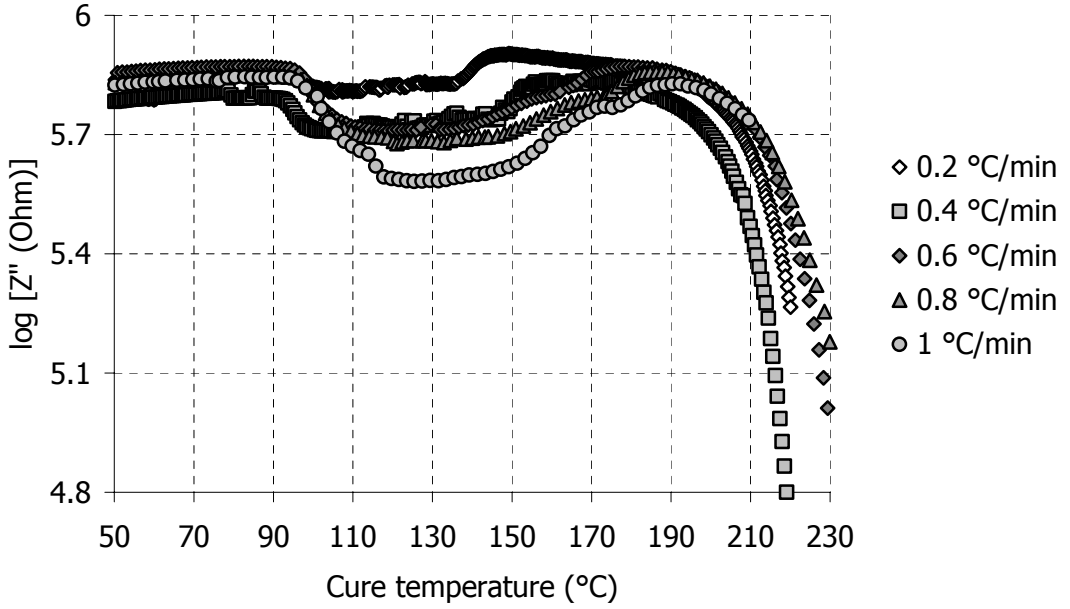

Figure 5-39 *Imaginary impedance evolution at 100 kHz for all dynamic runs*

The real and imaginary impedances at 100 kHz show similar behaviour at all heating rates but the superposition at the beginning is not so obvious. Some curves seem to

superimpose initially (for example the curves corresponding to 0.4°C/min and 1°C/min runs or the curves corresponding to 0.2°C/min and 0.8°C/min in Figure 5-38).
The different trends observed at different frequencies indicate the variable influence the electrode, ionic and dipolar polarisation mechanisms have on the obtained signal. In the next section the analysis will be focused in specific frequency areas where separate phenomena can be studied.

5.4 Phenomena manifestation in the dielectric signal

From the analysis of the real and imaginary impedance spectra, we can identify the frequency regions where each of the three phenomena discussed in Chapter 4 are discernible. Electrode polarisation can be mainly observed in the imaginary impedance spectrum at low frequencies. Charge migration dominates a large frequency area around the maximum in the Z'' spectrum. The plateau area in the Z' spectrum also shows the resistive nature of the material. Dipolar polarisation becomes visible at high frequencies in both the real and imaginary impedance spectra.

5.4.1 Electrode Polarisation

As analysed in § 4.2.1 the polarisation of the sensor electrodes depends on both the sensor characteristics and the material state. Figure 5-40 shows imaginary impedance spectra at various stages for the dynamic cure of RTM6 at 0.6°C/min.
The spectra are representative of the trends observed at low frequencies (below 100 Hz). The spectrum at 150°C exhibits a minimum point between 10 and 100 Hz. This point marks a boundary in the spectrum: at frequencies below the minimum, Z'' decreases log – linearly with frequency, a behaviour which can be described by the CPE model (eq. (4.29)). As the cure progresses, Z'' values increase and the whole spectrum shifts to lower frequencies (spectrum at 157°C in Figure 5-40). The electrode polarisation region seems to be unaffected by the spectrum shift. The spectrum moves along the low frequency line similarly to the movement along the high frequency line. This is something observed in all dynamic runs in the region where the reaction dominates the signal. The minimum point moves to lower frequencies, following the spectrum shift. At some point the minimum moves out of the frequency window of the experiment. The spectrum at 170°C exhibits no minimum.

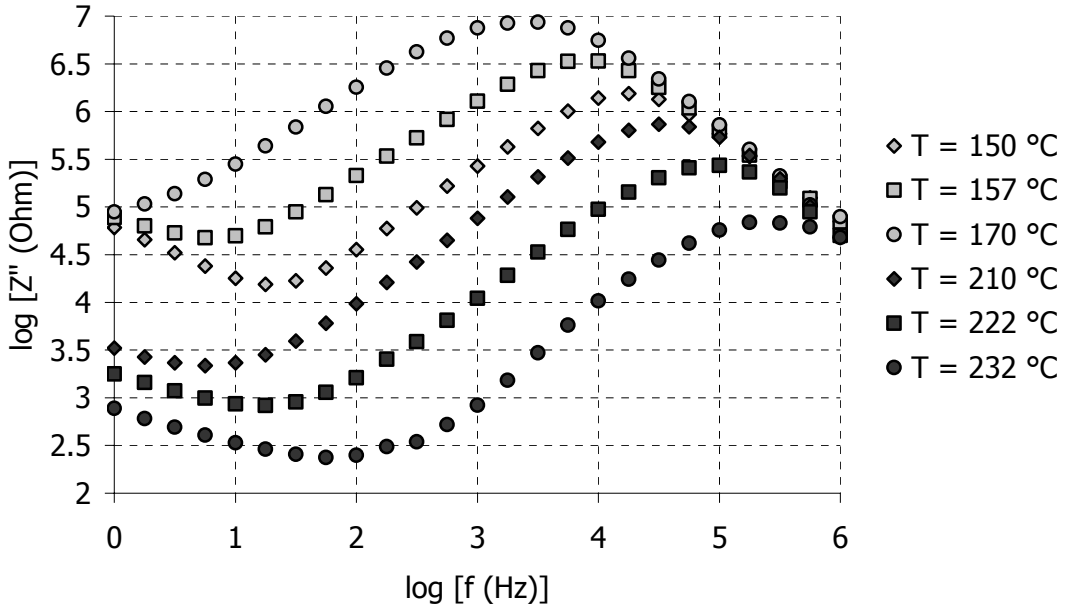

Figure 5-40 *Imaginary impedance spectra at six different temperatures from the RTM6 cure at 0.6°C/min. Light grey was used for the spectra that shift to higher Z" values – lower frequencies. Heavy grey was used for the spectra that shift to lower Z" values – higher frequencies.*

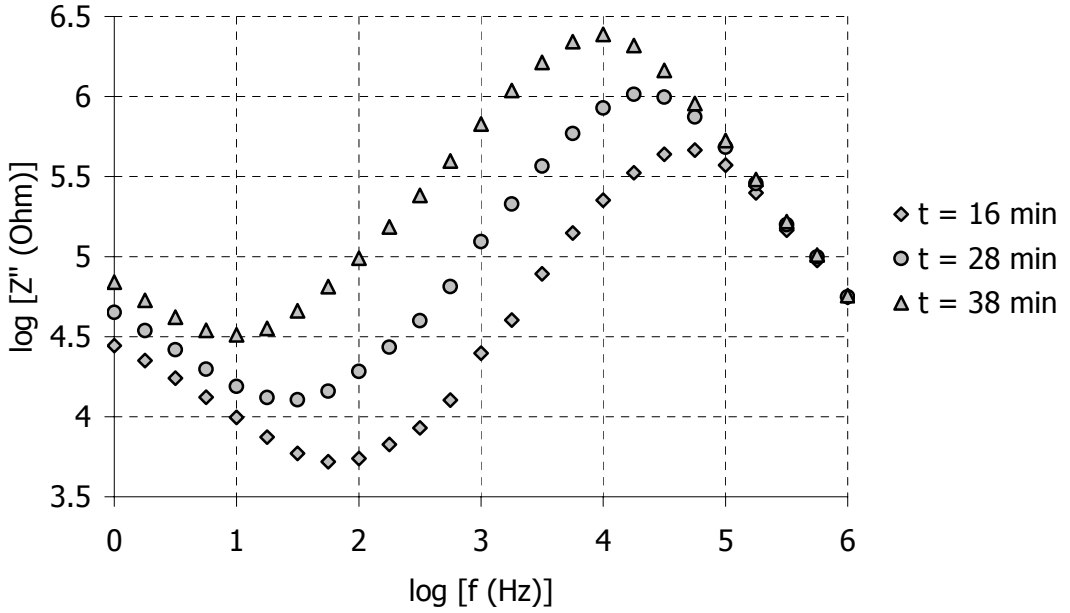

Figure 5-41 *Imaginary impedance spectrum during the cure of RTM6 at 150°C*

At even higher temperatures, when the curing reaction is over, the spectra move to the opposite direction (see Figure 5-30). The minimum point reappears but this time the spectrum does not move alongside the electrode polarisation line at low frequencies. The slope of the electrode polarisation region in the logarithmic plot seems to remain the same. This behaviour is also observed in the early stages of the cure where the reaction has not started. In isothermal runs, where there is no effect from temperature changes, the spectra move in the same way, as shown in Figure 5-41. It is therefore concluded that the electrode polarisation features remain unchanged only in dynamic experiments, when both the reaction advancement and the temperature changes affect the signal. If the signal is affected by just the reaction or the temperature then the low frequency side of the *Z″* spectrum follows the shift of the whole spectrum.

One possible explanation for the constant electrode polarisation values when the spectra shift to higher impedance levels and lower frequencies (light grey spectra in Figure 5-40) is the mutual cancellation of the effect of temperature and the effect of the reaction on the signal at low frequencies. The higher reaction rates attained at higher heating rates are compensated by the faster temperature changes also due to the higher heating rates.

In § 6.3.2 the movement of the minimum point will be modelled by using the simplified equivalent circuit, pictured in Figure 4-18.

5.4.2 Charge migration

The existence of a clear maximum in the experimental *Z″* spectra is direct evidence that migrating charges dominate the dielectric signal over an extensive frequency range. The IIM development in time illustrates the shift of the spectra during the cure.

The evolution of IIM in the cure of RTM6 under isothermal conditions is shown in Figure 5-42.

Initially, the Z’ and Z” spectra shift is fast. Towards the end of cure, IIM changes become slow and almost stop, seemingly reaching a plateau. The experiment at 120°C does not show any plateau because the curing continues after 250 minutes as can be seen in the calorimetric results (Figure 5-1). A close inspection of the plateau values, however, reveals that the IIM continues to increase at a slow rate. This is shown in Figure 5-43 for the runs at 150°C and 160°C. In the same graph, dotted arrows designate the vitrification point of the curing system and solid arrows indicate the end

of cure obtained by the DSC measurements. We can see that after vitrification the changes in the IIM are very slow.

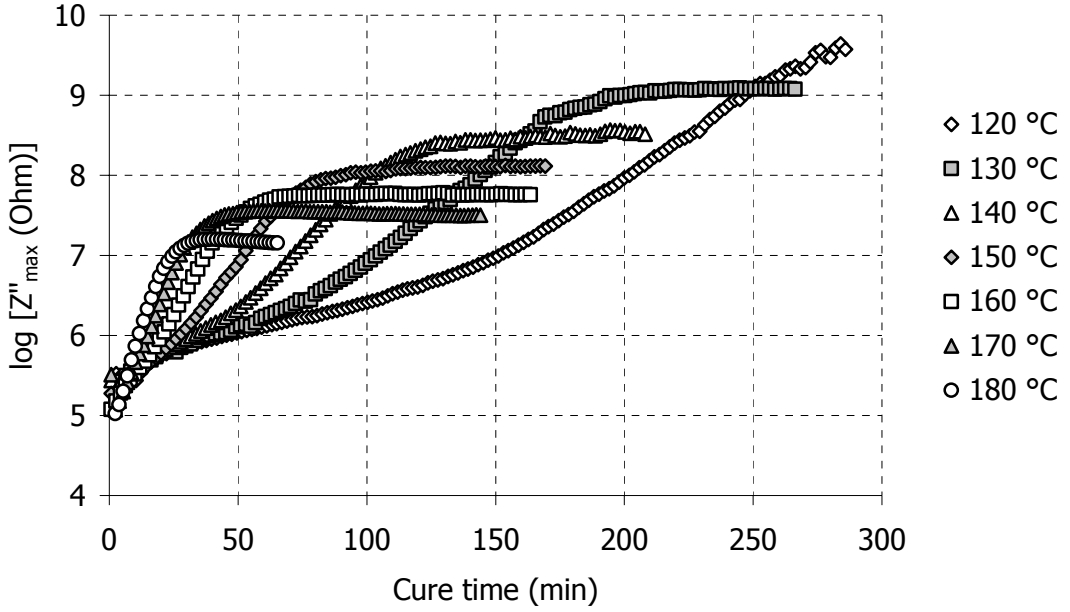

Figure 5-42 *IIM evolution during the isothermal cure of RTM6*

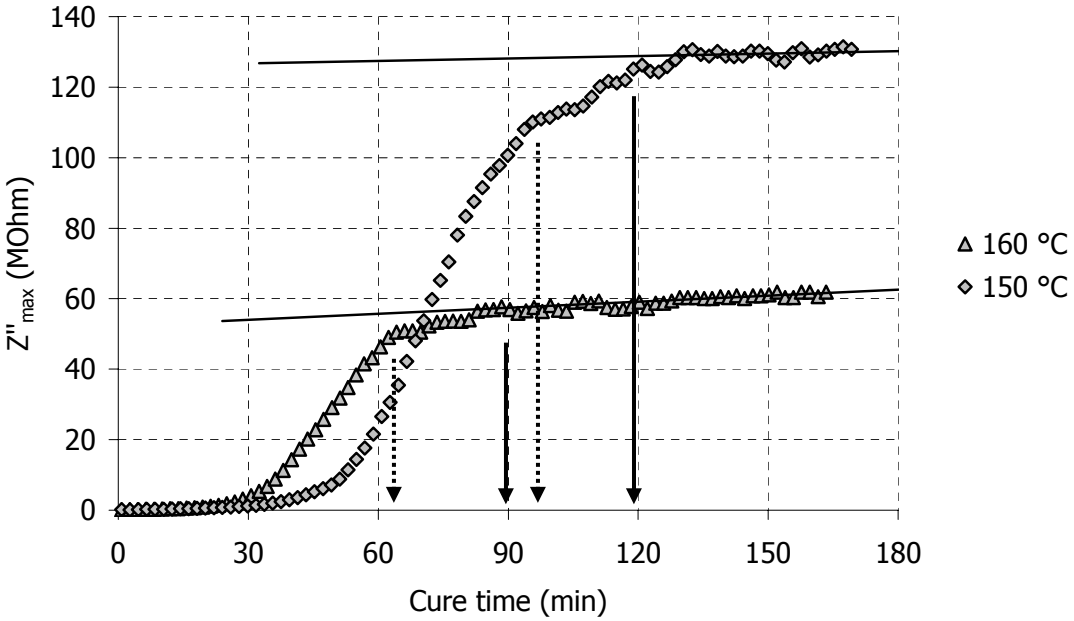

Figure 5-43 *IIM evolution for the isothermal cure of RTM6 at 150°C and 160°C. After the end of cure, indicated by the black arrows, Z" values continue to increase slowly. The dotted arrows indicate the vitrification time. The black lines are linear fits of the points after the end of cure.*

The IIM evolution during the dynamic cure of RTM6 is shown in Figure 5-44. The features of the graph are similar to Figures 5-35 and 5-37 in the sense that the curves superimpose up to about 100°C and after 180°C. Between these two zones the IIM increases and reaches a maximum. The curves corresponding to lower heating rates arrive at higher IIM values before starting to decrease.

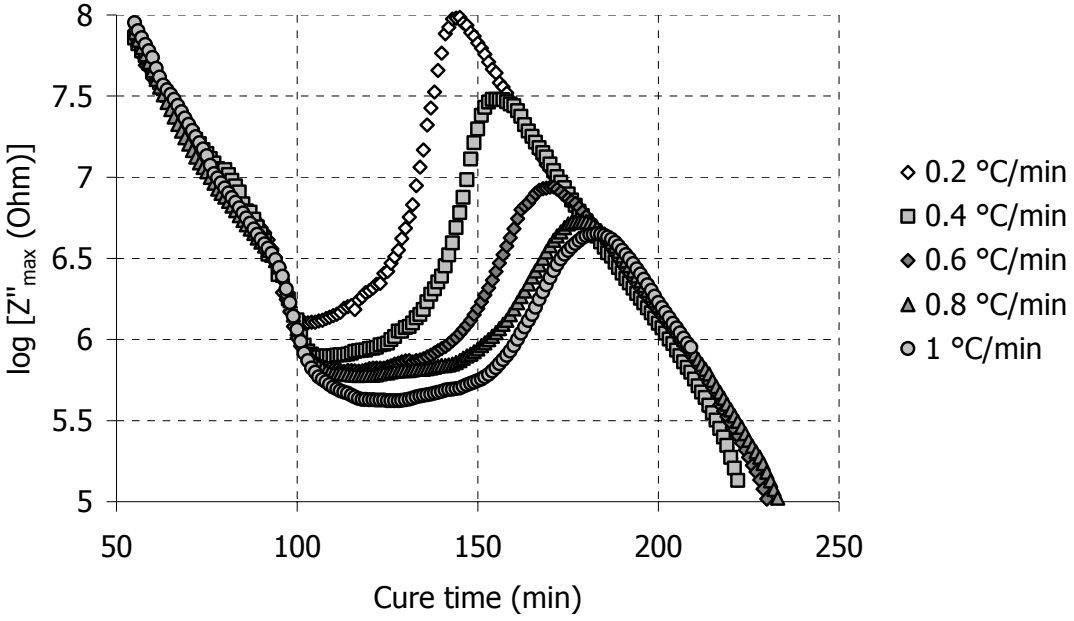

Figure 5-44 *IIM evolution during the dynamic cure of RTM6*

Table 5-IV lists the temperatures of the minimum and the maximum points in Figure 5-44 and compares them with the temperatures of the reaction onset, the reaction end and the vitrification temperature obtained by calorimetric measurements. We can see that the temperature of IIM minimum is close to the temperature of the reaction onset. This means that the spectrum shift is reversed when the curing reaction commences. Before the IIM minimum, only temperature affects the signal. Therefore the material state does not change and the spectra from all the dynamic experiments superimpose. Also, the temperature of IIM maximum correlates well with the vitrification temperature. This means that when the resin vitrifies, the influence of the reaction advancement on the signal is reduced and the influence from the temperature change shifts the spectra to higher frequencies. After vitrification the spectra begin to superimpose again, despite the fact that the material state is not the same (conversion at vitrification is different, as shown in Table 5-III). This implies that despite the

negative effect the reaction has on the mobility and concentration of migrating charges, the effect of temperature on the vitrified state is much stronger.

Table 5-IV: *Correlation between IIM features, onset and end of the curing reaction and vitrification for the dynamic cure of RTM6*

Heating rate r (°C/min)	Dielectric measurements		Calorimetric measurements		
	T_{min} (°C)	T_{max} (°C)	$T_{\alpha = 0.01}$ (°C)	$T_{vitr.}$ (°C)	$T_{\alpha = 100}$ (°C)
0.2	103	146	106	-	218
0.4	107	156	122	159	221
0.6	118	172	125	172	222
0.8	123	180	128	181	225
1	128	183	134	190	230

As was pointed out in § 4.3.2 the existence of charge carriers is related with the IIM point through eq. (4.27), provided that the influence of dipolar relaxation is very low. Eq. (4.28) provides a way of examining whether the IIM can be attributed solely to migrating charges throughout the cure. Figure 5-45 shows the product of $Z''_{max} \times f_{max}$ for three isothermal experiments.

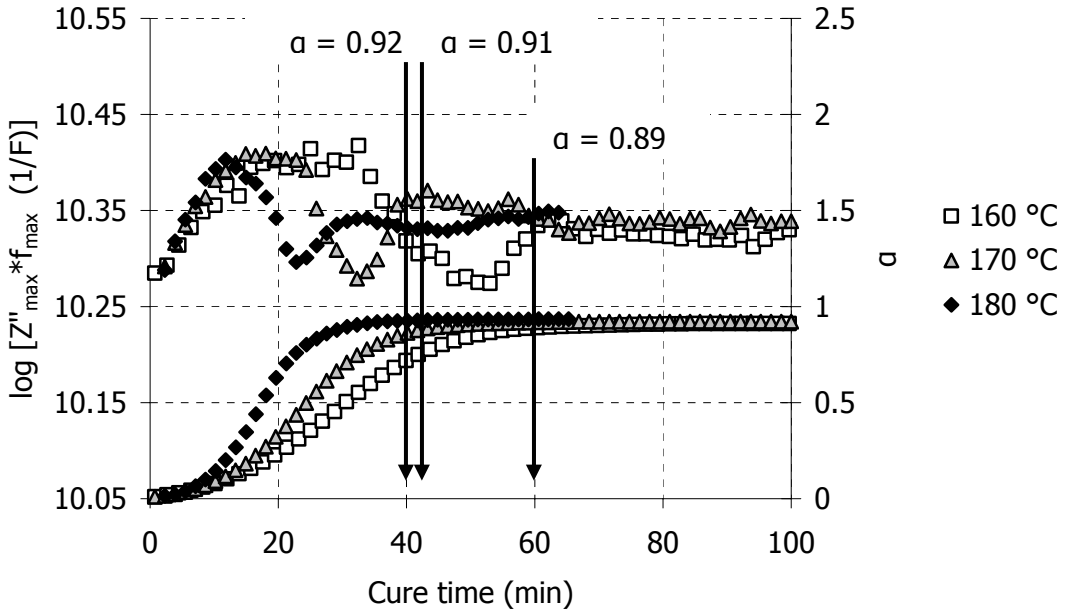

Figure 5-45 *Product of Z''_{max} and f_{max} for the isothermal cure of RTM6 and the corresponding conversion profiles. The arrows show the vitrification point measured by MDSC.*

The product remains relatively constant (the y – axis scale is very narrow). However, in the scale of Figure 5-45 we can see that there is a small minimum point appearing at a specific point into the cure. Vitrification seems to occur at the end of this minimum region. The correlation between the calorimetric and the dielectric results shown in Figure 5-45 was performed by applying the kinetic model using the temperature profile recorder in the resin during its cure.

This feature is also present in the dynamic runs, as shown in Figure 5-46. Here, the minimum is closer to the vitrification point of the resin, apart from the experiment at 1°C/min.

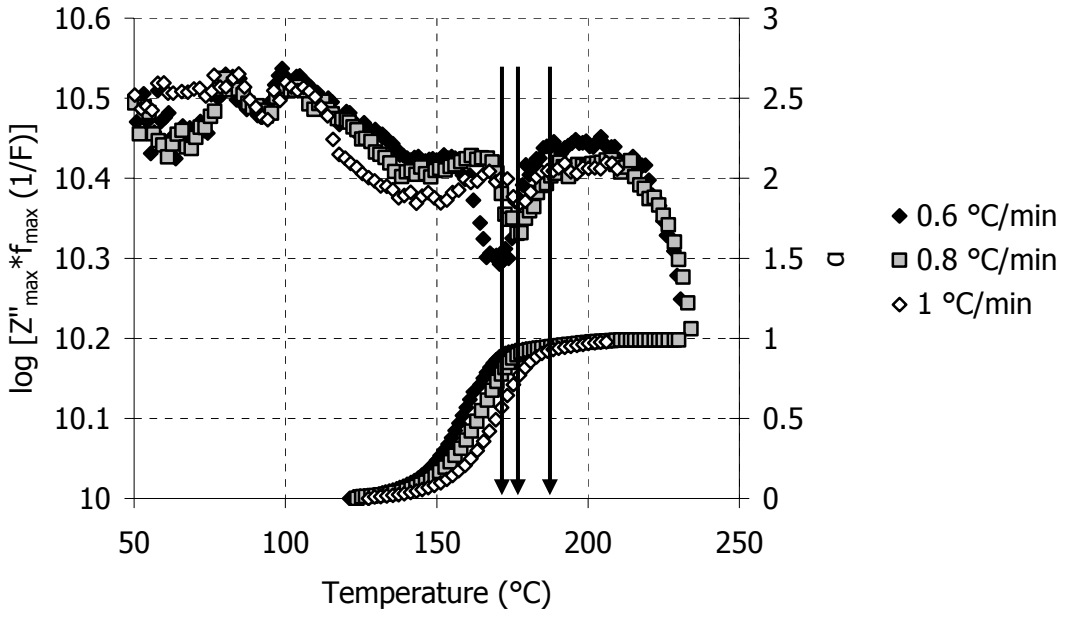

Figure 5-46 *Product of Z''_{max} and f_{max} for the dynamic cure of RTM6 and the corresponding conversion profiles. The arrows show the vitrification point measured by MDSC*

The appearance of the minimum point in the $Z''_{max} \times f_{max}$ product is due to the increase of the relaxation time, τ_{dip}, as vitrification approaches. Figure 5-47 shows the $Z''_{max} \times f_{max}$ development when R_{ion} and R_{dip} values change. For the construction of the artificial data eq. (4.35) was used with no electrode polarisation term. Changes in R_{ion} reflect the changes in the conductivity of the curing system. Changes in R_{dip} simulate the increase of the dipolar relaxation time, according to eq. (4.33). We can see that as R_{dip} values reach the same order of magnitude as R_{ion} values, the product $Z''_{max} \times f_{max}$ slightly decreases. When R_{dip} is kept constant and R_{ion} continues to increase, the

$Z''_{max} \times f_{max}$ returns to the initial value. The change in the product value is relatively small (from about 9.95 to 9.6 in Figure 5-47) as in the experimental results shown in Figures 5-45 and 5-46. This due to the fact that the value of the product $Z''_{max} \times f_{max}$ depends on permittivity and not on the relaxation time. For the construction of Figure 5-47 ε_u = 9 and ε_r = 3 which means that the maximum change in $Z''_{max} \times f_{max}$ will be log3 ~ 0.48 in logarithmic units.

In Figure 5-48, Z''_{max} is plotted against f_{max}. Arrows show the region where the minimum in the $Z''_{max} \times f_{max}$ product occurs. A small shoulder signifies the area of the minimum. We can see that the difference in the IIM location from the effect described above is minor.

Therefore, the IIM is considered to be affected only by the charge carriers concentration and mobility.

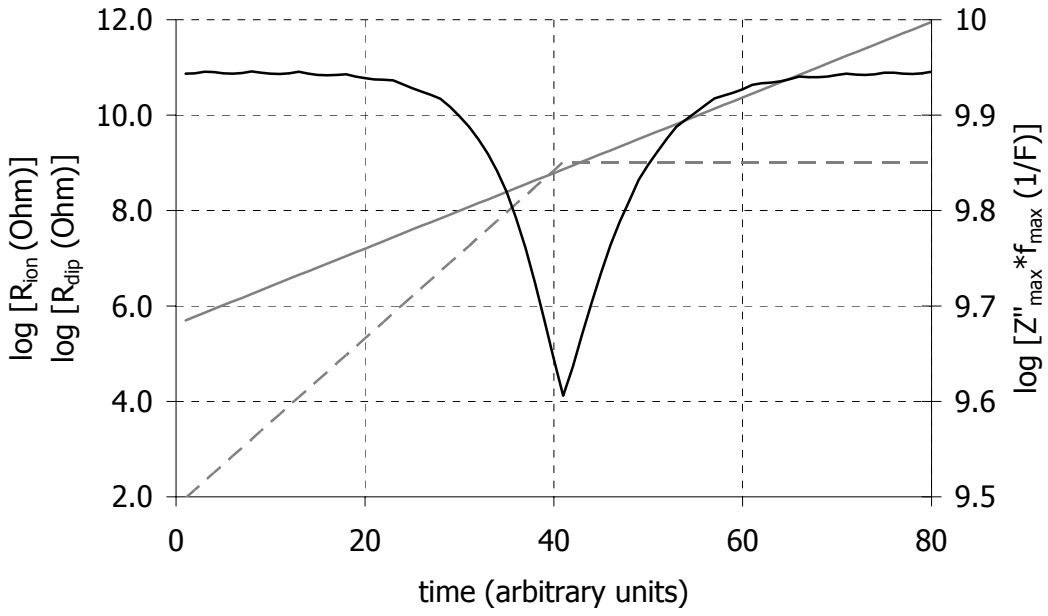

Figure 5-47 *Simulation of the minimum feature in IIM. The minimum occurs when R_{dip} (dashed grey line) value becomes similar to the R_{ion} value (solid grey line). For the construction of the spectra, eq. (4.35) was used with $C_{dip} = 5 \times 10^{-11}$ F and $C_{ind} = 3 \times 10^{-11}$ F. The CPE was not used.*

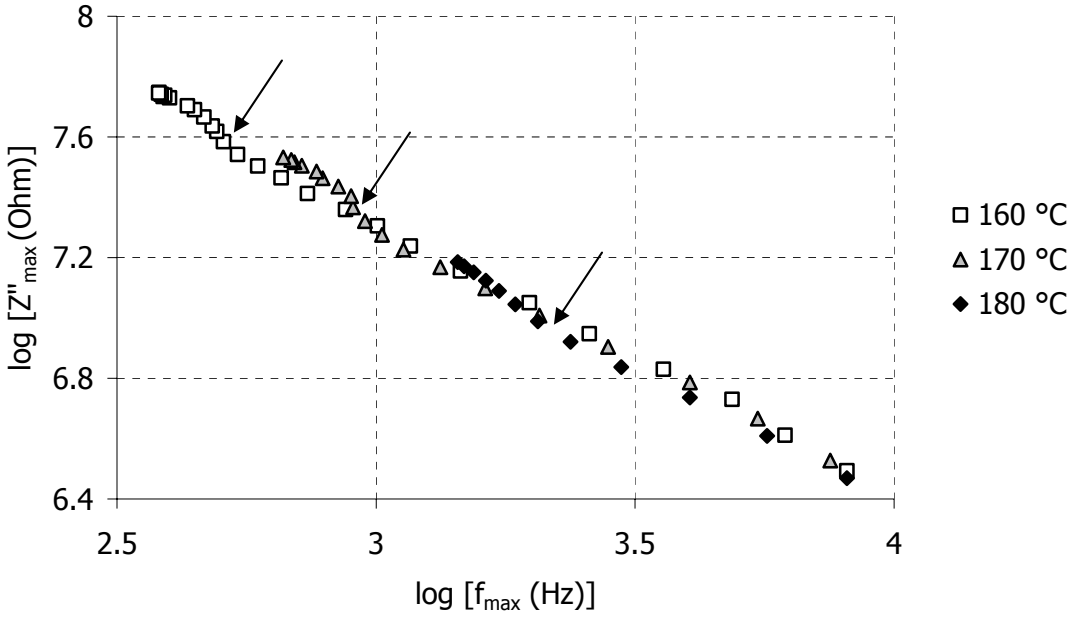

Figure 5-48 *Z''_{max} versus f_{max} for the isothermal cure of RTM6. Arrows indicate the areas where the minimum in the $Z''_{max} \times f_{max}$ product is observed.*

5.4.3 Dipolar movements

The effect from the relaxing dipoles is observed at high frequencies in the experimental spectra. The manifestation of dipolar movements is a small peak in the real impedance curve and a shoulder in the imaginary impedance curve (103). These features have been noted in Figures 5-26, 5-27, 5-38 and 5-39. The frequencies at which dipolar relaxation can be seen are always positioned after the IIM where the material exhibits capacitive behaviour, as was demonstrated in § 4.3 and eq. (4.26) in particular. At these frequencies, the effect from migrating charges is minimum. Figure 5-49 shows the spectra evolution at frequencies above 100 kHz for the time interval 38 – 53 minutes. We can see the shift of the *Z″* spectrum and the crossover in the *Z′* spectrum. The time evolution of the *Z′* and *Z″* values at 316 kHz is shown in Figure 5-50. The shift in the *Z″* spectra results in a step increase. The crossover in the *Z′* spectra shows as a peak.

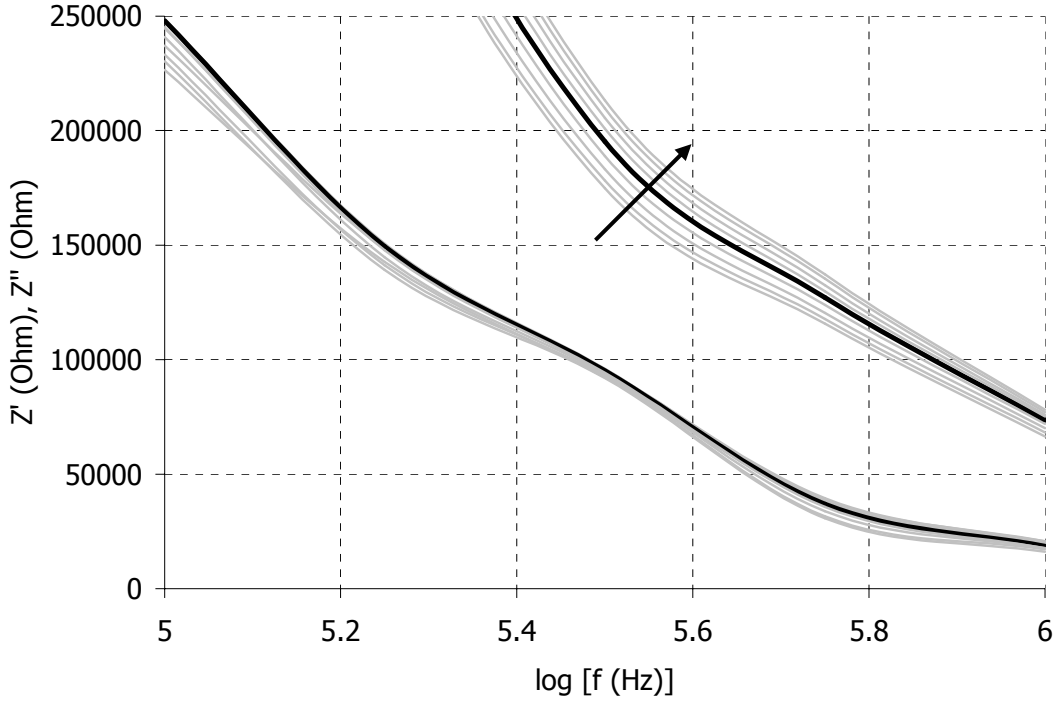

Figure 5-49 *Real and imaginary impedance spectra at high frequencies for the cure of RTM6 at 160°C. The spectra cover times from 38 – 53 min. The black line corresponds to 45 min. The arrow shows the time direction. In the real impedance spectra no arrow is used because the spectra cross over.*

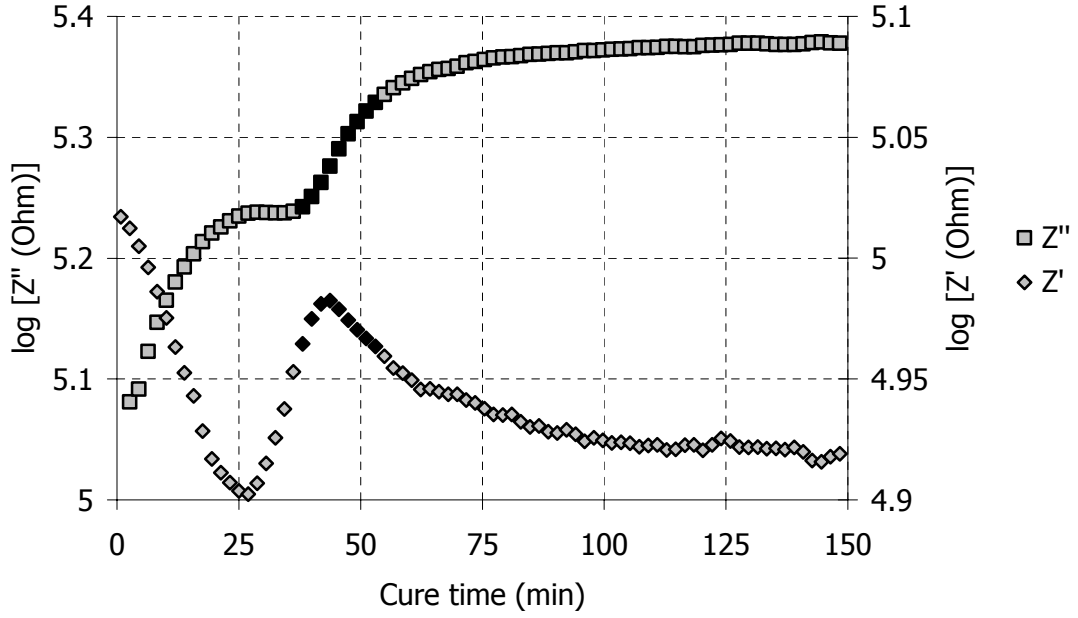

Figure 5-50 *Real and imaginary impedance spectra evolution at 316 kHz for the cure of RTM at 160°C. The black points represent the region of the spectra shown in Figure 5-49.*

The above features have also been analysed in § 4.3.1, where the impedance spectrum in which the dipolar movements are the only contributing factor was studied. The crossover in the real impedance is pictured in the inset graph in Figure 4-10. The shift in the imaginary impedance spectra is pictured in the inset graph in Figure 4-11.

6 Cure Characterisation: Modelling

6.1 Scope and objectives

The modelling of the experimental spectra that were analysed in the previous chapter is the main scope of this chapter. The genetic algorithm which was developed and optimised in Chapter 5 was applied to all experiments. The evolution of the equivalent circuit parameters during the cure is analysed. The simplified equivalent circuit presented in § 4.5.4 is used for the separation from each other of the three phenomena that together produce the total signal. The regions where each phenomenon can be studied separately are identified and mapped during the whole cure cycle. Finally, the correlation between the dielectric signal and the material state is described and modelled.

6.2 Modelling results

In order to assess the repeatability of the modelling algorithm and to estimate the fitting error for each parameter, the dielectric experiment at 1°C/min was modelled 10 consecutive times. In Figure 6-1, the results of the modelling are shown for the spectrum corresponding to 117°C. The modelling lines in the graph are calculated by averaging the results from the 10 runs. The average overall fitting error was 0.005 (too

small to be visible on the scale of the graph in Figure 6-1). This value is determined by calculating the difference between the experimental data and the modelling results at each frequency and averaging over all frequencies. The very small error means that the algorithm reaches the same solution for the equivalent circuit parameters in all 10 fits. The average fitness value for the modelling of the particular spectra was 63.0 ± 0.7.

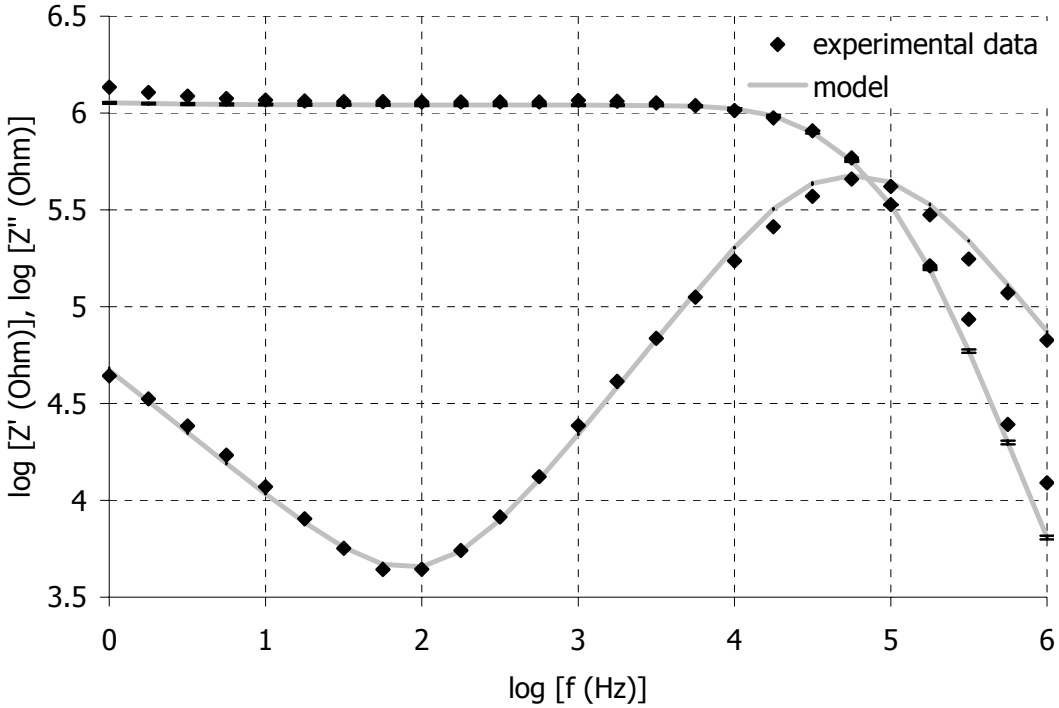

Figure 6-1 *Impedance spectra modelling. The experimental data are from the cure of RTM6 at 1°C/min (117°C). For the modelling lines, the results from 10 runs of the algorithm are averaged. Error bars are barely visible at the two ends of the frequency range in the real impedance curve.*

Figure 6-2 illustrates the estimated parameters from the 10 runs on the spectrum of Figure 6-1. The average value of all the estimations and the error (95% level of confidence) are also shown. The scale of the x – axis illustrates the variations on the estimation of each parameter. The parameters with the highest deviation compared to the average value are R_{dip} and C_{dip}. The deviation to average value ratio for these two parameters is 0.125 and 0.126 respectively. On the other hand, the ratio for R_{ion} is 0.009 and for C_{ind} is 0.002 which means that these parameters are determined more accurately. These results agree with the sensitivity analysis on the circuit elements

described in § 4.5.5. However, the shift of the spectra during the cure will alter the accuracy in the determination of the equivalent circuit parameters.

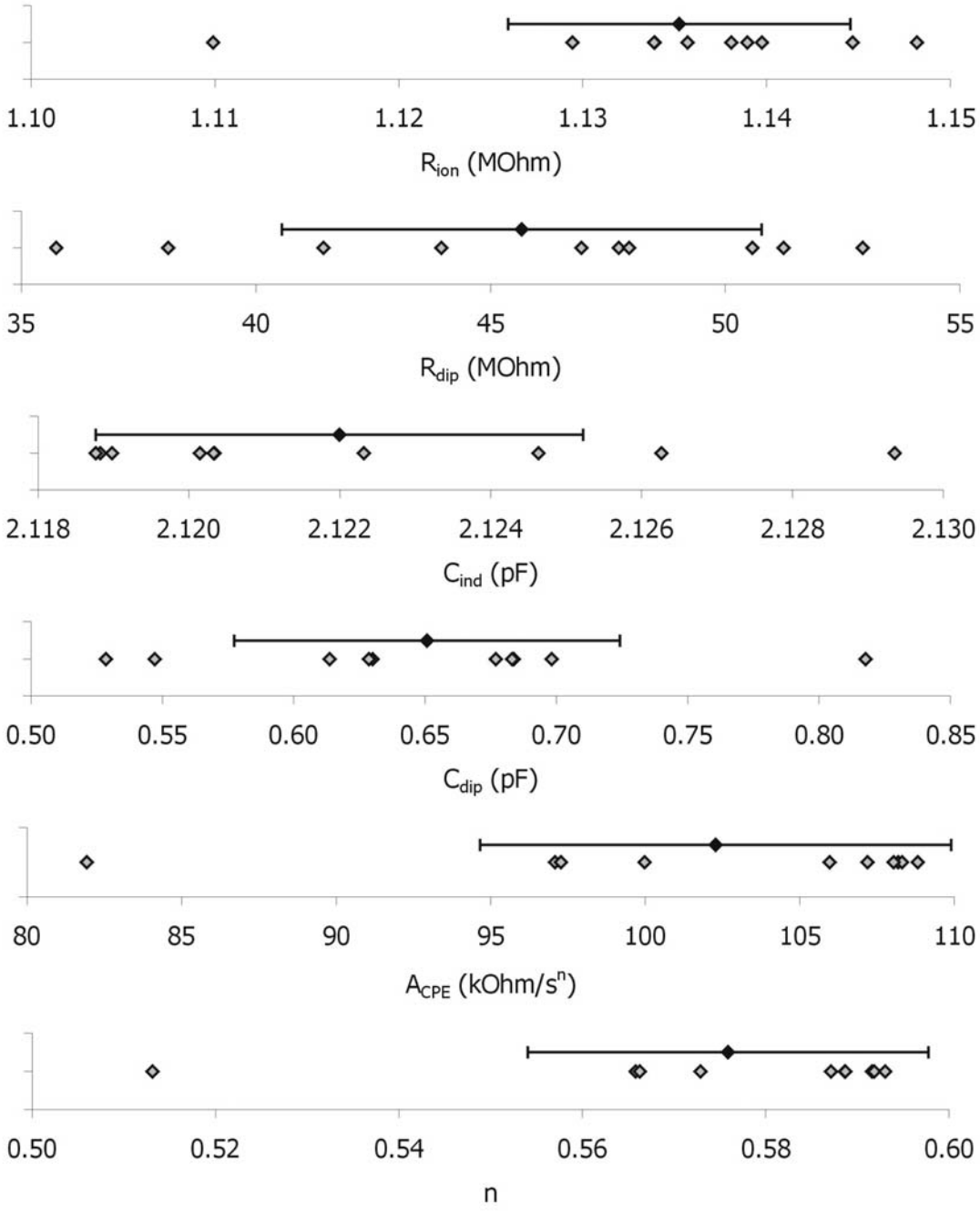

Figure 6-2 *Results from the modelling of the spectrum of Figure 6-1. The grey points are the estimations of the parameters from the 10 consecutive fits. The black point is the average value. The bars show the standard deviation.*

6.2.1 Isothermal cure

Modelling results for the cure of RTM6 at different temperatures are shown in Figure 6-3. We can see that the modelling of the experimental data is very accurate. The slope in the low frequency side of the spectrum is similar for the three spectra and remains relatively unchanged during the whole cure, as will be shown also in Figure 6-9 below. This has been observed in all isothermal experiments. It is an indication that the dielectric sensors used in the experiments exhibit similar behaviour and the cure does not influence the value of *n*.

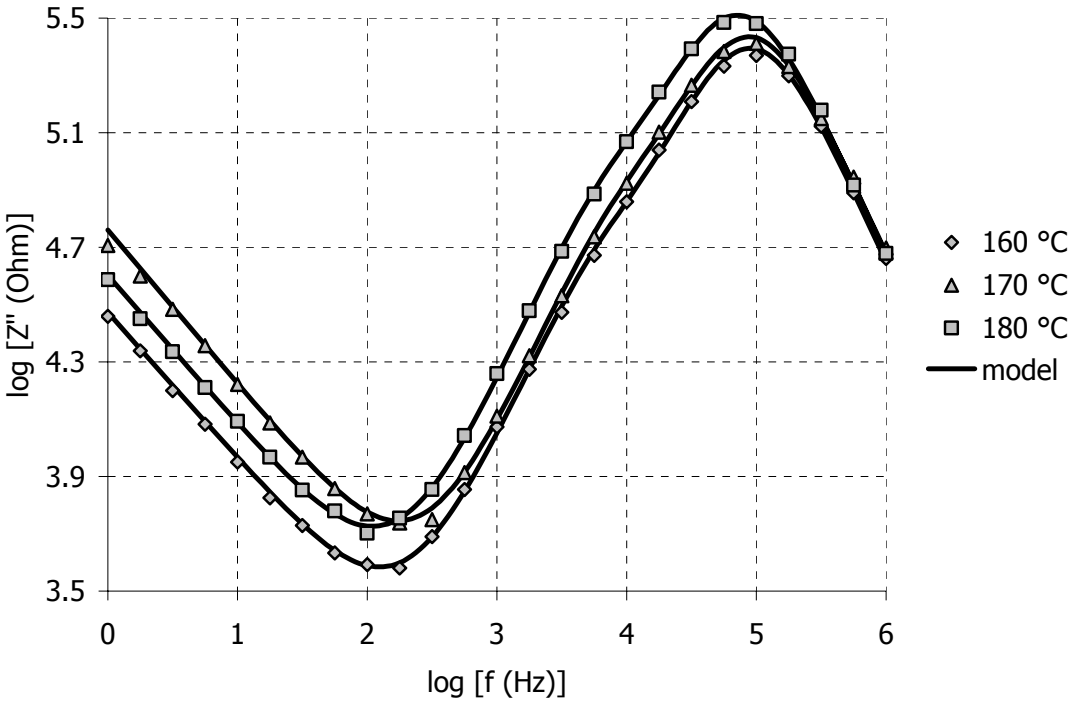

Figure 6-3 *Modelling results for three imaginary impedance spectra. The spectra correspond to early cure stages (~7 minutes into the cure)*

The evolution of the migrating charges resistance R_{ion} is presented in Figure 6-4. R_{ion} evolution is similar to the IIM evolution (Figure 5-42) during the isothermal cure. It increases and then reaches a plateau. The final value of the plateau is lower at higher cure temperatures.

The dipolar resistance R_{dip} is shown in Figure 6-5. We can see that R_{dip} increases continuously and reaches a plateau. The values corresponding to 160°C also show a plateau at the beginning. According to eq. (4.33) the dipolar resistance reflects the changes of the dipolar relaxation time, τ_{dip}. During epoxy cure, τ_{dip} increases

exponentially until the material vitrifies (43, 85). We can see that R_{dip} follows the same trend. The increase in R_{dip} is not instantaneous.

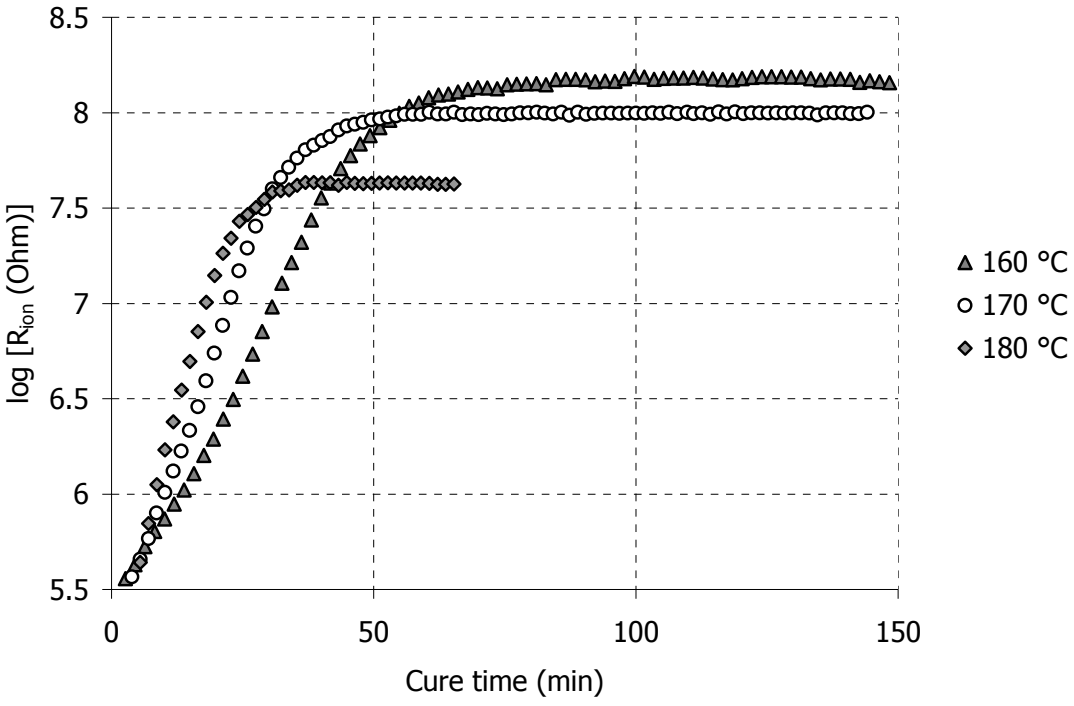

Figure 6-4 *Modelling results for R_{ion} during the isothermal cure of RTM6*

It covers about 50 minutes in the experiment at 160°C which is about three times more than the time span observed in the MDSC measurements (76 min – 60 min = 16 min as shown in Table 5-II).

Figure 6-5 also shows the vitrification point at each temperature, calculated by using the cure kinetics model with the temperature profile recorded in the curing resin as input. From the output conversion profile, the vitrification time is calculated using the conversion values in Table 5-II for the isothermal runs and Table 5-III for the the non – isothermal runs.

Vitrification occurs at the point R_{dip} reaches the plateau value. Therefore, the changes in R_{dip} can provide information about the onset of vitrification.

The dipolar capacitance is shown in Figure 6-6. C_{dip} has a value of about 1 pF at the beginning. At some point C_{dip} undergoes a step increase and settles at a plateau. This increase coincides with the increase of R_{dip} towards the end of the step. The plateau varies from about 2.1 to 2.9 pF. As in R_{dip} evolution, the vitrification point was located after the final C_{dip} value was attained.

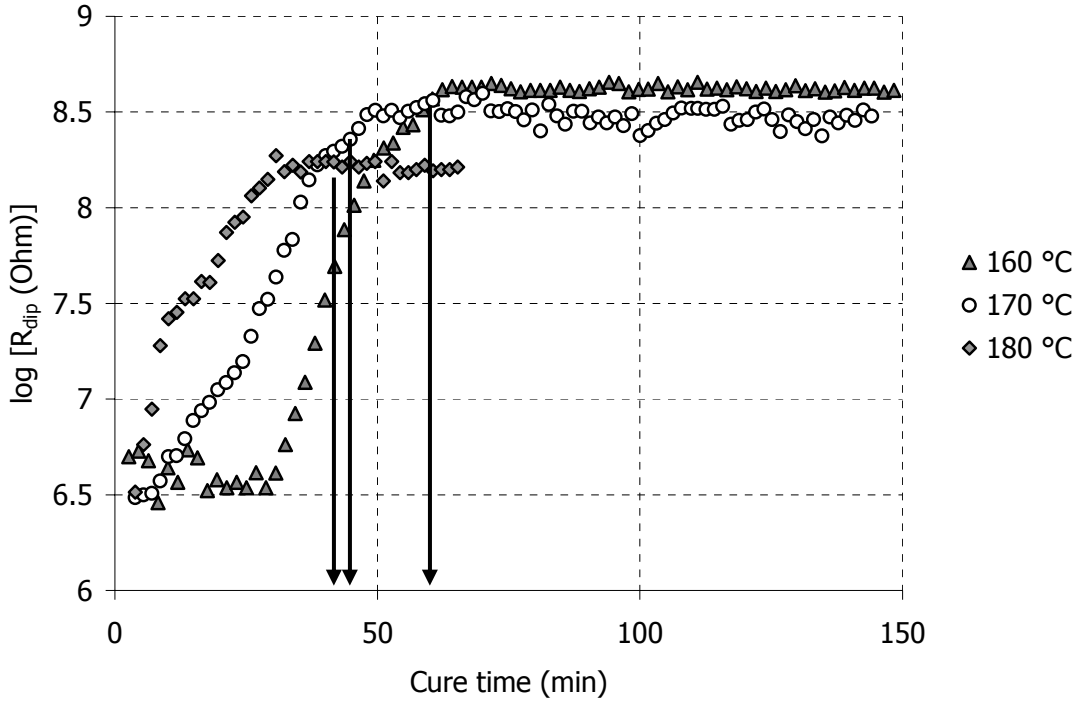

Figure 6-5 *Modelling results for R_{dip} during the isothermal cure of RTM6. The arrows indicate the vitrification point.*

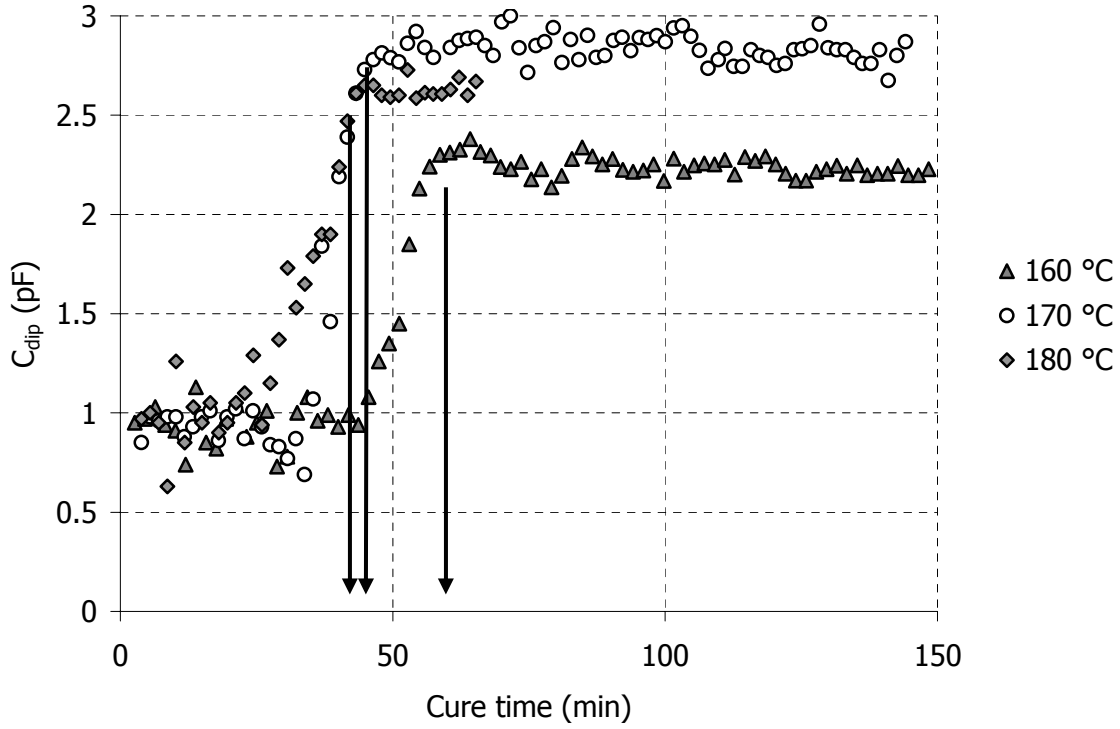

Figure 6-6 *Modelling results for C_{dip} during the isothermal cure of RTM6. The arrows indicate the vitrification point*

The changes in the capacitance of the induced dipoles are very small as shown in Figure 6-7. In all isothermal experiments C_{ind} varies only about 0.3 pF during the whole cure. This is expected since C_{ind} accounts for all the fast polarisation processes that are present in all frequencies and are not affected by the curing reaction or other physicochemical transitions (84, 85).

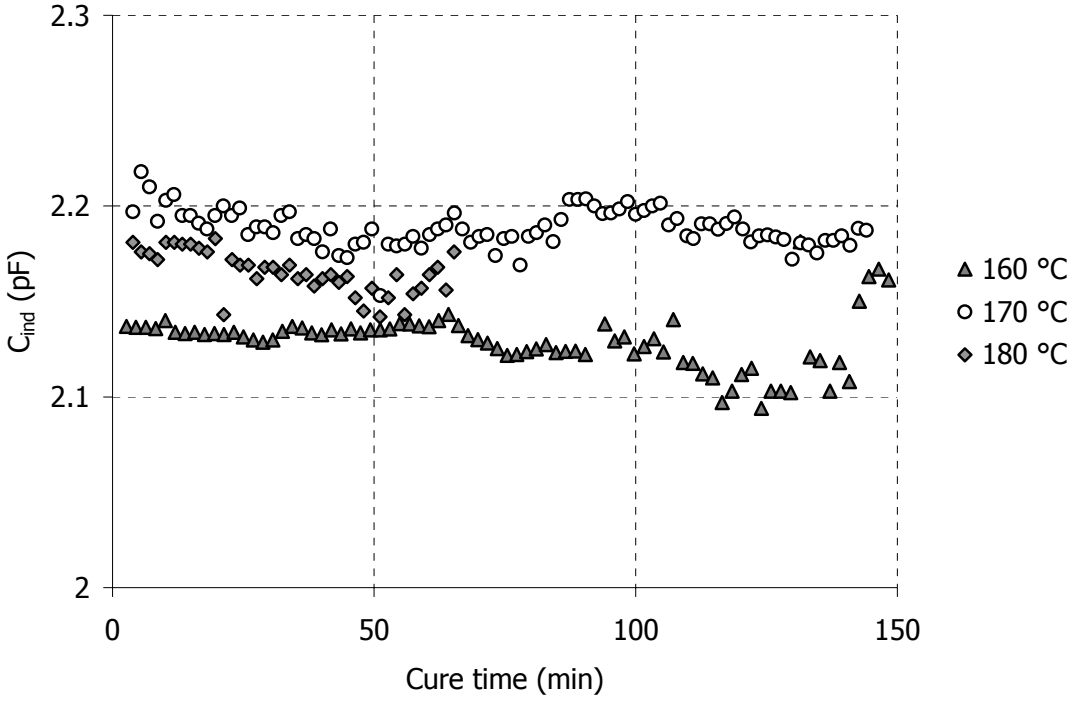

Figure 6-7 *Modelling results for C_{ind} during the isothermal cure of RTM6*

The CPE parameters A_{CPE} and n which model the polarisation of the electrodes are given in Figures 6-8 and 6-9 respectively. A_{CPE} increases as the cure progresses and reaches a final value. As can be observed in Figure 6-8 the final A_{CPE} value can vary by as much as one order of magnitude. This is possibly because the sensitivity in the estimation of A_{CPE} (and n) at the end of the isothermal cure is low because of the movement of the impedance spectra towards higher impedance values and lower frequencies (see Figure 5-18). The exponent n varies from 0.42 to 0.58 with more values being close to 0.5. This value, which agrees with previous studies on the same resin (211), means that the electrodes surface is not flat but has a fractal geometry as discussed in § 4.5.1.

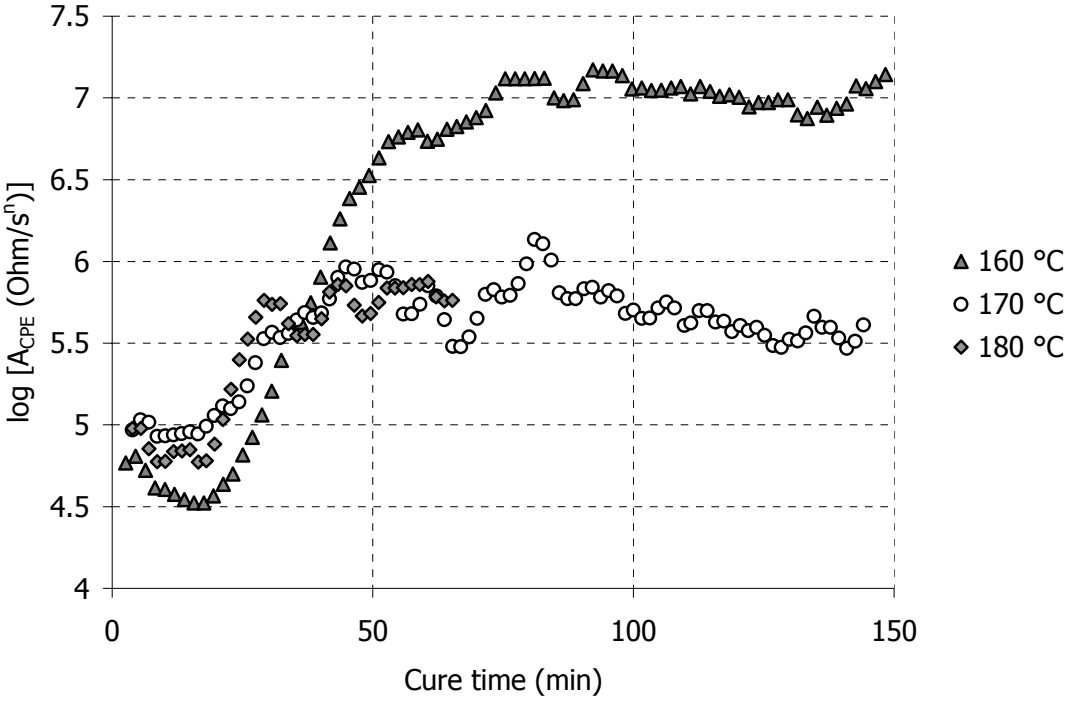

Figure 6-8 *Modelling results for A_{CPE} for the isothermal cure of RTM6*

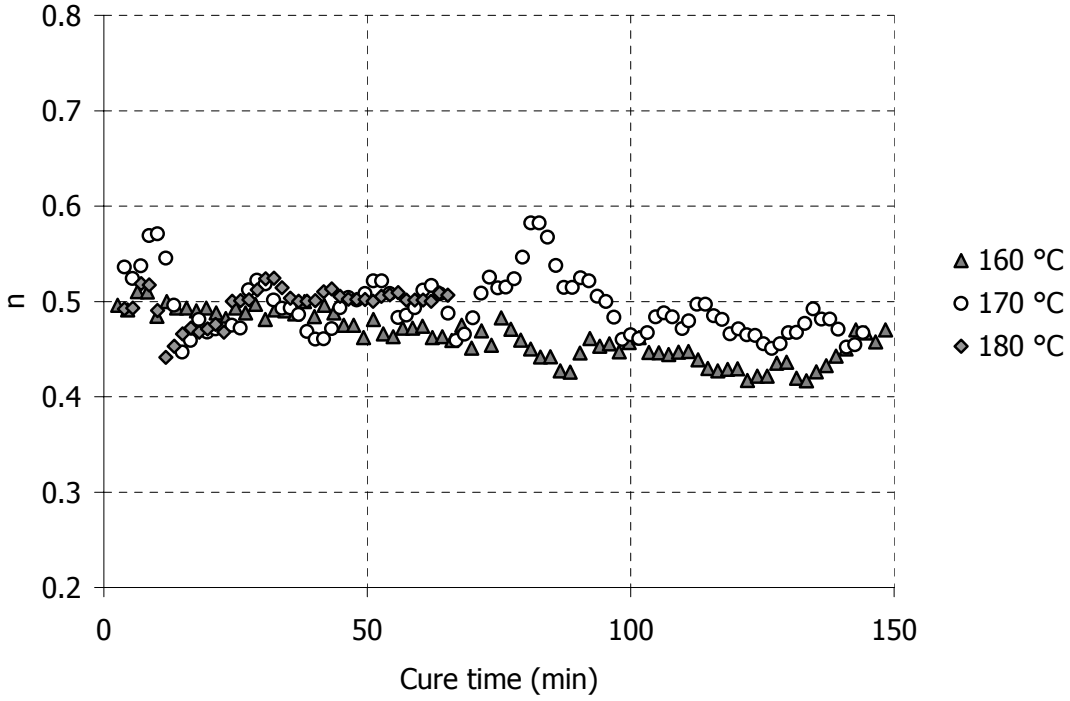

Figure 6-9 *Modelling results for n during the isothermal cure of RTM6*

The initial increase in A_{CPE} and the relatively constant value of n are in agreement with the comments made in § 5.4.1 and explain the spectra movements in Figure 5-41. The evolution of A_{CPE} is similar to IIM which explains the mutual shift of the maximum and minimum points in the imaginary impedance spectrum. The constant slope at low frequencies is justified by the relatively unchanged value of n.

6.2.2 Non – isothermal cure

Results from the modelling of the cure of RTM6 under dynamic conditions are shown in Figure 6-10. We can see that the model curves are very close to the experimental data, even when the spectrum contains outliers as in the spectra at 0.4°C/min and 0.8°C/min.

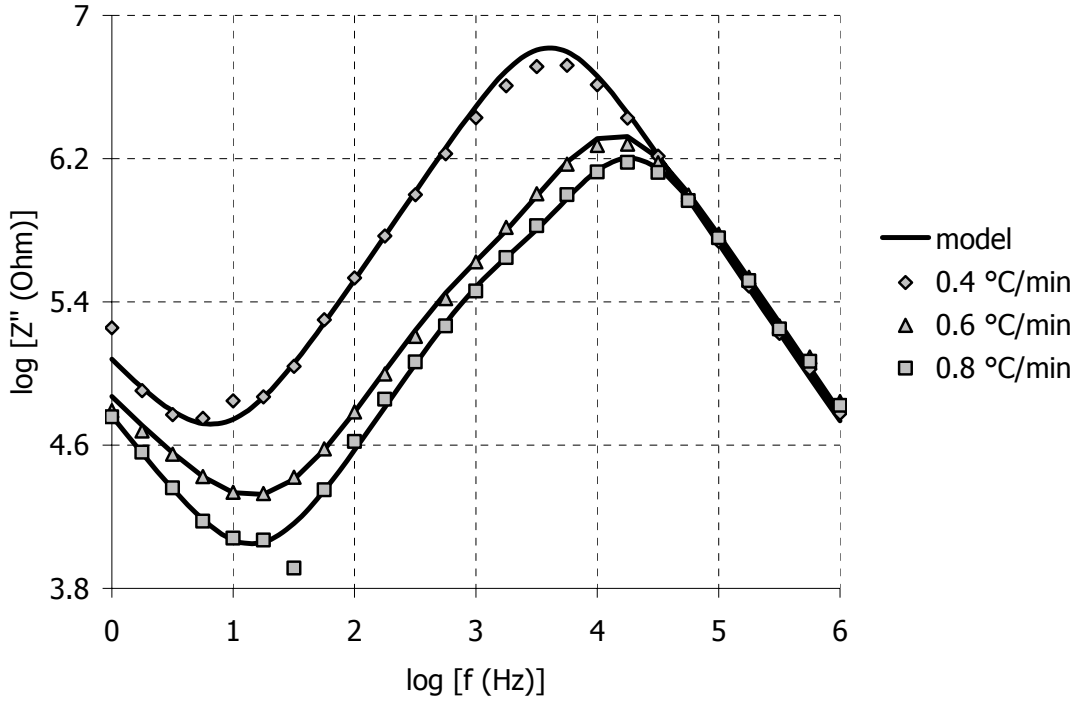

Figure 6-10 *Modelling results for imaginary impedance spectra during the dynamic cure of RTM6. The spectra correspond to similar conversion (~30%)*

The evolution of R_{ion} for the dynamic cure of RTM6 is presented in Figure 6-11. As in the isothermal case, R_{ion} follows the changes of the IIM. This indicates that the movements of migrating charges is the dominant phenomenon that affects the IIM. At the beginning and after the end of cure R_{ion} is the same in all experiments since in these regions the migrating charges movements are affected only by temperature. The superposition at the beginning means that the concentration and mobility of migrating

charges is the same in all experiments. This is expected since the same resin batch was used for all the runs in this study. At around 100°C there is a drop in R_{ion} in all experiments. This is related to some physical process in the resin since the polymerisation reaction commences at higher temperatures (~110°C at 0.2°C/min according to the calorimetric measurements presented in § 5.2.1). The dissolution of one of the initial constituents of the resin could produce an increase in the concentration of the migrating charges and thus reduce the total impedance of the system. The superposition after the end of cure means that the concentration and the mobility of the migrating charges in the fully cured resin is the same. It also indicates that the dielectric properties of the fully cured material are independent of the thermal history. At very high temperatures, after 210°C, we can observe a gradual break up in the R_{ion} curves. This can be related to the devitrification process which occurs at around 220°C, according to the glass transition measurements presented in § 5.2.3.

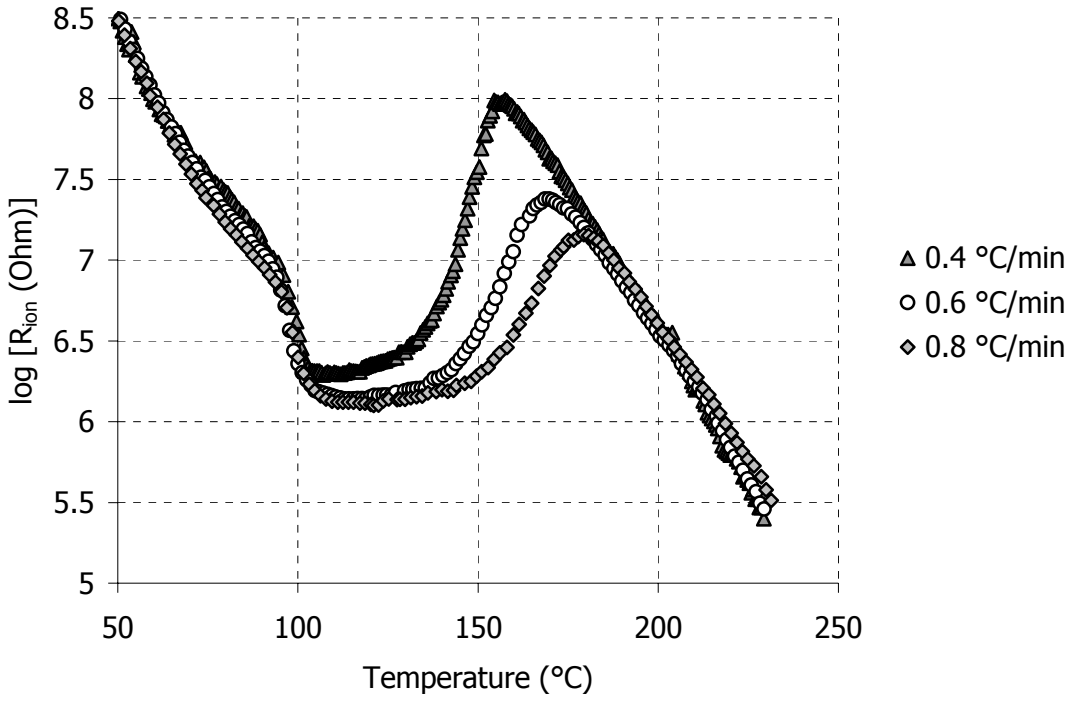

Figure 6-11 *Modelling results for R_{ion} during the dynamic cure of RTM6*

The evolution of R_{dip} is presented in Figure 6-12. We can see that, at the beginning, the R_{dip} estimated values decrease as temperature increases. This trend is similar to the slow increase in c_P before vitrification (Figure 5-16). R_{dip} undergoes a step increase of about one order of magnitude and then settles for up to 200°C.

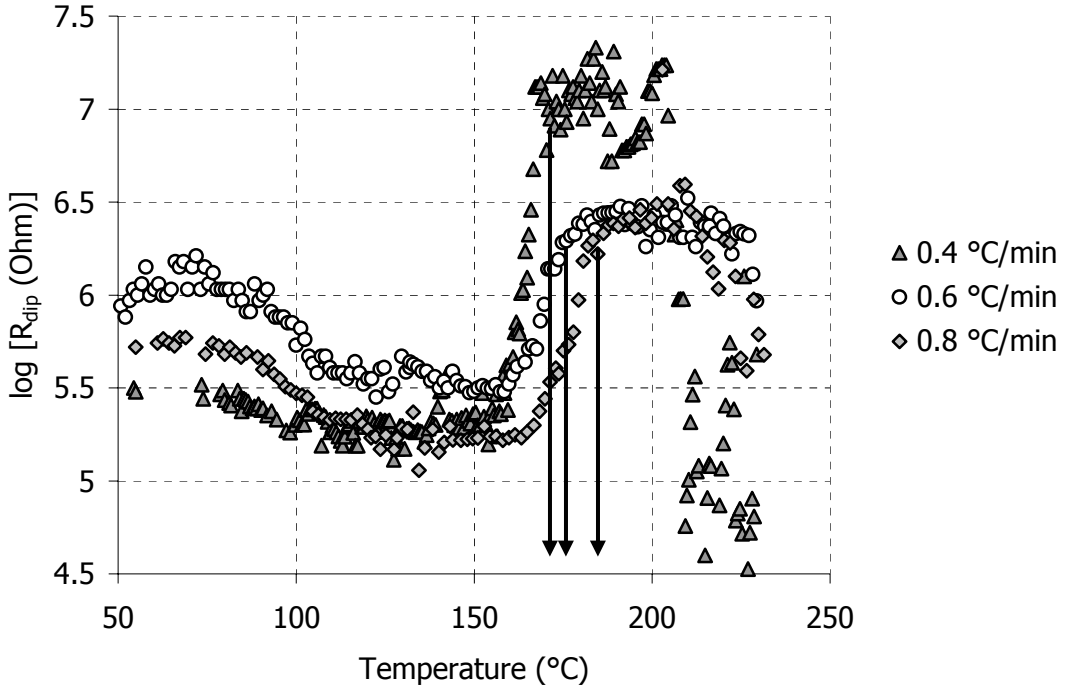

Figure 6-12 *Modelling results for R_{dip} during the dynamic cure of RTM6. The arrows indicate the vitrification point*

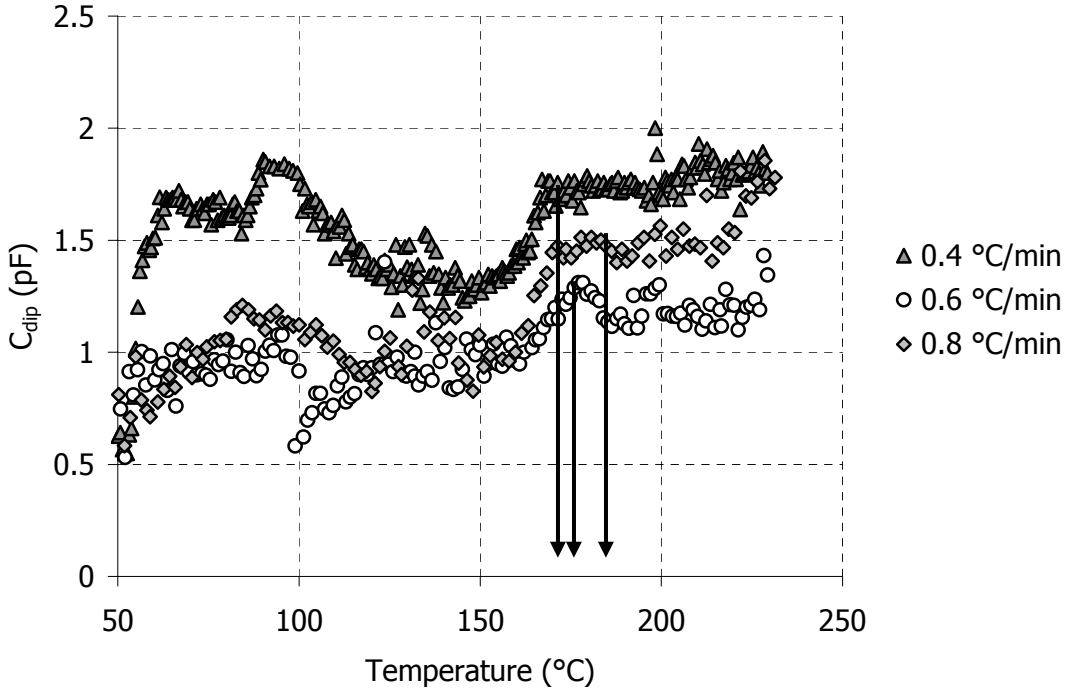

Figure 6-13 *Modelling results for C_{dip} during the dynamic cure of RTM6. The arrows indicate the vitrification point*

The vitrification point is located right after the end of the step increase like in the isothermal experiments. At even higher temperatures R_{dip} decreases rapidly, because of the devitrification process.

The dipolar capacitance C_{dip} stays relatively unchanged throughout the cure, as shown in Figure 6-13. A small shoulder of about 0.5pF can be identified at the same temperature range where R_{dip} increases. However, the sensitivity in the estimation of C_{dip} is low and such small changes in C_{dip} cannot be discerned accurately.

The capacitance of the induced dipoles does not change significantly throughout the cure as we can see in Figure 6-14. C_{ind} values are in the region of 1.4pF – 1.9pF which is slightly lower than the values obtained from the modelling of the isothermal curves.

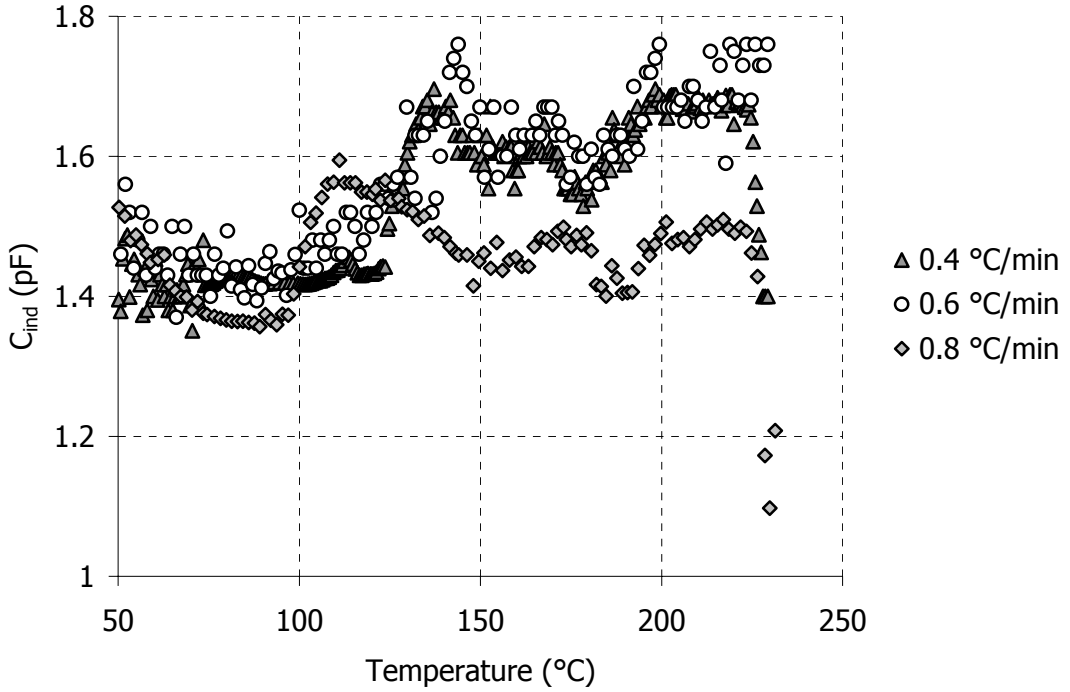

Figure 6-14 *Modelling results for C_{ind} during the dynamic cure of RTM6*

The A_{CPE} evolution is shown in Figure 6-15. We can see that, initially, A_{CPE} is insensitive to the curing reaction unlike the isothermal case. After about 150°C there is a steady decline in A_{CPE} values. In this region A_{CPE} follows the trend of the IIM. This behaviour explains the different trends described in § 5.4.1 (Figure 5-40 in particular). At the beginning and during the cure of RTM6, A_{CPE} values remain relatively constant, which means that the low frequency side of the imaginary impedance spectrum does not shift alongside the rest of the spectrum. After a point, where the conversion is around 30%

- 35%, A_{CPE} values follow the IIM evolution which means that the low frequency side of the spectrum follows the shift of the whole spectrum.

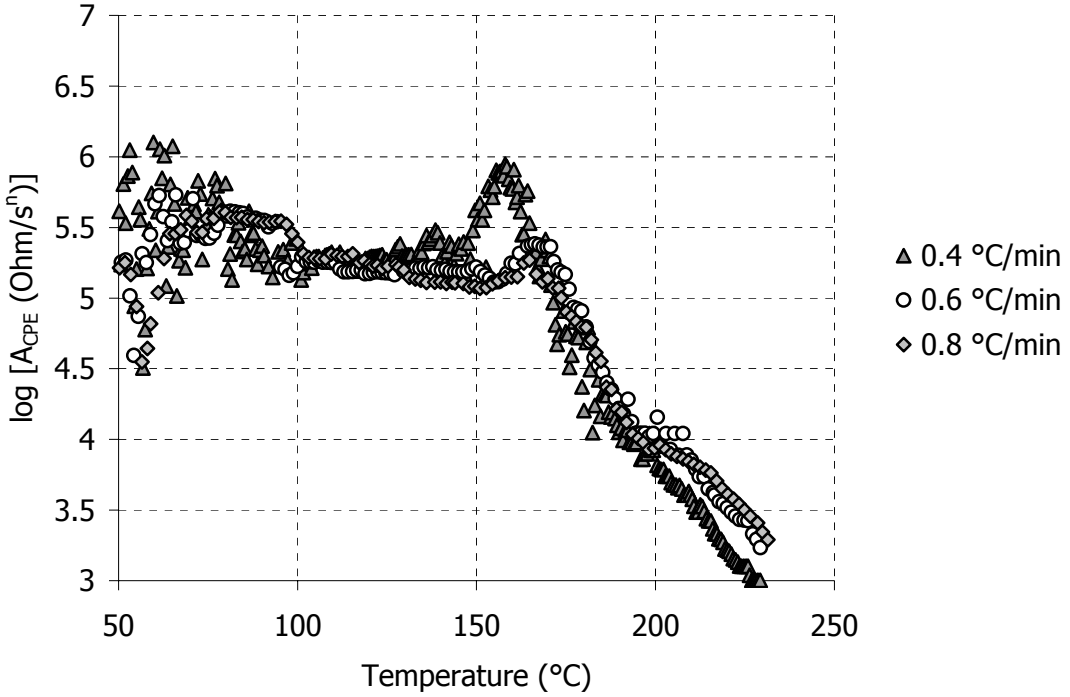

Figure 6-15 *Modelling results for A_{CPE} during the dynamic cure of RTM6*

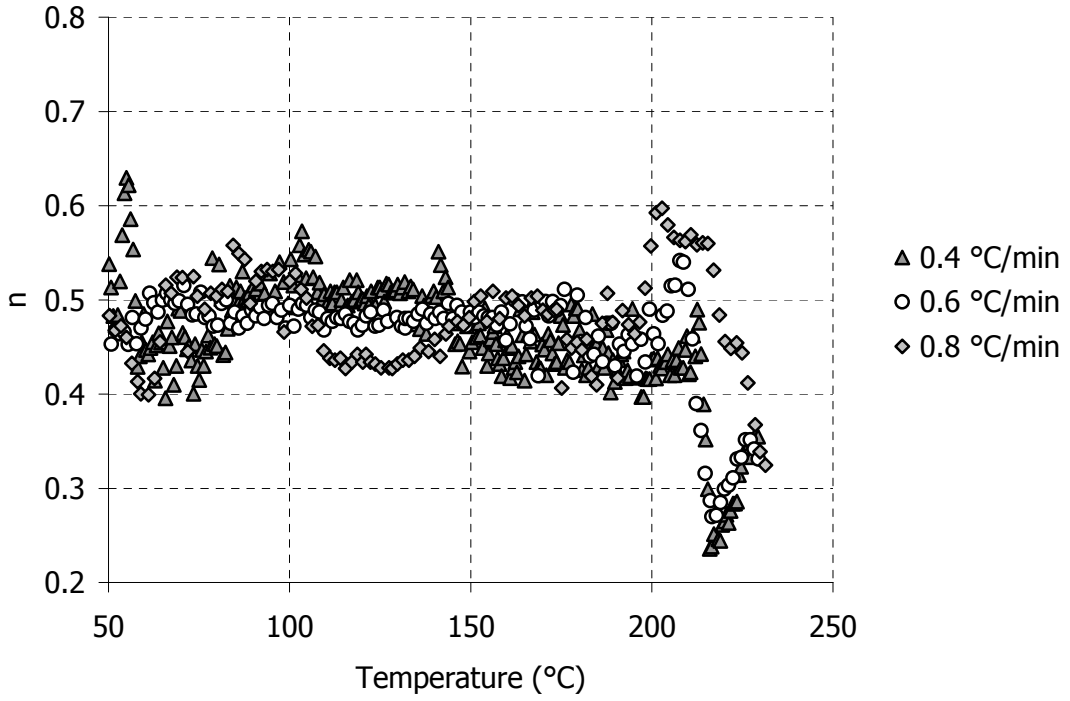

Figure 6-16 *Modelling of n for the dynamic cure of RTM6*

In Figure 6-16, the evolution of the exponent *n* under dynamic cure conditions is shown. The exponent remains relatively constant at values close to 0.5, as in the modelling of the isothermal curves. This is evidence that the exponent *n* is not affected by the cure but is a characteristic of the dielectric sensor.

6.3 Phenomena disentanglement

The analysis of the equivalent circuit parameters evolution during cure revealed the sensitivity of certain parameters to certain phenomena, as expected from the definition of these parameters. In this section, the results from the modelling are used in order to reconstruct the impedance curves in the time domain at different frequencies.

6.3.1 Vitrification identification

The vitrification point has been identified as a small peak in the real and as a shoulder in the imaginary impedance curves (106, 108). In Figure 6-17 these features are shown at high frequencies for the dynamic cure of RTM6 at 0.6°C/min. We can see that dielectric vitrification (black arrow) is close to the calorimetric vitrification.

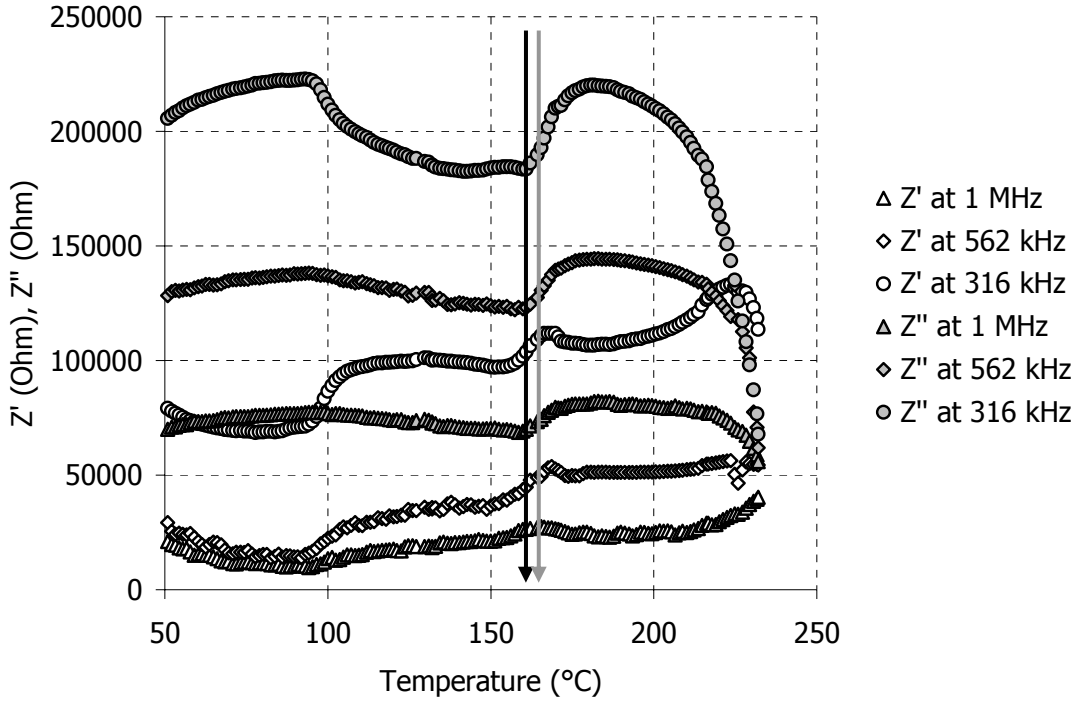

Figure 6-17 *Z' and Z'' impedance evolution at high frequencies during the cure of RTM6 at 0.6°C/min. The black arrow marks the point of the peak in real impedance and shoulder in imaginary impedance at 168°C. The grey arrow shows the vitrification point as measured by MDSC at 172°C.*

This correlation is observed in all experiments as shown in Table 6-I. Dielectric vitrification occurs slightly before calorimetric vitrification. This is owed to the different time scales of the measurement techniques used for the determination of vitrification (168). MDSC measurements were performed with a modulation period of 1 minute which results in a frequency of ~0.02 Hz. Dielectric vitrification is identified at frequencies over 100 kHz. Therefore vitrification is identified on different time scales in the two techniques and is expected to be seen earlier at the higher frequencies of the dielectric experiments.

Table 6-I: *Conversion at the vitrification point as measured by MDSC and DEA*

Temperature profile	Calorimetric vitrification	Dielectric vitrification
120 °C	0.71	0.68
130 °C	0.72	0.69
140 °C	0.82	0.76
150 °C	0.86	0.79
160 °C	0.87	0.83
170 °C	0.91	0.85
180 °C	0.91	0.87
0.4 °C/min	0.81	0.78
0.6 °C/min	0.88	0.84
0.8 °C/min	0.90	0.90
1 °C/min	0.92	0.77

Using the equivalent circuit parameter estimations, the features corresponding to vitrification in the dielectric signal can be reproduced. In Figure 6-18 the imaginary impedance of the dynamic cure of RTM6 at 0.6°C/min is plotted alongside the model prediction (eq. (4.35)) at high frequencies. We can see that the predicted points are close to the experimental points. This means that the modelling algorithm can identify the dipolar contributions in the spectrum, despite the fact that these contributions are very small compared to the contributions from other phenomena like migrating charges. The signal changes shown in Figure 6-18 are barely visible in the logarithmic Z'' spectra of Figure 5-30 where the same experimental data – dynamic cure at 0.6°C/min – are presented.

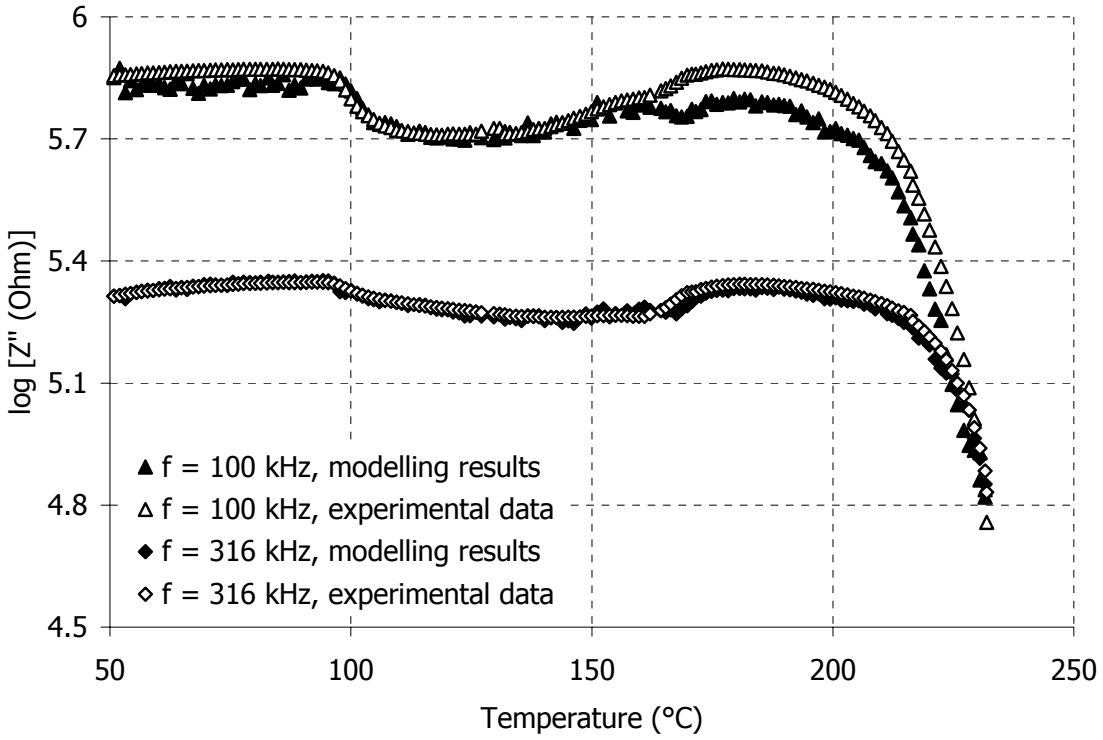

Figure 6-18 *Comparison between experimental points and modelling results at high frequencies. Experimental data are from the dynamic cure of RTM6 at 0.6°C/min.*

6.3.2 Modelling of the optima in the imaginary impedance spectrum

The maximum and the minimum points in the imaginary impedance spectrum form boundaries of the frequency ranges where each of the three phenomena that comprise the dielectric signal dominates. In order to produce an analytical model for the prediction of these two points, the equivalent circuit of Figure 4-18 was utilised instead of the standard circuit of Figure 4-16. The benefit of using the new circuit is that the circuit which describes the charge migration and the dipolar movements is broken into two simple parallel R-C circuits. The evolution of these two circuits during cure is easier to follow and the calculations for the determination of the two optima become simpler. All the calculations for the maximum and the minimum point in the Z" spectrum are given in Appendix C. The frequency of the IIM is the solution of a cubic equation (eq. (C29) in the Appendix) in which the coefficients are complex functions of the circuit parameters. For the formulation of the equation electrode polarisation was assumed to have negligible influence in the frequency region around the IIM. For the calculation of the minimum point two assumptions were made; firstly only one of the two sub –

circuits influences the signal in the frequency area around the minimum and secondly the minimum is not close to the maximum.

The analysis of the spectrum in terms of the new circuit can be viewed in Figure 6-19 where the dielectric signal is broken into the three sub – circuits of Figure 4-18. The relationships of Table 4-IV were used in order to determine the elements of the new circuit from the elements of the standard circuit. We can see that circuit A is the dominant circuit and circuit B becomes influential only at frequencies above 10 kHz.

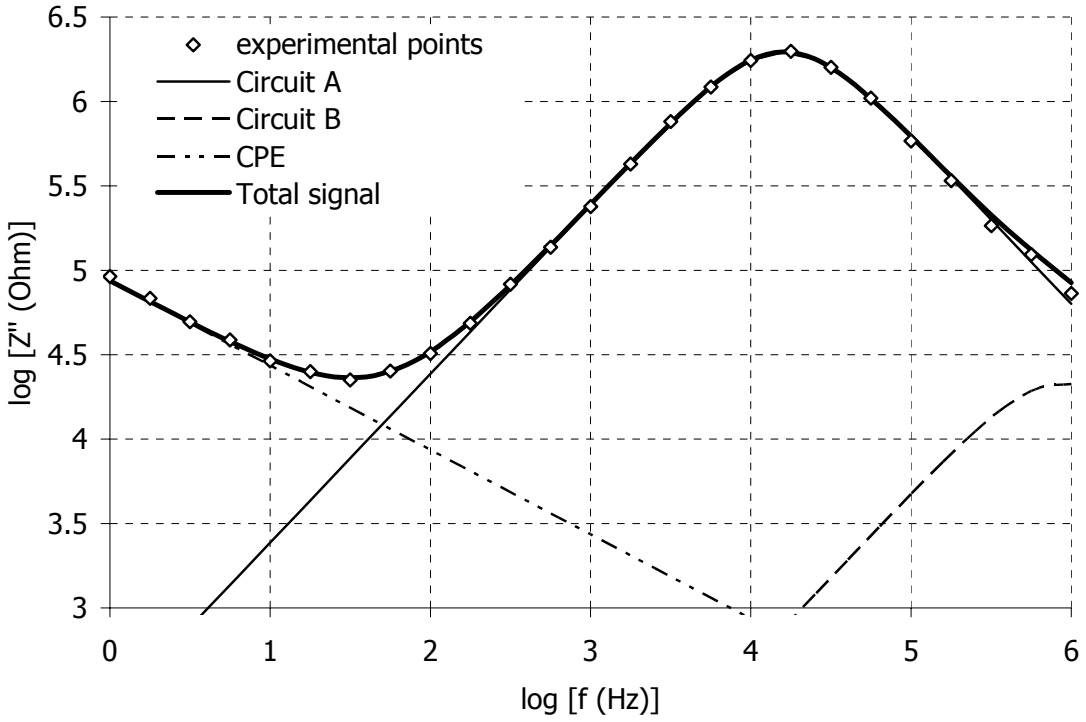

Figure 6-19 *Analysis of the imaginary impedance spectrum in terms of the circuit of Figure 4-18. Experimental points are from the cure of RTM6 at 0.6°C/min.*

From the above graph we can also comment on the assumptions made for the calculation of the optima. Electrode polarisation, which is described by the CPE, becomes unimportant at frequencies higher than 1 kHz and thus does not affect the maximum point. On the other hand, the influence of Circuit B can be neglected at frequencies below 100 kHz. The frequencies of the two optima points are separated by more than two orders of magnitude so that only the low frequency side of Circuit A can be considered for the calculation of the minimum point.

In Figure 6-19 we can also see that Circuit A dominates the signal around the maximum. This happens when migrating charges dominate the dielectric response of

the curing material, something common in commercial systems (104, 124). In terms of the equivalent circuit model, the migrating charges domination means that $R_{ion} >> R_{dip}$. From Table 4-IV we can see that this inequality leads to a k value very close to unity:

$$\lim_{\frac{R_{ion}}{R_{dip}} \to \infty} k = 1 \tag{6.1}$$

Using the rest of the relationships of Table 4-IV we find the following values for the elements of the new circuit:

$$R_A \xrightarrow{k \to 1} R_{ion} \quad C_A \xrightarrow{k \to 1} C_{ind} + C_{dip} \qquad R_B \xrightarrow{k \to 1} 0 \quad C_B \xrightarrow{k \to 1} \infty \tag{6.2}$$

The physical meaning of the above relationships is that when migrating charges dominate the dielectric signal, a simple parallel R_A-C_A circuit can be used in order to describe the resin response (in conjunction to the CPE). Mijovic and Yee (103) have reached the same conclusion by qualitative examination of the experimental data.

The modelling of the IIM is shown in Figure 6-20. We can see that the frequency and the imaginary impedance at the maximum are accurately modelled throughout the cure.

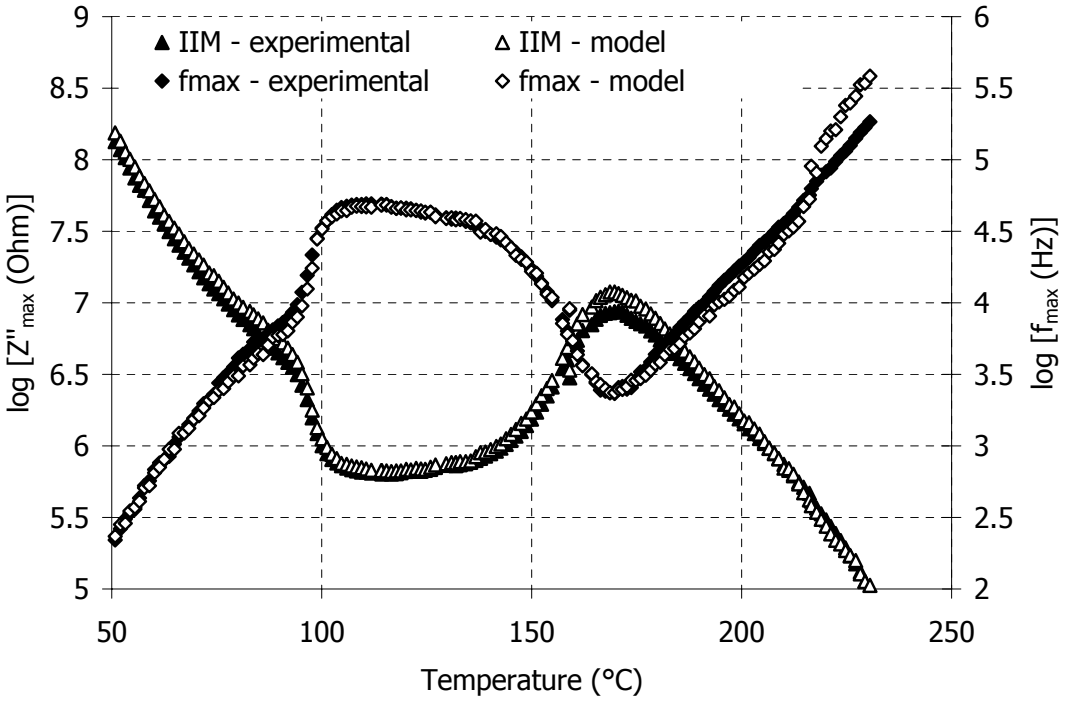

Figure 6-20 *Modelling of the IIM for the cure of RTM6 at 0.6°C/min*

The modelling of the imaginary impedance minimum is shown in Figure 6-21. The agreement with the experimental points is good. Furthermore, the equivalent circuit models the imaginary impedance minimum in areas outside the experimental frequency window. These areas are at the beginning of cure, from 50°C to 65°C, and from 155°C to 195°C. At 175°C, where the shift of the Z" spectrum changes direction, a minimum point f_{min} is attained. This indicates that the effect of electrode polarisation can be modelled even when its influence on the dielectric signal is not visible in the frequency range of the measurement.

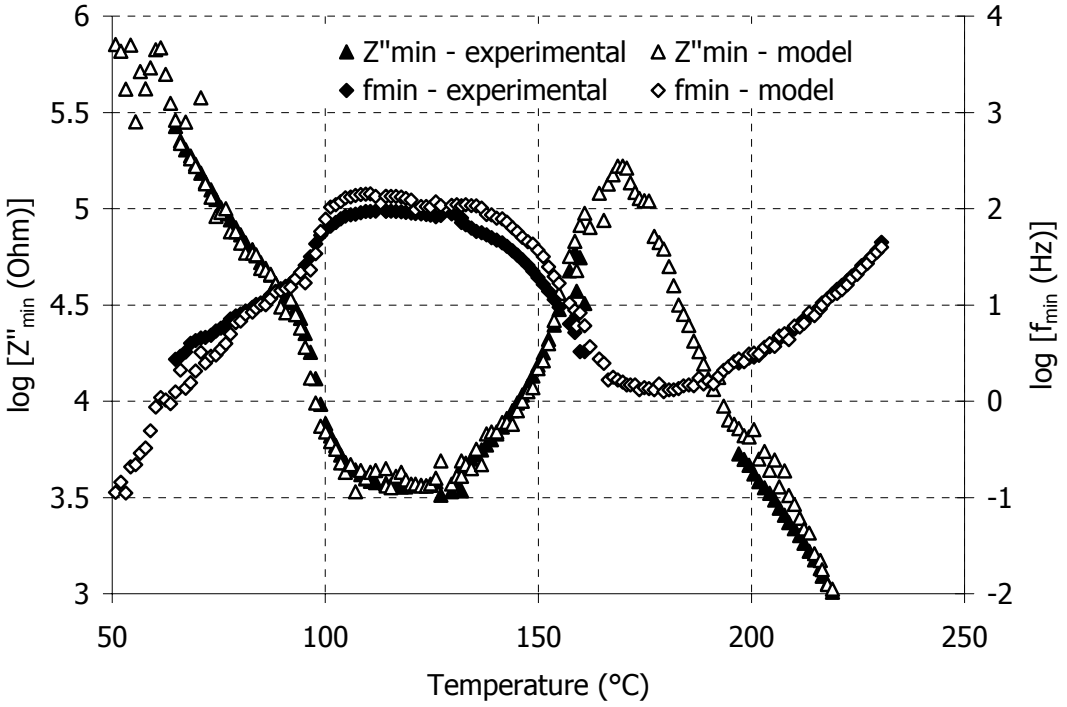

Figure 6-21 *Modelling of the minimum point in the Z'' spectrum (shown in Figure 5-30) for the cure of RTM6 at 0.6°C/min*

This successful modelling of the optima in the imaginary impedance spectrum is evidence that the equivalent circuit model describes the impedance spectrum throughout the cure.

6.3.3 Frequency mapping

When dielectric cure monitoring is applied in – situ to the processing of thermosets it is usually the case that specific information is sought rather than a complete model of the curing material. Examples of such processing information are the point of minimum viscosity of the resin, the vitrification point or the end of the curing reaction.

Monitoring at specific frequencies – instead of recording frequency sweeps – usually suffices to answer such questions. On the other hand, a complete model of the dielectric signal is required in order to select the appropriate monitoring frequency.
In Figure 6-22 a frequency mapping for the experiment of RTM6 at 0.6°C/min is presented. Three regions are identified, corresponding to the three phenomena that together comprise the dielectric signal. At low frequencies, electrode polarisation dominates the signal. At intermediate frequencies, the effect of migrating charges overshadows any other contribution. At very high frequencies, the contribution of relaxing dipoles begins to influence the signal, although their effect is never dominant.

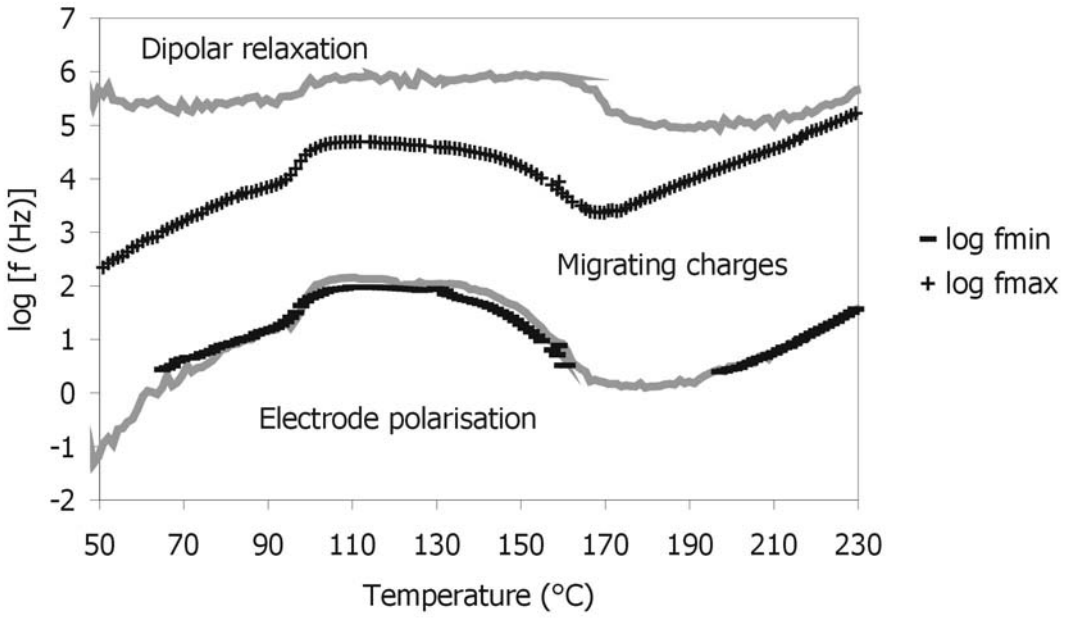

Figure 6-22 *Frequency mapping of RTM6 cure at 0.6°C/min.*

Two boundaries (thick grey lines) define the three regions in Figure 6-22. The imaginary impedance minimum point delineates the electrode polarisation region from the charge migration region. The maximum of Circuit B (see Figure 6-19) is used to designate the region where dipoles influence the signal since after that point the values of Circuit A and Circuit B have the minimum difference. However, it has to be noted that Circuit B cannot be attributed solely to dipolar movements. It is the relative positions between Circuit A and Circuit B in the spectrum that specified whether the effect of dipoles is observable or not. For the particular resin system, the influence of dipoles can only be seen at frequencies above 100 kHz. Therefore the vitrification of RTM6 can be monitored at frequencies over 100 kHz.

The frequency region where migrating charges dominate covers most of the experimental frequency window. This means that the effect of the migrating charges can be monitored not only by following the changes in the IIM, but also by monitoring at a specific frequency inside that region. In Figure 6-23 we can see the one – to – one correlation between the IIM and the imaginary impedance at frequencies that lie within the migrating charges domination region.

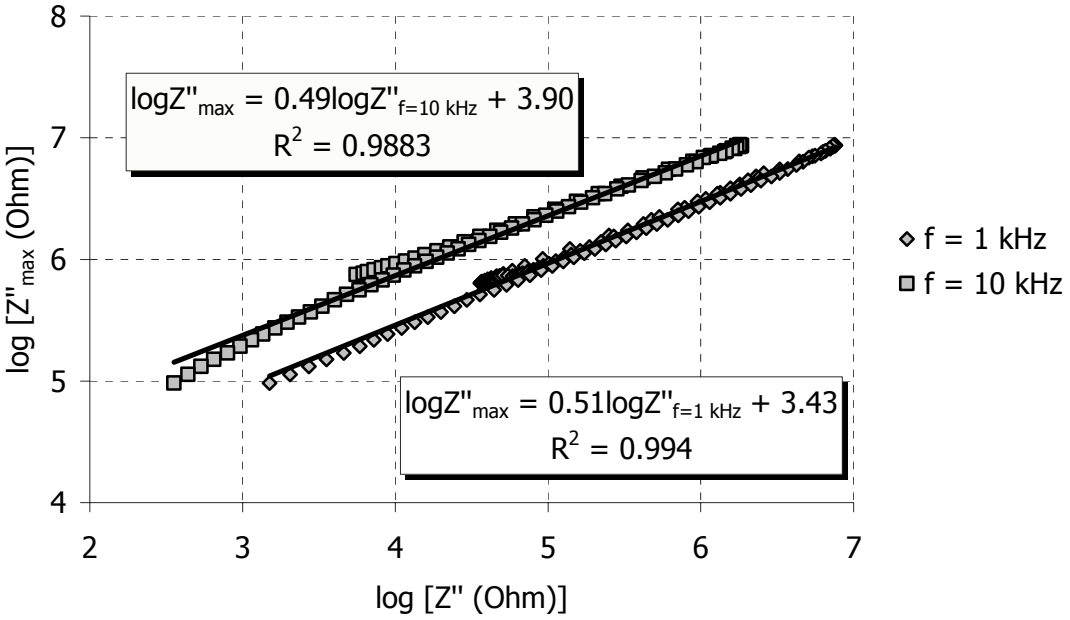

Figure 6-23 *Correlation between the IIM and the imaginary impedance at frequencies within the region where migrating charges dominate.*

Using the signal at a particular frequency instead of the IIM is advantageous. In order to follow the changes in the IIM signal, the frequency window of the measurement either has to cover a large number of frequencies or be programmed to follow the shift of the IIM, which is not possible with the current acquisition hardware/software. On the other hand, single frequency measurements are more straightforward to interpret when a frequency mapping like the one shown in Figure 6-22 is available and can be recorded very quickly, which is important in fast reacting materials.

The frequency mapping of RTM6 is utilised in TMDA measurements (Chapter 7) where, due to the nature of the experimental technique, only single frequency measurements can be made. The chosen frequency (1 kHz) was found to lie always in the migrating charges region.

6.4 Material state information

The polymerisation reaction has been linked with the migrating charges movements (103, 109). The concentration and the mobility of these charges determine the conductivity levels in the curing material. Although there are cases where charges are produced by the reaction (173), the conductivity usually decreases as reaction progresses in thermosetting materials.

The polymerisation reaction can be monitored through R_{ion} or the IIM since the dielectric response of RTM6 is dominated by the migrating charges. The dependence of the IIM on the reaction conversion is shown in Figure 6-24 for the isothermal cure of RTM6.

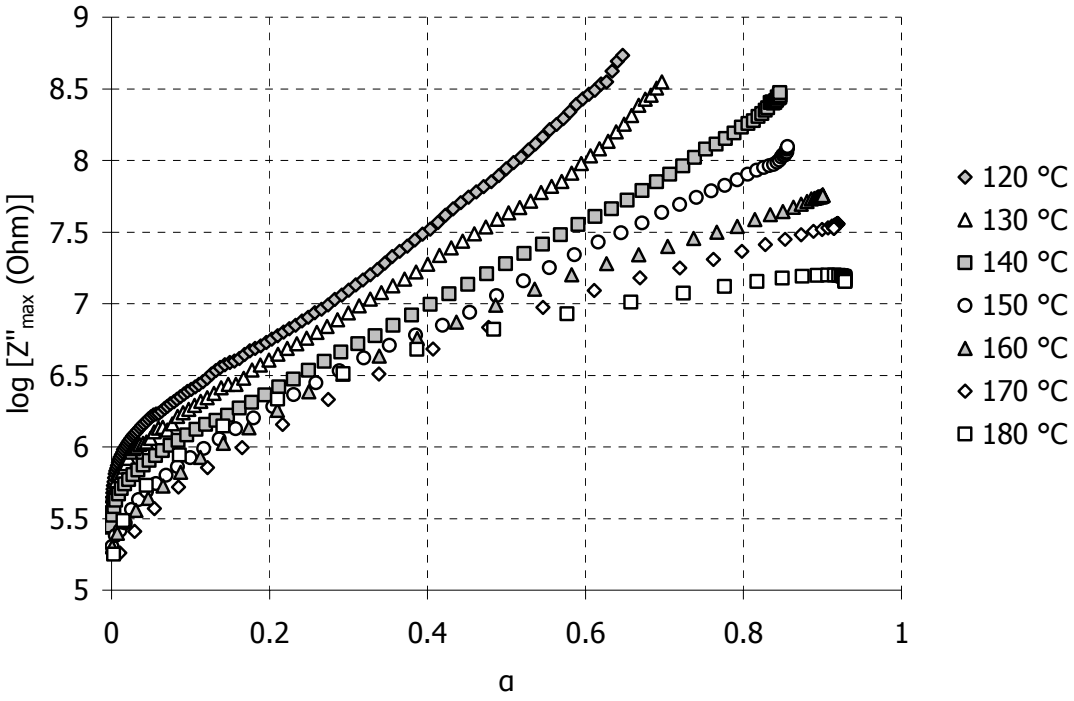

Figure 6-24 *Imaginary Impedance maximum sensitivity to reaction for the isothermal cure of RTM6*

Imaginary Impedance maximum has a log linear dependence on conversion, except in the early stages of the reaction ($\alpha < 0.1$) where the IIM increases at a higher rate. This is mainly because in the isothermal experiments the cell was heated up to the cure temperature before the resin was inserted. The thermal shock caused an abrupt temperature increase in the resin which led to a quick advancement of the reaction in

the early stages. Results from linear regression for the rest of the cure are given in Table 6-II.

Table 6-II: *Regression results for the log – linear dependence of IIM and conversion*

Cure Temperature	Slope [log (Ohm)]	Intercept [log (Ohm)]	R^2
120 °C	4.12	5.92	0.9942
130 °C	3.51	5.89	0.9975
140 °C	3.15	5.73	0.9979
150 °C	2.73	5.72	0.9990
160 °C	2.15	5.84	0.9897
170 °C	1.92	5.80	0.9857
180 °C	1.12	6.17	0.9440

We can see that the regression coefficient R^2 is close to unity for all experiments except for the one at 180°C. In this experiment the quick advancement of the curing reaction, which is observed in the rest of the experiments at conversions below 10%, continues for up to about 40% conversion. Therefore the experiment at 180°C will not be considered in the rest of the discussion.

The intercept is relatively constant in all experiments (5.82 ± 0.10). This does not mean that the reaction starts at a specific IIM value, since in the early cure stages the log – linear relationship between IIM and conversion does not hold. It is an indication though that the IIM value at the beginning the polymerisation reaction does not depend strongly on temperature. This is also observed in the non – isothermal runs, which are presented below.

The slope has a linear dependence with the curing temperature:

$$slope = 9.315 - 0.044T_{cure} \qquad R^2 = 0.989 \tag{6.3}$$

The above relationship can be incorporated in a model that relates the IIM with the conversion and the curing temperature:

$$\log Z''_{\max} = \left(9.315 - 0.044T_{cure}\right)\alpha + 5.82 \tag{6.4}$$

The above equation provides a starting point in the investigation of the relationship between the dielectric signal, the curing temperature and the reaction advancement. Although eq. (6.4) results from the analysis of the isothermal experiments, it will be

shown that such a relationship can also explain the trends observed during non – isothermal cure.

The IIM dependence on conversion for the non – isothermal experiments is shown in Figure 6-25. The vertical drop of IIM values at the beginning (*α = 0%*) and after the end of the polymerisation reaction is the result of the temperature changes. In all the experiments, the reaction starts at an IIM value similar (5.83 ± 0.33) to the intercept reported in Table 6-II, except for the experiment at 0.2°C/min where the reaction starts at a higher IIM value (*log Z″$_{max}$ = 6.12*).

The interplay between the increasing temperature and the reaction advancement is evident by the changes in the IIM. At the beginning, IIM increases in a log – linear fashion, just like in the isothermal experiments. At later stages, the changes in the IIM increase become smaller and towards the end of the reaction (*α > 85%*) the effect of temperature dominates and IIM values drop rapidly.

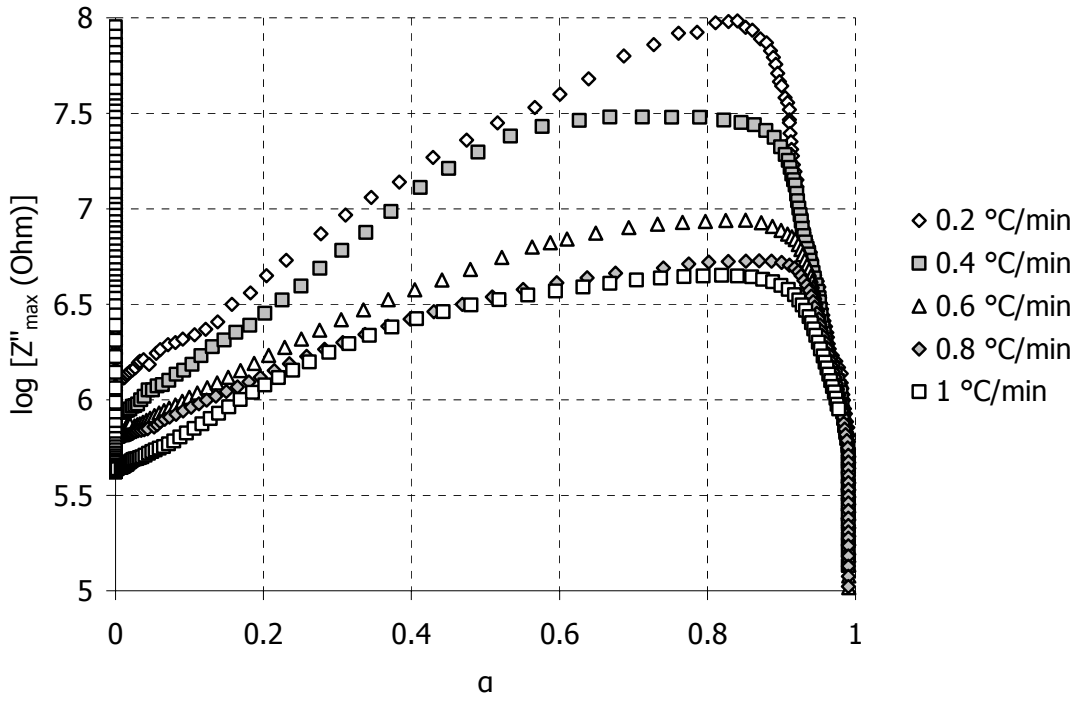

Figure 6-25 *Imaginary Impedance maximum sensitivity to reaction for the non - isothermal cure of RTM6*

An investigation on the mutual effects of temperature and reaction advancement on the IIM can be carried out if we consider the IIM to be a complex function of temperature and conversion:

$$\log Z''_{\max} = f(a,T) \tag{6.5}$$

Following the analysis steps of Parthun and Johari (101) we write the differential of the above equation:

$$d\log Z''_{\max} = \frac{\partial f(a,\mathrm{T})}{\partial a}da + \frac{\partial f(a,T)}{\partial T}dT \tag{6.6}$$

We assume that *f(a,T)* has the form of eq. (6.4):

$$f(a,T) = (\kappa_1 + \kappa_2 T)a + \kappa_3 \tag{6.7}$$

Then, the partial derivatives in will be:

$$\frac{\partial f(a,T)}{\partial a} = \kappa_1 + \kappa_2 T \tag{6.8}$$

$$\frac{\partial f(a,T)}{\partial T} = \kappa_2 a \tag{6.9}$$

Substituting the partial derivatives expression in eq. (6.6) gives:

$$d\log Z''_{\max} = (\kappa_1 + \kappa_2 T)da + \kappa_2 a dT \tag{6.10}$$

Taking the first time derivative of eq. (6.10) yields:

$$\frac{d\log Z''_{\max}}{dt} = (\kappa_1 + \kappa_2 T)\frac{da}{dt} + \kappa_2 a\frac{dT}{dt} \tag{6.11}$$

For the case of an isothermal cure, the second term in eq. (6.11) becomes zero and the time derivative of $logZ''_{max}$ is proportional to the reaction rate:

$$\frac{d\log Z''_{\max}}{dt} = \underbrace{(\kappa_1 + \kappa_2 T_{cure})}_{constant}\frac{da}{dt} + \cancel{\kappa_2 a\frac{dT}{dt}} = \kappa\frac{da}{dt} \tag{6.12}$$

The analogy between the time derivative of the IIM and the reaction rate has already been reported by Skordos and Partridge (124). The time derivative of the IIM for the isothermal experiments is shown in Figure 6-26 alongside the reaction rate curves. The experimental data support the linear correlation between the two quantities, as predicted by eq. (6.12).

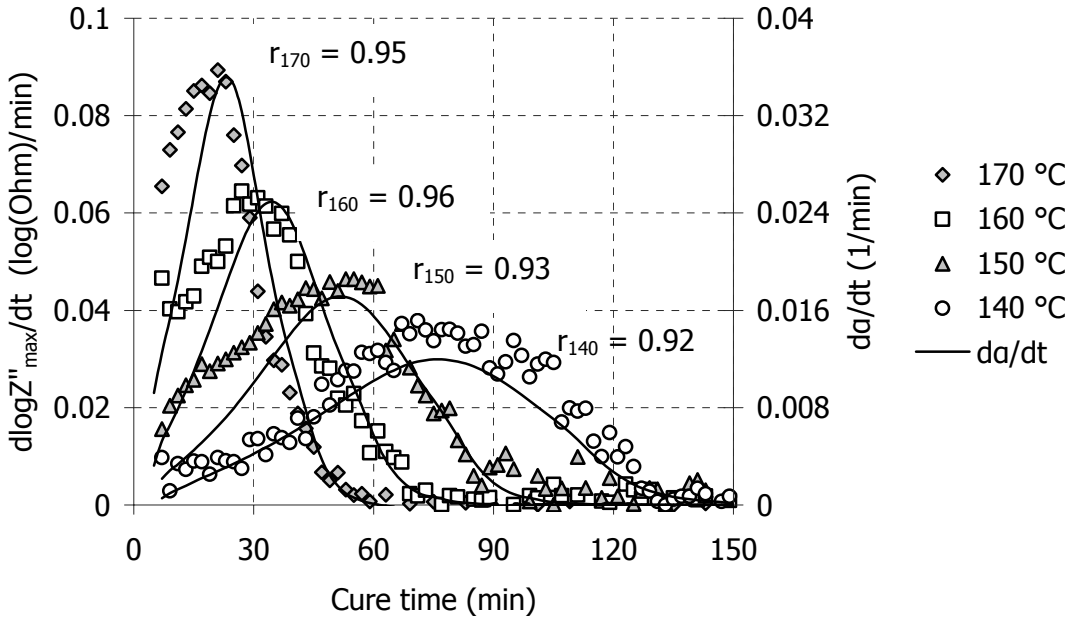

Figure 6-26 *Time derivate of logZ"$_{max}$ for the isothermal cure of RTM6. The black lines are the reaction rates at the dwell temperatures. The correlation coefficients for each set of data are also shown.*

When the cure is performed at a constant heating rate, *r*, then eq. (6.11) becomes:

$$\frac{d\log Z''_{\max}}{dt} = \underbrace{\left(\kappa_1 + \kappa_2 rt\right)\frac{d\alpha}{dt}}_{term\ 1} + \underbrace{\kappa_2 \alpha r}_{term\ 2} \tag{6.13}$$

The effect of the two terms of the right hand side in the above equation is shown in Figure 6-27 for the experiment at 0.6°C/min. The values obtained from the isothermal runs (eq. (6.3)) were used for κ_1 and κ_2.

We can see that "term 1" follows the changes of the reaction rate, although the presence of time in the parenthesis in eq. (6.13) means that the dependence is not proportional, as in the isothermal case. However, as it can be seen in Figure 6-28, the difference is not significant because of the bell shape of the reaction rate curve. The small values of *dα/dt* at the beginning and end of cure smoothes the differences induced by the term in parenthesis. After 200°C though the second small peak in the reaction rate curve, which is owed to devitrification (§ 5.2.1) is smeared by the low value of the term in the parenthesis. What remains is a faint shoulder, barely observable in Figure 6-28.

The shape of "term 2" is mainly determined by the shape of the conversion evolution. This term acts as a baseline for the total signal.

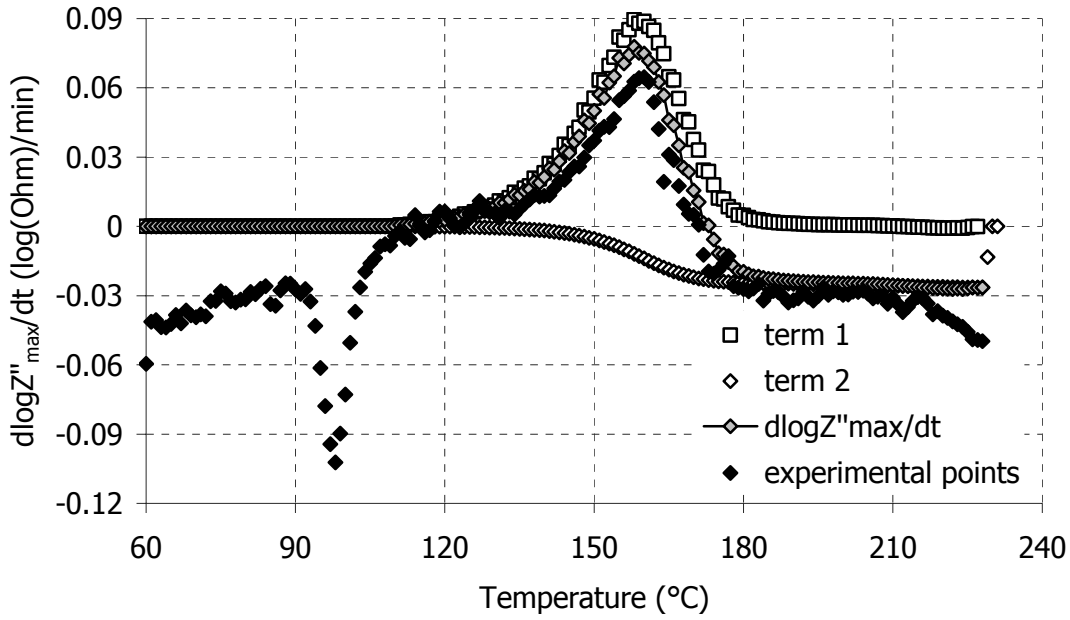

Figure 6-27 *Analysis of eq. (6.13) and comparison with experimental data from the cure of RTM6 at 0.6°C/min*

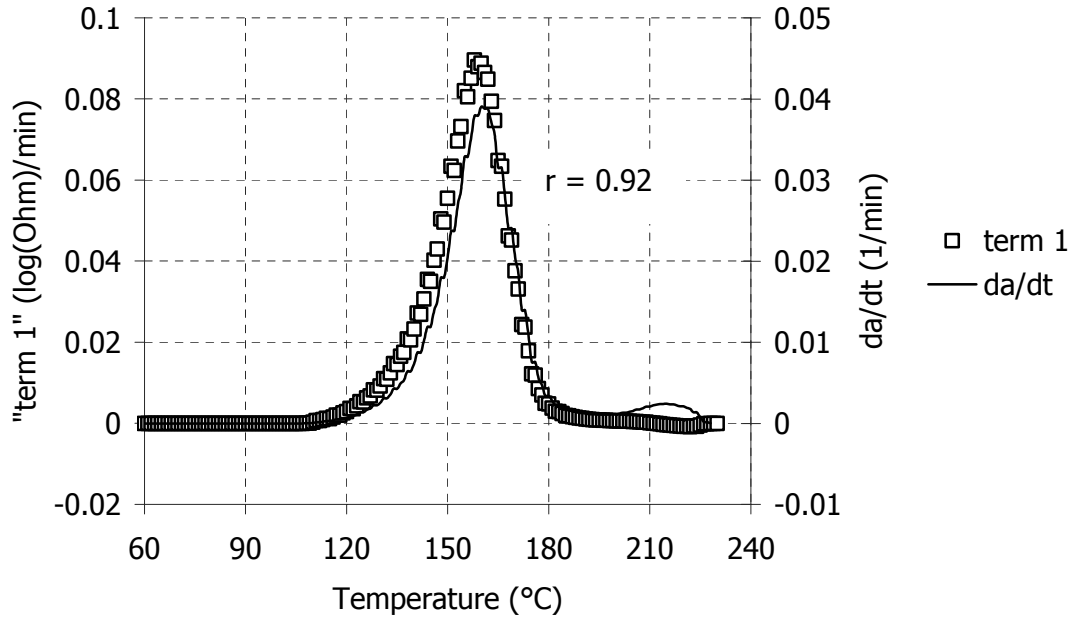

Figure 6-28 *Comparison of the reaction rate (obtained from calorimetric experiment) and "term 1" of eq. (6.13) for the cure of RTM6 at 0.6 °C/min. The correlation coefficient between the two data sets is also given.*

As we can see in Figure 6-27 the experimental data agree with the model of eq. (6.13) despite the fact that the parameters κ_1 and κ_2 are calculated from the isothermal experiments. This agreement suggests that eq. (6.13) describes the temperature and conversion dependence of the IIM in isothermal and non – isothermal cases.

Figure 6-29 illustrates that the IIM time derivative shows the same trend in all non – isothermal experiments. The negative peak around 100°C, also observed in Figure 6-27, corresponds to the physical processes discussed in § 6.2.2 (possible dissolution of low molecular weight chemical species in the resin).

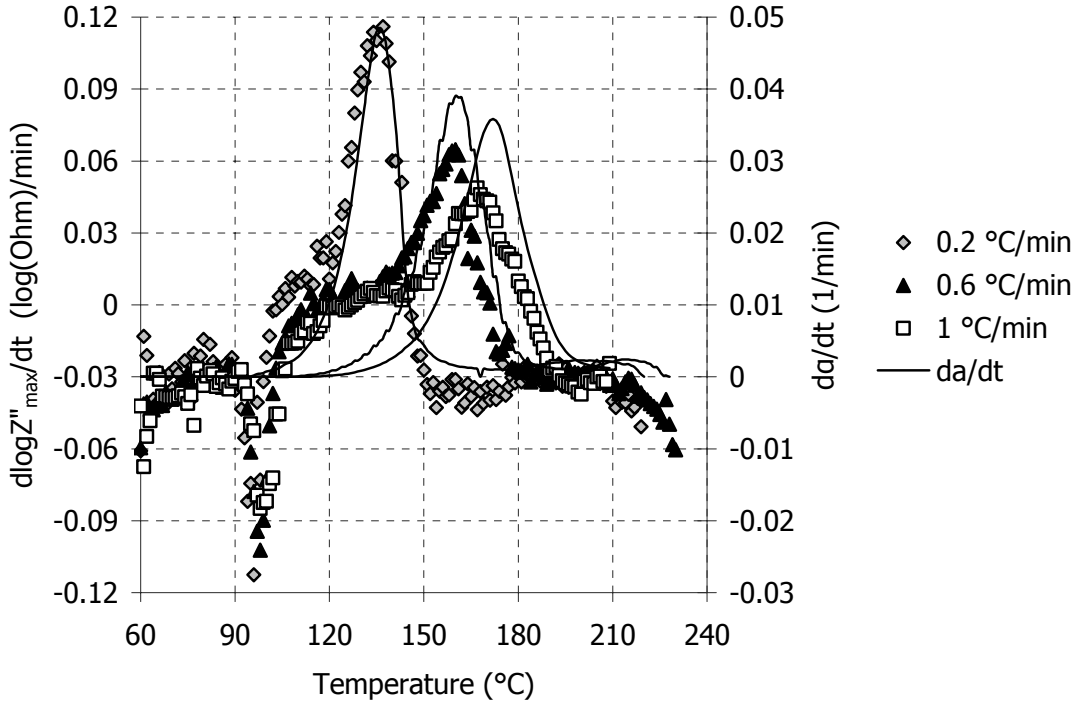

Figure 6-29 *Time derivative of the IIM for the non isothermal cure of RTM6. The reaction rate curves are also drawn for comparison with the dielectric data.*

The use of eqs. (6.12) and (6.13) enables the prediction of the reaction rate to be made and subsequently conversion established from dielectric data. The analysis is straightforward in the isothermal case where the reaction rate is proportional to the time derivative of the IIM. In the non – isothermal case, the dielectric signal sums the effect of two terms, one affected by the reaction rate and the other by conversion as described by eq. (6.13). The separation of these two terms without the need of kinetic data will provide a baseline ("term 2") from which the signal related to the reaction rate ("term 1") could be determined. This will be the topic of Chapter 7 where a new

method, based on temperature modulations, is introduced. Then, in Chapter 8 the validity of the model (eq. (6.7)) relating the dielectric signal (IIM) to the temperature and reaction advancement in other thermosetting systems is discussed.

7 Temperature Modulated Dielectric Analysis

7.1 Scope and objectives

An early development of a new experimental technique is outlined in this chapter. Temperature Modulated Dielectric Analysis (TMDA) uses temperature modulated cure profiles in order to obtain information about the reaction advancement directly from the dielectric signal. From the mathematical analysis it is shown that the amplitude of the modulated component of the dielectric signal is related to the reaction conversion through a simple linear relationship. An appropriate experimental cell was designed, built and tested for the measurements. The technique can be applied to isothermal and non – isothermal experiments. The main objectives of the work presented here were to prove the feasibility of temperature modulated dielectric measurements and to validate the results obtained.

7.2 Temperature and reaction effects on the dielectric signal

The mutual effects of the reaction and the temperature on the dielectric signal have already been discussed when the IIM curves were analysed in § 5.4.2 and § 6.3.2. The same remarks can be made for dielectric signals at frequencies where migrating charges dominate, as shown in § 6.3.3.

The imaginary impedance at 1 kHz during the dynamic cure of RTM6 is shown in Figure 5-37. It is reproduced in Figure 7-1. As in the IIM curves, data superimpose at the beginning and the end of cure, when the material is unreacted or fully cured respectively. In these areas, there is a log – linear dependence between the dielectric signal and temperature. In order to incorporate these dependencies, the model for the signal dependence on temperature and reaction described by eq. (6.7) is generalised:

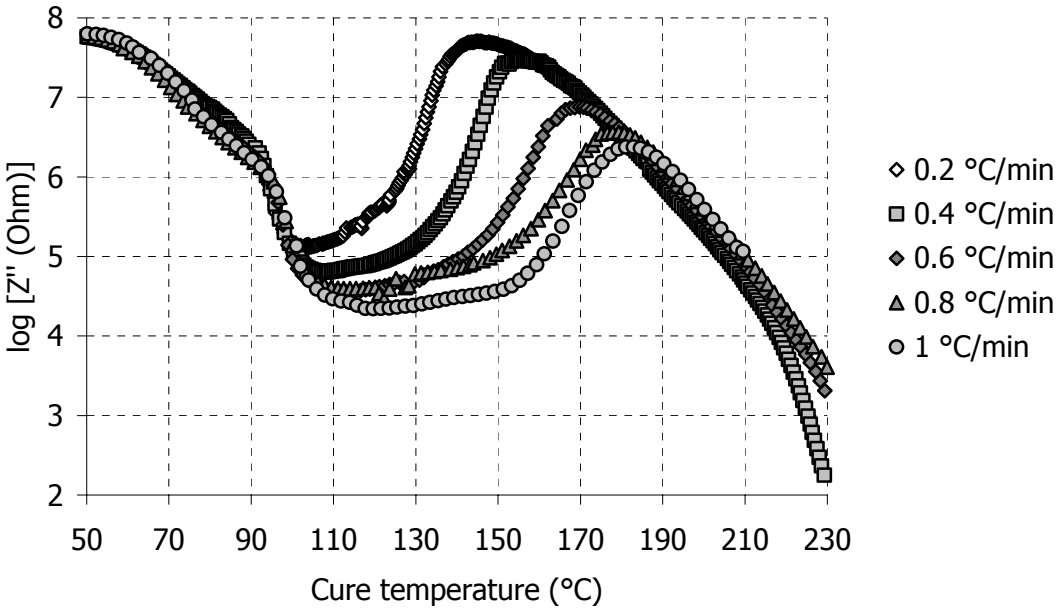

Figure 7-1 *Imaginary impedance at 1 kHz for the dynamic cure of RTM6.*

$$\log Z'' = f(\alpha, T) = (\kappa_1' + \kappa_2' T)\alpha + (\kappa_3' + \kappa_4'\alpha)(T - \kappa_5') \tag{7.1}$$

The coefficients κ_i', $i=1,2...5$ are similar to κ_1 and κ_2 used in § 6.4. When reaction has not commenced eq. (7.1) becomes:

$$\log Z''_{\alpha=0} = f(0, T) = \kappa_3' T - \kappa_3'\kappa_5' \tag{7.2}$$

When the material is fully cured, eq. (7.1) becomes:

$$\begin{aligned} \log Z''_{\alpha=1} = f(1, T) = (\kappa_1' + \kappa_2' T) + (\kappa_3' + \kappa_4')(T - \kappa_5') \Rightarrow \\ f(1, T) = (\kappa_2' + \kappa_3' + \kappa_4')T + \kappa_1' - \kappa_5'(\kappa_3' + \kappa_4') \end{aligned} \tag{7.3}$$

In the case of isothermal cure, only the conversion affects the dielectric signal:

$$\log Z'' = f(\alpha, T_c) = \underbrace{(\kappa_1' - \kappa_4'\kappa_5' + (\kappa_2' + \kappa_4')T_c)}_{\text{slope}}\alpha + \underbrace{\kappa_3'(T_c - \kappa_5')}_{\text{intercept}} \tag{7.4}$$

where T_c is the dwell temperature. Eq. (7.4) predicts a log – linear relationship between the dielectric signal and conversion, just like eq. (6.4) in § 6.4 (Figure 6-24). The coefficients κ'_i can be determined from the experimental data using eqs. (7.2) – (7.3). The calculation of the slope and intercept in eqs. (7.2) and (7.3) is pictured in Figure 7-2 for the cure at 1°C/min. The results from all the dynamic experiments are given in Table 7-I.

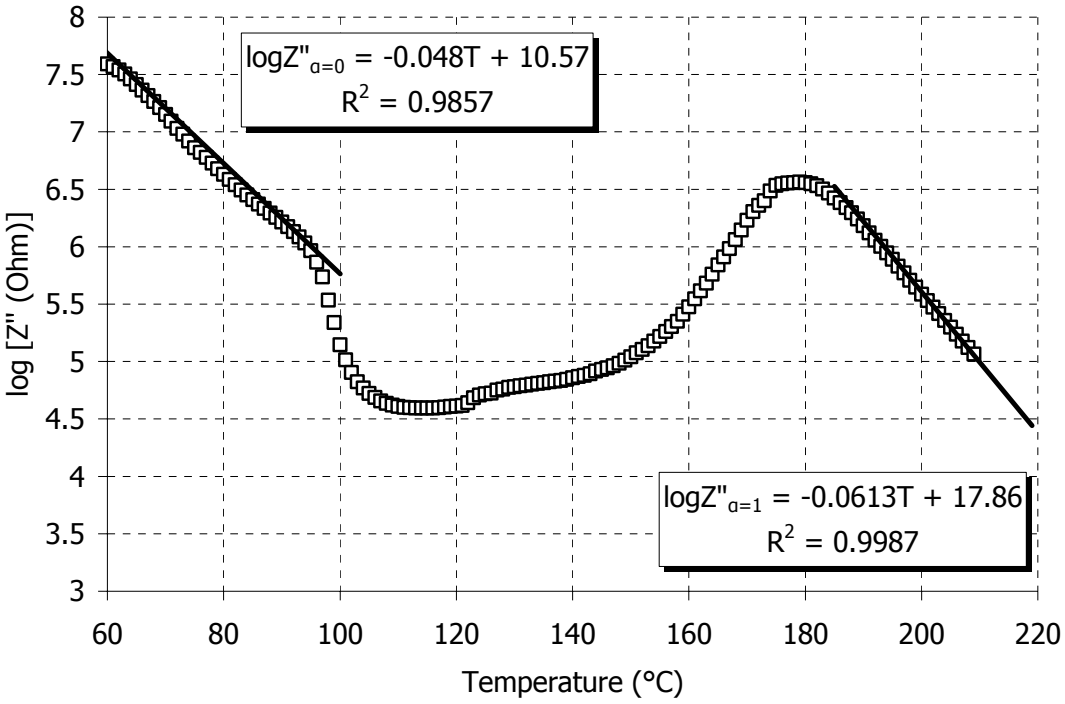

Figure 7-2 *Calculation of the temperature dependence of the dielectric signal at 1 kHz before and after the polymerisation reaction for the dynamic cure at 1°C/min*

Table 7-I: *Regression analysis results for eq. (7.2) and (7.3)*

Heating rate	logZ"α=0			logZ"α=1		
	slope	intercept	R^2	slope	intercept	R^2
0.2 °C/min	- 0.039	9.93	0.9836	- 0.066	18.5	0.9915
0.4 °C/min	- 0.039	9.96	0.9887	- 0.071	19.1	0.9945
0.6 °C/min	- 0.044	10.3	0.9847	- 0.060	17.4	0.9968
0.8 °C/min	- 0.047	10.4	0.9812	- 0.059	17.4	0.9985
1 °C/min	- 0.048	10.6	0.9857	- 0.061	17.9	0.9987
Average	*- 0.0434*	*10.24*		*- 0.0634*	*18.06*	

From the values of Table 7-I, the following values for the coefficients κ'_i are calculated:

$$\begin{aligned} \kappa'_3 &= \text{- 0.043 log(Ohm)/°C} \\ \kappa'_5 &= \text{ 236 °C} \\ \kappa'_2 + \kappa'_4 &= \text{- 0.020 log(Ohm)/°C} \\ \kappa'_1 - \kappa'_4\kappa'_5 &= \text{ 7.82 log(Ohm)} \end{aligned} \tag{7.5}$$

7.3 Theoretical aspects of TMDA

In this section the mathematical theory of TMDA is presented. The analysis is based on the general considerations and assumptions of the techniques that use temperature modulation, which is presented in Chapter 2.

7.3.1 Equations formulation

The mathematical analysis of TMDA starts by taking the time derivative of eq. (7.1) for the imaginary impedance at a particular frequency:

$$\frac{d\log Z''}{dt} = \left(\kappa'_1 - \kappa'_4\kappa'_5 + \left(\kappa'_2 + \kappa'_4\right)T\right)\frac{da}{dt} + \left(\kappa'_3 + \left(\kappa'_2 + \kappa'_4\right)a\right)\frac{dT}{dt} \tag{7.6}$$

The application of a modulated temperature profile, described by eq. (2.1), gives the following expressions for the temperature and its time derivative:

$$T = T_0 + rt + A_T \sin\left(\omega_T t\right) \tag{7.7}$$

$$\frac{dT}{dt} = r + A_T\omega_T \cos\left(\omega_T t\right) \tag{7.8}$$

Substitution of the last two equations into eq. (7.6) yields:

$$\frac{d\log Z''}{dt} = \overline{\frac{d\log Z''}{dt}} + \widetilde{\frac{d\log Z''}{dt}} \tag{7.9}$$

where

$$\overline{\frac{d\log Z''}{dt}} = \left(\kappa'_1 - \kappa'_4\kappa'_5 + \left(\kappa'_2 + \kappa'_4\right)\left(T_0 + rt\right)\right)\frac{da}{dt} + \left(\kappa'_3 + \left(\kappa'_2 + \kappa'_4\right)a\right)r \tag{7.10}$$

and

$$\widetilde{\frac{d\log Z''}{dt}} = A_{Z''} \sin\left(\omega_T t + \delta_{Z''}\right) \tag{7.11}$$

The amplitude $A_{Z''}$ and the phase $\delta_{Z''}$ are given by the following relationships*:

$$A_{Z''} = A_T \sqrt{\underbrace{\left(\kappa_2' + \kappa_4'\right)^2 \left(\frac{d\alpha}{dt}\right)^2}_{(term1)^2} + \underbrace{\left(\kappa_3' + \left(\kappa_2' + \kappa_4'\right)\alpha\right)^2 \omega_T^2}_{(term2)^2}} \tag{7.12}$$

$$\tan\delta_{Z''} = \frac{\left(\kappa_3' + \left(\kappa_2' + \kappa_4'\right)\alpha\right)\omega_T}{\left(\kappa_2' + \kappa_4'\right)\frac{d\alpha}{dt}} = \frac{term2}{term1} \tag{7.13}$$

The absolute values of the two terms denoted in eqs. (7.12) and (7.13) are plotted in Figure 7-3. The coefficient values were those of eq. (7.5). The values of *term2* are about three orders of magnitude higher than the values of *term1*. This is owed to the relatively high value of ω_T (for a period of 1 min → $\omega_T = 2\pi$ *rad/min*) compared to the values of α and $d\alpha/dt$. Consequently, the relationship for the amplitude is simplified and the conversion can be calculated directly:

$$A_{Z''} = A_T\left(\kappa_3' + \left(\kappa_2' + \kappa_4'\right)\alpha\right)\omega_T \Leftrightarrow \alpha = \frac{1}{\kappa_2' + \kappa_4'}\left(\frac{A_{Z''}}{\omega_T A_T} - \kappa_3'\right) \tag{7.14}$$

Eq. (7.14) shows that the conversion is proportional to the amplitude of the modulated signal.

In the calculations involved for the construction of the curves in Figure 7-3 it was assumed that the modulation of temperature will not alter the curing reaction significantly. This is proved in Figure 7-4 where the conversion profiles for the cure of RTM6 at 1°C/min with and without temperature modulation are given. The two profiles superimpose. The percentage difference between the conversion values obtained is less than 10% throughout the cure and close to zero at the end of cure.

* the trigonometric identity $a\sin(x) + b\cos(x) = c\sin(x+\varphi) \Leftrightarrow \begin{cases} \tan\varphi = \dfrac{b}{a} \\ c^2 = a^2 + b^2 \end{cases}$ has been used for the calculations of the amplitude and the phase

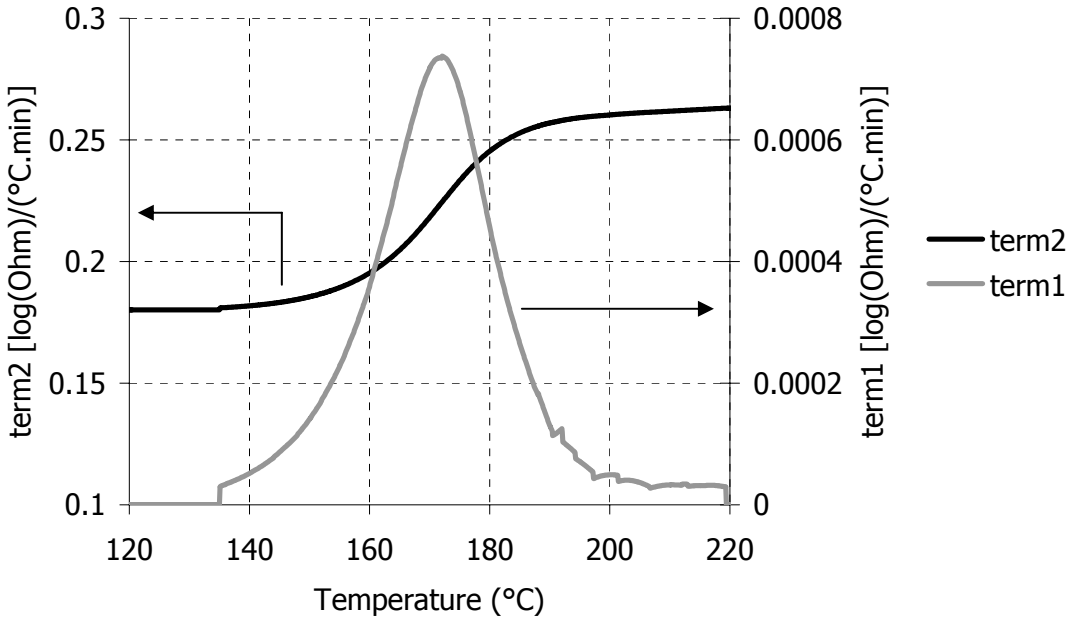

Figure 7-3 *Comparison between the absolute values of the two terms appearing in eqs. (7.12) and (7.13). For the construction of the graph A_T = 1°C, P = 1.5 min and r = 1°C/min.*

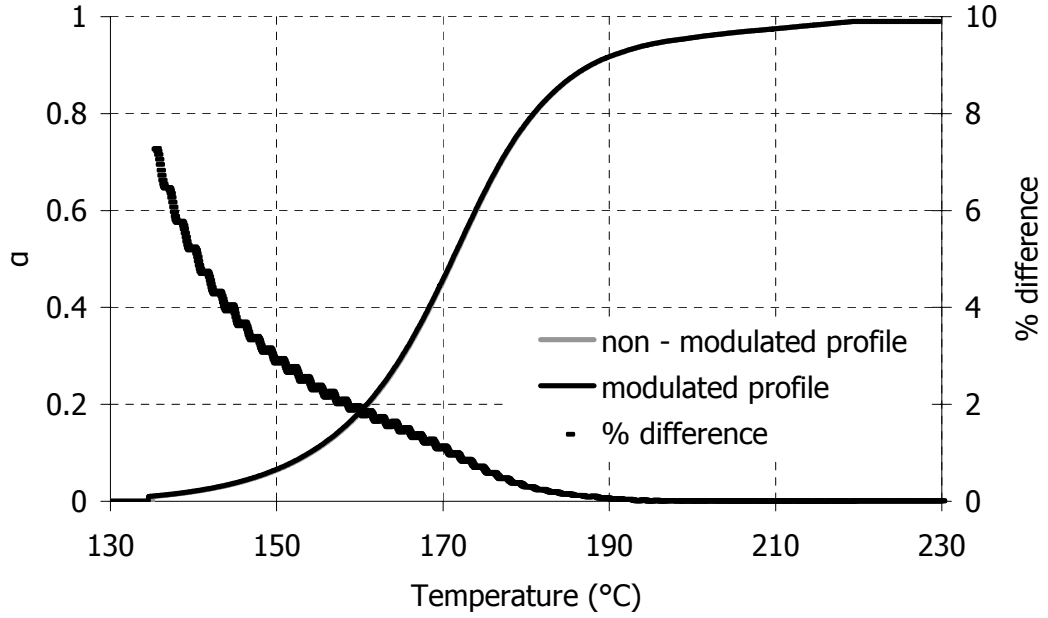

Figure 7-4 *Difference between the conversion profiles attained from modulated and non – modulated temperature profiles. The parameters used for the calculations are: r = 1°C/min, A_T = 1°C and P = 1.5 min.*

7.3.2 Linearity issues

The linearity of the TMDA signal can be investigated by using Lissajous plots, as is discussed in § 2.3.2. A Lissajous plot for the simulated TMDA signal used in the above paragraph (Figures 7-3 and 7-4) is presented in Figure 7-5. We can see that the ellipse height gradually decreases as the reaction progresses, following the changes in the amplitude $A_{Z''}$ which are shown in Figure 7-3. Note that in Figure 7-3 the absolute values of *term1* and *term2* are plotted; the real values are negative due to the negative values of the coefficients κ'_1, κ'_2 and κ'_3.
Lissajous plots of experimental TMDA data are presented in § 7.6.1.

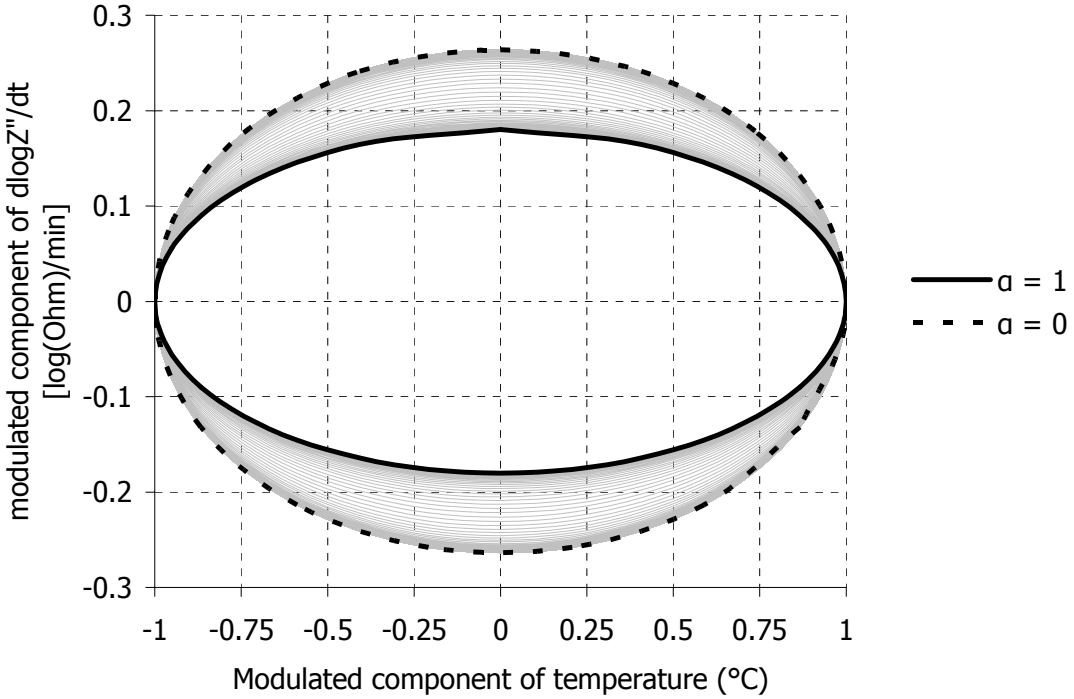

Figure 7-5 *Lissajous plot for the simulated TMDA signal. The two black lines denote the ellipse shape before the reaction onset (dotted line, α = 0) and after the reaction end (solid line, α = 1).*

7.3.3 Signal deconvolution

The TMDA signal can be treated the same way as the MDSC signal. The separation of the modulated from the non – modulated component is performed by means of signal averaging, as described in § 2.3.3. However, the TMDA signal is noisier than the MDSC signal as shown in Figure 7-6 where the Fourier transforms of two sets of data from the two experimental techniques are presented. The high values at the beginning of

the x - axis verify the existence of a non – modulated component in both sets of data. The single peak is evidence that the response to the temperature modulation is linear. The difference in the magnitude of the Fourier transform of the two sets of data means that the noise level in the TMDA measurement is higher compared to the MDSC measurement. The larger amount of resin used in the TMDA experiment (~2g instead to ~5mg used in MDSC) and the lower accuracy of the dielectric measurement compared to the calorimetric measurement are the main reasons for the poor quality of the TMDA data compared to the MDSC. On the other hand Figure 7-6 shows that the TMDA signal is exploitable since the peak at the modulation period is clear and rises well above the noise level.

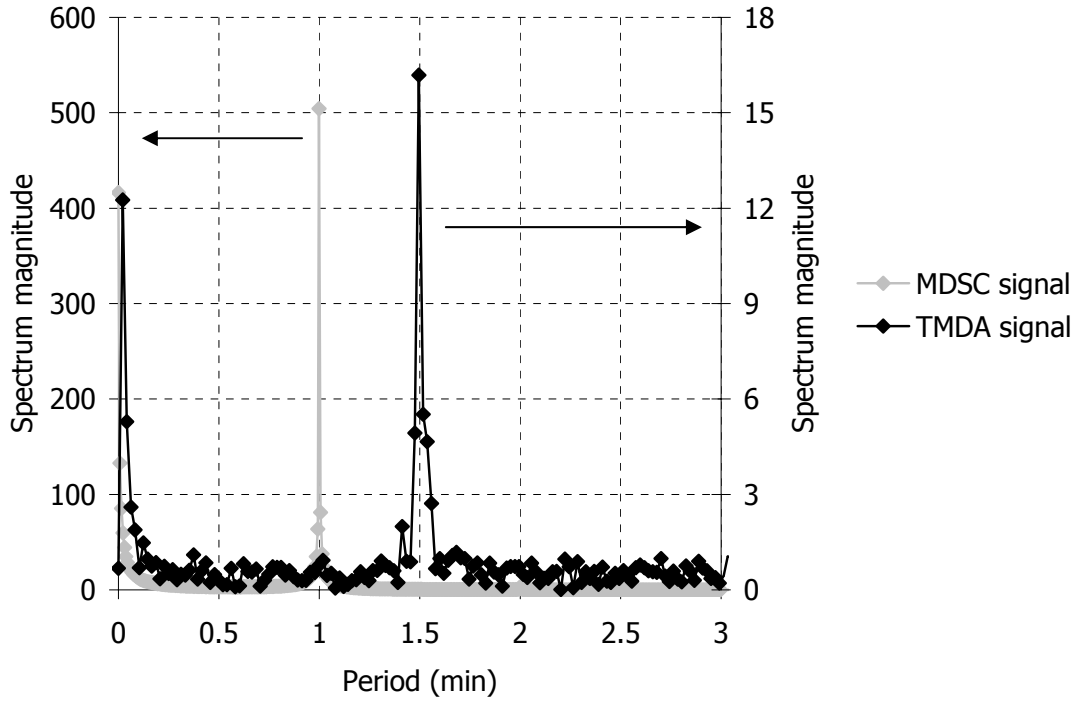

Figure 7-6 *Fourier transform of the MDSC and the TMDA signal. The MDSC data are from the cure of RTM6 at 0.6°C/min. The TMDA data are from the cure of RTM6 at 1°C/min. The frequency of the voltage excitation is 1 kHz.*

7.4 Construction and testing of new experimental cell

In order to impose steady temperature modulations in the curing material, a new experimental cell was designed and constructed. The main design objective was to achieve a quick thermal response to the imposed temperature profile. This objective led to the following guidelines for the manufacturing of the cell:

- Small amount of metal so that heat could be transferred to the resin quickly
- High surface to volume ratio for rapid cooling of the resin, which led to the use of fins

The building material of the cell was copper.

7.4.1 Design

The geometry of the experimental cell is given in Figure 7-7. Four series of eight fins enhanced the cooling of the main cylindrical block in the centre. The fins were placed on the top and bottom of the side, leaving a space of 7 mm in the middle. In this space a custom made heating element was wrapped around the main block. The heating wire was a Nickel – Chrome alloy*.

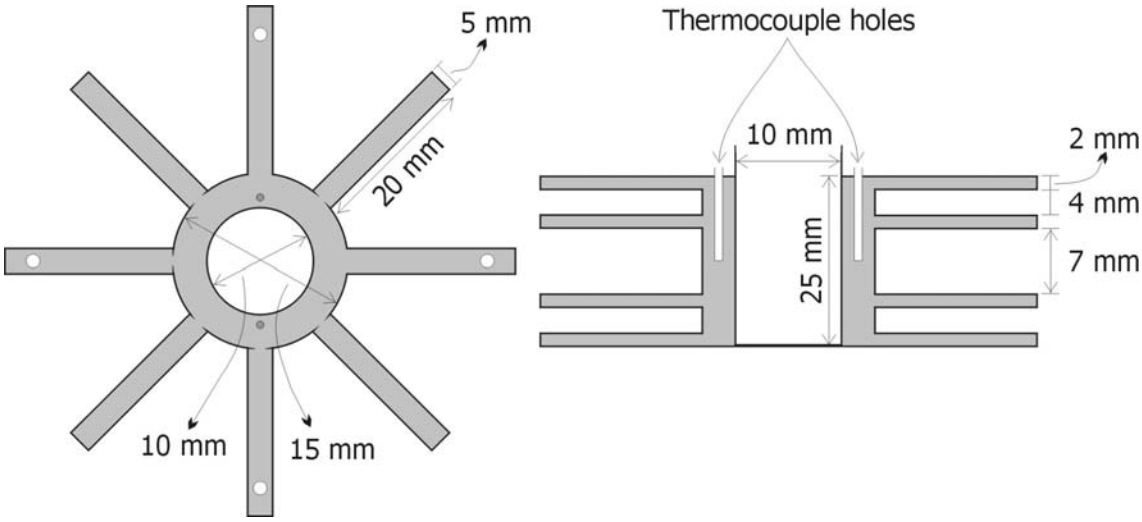

Figure 7-7 *Experimental cell for TMDA measurements*

Inside the 10 mm hole in the centre a disposable copper tube could be fitted. The tube contained the resin and it was 3 mm higher than the total height of the cell (25 mm) in order to prevent spillage from the resin expansion. Two small holes (1 mm in diameter) were drilled close to the central hole for temperature monitoring of the cell temperature.

7.4.2 Testing

The temperature profiles of the experimental cell and the curing resin are shown in Figure 7-8. The parameters of the temperature profiles are listed in Table 7-II. The

* purchased from Omega Engineering, Inc. (http://www.omega.co.uk)

parameters for the cell and the resin temperature profiles are determined by least squares regression. The phase is calculated with respect to the set temperature.

Table 7-II: *Parameters of the temperature profiles shown in Figure 7-8*

	T_0 (°C)	r (°C/min)	A_T (°C)	Period (min)	Phase
Set temperature	50	1	1.5	1.5	0
Cell temperature	49.7	0.996	1.38	1.50	- 48°
Resin temperature	49.5	0.997	0.85	1.50	- 83°

The cell temperature follows the set temperature with a delay of about 12 seconds*. The delay in the resin temperature profile is a constant 20 seconds. This value is lower than the modulation period (90 seconds) which means that the temperature profile in the resin cannot be distorted by the imposed temperature due to slow response.

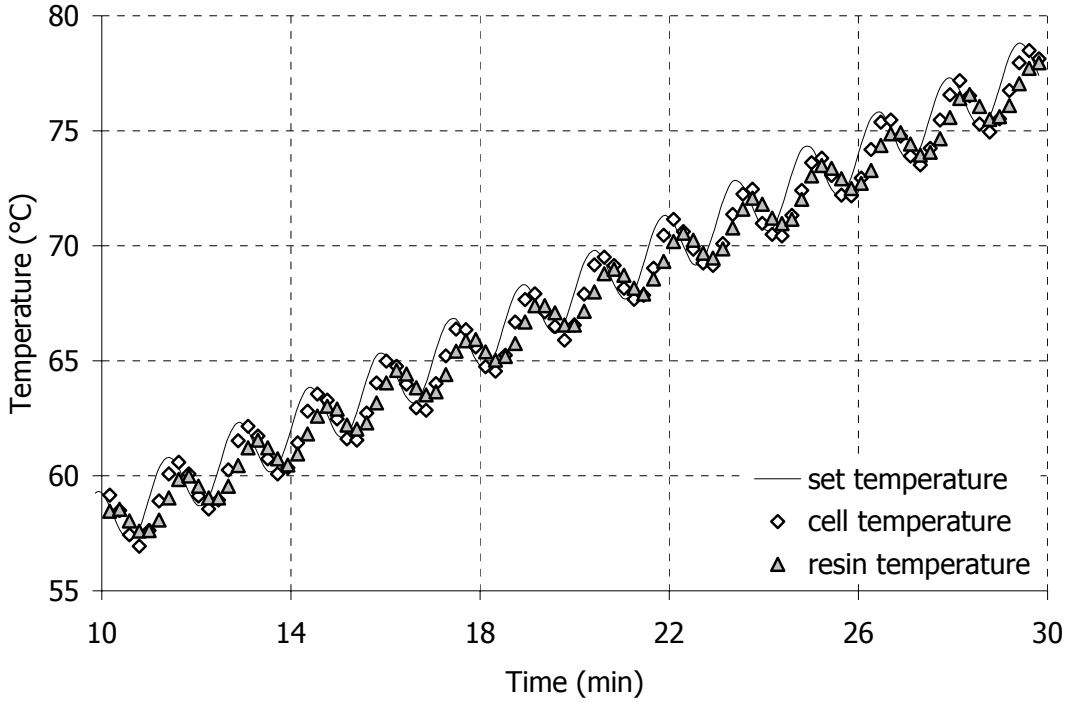

Figure 7-8 *Thermal response of the TMDA experimental cell*

* $delay = \frac{Period * phase}{360}$

The amplitude of the temperature modulation felt by the resin is less than 1°C. This puts a constraint on the lower acceptable value for the amplitude A_T. A_T should be high enough so that clear temperature modulations can be felt by the resin. On the other hand a very large value of A_T demands a very high instantaneous heating rate (214). Furthermore the whole measurement, like all the techniques using temperature modulation, is based on the assumption that the material state will not change significantly during one cycle. This sets limitations on the modulation period P. From the calorimetric experiments we can measure the maximum reaction rates and further calculate the conversion changes for a specific heating rate and period. For a heating rate of 1°C/min, the conversion at the maximum reaction rate will change by more than 5% when the period exceeds 2 min. Therefore periods between 1 and 2 minutes are best suited for imposing sufficient temperature modulations in the curing resin and maintaining stationary conditions during one cycle.

7.5 Application to thermoset cure

The experimental setup for the TMDA experiments is shown in Figure 7-9. A special purpose code was created (using Microsoft® Visual Basic®) in order to communicate with the dielectric analyzer, the temperature controller and the temperature recorder. The following signals are involved in the measurement:

1. Set temperature point to be followed according to the modulated temperature profile
2. Set frequency and voltage amplitude for the dielectric measurement
3. Heat/cool experimental cell according to temperature setpoint
4. Control thermocouple
5. Send excitation to the dielectric sensor
6. Read sensor response
7. Store dielectric measurements
8. Record cell temperature and resin temperature
9. Store temperature readings

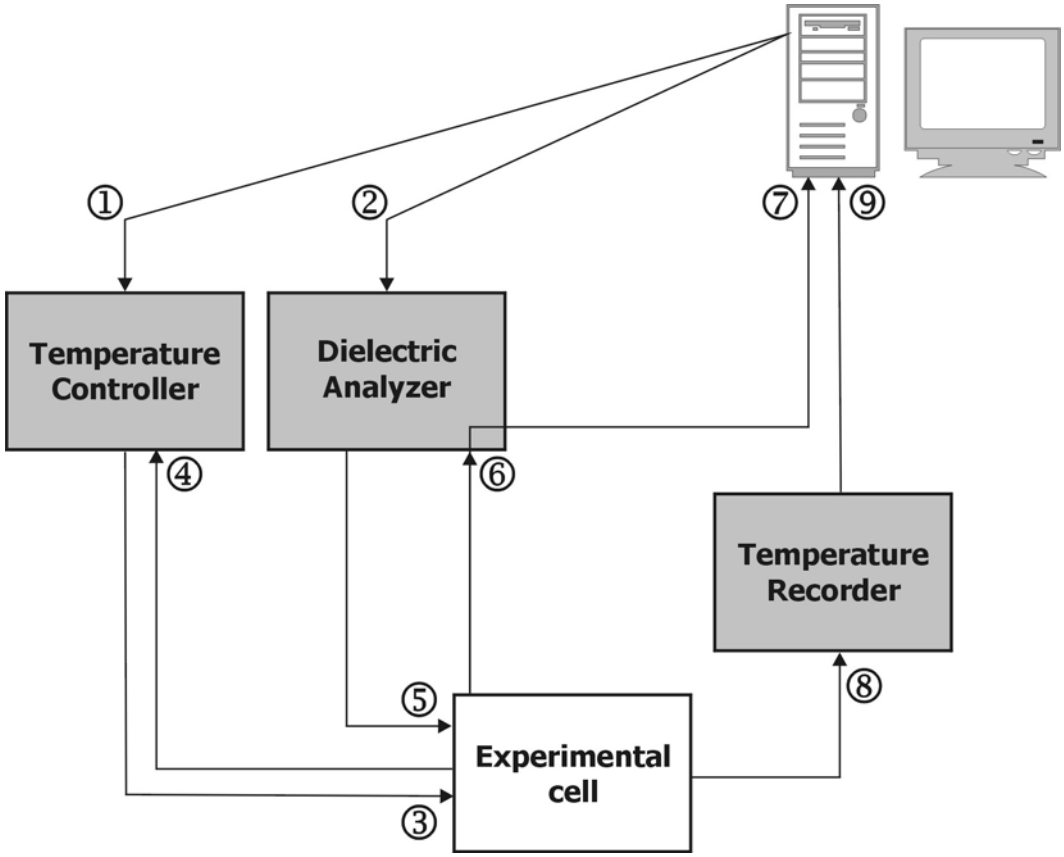

Figure 7-9 *Experimental setup for TMDA measurements. The numbers designate the different signals involved in the measurement.*

7.5.1 Quasi – isothermal runs

Experiments at quasi – isothermal conditions were performed at 130°C, 140°C, 150°C and 160°C. The modulation amplitude was 1.5°C and the period 1 minute. Dielectric data were collected at 1 kHz every 2.5 seconds. Some 20 experimental points were recorded during every cycle.

Experimental results for the cure at 130°C are shown in Figure 7-10. The amplitude of the temperature modulations felt by the resin was about 0.5°C. In the same graph we can see that the dielectric signal is out of phase with the temperature modulations. This suggests that $\delta_{Z''} \rightarrow 90°$.

The Fourier transform of the dielectric signal is given in Figure 7-11 alongside the Fourier transform of a signal in which the underlying temperature increased at a rate of 1°C/min. No secondary modulation period is observed in the transformed signal. The material response to the temperature modulation is linear as will be also shown in the Lissajous plots in § 7.6.1.

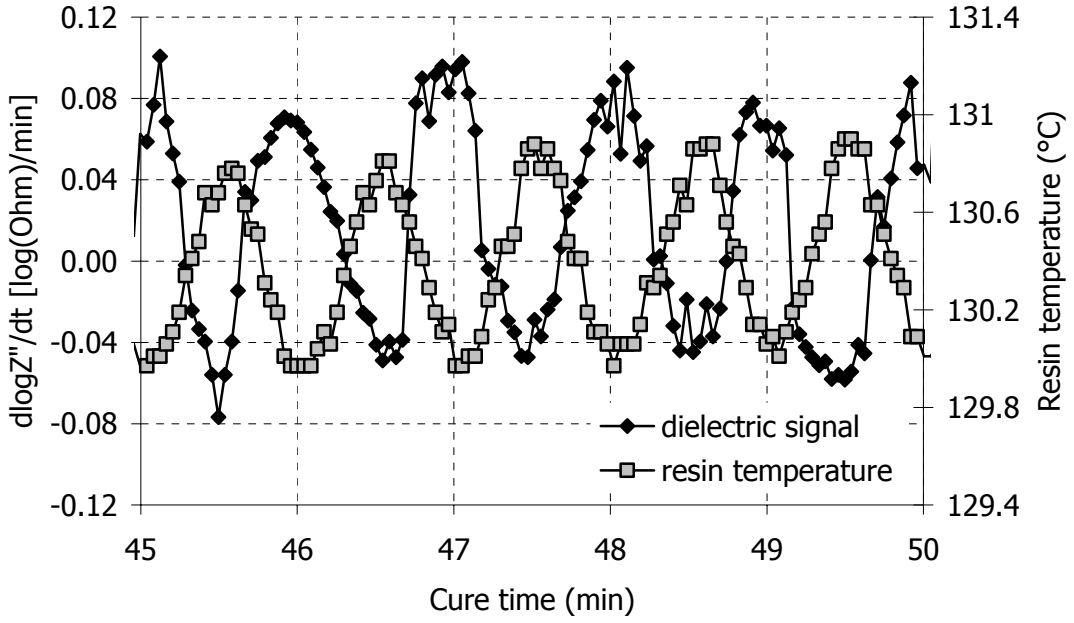

Figure 7-10 *Dielectric signal and temperature profile followed by RTM6. The cure is quasi – isothermal at 130°C. The modulation parameters are: A_T = 1.5°C, P = 1 min. The temperature amplitude in the resin is ~ 0.5°C.*

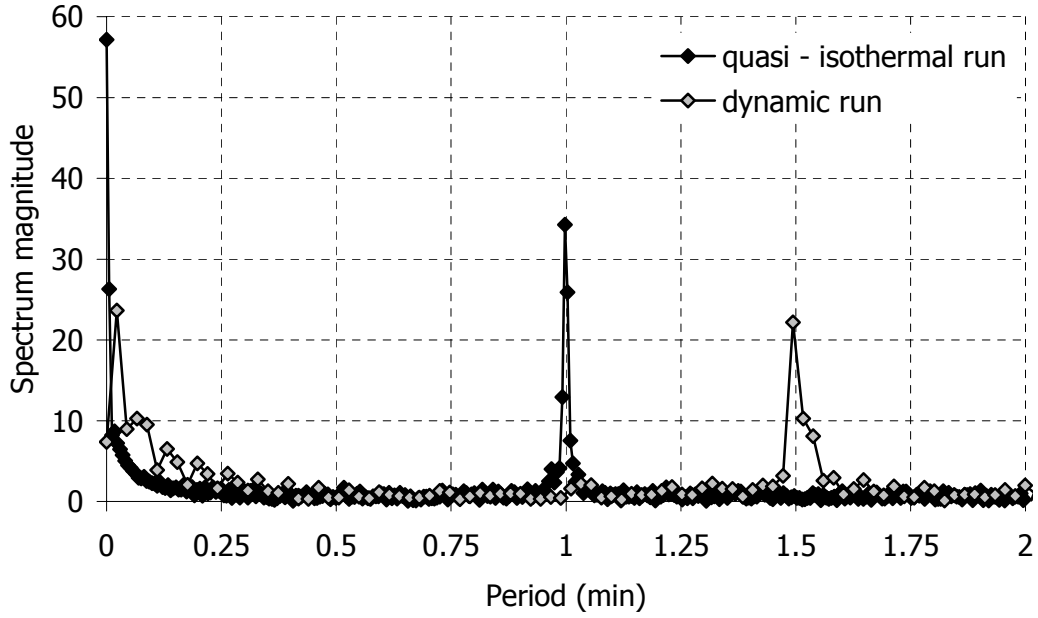

Figure 7-11 *Fourier transform of the dielectric signal of the cure of RTM6 under quasi - isothermal conditions at 130°C (black points) and under dynamic conditions (grey points).*

7.5.2 Non – isothermal runs

Non – isothermal experiments were conducted at 0.4°C/min and 1°C/min. Dielectric measurements were recorded at three different frequencies, 1 kHz, 10 kHz and 100 kHz. The modulation period was 1.5 min and the amplitude 1.5°C. Eight experimental points were recorded during one temperature cycle (~ 12 seconds per measurement). Experiments where the amplitude was 2°C were also made. In those runs the experimental points per cycle were more than 15.

The dielectric signal and the recorded temperature in the curing resin are shown in Figure 7-12. The amplitude of the temperature oscillations shown in the graph is 0.8°C. The dielectric signal is generally noisier than the quasi – isothermal experiments. This can be seen in the Fourier transform of the signal, which is shown in Figure 7-11. The magnitude of the peak is only 20 compared to the value of 35 obtained in the quasi – isothermal run. The fewer data points per temperature cycle also contribute to the low peak value in the transformed signal.

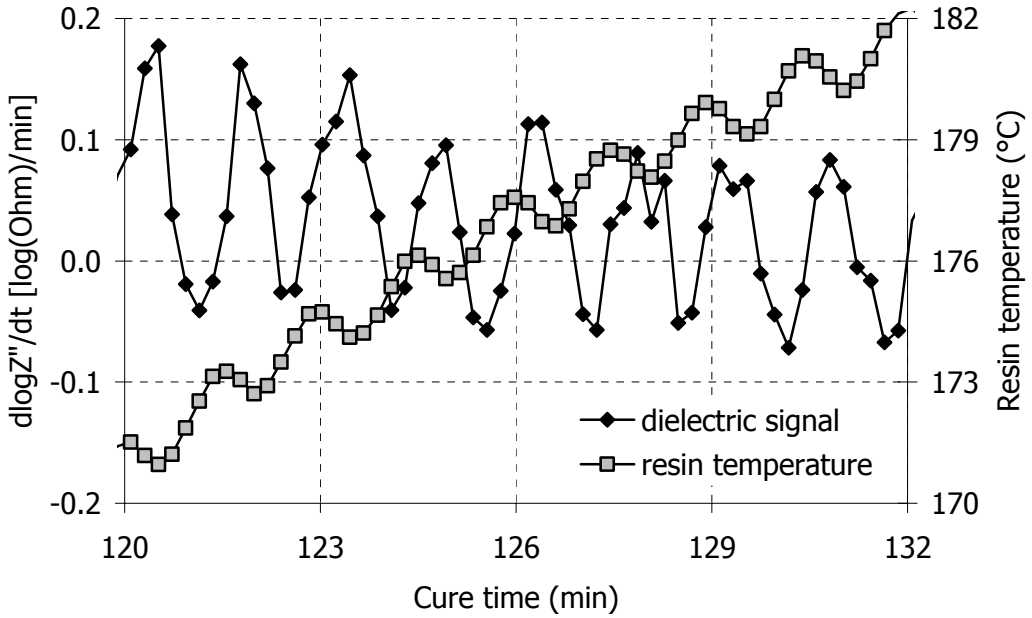

Figure 7-12 *Dielectric signal and resin temperature followed by RTM6. The cure is dynamic at 1°C/min. The modulation parameters are: A_T = 1.5°C, P = 1.5 min.*

7.6 Signal Analysis

The analysis of the dielectric signal was performed using the numerical analysis described in § 2.3.3, also used in the analysis of the MDSC signals (§ 5.2.3). A computer code that carried out all the calculations was written in Visual Basic® for Applications*. All the results were output in a single Microsoft® Excel Spreadsheet.

7.6.1 Investigation of linear response

A Lissajous plot of the dielectric signal against the temperature excitation is shown in Figure 7-13. The data of the plot correspond to times before and after the cure of the resin. We can see that the ellipse is retained in both cases, although the noise in the experimental points is considerable especially when this plot is compared with Figure 5-14 (Lissajous plot of MDSC data). The ellipse narrows as the cure progresses. This pattern, which has been discussed in § 7.3.2, means that the amplitude of the modulated component of the dielectric signal decreases as the cure progresses.

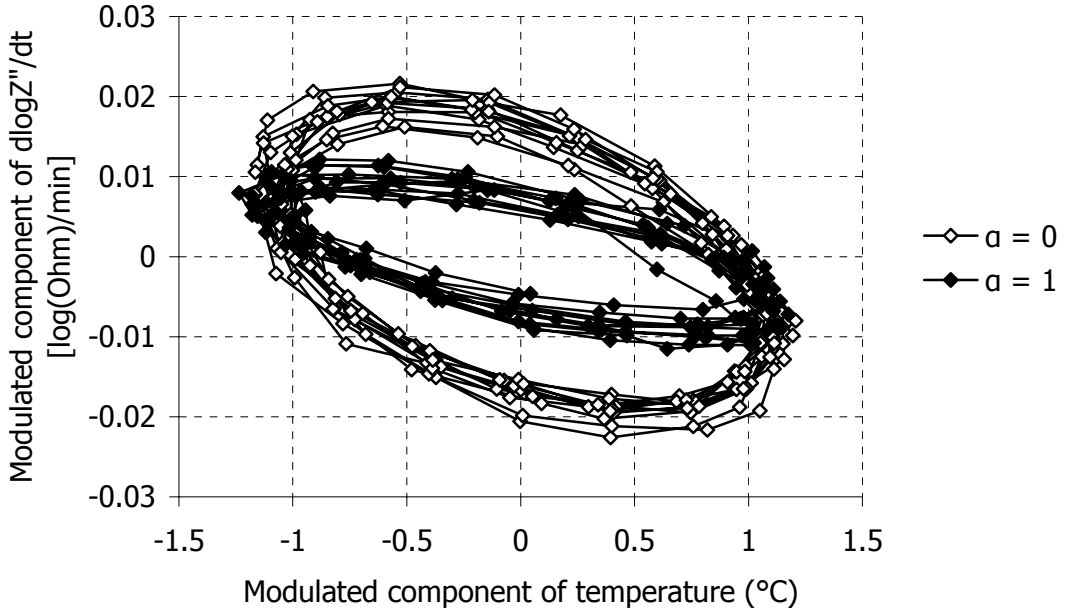

Figure 7-13 *Lissajous plot of the dielectric signal against the temperature modulation. Data are from the cure of RTM6 at 0.4°C/min. The modulation parameters are: A_T = 2°C and P = 1.5 min.*

* Visual Basic for Applications (VBA) is an integral part of the Microsoft Office suite

7.6.2 Analysis of the signal in reversing and non – reversing components

The raw data of the TMDA signal is shown in Figure 7-14 for the cure of RTM6 at 0.4°C/min. In the same graph the underlying non – modulated component of the signal is shown.

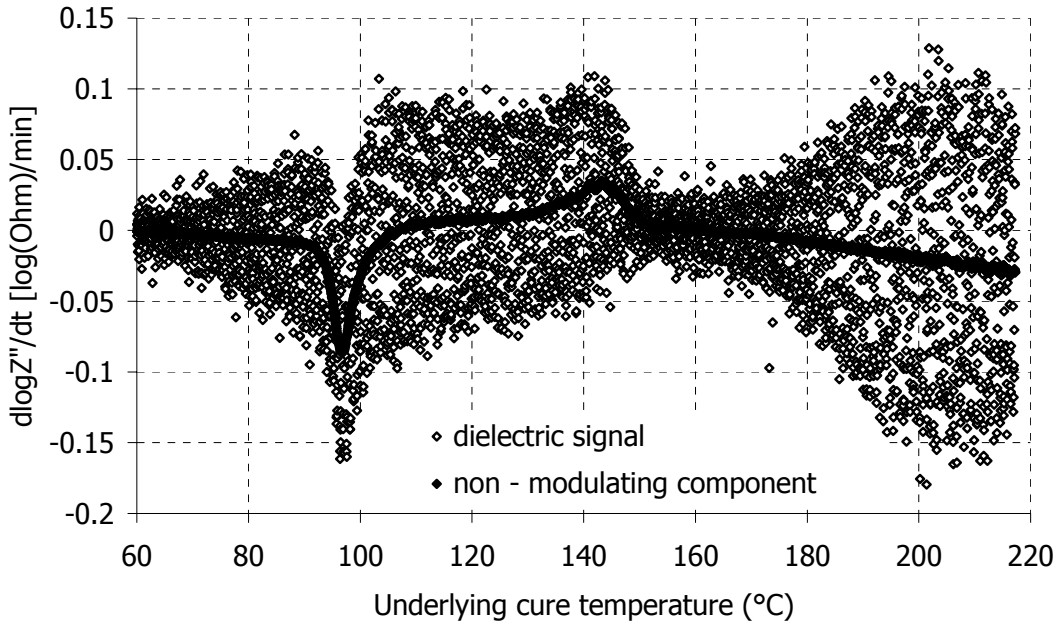

Figure 7-14 *TMDA dielectric signal and the deconvoluted non - modulated component*

Subtraction of the non – modulated component from the total signal results in the modulated component which is shown in Figure 7-15 for the same experiment. The amplitude $A_{Z''}$ is also shown in the graph.

In order to assess how successful is the separation of the underlying and the modulating component of the signal, the Fourier Transform of the two components was taken. The transformed components are shown in Figure 7-16. We can see that the entire signal corresponding to the peak at 1.5 minutes belongs to the modulated component. The signal magnitude of the non – modulated component is high only at the beginning of the x – axis (low frequency part of the signal). This means that the non – modulated component encompasses only the underlying part of the signal. Figure 7-16 proves that the deconvolution of the signal is successful.

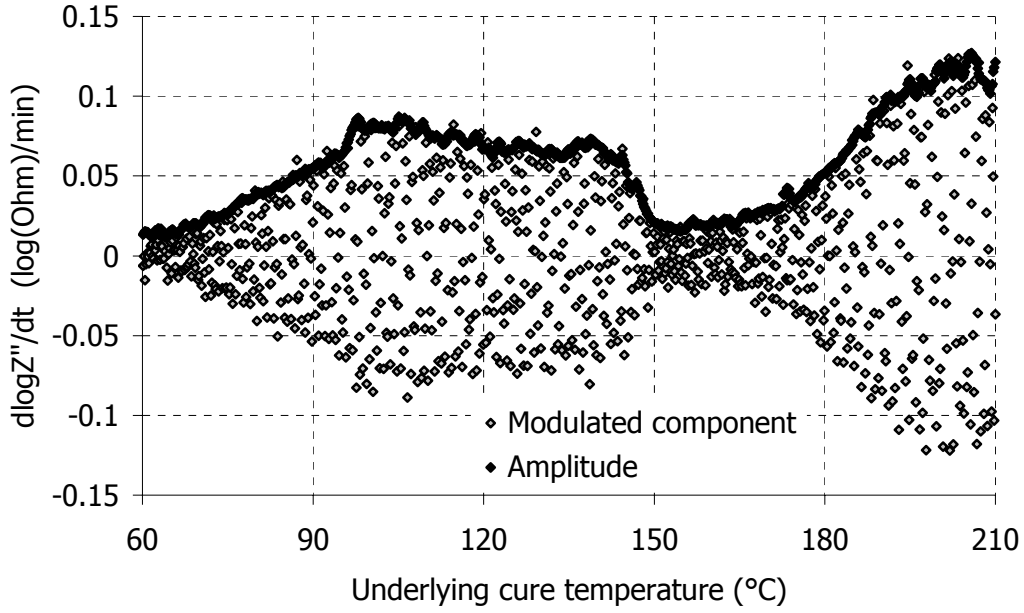

Figure 7-15 *Modulated component and amplitude $A_{Z''}$ of the TMDA signal*

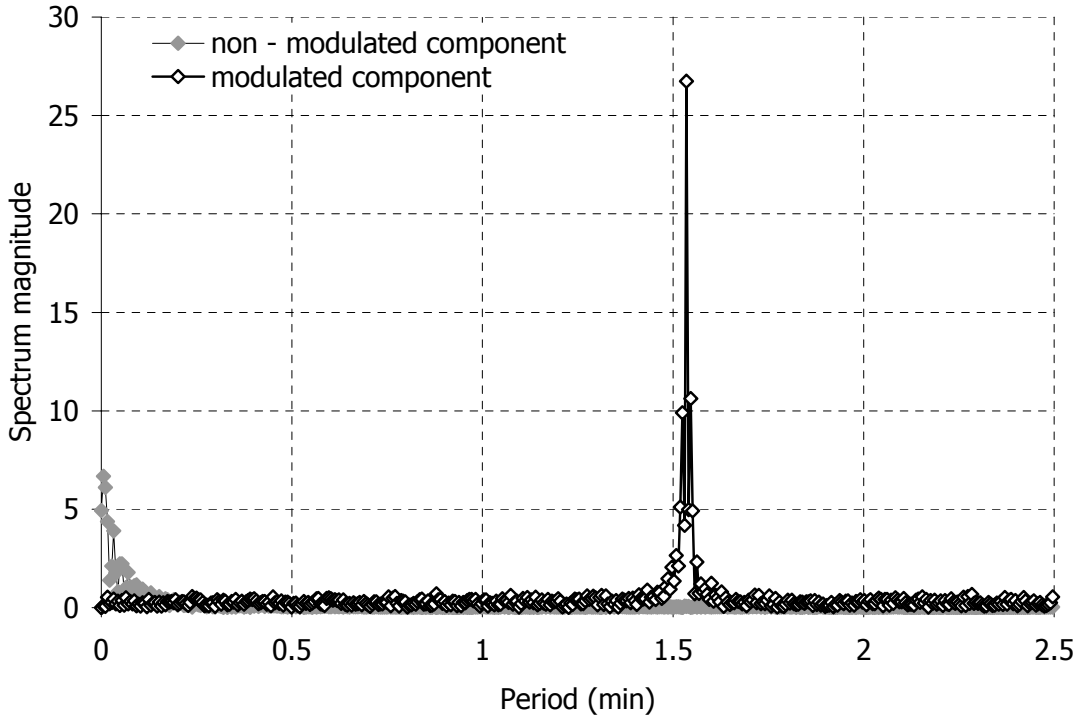

Figure 7-16 *Fourier Transform of the underlying and the modulating component of the TMDA signal.*

7.6.3 Correlation with material state

A comparison between the information contained in the underlying signal and in the IIM is shown in Figure 7-17. The features in the two signals agree except in the later cure stages. The peak at 100°C is reproduced accurately. The peak due to the polymerisation reaction is less pronounced in the TMDA signal. This is because the IIM point has the highest sensitivity in reflecting the changes due to the movements of the migrating charges which give information about the reaction advancement. The TMDA signal is recorded at a specific frequency (1 kHz) and the sensitivity to the movements of the migrating charges depends on how close that frequency is to the IIM (§ 6.3.3). In any case, Figure 7-17 shows that the underlying signal contains information equivalent to the IIM signal despite being a single frequency measurement.

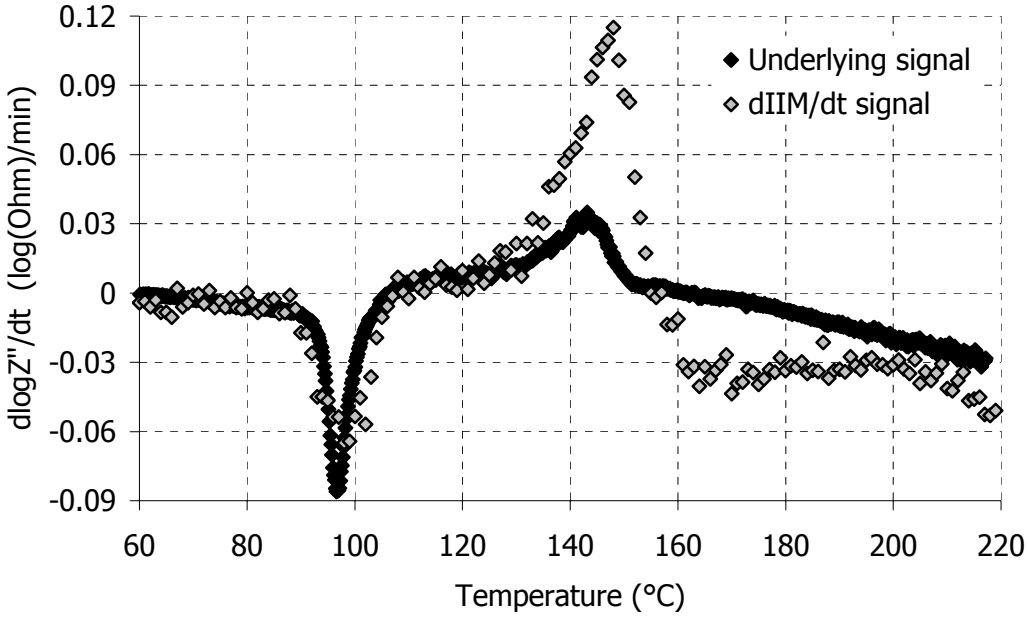

Figure 7-17 *Comparison of the information obtained by the IIM and the underlying component of the TMDA signal for the cure of RTM6 at 0.4°C/min.*

The conversion profile calculated by eq. (7.14) is plotted alongside the cure kinetics model prediction in Figure 7-18. The agreement of the two prediction is fair (correlation coefficient 0.92) only in the region where the polymerisation reaction dominates the signal. In Figure 7-18 this region is set from 120°C to 170°C. At earlier and later stages of the cure, the temperature dependence in the values obtained by eq. (7.14) is obvious in the graph. This means that the model arising from eq. (7.1) is

not adequate for describing the imaginary impedance changes in the regions where only temperature affects the dielectric signal.

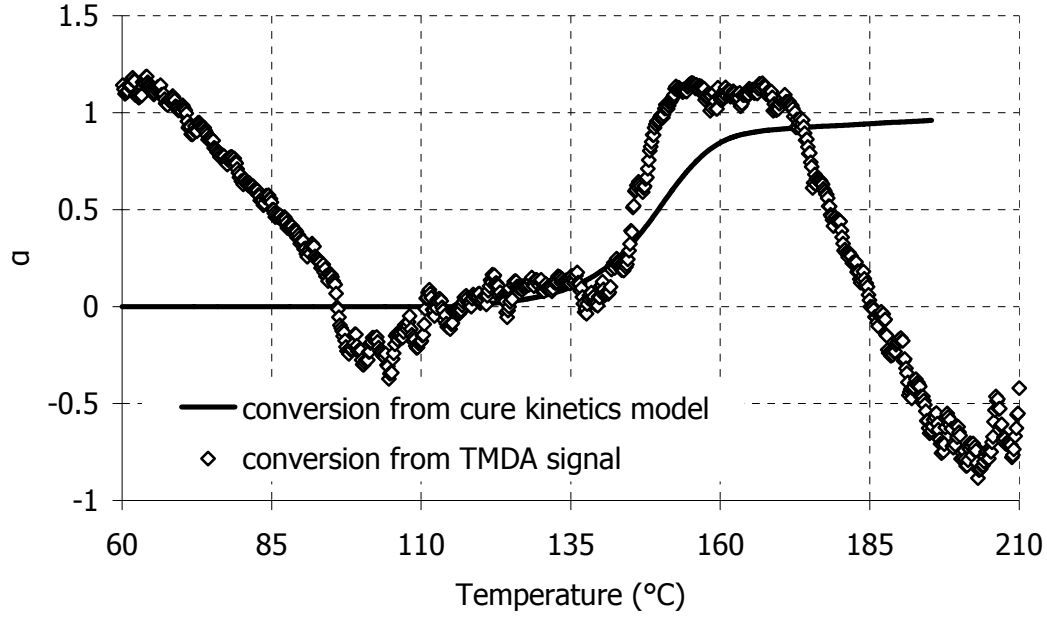

Figure 7-18 *Comparison between the conversion calculated from the TMDA signal and the cure kinetics model result for the cure of RTM6 at 0.4°C/min*

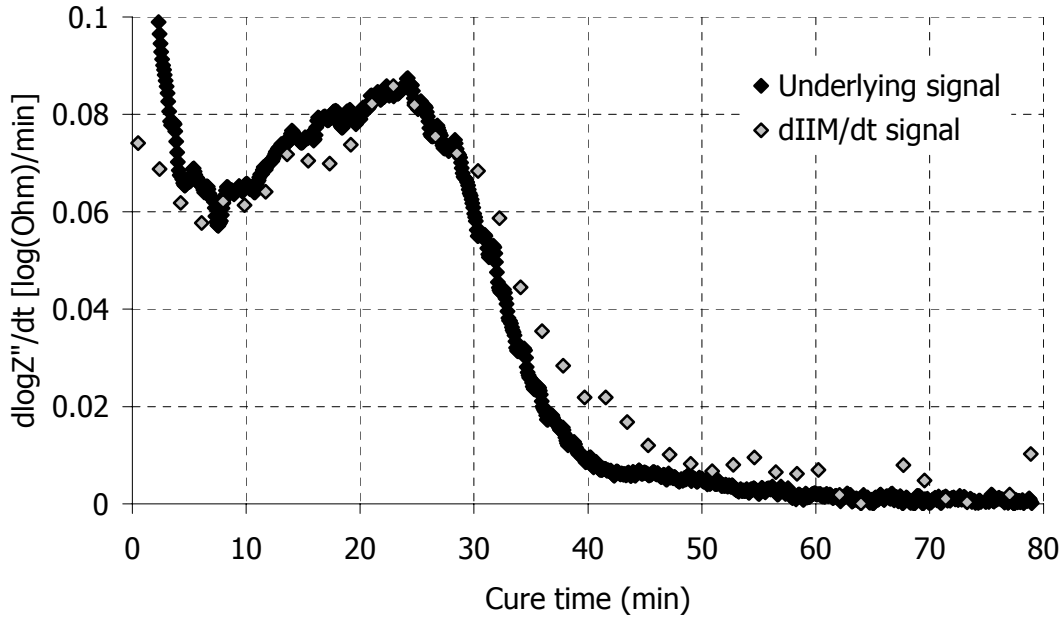

Figure 7-19 *Comparison of the information obtained by the IIM and the underlying component of the TMDA signal for the cure of RTM6 at 160°C.*

The success of the model in quasi – isothermal conditions is pictured in Figures 7-19 and 7-20. The underlying signal follows the changes of the IIM signal throughout the cure. The predicted conversion profile correlates well with the cure kinetics model (correlation coefficient 0.98).

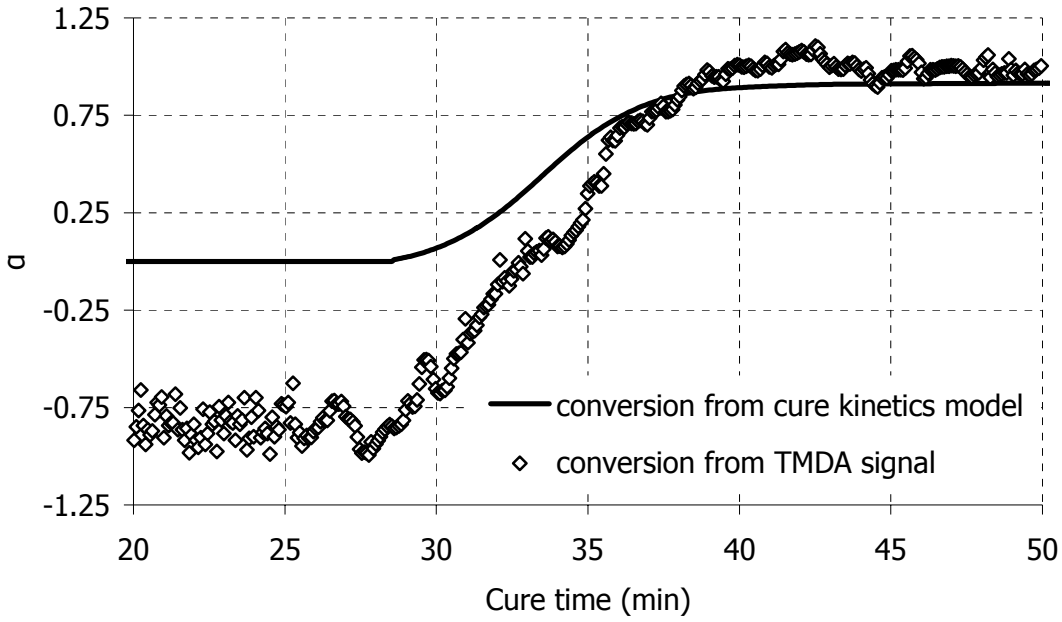

Figure 7-20 *Comparison between the conversion calculated from the TMDA signal and the cure kinetics model result for the cure of RTM6 at 160°C*

These early results show that the principle of the measurement is sound. However, the use of a single frequency instead of the IIM point reduces the sensitivity of the signal to the polymerisation reaction. In addition, the model adopted for the analysis of the results (eq. (7.1)) is not adequate in describing the dielectric response before the reaction onset and after its end, despite it being more general than eq. (6.7). These issues are further discussed in chapter 8, where a possible way of performing TMDA measurements and simultaneously follow the IIM is proposed.

8 Overall Discussion

Apart from the scientific challenges presented in dielectric cure monitoring, mainly posed by the complexity of the cure process, one of the most important prerequisites for any cure monitoring technique to be considered successful is to provide information about the curing system in a context suitable for application in industrial environments. In this study, issues concerning the measurement and interpretation of dielectric cure monitoring signals were investigated. Instead of a model, custom made, epoxy/amine formulation a commercial system was chosen as the case study material. The rationale behind this choice was that the dielectric signal of a clean, laboratory made, thermoset would not have been representative of the response of the industrial manufactured resin system.

The dielectric signal can be translated to any of the four immitance functions listed in Table 4-II. Complex permittivity and complex impedance are the most commonly used variables in cure monitoring studies. In this study complex impedance was chosen as the most appropriate variable for two main reasons:

- It is better suited to describing relatively conductive systems such as those used in industrial applications. On the other hand, complex permittivity gives

better insight in cases when dipolar or interfacial polarisation phenomena are not masked by the migrating charges contribution.

- It is straightforward to model the complex impedance signal using equivalent electrical circuitry

A further advantage of using complex impedance is that it does not require a sensor calibration function in order to be calculated. The calculation of a calibration function suitable for the complex geometries of comb electrodes typically used in dielectric cure monitoring studies requires the modeling of the whole electric field that is being produced around the sensor. Knowledge of the properties of the materials used for the manufacturing of the sensor is also needed. Such studies have been published (215, 216) and are very useful when one can afford (both time and resources) to design and manufacture a complete new sensor. Commercially available sensors, such as the GIA sensor used in this study, do not come with such information. It is the user that has to assess the applicability of the sensor for a specific process and the validity of the results obtained. In the work presented here, the GIA sensor was tested by using standard liquids and by measuring its response in the whole temperature range of use. The substrate influence on the reaction advancement of the resin was also measured and found to be negligible. The conclusion from the investigation was that the GIA sensor is suitable for monitoring the cure of RTM6.

Interpreting dielectric spectra

A comparison between the complex permittivity and the complex impedance interpretations of the charge migration and the dipolar relaxation phenomena was performed in a series of case studies. Permittivity and dielectric loss curves were transformed into real and imaginary impedance curves. So far, such a comparison has only been reported between the complex permittivity and the dielectric modulus (188). The shift of the real and imaginary impedance spectra was simulated by altering the values of specific parameters. These simulations helped in identifying the influence of the different parameters on the shifts observed in the experimental spectra.

The numerical algorithm that modelled the impedance spectra was designed according to the following key considerations:

- The modelling of whole cure monitoring experiments should be possible without any intermediate intervention. This makes the numerical procedure available to any cure control scheme. The algorithm has the potential of providing on – line

information about the evolution of the equivalent circuit parameters as the only input required is the first set of representative dielectric measurements in any given cure run.

- The modelling of spectra containing outliers should not cause significant deviations in the estimated values of the equivalent circuit parameters. This feature is very important for the use of the numerical procedure with data acquired during thermoset cure in moulds or autoclaves where the noise levels are much higher compared to laboratory environments.

The automatic estimation of consecutive spectra is possible by using genetic algorithms. Genetic algorithms do not need an initial estimation of the model parameters. Furthermore they lend themselves to parallel programming which could dramatically reduce the duration needed for the modelling of the data, a prerequisite for any real time monitoring and control configuration. Currently, the average time for modelling a single spectrum is in the order of 20 seconds*.

Modelling Procedure

The applicability of the equivalent circuit model and the numerical algorithm was tested with different materials. Typical results are shown in Figure 8-1 for the isothermal cure of the AY105 – HY2958 structural adhesive and in Figure 8-2 for the dynamic cure of Fibredux® 913.

In both systems the trends that the real and imaginary impedance spectra follow are similar to the trends described for RTM6. In general, the shift of the impedance spectra is driven by the involvement of the intrinsic and extrinsic charges in the curing reaction mechanisms and can be different in different material formulations (173). Nonetheless, experience with thermosets used in commercial and military (aerospace mainly) applications suggests that the trends observed in the cure of RTM6 (impedance increases as cure progresses and decreases when temperature increases before and after the reaction) are also observed in those systems.

* 22 seconds in a PC with an AMD Athlon XP 3000 processor and 1 GB RAM

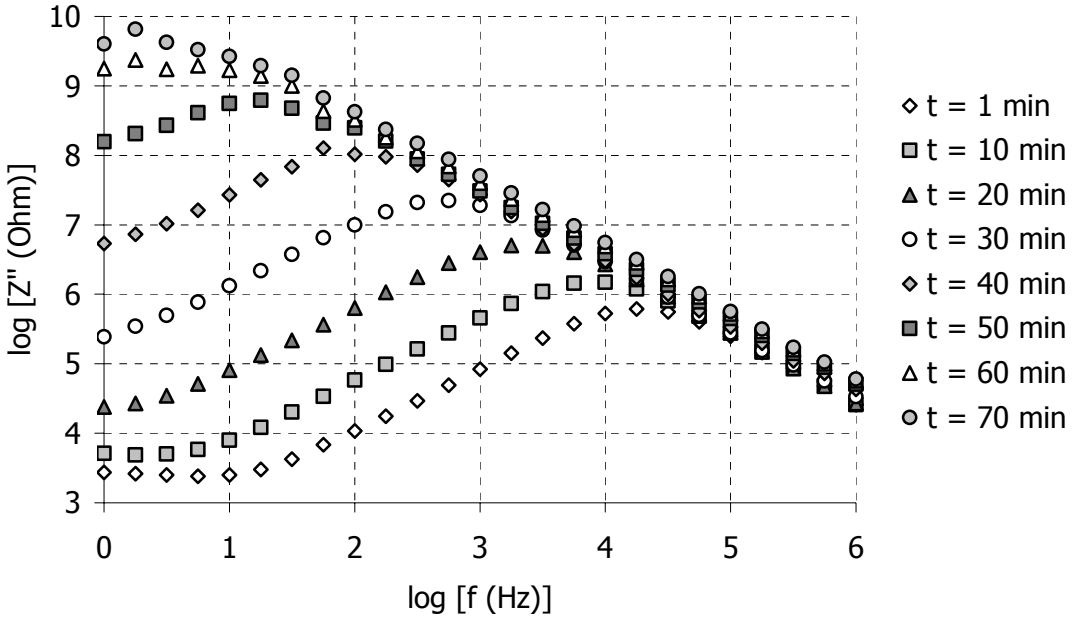

Figure 8-1 *Imaginary impedance spectrum during the cure of AY105 - HY2958 at 30°C*

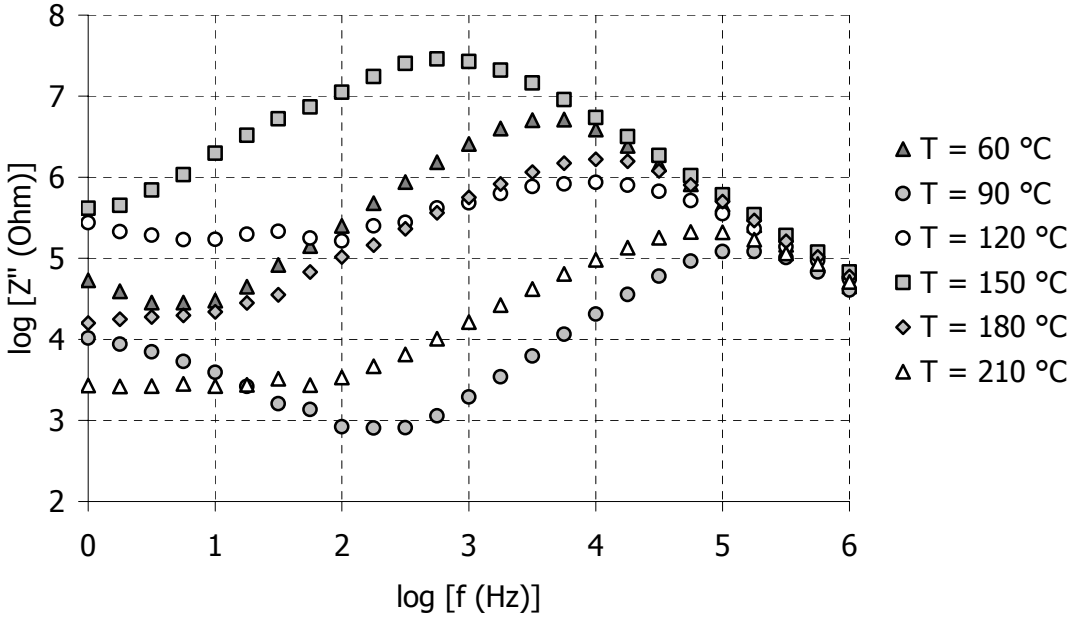

Figure 8-2 *Imaginary impedance spectrum during the dynamic cure of Fibredux® 913 at 1°C/min*

The modelling algorithm was also tested on a bismaleimide based system (Cycom® 5250 – 4RTM manufactured by Cytec (217)). This system does not follow the standard equivalent circuit. The area around the peak in the imaginary impedance spectrum is wider (the response of charged species is dispersed) and no electrode polarisation effects are detected up to 1 Hz. The curves were modelled using the Havriliak – Negami element. The estimation accuracy was similar to that obtained in RTM6 results, as can be seen in Figure 8-3.

The conclusion drawn from the analysis of these systems is that a thorough study of the material behaviour on a laboratory level is necessary before deciding on a model circuit or on a monitor – and – control strategy for the cure process of any new system.

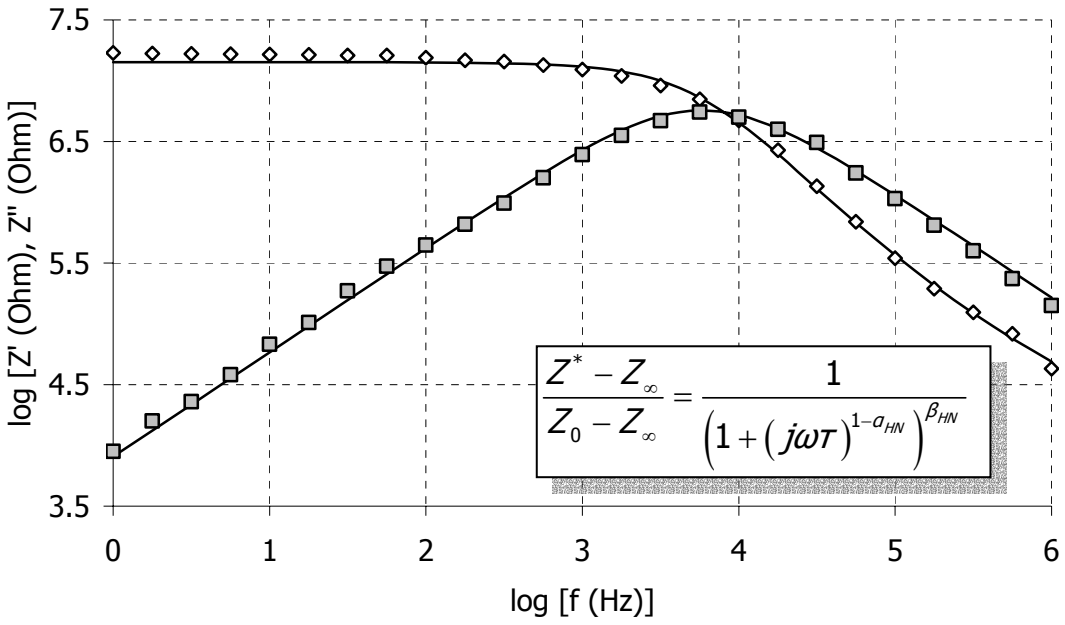

Figure 8-3 *Modelling of the real and imaginary impedance spectrum of the cure of bismaleimide resin at 200°C. The spectra are modelled by the Havriliak – Negami element.*

Frequency Mapping

The frequency mapping of the regions where each of the three phenomena manifested in the dielectric signal can be monitored most effectively is an important tool when fast reacting systems (polyester resins for example) are to be monitored. The polymerisation reaction in these systems could be complete within minutes. This means that measuring over a wide frequency range is not helpful since the material

state would have changed significantly during the frequency sweep and the number of spectra reflecting the changes due to the reaction will be small. Measurements at a few specific frequencies are more effective in such systems. For example, in the case of RTM6, impedance measurements at 1 kHz will primarily contain contributions from the migrating charges movements while measurements at 100 kHz will give information about the vitrification of the system. Monitoring a parameter that follows the shift of the spectra, such as the IIM, during cure is more difficult. The commercially available dielectric analysers do not have the ability to process the measurements and find features like the IIM in the obtained results. Therefore they cannot adjust the experimental frequency window accordingly. However, one can manage to follow the IIM by controling the instrument externally through a computer program. Preliminary results of such measurement are presented in Figure 8-4.

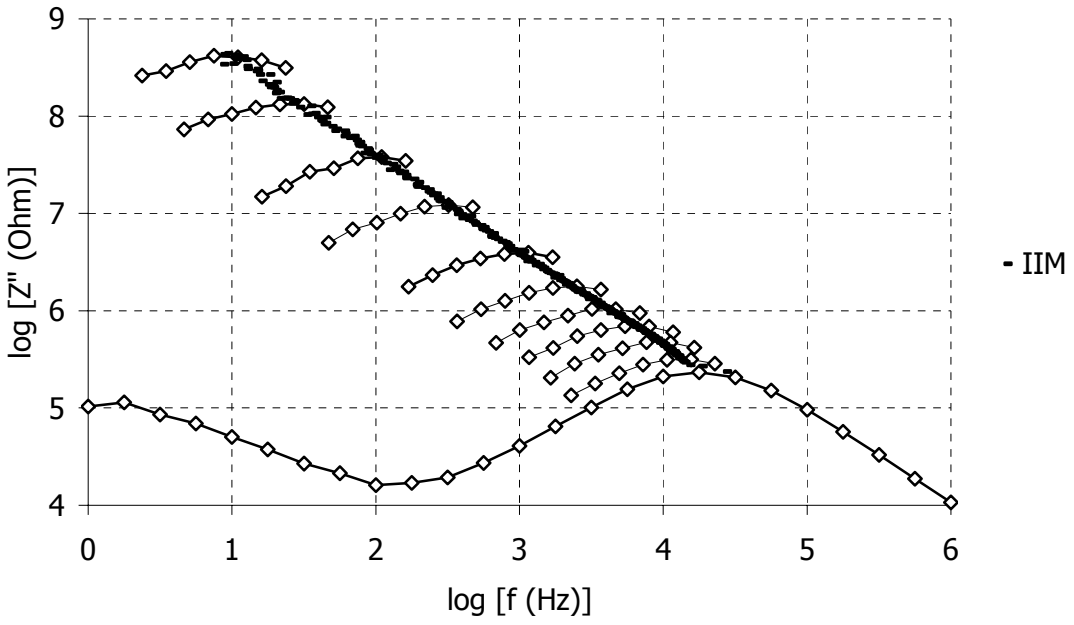

Figure 8-4 *Dynamic measurement of the IIM during the isothermal cure of RTM6 at 140°C. The first sweep covers the whole frequency window. Subsequent sweeps are calcluated according to the position of the IIM and consist of only seven frequencies. The spectra shown in the graph have a time difference of 10 minutes.*

RTM6 was cured isothermally at 140°C. The first spectrum was taken in full, covering a frequency range from 1 Hz to 1 MHz. Then the IIM was located numerically and seven new monitoring frequencies around the IIM were calculated covering a total frequency range of one order of magnitude. Measurements were performed at those frequencies

and the procedure iterated until the end of cure. The IIM was monitored effectively and the frequency sweeps had a duration of tens of seconds. The duration was higher towards the end of cure because of the low frequency measurements.

The inability of the available instruments to follow the shift of the impedance spectra and adjust parameters like the testing frequency stems from the fact that dielectric bridges are not primarily designed for cure monitoring studies. Most dielectric analysers have problems measuring accurately the very small electrical currents occuring towards the end of the cure. The conductivity of a fully cured thermoset can be as low as 10^{-14} S/m which corresponds to a resistance value in the order of 100 GOhm at frequencies close to 1 Hz. Such resistances cannot be measured by most analysers. The use of external interfaces, coupled to the main analyser, offers increased accuracy at measuring high resistances but lengthens the measurement time considerably. When a dielectric interface* was coupled to the 1260 Dielectric Analyser used in this study, the duration of the frequency sweep 1 Hz – 1 MHz almost doubled. A dielectric bridge designed specifically for cure monitoring studies could provide accurate measurements and incorporate features such as monitoring the IIM.

Identifying the Material State

The correlation between the time derivative of the IIM and the reaction rate has the potential to simplify the interpretation of the dielectric signal since the signal can be treated similarly to the signal obtained by calorimetric studies (124). In this study, an explanation of this correlation is put forward, based on eq. (6.7) which links the dielectric signal, the curing temperature and the reaction conversion in one simple expression. The validity of eq. (6.7) is supported by the experimental data of the isothermal runs. The predictions for non – isothermal cases agree well with the actual experimental data in the region where the polymerisation reaction dominates the material response. Further investigation of the relationship between the dielectric signal, the curing temperature and the conversion is needed in order for the model to account for the changes in the signal observed before the start and after the end of the polymerisation reaction. The time derivative of the IIM provides information even in complex cure cycles as demonstrated in Figure 8-5.

* 1296 Dielectric Interface by Solartron Analytical (http://www.solartronanalytical.com)

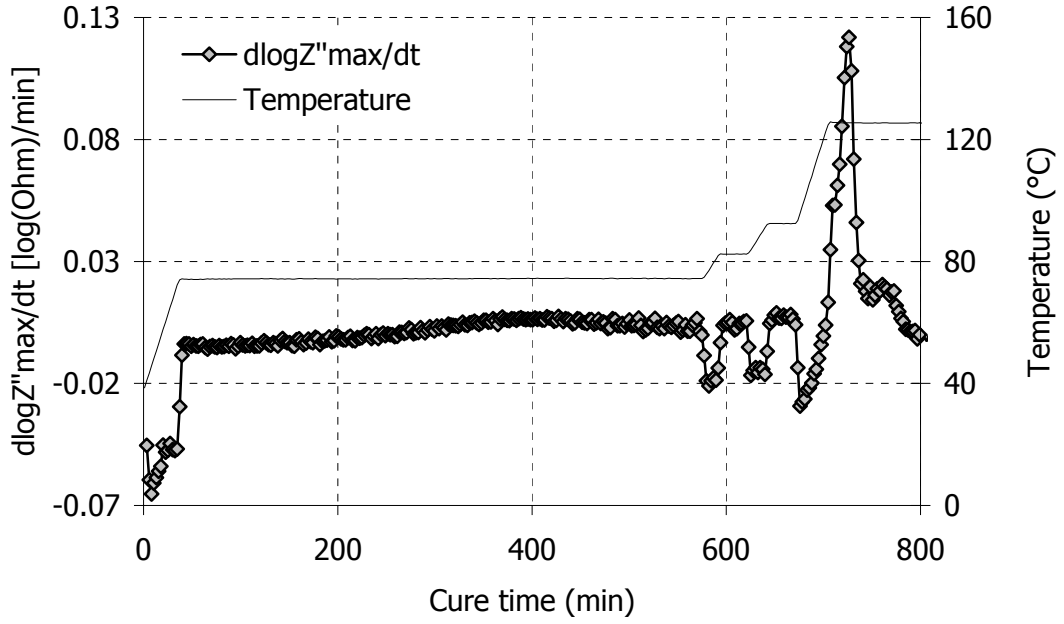

Figure 8-5 *Evolution of the time derivative of IIM during the complex cure of Fibredux® 913.*

The accuracy of the experimental data is more important when the calculation of derivatives is concerned because at least two experimental points are involved in the calculation of each derivative (if one assumes that time measurements are error free). The measurement errors add up and the error of each derivative calculation will be the sum of the errors of the two experimental points. Furthermore, one could ask why not use model relationships like eq. (6.7) and calculate the reaction conversion directly from the impedance data. The problem in calculating the conversion in such a way is that the dielectric signal in some materials is not completely reproducible from run to run. The reproducibility in RTM6 runs was very good but in the Fibredux® 913 resin system curves from identical experiments deviate, as shown in Figure 8-6. The calculation of the time derivative of the imaginary impedance eliminates these discrepancies, as can be seen in the same graph.

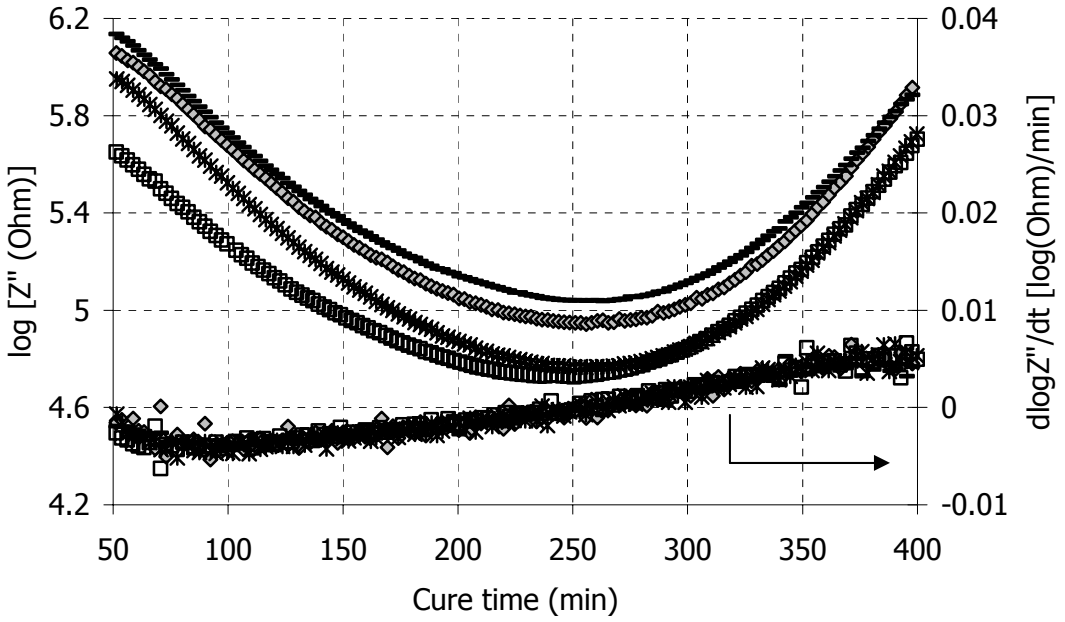

Figure 8-6 *Imaginary impedance evolution at 1 kHz for the cure of Fibredux® 913 at 74°C. Each curve corresponds to a different run. The samples were all prepared from the same batch and the GIA sensor was used in all runs. The time derivative of the same points eliminates the deviation observed.*

Temperature Modulated Dielectric Analysis

The TMDA measurements, presented here for the first time, provide a possible way of direct calculation of the reaction conversion from the dielectric signal. The work presented here focused on the feasibility of such measurements since there was no previous experience on how the system will respond under two external excitations: voltage excitation for the dielectric measurement acting locally in the area of the sensor and temperature oscillations felt by the whole sample. The results showed that the two excitations do not interfere and that the dielectric response is linear to the temperature modulation. The obtained linearity confirms another important issue. In order for the response to be linear, the correlation between the temperature and the dielectric signal has to be linear also. Any higher order dependence would mean that higher harmonic oscillations would be present in the signal.

In order for the deconvolution of the TMDA signal to be numerically correct, a considerable amount of experimental points has to be collected within one temperature cycle. For example, for 10 points to be collected in a 1 min cycle, measurements have to be made every 6 seconds. This means that multi – frequency TMDA measurements

are not possible at present. A single frequency has to be selected for the measurement. In this study the frequency of 1 kHz was selected because in most of the RTM6 cure monitoring experiments this frequency was located within the area where migrating charges dominate the material response. However, if direct measurements of the IIM, with a technique similar to the one shown in Figure 8-4, are optimised, it is possible for the TMDA measurements to be performed on the IIM. This will simplify the analysis and increase the accuracy of the results. Furthermore, it could provide a baseline for the integration of the IIM derivative curves which would further simplify the signal interpretation.

9 Suggestions for Further Work

The comparison between the interpretation of complex permittivity and complex impedance performed in this study resulted in some interesting relationships which relate the features in the complex impedance spectra to the features in the complex permittivity spectra. Some of these features are not possible to be observed in commercial curing systems because they are usually contaminated with high concentrations of charges and because the chemical composition of the constituents is not available. Validation of these relationships could be possible if a custom made resin formulation is used with known chemistry and reaction mechanisms.

Especially for the case study described in § 4.3.1 (dipoles dominate the dielectric signal) a system where the inequality $\varepsilon_r > 9\varepsilon_u$ holds will confirm the existence of an extra peak in the imaginary impedance spectrum caused by the relaxing dipoles.

A model resin formulation could also help correlate the signals obtained by different cure monitoring techniques. For example, signals from dielectric measurements could be compared against signals from ultrasonic measurements. The response of the different molecular species to pressure and electric waves could then be studied.

The application of the modelling algorithm presented here in a semi – industrial environment would further prove the effectiveness of the procedure and test its control

capability. Furthermore, if a heat transfer model is coupled with the monitoring information, a state – based control system could be built for the semi – industrial process. Such a system could help in revealing possible scientific and technical issues before implementation in full scale industrial processes is attempted.

In the area of instrumentation, a dielectric analyser designed and built specifically for cure monitoring studies would give more flexibility in optimising the measurement parameters and improving the accuracy of the results. In this study a custom made computer program guided the bridge by transmitting all the necessary information to the instrument, such as the signal integration time (which depended on the testing frequency), or the voltage excitation.

The influence of temperature and degree of cure on the dielectric signal was tackled here by adopting a linear relationship (eq. (6.7)) between the three parameters. This phenomenological relationship described both isothermal and dynamic data and explained the similarities between the derivative of the IIM and the reaction rate recently observed by Skordos and Partridge (124). The model however failed to describe the dielectric signal in regions where only temperature changes (before the curing reaction onset and after its end) occur. The existence of a closed – form mathematical expression that connects the dielectric signal, the temperature and the reaction conversion is by no means certain or guaranteed. Investigation should be targeted on assessing whether or not such a relationship exists and if it does developing a more complete model than the one used here.

Further development of the TMDA technique is needed in both the instrumentation and the analysis sides. An experimental cell with a built – in cooler and more powerful heating elements will expand the ranges of the modulation period and amplitude that can be achieved. The use of sensors with smaller area will also enhance the overall performance and reduce the thermal lag because of the smaller resin quantities that would be needed for the experiment. Such improvements will reduce the noise levels of the results and permit faster data acquisition which in turn will improve the deconvolution of the signal.

The interpretation of the modulated signal is based on relationships like eq. (6.7). Any advance on the study of the relationship between the dielectric signal, the temperature and the reaction conversion will pass on the analysis of the TMDA signal. The monitoring of the IIM instead of a single frequency measurement will also simplify the

analysis since there will be no need of correlating the single frequency signal to the migrating charges movements as has been done in this study.

At a later stage, the TMDA measurement can reach the automation level of MDSC measurements where suitable software sets the measurement parameters, controls the heater and the cooler and subsequently analyses the obtained results.

10 Conclusions

The main conclusions drawn from this study are the following:

- The cure of thermosets can be monitored using any of the immitance functions (complex permittivity, complex impedance, complex admittance, complex electric modulus).
- Complex impedance is better suited than complex permittivity in monitoring systems where migrating charges dominate the signal. Commercial systems usually fall into that category.
- The calculation of a sensor calibration function based on the assumption that the sensor substrate dielectric properties do not change during the cure is not always valid. The effect of temperature and the possible interactions with the curing material should be investigated before the sensor is used in cure monitoring experiments.
- The complex impedance signal is modelled using electrical equivalent circuits.

- A numerical procedure, based on Genetic Algorithms, allows the subsequent modelling of complex impedance spectra throughout the cure.
- A regularisation term enhances the robustness of the numerical procedure.
- The main features of the imaginary impedance spectrum, namely the local minimum and maximum, have been modelled successfully.
- The manifestation of vitrification at high frequencies (>100 kHz) can also be modelled despite its negligible influence on the overall signal.
- Frequency regions where each one of the three phenomena that comprise the dielectric signal can be effectively monitored are identified by using a new equivalent circuit.
- A mathematical model explains the correlation between the time derivative of the maximum of the imaginary impedance spectrum and the rate of the polymerisation reaction. The model is based on a linear dependence of the imaginary impedance maximum signal on temperature and conversion.
- A new experimental technique, named Temperature Modulated Dielectric Analysis (TMDA) has been developed. Small amplitude temperature modulations are superimposed on an underlying thermal profile. The resulting dielectric signal comprises of an underlying component and a modulated component. The technique aims in simplifying the interpretation of cure monitoring dielectric signals.
- TMDA signals are linear with respect to the temperature excitation. The resulting dielectric signal contains only the temperature modulation frequency.
- No higher order harmonics were observed in the acquired signals. This means that the dielectric signal changes with temperature on a linear fashion.
- Results from the TMDA measurements indicate that the amplitude of the modulated component of the signal can be correlated to the reaction conversion.
- Further development of the TMDA is needed in order to reduce the noise levels and improve the analysis of the measurement.

11 References

1. J.-P. Pascault, H. Sautereau, J. Verdu, R.J.J. Williams, "Thermosetting Polymers", *Marcel Dekker*, New York 2003, (ISBN: 0-8247-0670-6)
2. P. Hedvig, "Dielectric Spectroscopy of Polymers", *Adam Hilger Ltd*, Bristol 1977, (ISBN: 0-85274-247-9)
3. P.J. Flory, "Principles of Polymer Chemistry", *Cornell University Press*, New York 1953, (ISBN: 0-8014-0134-8)
4. J.B. Enns, J.K. Gillham, "Time – temperature – transformation (TTT) cure diagram: Modeling the cure behaviour of thermosets", *Journal of Applied Polymer Science*, **28** (1983) 2567 – 2591
5. I.K. Partridge, G.M. Maistros, "Dielectric cure monitoring for process control" in "Comprehensive Composites Materials", vol. 5, *Elsevier Science*, New York 2000, (ISBN: 0-08-043723-0), URL: http://www.compcompmat.com/mrw4/show/
6. H. Fröhlich, "Theory of Dielectrics", 2nd edition, *Oxford University Press*, New York (1958)
7. P. Debye, "Polar Molecules", *Dover Publications*, New York (1945)
8. P. Lunkenheimer, "Dielectric spectroscopy of glassy dynamics", *Shaker Verlag*, Aachen 1999, (ISBN: 3-8265-6802-8)

9. D.A. Seanor, "Electrical properties of polymers", *Academic Press*, New York 1982, (ISBN: 0-12-633680-6)
10. C.W. Wise, W.D. Cook, A.A. Goodwin, "Chemico – diffusion kinetics of model epoxy – amine resins", *Polymer*, **38** (1997) 3251 – 3261
11. C.C. Riccardi, F. Fraga, J. Dupuy, R.J.J. Williams, "Cure kinetics of diglycidylether of bisphenol A – ethylenediamine revisited using a mechanistic model", *Journal of Applied Polymer Science*, **82** (2001) 2319 – 2325
12. K.C. Cole, "A new approach to modelling the cure kinetics of epoxy amine thermosetting resins. 1. Mathematical development", *Macromolecules*, **24** (1991) 3093 – 3097
13. M.-K. Um, I.M. Daniel, B.-S. Hwang, "A study of cure kinetics by the use of dynamic differential scanning calorimetry", *Composites Science and Technology*, **62** (2002) 29 – 40
14. M.L. Auad, M.I. Aranguren, G. Elićabe, J. Borrajo, "Curing kinetics of divinyl ester resins with styrene", *Journal of Applied Polymer Science*, **74** (1999) 1044 – 1053
15. J.E.K. Schawe, "A description of chemical and diffusion control in isothermal kinetics of cure kinetics", *Thermochimica Acta*, **388** (2002) 299 – 312
16. M.R. Kamal, S. Sourour, M. Ryan, "Integrated thermo – rheological analysis of the cure of thermosets", *Society of Plastics Engineers Technical Papers*, **19** (1973) 187 – 191
17. S. Sourour, M.R. Kamal, "Differential scanning calorimetry of epoxy cure: isothermal cure kinetics", *Thermochimica Acta,* **14** (1976) 41 - 59
18. M.E. Ryan, A. Dutta, "Kinetics of epoxy cure: a rapid technique for kinetic parameter estimation", *Polymer*, **20** (1979) 203 – 206
19. P.I. Karkanas, I.K. Partridge, "Cure modelling and monitoring of epoxy/amine resin systems. I. Cure kinetics modelling", *Journal of Applied Polymer Science*, **77** (2000) 1419 – 1431
20. D. Roşu, C.N. Caşcaval, F. Mustaţă, C. Ciobanu, "Cure kinetics of epoxy resins studied by non – isothermal DSC data", *Thermochimica Acta*, **383** (2002) 119 – 127
21. D.J. O'Brien, S.R. White, "Cure kinetics, gelation and glass transition of a bisphenol F epoxide", *Polymer Engineering and Science*, **43** (2003) 863 – 874
22. J.L. Vilas, J.M. Laza, M.T. Garay, M. Rodriguez, L.M. Leon, "Unsaturated Polyester Resins Cure: Kinetic, Rheologic, and Mechanical Dynamical Analysis. I. Cure

Kinetics by DSC and TSR", *Journal of Applied Polymer Science*, **79** (2001) 447 – 457

23. J.L. Vilas, J.M. Laza, M.T. Garay, M. Rodriguez, L.M. Leon, "Unsaturated Polyester Resins Cure: Kinetic, Rheologic, and Mechanical Dynamical Analysis. II. The Glass Transition in the Mechanical Dynamical Spectrum of Polyester Networks", *Journal of Polymer Science Part B: Polymer Physics*, **39** (2001) 146 – 152
24. B.A. Rozenberg, E.A. Dzhavadyan, R. Morgan, E. Shin, "High – performance Bismaleimide Matrices: Cure Kinetics and Mechanism", *Polymers for Advanced Technologies*, **13** (2002) 837 – 844
25. J.L. Hopewell, G.A. George, D.J. Hill, "Analysis of the kinetics and mechanism of the cure of a bismaleimide – diamine thermoset", *Polymer*, **41** (2000) 8231 – 8239
26. A. Bonnet, J.P. Pascault, H. Sautereau, M. Taha, Y. Camberlin, "Epoxy-diamine thermoset/thermoplastic blends. 1. Rates of reactions before and after phase separation", *Macromolecules*, **32** (1999) 8517 – 8523
27. P.I. Karkanas, I.K. Partridge, D. Attwood, "Modelling the cure of a commercial epoxy resin for applications in resin transfer moulding", *Polymer International*, **41** (1996) 183 – 191
28. A.A. Skordos, I.K. Partridge, "Cure kinetics modelling of epoxy resins using a non – parametric numerical procedure", *Polymer Engineering and Science*, **41** (2001) 793 – 805
29. J.D. Ferry, "Viscoelastic properties of polymers", 3rd edition, *John Wiley & Sons*, New York 1980, (ISBN: 0-4710-4894-1)
30. J. Lange, N. Altmann, C.T. Kelly, P.J. Halley, "Understanding vitrification during cure of epoxy resins using dynamic scanning calorimetry and rheological techniques", *Polymer*, **41** (2000) 5949 – 5955
31. L. Matejka, "Rheology of epoxy networks near the gel point", *Polymer Bulletin,* **26** (1991) 109 – 116
32. F. Stephan, A. Fit, X. Duteurtre, "In-process control of epoxy composite by microdielectrometric analysis", *Polymer Engineering and Science*, **37** (1997) 436 – 449
33. P.I. Karkanas, I.K. Partridge, "Cure Modeling and Monitoring of Epoxy/Amine Resin Systems. II. Network Formation and Chemoviscosity Modeling", *Journal of Applied Polymer Science*, **77** (2000) 2178 – 2188

34. G.V. Assche, B.V. Mele, E. Verdonck, "Interrelations between mechanism, kinetics and rheology in an isothermal cross-linking chain-growth copolymerization", *Polymer*, **42** (2001) 2959 – 2968
35. A. Maffezzoli, A. Trivisano, M. Opalicki, J. Mijovic, J.M. Kenny, "Correlation between dielectric and chemorheological properties during cure of epoxy-based composites", *Journal of Materials Science*, **29** (1994) 800 – 808
36. J. Mijovic, C.H. Lee, "Modeling of chemorheology of thermoset cure by modified WLF equation", *Journal of Applied Polymer Science*, **37** (1989) 889 – 900
37. W. Zurawski, L. Nicolais, I. Mondragon, B. Fitz, J. Mijovic, F. Bellucci, I. Abrahams, "Impedance spectroscopy of reactive polymers. 3. Correlations between dielectric, spectroscopic and rheological properties during cure of a trifunctional epoxy resin", *Journal of Polymer Science: Part B: Polymer Physics*, **34** (1996) 379 – 388
38. M.B.M. Mangion, G.P. Johari, "Relaxations in thermosets. IX. Ionic conductivity and gelation of DGEBA-based thermosets cured with pure and mixed amines", *Journal of Polymer Science: Part B: Polymer Physics*, **29** (1991) 1117 – 1125
39. A.J. MacKinnon, S.D. Jenkins, P.T. McGrail, R.A. Pethrick, "A dielectric, mechanical, rheological, and electron microscopy study of cure and properties of a thermoplastic-modified epoxy resin", *Macromolecules*, **25** (1992) 3492 – 3499
40. J.P. Pascault, A. Bonnet, H. Sautereau, Y. Camberlin, "Epoxy-diamine thermoset/thermoplastic blends. 2. Rheological behavior before and after phase separation", *Macromolecules*, **32** (1999) 8524 – 8530
41. K. Char, H. Kim, "Effect of phase separation on rheological properties during the isothermal curing of epoxy toughened with thermoplastic polymer", *Industrial and Engineering Chemistry Research*, **39** (2000) 955 – 959
42. R. Zallen, "The physics of amorphous solids", *Wiley Interscience*, New York 1998, (ISBN: 0-471-29941-3)
43. I.M. Hödge, "Enthalpy relaxation and recovery in amorphous materials", *Journal of Non – Crystalline Solids*, **169** (1994) 211 – 266
44. J.P. Runt, J.J. Fitzgerald, "Dielectric Spectroscopy of Polymeric Materials: fundamentals and applications", *American Chemical Society*, Washington DC 1997, (ISBN: 0-8412-3335-7)
45. M.T. DeMeuse, J.K. Gillham, F. Parodi, "Evolution of properties of an Isocyanate/Epoxy thermosetting system during cure: Continuous heating (CHT)

and isothermal time – temperature – transformation (TTT) cure diagrams, *Journal of Applied Polymer Science*, **64** (1997) 15 – 25

46. M.B.M. Mangion, G.P. Johari, "Relaxations in thermosets. VI. Effects of Crosslinking on sub-T_g relaxations during the curing and aging of epoxide-based thermosets", *Journal of Polymer Science: Part B: Polymer Physics*, **29** (1991) 437 – 449
47. R. Casalini, S. Corezzi, D. Fioretto, A. Livi, P.A. Rolla, "Unified dielectric description of the dynamics of polymeric systems undergoing either thermal or chemical vitrification", *Chemical Physics Letters*, **258** (1996) 470 – 476
48. B. Fitz, S. Andjelic, J. Mijovic, "Reorientational dynamics and intermolecular cooperativity of reactive polymers. 1. Model epoxy – amine systems", *Macromolecules*, **30** (1997) 5227 – 5238
49. S. Andjelic, B. Fitz, J. Mijovic, "Reorientational dynamics and intermolecular cooperativity of reactive polymers. 2. Multifunctional epoxy – amine systems", *Macromolecules*, **30** (1997) 5239 – 5248
50. S. Andjelic, J. Mijovic, "Dynamics of reactive polymer networks in the presence of a nonpolar solvent by dielectric relaxation spectroscopy", *Macromolecules*, **31** (1998) 2872 – 2882
51. J. Mjovic, "Dynamics and cooperativity in thermoset networks by dielectric relaxation spectroscopy" , *Journal of Non – Crystalline Solids*, **235 – 237** (1998) 587 – 595
52. B.D. Fitz, J. Mijovic, "Segmental dynamics and density fluctuations in polymer networks during chemical vitrification", *Macromolecules*, **32** (1999) 4134 – 4140
53. V. Antonucci, M. Giordano, K.T. Hsiao, S.G. Advani, "A methodology to reduce thermal gradients due to the exothermic reactions in composites processing", *International Journal of Heat and Mass Transfer*, **45** (2002) 1675 – 1684
54. V. Antonucci, M. Giordano, S.I. Omparato, L. Nicolais, "Analysis of Heat Transfer in Autoclave Technology", *Polymer Composites*, **22** (2001) 613 – 620
55. J. Mijovic, S. Andjelic, C.F.W. Yee, F. Bellucci, L. Nicolais "A study of reaction kinetics by near-infrared spectroscopy. 2. Comparison with dielectric spectroscopy of model and multifunctional epoxy/amine systems", *Macromolecules*, **28** (1995) 2797 – 2806
56. H. Günzler, H.-U. Gremlich, "IR Spectroscopy. An introduction", *Wiley – VCH Verlag GmbH*, Weinheim 2002, (ISBN: 3-527-28896-1)

57. http://scienceworld.wolfram.com/physics/BeersLaw.html, Eric Weinstein's World of Mathematics, Wolfram Research, accessed June 21st 2003
58. J. Mijovic, S. Andjelic, "Monitoring of reactive processing by remote mid infra-red spectroscopy", *Polymer*, **37** (1996) 1295 – 1303
59. R.-H. Lin, "In situ FTIR and DSC investigation on cure reaction of liquid aromatic dicyanate ester with different types of epoxy resin", *Journal of Polymer Science: Part A: Polymer Chemistry*, **38** (2000) 2934 – 2944
60. F. Fraga, S. Burgo, E.R. Núñez, "Curing kinetic of the epoxy system BADGE n = 0/1, 2 DCH by Fourier transform infrared spectroscopy (FTIR)", *Journal of Applied Polymer Science*, **82** (2001) 3366 – 3372
61. L. Rey, J. Galy, "Near-infrared spectroscopy for in situ cure monitoring of dimethacrylate-based networks", *Applied Spectroscopy*, **54** (2000) 39 – 43
62. P. Musto, E. Martuscelli, G. Ragosta, P. Russo, P. Villano, "Tetrafunctional epoxy resins: Modelling the curing kinetics based on FTIR spectroscopy data", *Journal of Applied Polymer Science*, **74** (1999) 532 – 540
63. J.Mijovic, S. Andjelic, "In situ real-time monitoring of reactive systems by remote fibre-optic near-infra-red spectroscopy", *Polymer*, **36** (1995) 3783 – 3786
64. Q. Wang, B.K. Storm, L.P. Houmoller, "Study of the Isothermal Curing of an Epoxy Prepreg by Near-Infrared Spectroscopy" *Journal of Applied Polymer Science*, **87** (2003) 2295 – 2305
65. E.P. Papadakis, "Monitoring the moduli of polymers with ultrasound", *Journal of Applied Physics*, **45** (1974) 1218 – 1222
66. J.H. Speake, R.G.C. Arridge, G.J. Curtis, "Measurement of the cure of resins by ultrasonic techniques", *Journal of Physics D: Applied Physics*, **7** (1974) 412 – 424
67. A. Maffezzoli, E. Quarta, V. A. M. Luprano, G. Montagna, L. Nicolais, "Cure monitoring of epoxy matrices for composites by ultrasonic wave propagation", *Journal of Applied Polymer Science*, **73** (1999) 1969 – 1977
68. R.J. Freemantle, R.E. Challis, "Combined compression and shear wave ultrasonic measurements on curing adhesive", *Measurement Science and Technology*, **9** (1998) 1291 – 1302
69. R.E. Challis, T. Alper, A.K. Holmes, R.P. Cocker, "Near-plane-wave acoustic propagation measurements in thin layers of adhesive polymer", *Measurement Science and Technology*, **2** (1991) 59 – 68

70. J.D. Ferry, "Viscoelastic properties of Polymers", 3rd edition, *John Wiley & sons*, New York 1980, (ISBN: 0-47104-894-1)
71. R.E. Challis, M.E. Unwin, D.L. Chadwick, R.J. Freemantle, I.K. Partridge, D.J. Dare, P.I. Karkanas, "Following network formation in an epoxy/amine system by ultrasound, dielectric, and nuclear magnetic resonance measurements: a comparative study", *Journal of Applied Polymer Science*, **88** (2003) 1665 – 1675
72. C. Pindinelli, G.Montagna, V.A.M. Luprano, A. Maffezzoli, "Network development during epoxy curing: Experimental ultrasonic data and theoretical predictions", *Macromolecular Symposia*, **180** (2002) 73 – 88
73. S.R. White, P.T. Mather, M.J. Smith, "Characterization of the cure-state of DGEBA-DDS epoxy using ultrasonic, dynamic mechanical and thermal probes", *Polymer Engineering and Science*, **42** (2002) 51 – 67
74. M. Younes, S. Wartewig, D. Lellinger, B. Strehmel, V. Strehmel, "The curing of epoxy resins as studied by various methods", *Polymer*, **35** (1994) 5269 – 5278
75. I. Alig, D. Lellinger, G.P. Johari, "Relaxations in thermosets. XVIII. Ultrasonic studies of curing kinetics of ethylene-diamine-cured epoxide", *Journal of Polymer Science: Part b: Polymer Physics*, **30** (1992) 791 – 799
76. R.P. Cocker, D.L. Chadwick, D.J. Dare, R.E. Challis, "A low resolution pulsed NMR and ultrasound study to monitor the cure of an epoxy resin adhesive", *International Journal of Adhesion and Adhesives*, **18** (1998) 319 – 331
77. C. Pindinelli, G. Montagna, V.A.M. Luprano, A. Maffezzoli, "Network development during epoxy curing: Experimental ultrasonic data and theoretical predictions", *Macromolecular Symposia*, **180** (2002) 73 – 88
78. R.E. Challis, R.J. Freemantle, R.P. Cocker, D.L/ Chadwick, D.J. Dare, C. Martin, A. Mahendrasingam, W. Fuller, "Ultrasonic measurements related to evolution of structure in curing epoxy resins", *Plastics, Rubber and Composites*, **29** (2000) 109 – 118
79. S. Dixon, D. Jaques, S.B. Palmer, "The development of shear and compression elastic moduli in curing epoxy adhesives measured using non-contact ultrasonic transducers", *Journal of Physics D: Applied Physics*, **36** (2003) 753 – 759
80. D.D. Shepard, K.R. Smith, "A new ultrasonic measurement system for the cure monitoring of thermosetting resins and composites", *Journal of Thermal Analysis*, **49** (1997) 95 – 100

81. T.M. Whitney, R.E. Green Jr, "Cure monitoring of carbon epoxy composites: an application of resonant ultrasound spectroscopy", *Ultrasonics*, **34** (1996) 347 – 353
82. F. Kremer, A. Schönhals, "Broadband Dielectric Spectroscopy", *Springer – Verlag*, Würzburg 2003, (ISBN: 3-540-43407-0)
83. G.M. Maistros, C.B. Bucknall, "Modeling the dielectric behavior of epoxy resin blends during curing", *Polymer Engineering and Science*, **34** (1994) 1517 – 1528
84. J.R. Macdonald, "Impedance Spectroscopy. Emphasizing solid materials and systems", *John-Interscience*, New York 1987, (ISBN: 0471831220)
85. S.D. Senturia, N.F. Sheppard, "Dielectric analysis of thermoset cure", *Advances in Polymer Science*, **80** (1986) 1 – 47
86. R.A. Pethrick, D. Hayward, "Real time dielectric relaxation studies of dynamic polymeric systems", *Progress in Polymer Science*, **27** (2002) 1983 – 2017
87. J.W. Lane, J.C. Seferis, M.A. Bachmann, "Dielectric studies of the cure of epoxy matrix systems", *Journal of Applied Polymer Science*, **31** (1986) 1155 – 1167
88. K.A. Nass, J.C. Seferis, "Analysis of the dielectric response of thermosets during isothermal and nonisothermal curing", *Polymer Engineering and Science*, **29** (1989) 315 – 324
89. T. Koike, "Dielectric relaxation during isothermal cure of epoxy resin with aromatic amine", *Journal of Applied Polymer Science*, **44** (1992) 679 – 690
90. D. Lairez, J.R. Emery, D. Durrand, D. Hayward, R.A. Pethrick, "Real time dielectric measurements of network formation in a crosslinked epoxy resin system", *Plastics, Rubber and Composites Processing and Applications*, **16** (1991) 231 – 238
91. W.W. Bidstrup, S.D. Senturia, "Monitoring the cure of a composite matrix resin with microdielectrometry", *Polymer Engineering and Science*, **29** (1989) 290 – 294
92. S.A. Bidstrup, N.F. Sheppard Jr, S.D. Senturia, "Dielectric analysis of the cure of thermosetting epoxy/amine systems", *Polymer Engineering and Science*, **29** (1989) 325 – 328
93. D.R. Day, "Dielectric determination of cure state during non-isothermal cure", *Polymer Engineering and Science*, **29** (1989) 334 – 338
94. H.W.L. Bruckman, M.P. de Goeje, "Dielectric method for monitoring the curing of polyester – melamine coatings", *Progress in Organic Coatings*, **20** (1992) 501 – 516

95. A. Livi, G. Levita, P.A. Rolla, "Dielectric behavior at microwave frequencies of an epoxy resin during Crosslinking", *Journal of Applied Polymer Science*, **50** (1993) 1583 – 1590
96. E. Butta, A. Livi, G. Levita, P.A. Rolla, "Dielectric analysis of an epoxy resins during cross-linking", *Journal of Polymer Science: Part B: Polymer Physics*, **33** (1995) 2253 – 2261
97. G. Levita, A. Livi, P.A. Rolla, C. Culicchi, "Dielectric monitoring of epoxy cure", *Journal of Polymer Science: Part B: Polymer Physics*, **34** (1996) 2731 – 2737
98. R.J. King, M.J. Werner, G.D. Mayorga, "Microwave dynamic dielectric analysis of curing neat resins", *Journal of Reinforced Plastics and Composites*, **12** (1993) 173 – 185
99. M.B.M. Mangion, G.P. Johari, "Relaxations in thermosets: 5. Dielectric studies of the effects of substitution of amines on curing kinetics and ageing of an epoxide thermoset", *Polymer*, **32** (1991) 2747 – 2754
100. M.B.M. Mangion, M. Wang, G.P. Johari, "Relaxations in thermosets. XII. Dielectric effects during curing of nonstoichiometric DGEBA-Based thermoset", *Journal of Polymer Science: Part B: Polymer Physics*, **30** (1992) 433 – 443
101. M.G. Parthun, G.P. Johari, "Relaxations in thermosets. 24. Theory and experiments on nonisothermal curing of thermoset polymers", *Macromolecules*, **25** (1992) 3149 – 3155
102. D.A. Wasylyshyn, G.P. Johari, "Dielectric effects of step-increased pressure on the mass- and diffusion-controlled linear chain and network macromolecules growth", *Chemical Physics*, **237** (1998) 345 – 358
103. J. Mijovic, C.F.W. Yee, "Use of complex impedance to monitor the progress of reactions in epoxy/amine model systems", *Macromolecules*, **27** (1994) 7287 – 7293
104. J. Mijovic, F. Bellucci, L. Nicolais, "Impedance spectroscopy of reactive polymers. Correlations with chemorheology during network formation", *Journal of the Electrochemical Society*, **142** (1995) 1176 – 1182
105. J. Mijovic, F. Bellucci, "Impedance spectroscopy of reactive polymers", *Trends in Polymer Science*, **4** (1996) 74 – 80
106. J. Mijovic, S. Andjelic, B. Fitz, W. Zurawsky, I. Mondragon, F. Bellucci, L. Nicolais, "Impedance Spectroscopy of reactive polymers. 3. Correlations between dielectric,

spectroscopic and rheological properties during cure of a trifunctional epoxy resin", *Journal of Polymer Science: Part B: Polymer Physics*, **34** (1996) 379 – 388

107. F. Bellucci, V. Maio, T. Monetta, L. Nicodemo, J. Mijovic, "Impedance spectroscopy of reactive polymers. 4. An improved experimental procedure for measurement of effective resistivity", *Journal of Polymer Science: Part B: Polymer Physics*, **34** (1996) 1277 – 1280
108. S. Andjelic, J. Mijovic, F. Bellucci, "Impedance spectroscopy of reactive polymers. 5. Impedance as a measure of chemical and physical changes in glass formers", *Journal of Polymer Science: Part B: Polymer Physics*, **36** (1998) 641 – 653
109. G. Williams, I.K. Smith, G.A. Aldridge, P. Holmes, S. Varma, "Changes in molecular dynamics during the bulk polymerisation of an epoxide/boroxine mixture as studied by dielectric relaxation spectroscopy, revealing direct evidence for a floor temperature for reaction", *Polymer*, **42** (2001) 3533 – 3557
110. P. Bartolomeo, J.L. Vernet, J.F. Chailan, "On the use of WLF equation to study curing by dielectric spectroscopy", *Polymer*, **42** (2001) 4385 – 4392
111. J.P. Eloundou, "Dipolar relaxations in an epoxy-amine system", *European Polymer Journal*, **38** (2002) 431 – 438
112. I. K. Partridge, G.M. Maistros, "Phase separation in thermosetting blends studied by dynamic dielectric analysis", *High Performance Polymers*, **8** (1996) 1 – 17
113. S. Poncet, G. Boiteux, J.P. Pascault, H. Sautereau, G. Seytre, J. Rogozinski, D. Kranbuehl, "Monitoring phase separation and reaction advancement in situ in thermoplastic/epoxy bleds", *Polymer*, **40** (1999) 6811 – 6820
114. A. Bonnet, J.P. Pascault, H. Sautereau, J. Rogozinski, D. Kranbuehl, "Epoxy-diamine thermoset/thermoplastic blends: Dielectric properties before, during, and after phase separation", *Macromolecules*, **33** (2000) 3833 – 3843
115. I. Alig, W. Jenninger, "Curing kinetics of phase separating epoxy thermosets studied by dielectric and calorimetric investigations: a simple model for the complex dielectric permittivity", *Journal of Polymer Science: Part B: Polymer Physics*, **36** (1998) 2461 – 2470
116. K. Nixdorf, G. Busse, "The dielectric properties of glass-fibre-reinforced epoxy resin during polymerisation", *Composites Science and Technology*, **61** (2001) 889 – 894
117. K.G. Bang, J.W. Kwon, D.G. Lee, J.W. Lee, "Measurement of the degree of cure of glass fibre-epoxy composites using dielectrometry", *Journal of Materials Processing Technology*, **113** (2001) 209 – 214

118. J.M. Kenny, A. Trivisano, L.A. Berglund, "Chemorheological and dielectric behavior of the epoxy matrix in a carbon fibre prepreg", *SAMPE Journal*, **27** (1991) 39 – 46
119. G.M. Maistros, I.K. Partridge, "Dielectric Monitoring of cure in a commercial carbon-fibre composite", *Composites Science and Technology*, **53** (1995) 355 – 359
120. G.M. Maistros, I.K. Partridge, "Monitoring autoclave cure in commercial carbon fibre/epoxy composites", *Composites Part B*, **29B** (1998) 245 – 250
121. A. McIlhanger, D. Brown, B. Hill, "The development of a dielectric system for the on-line cure monitoring of the resin transfer moulding process", *Composites: Part A*, **31** (2000) 1373 – 1381
122. N.F. Sheppard Jr, S.D. Senturia, "Chemical interpretation of the relaxed permittivity during epoxy resin cure", *Polymer Engineering and Science*, **26** (1986) 354 – 357
123. J.P. Pascault, R.J.J. Williams, "Glass transition temperature versus conversion relationships for thermosetting polymers", *Journal of Polymer Science: Part B: Polymer Physics*, **28** (1990) 85 – 95
124. A.A. Skordos, I.K. Partridge, "Determination of the degree of cure under dynamic and isothermal curing conditions using electrical impedance spectroscopy", paper accepted for publication in *Journal of Polymer Science: Part B: Polymer Physics*
125. D. Kranbuehl, S. Delos, M. Hoff, P. Haverty, W. Freeman, R. Hoffman, J. Godfrey, "Use of the frequency dependence of the impedance to monitor viscosity during cure", *Polymer Engineering and Science*, **29** (1989) 285 – 289
126. D.E. Kranbuehl, P. Kingsley, S. Hart, G. Hasko, B. Dexter, A.C. Loos, "In situ sensor monitoring and intelligent control of the resin transfer molding process", *Polymer Composites*, **15** (1994) 299 – 305
127. D.J. Melotik, M. Czaplicki, T.J. Whalen, D.R. Day, "Analysis of the resin transfer molding process using in-mold dielectric sensors", *Thermochimica Acta*, **217** (1993) 251 – 262
128. J.M. Methven, Y. Katramados, "In-line quality monitoring of pultruded profiles using dielectric measurements", *Polymers & Polymer Composites*, **5** (1997) 15 – 27
129. J.F. Maguire, M.A. Miller, S. Venketesan, "Processing of soft matter and composites: integration of material sensors with process models and intelligent control algorithms", *Engineering Applications of Artificial Intelligence*, **11** (1998) 605 – 618

130. E. Chailleux, M. Salvia, N. Jaffrezic-Renault, Y. Jayet, A. Mazzouz, G. Seytre, "In situ multidetection cure monitoring of an epoxy-amine system", *Journal of Advanced Science*, **12** (2000) 291 – 297
131. V. Shtrauss, A. Kalpinsh, U. Lomanovskis, J. Rotbahs, "Resin cure monitoring system based on non-destructive dielectric spectrometry", *Mechanics of Composites Materials*, **32** (1996) 279 – 285
132. V. Shtrauss, "A study on the information capability of dielectric spectra in monitoring nonisothermal cure processes", *Mechanics of Composite Materials*, **38** (2002) 181 – 186
133. O.M. Corbino, "Thermische oszillationen wechselstromdurchflossener lampen mit dünnem faden und daraus sich ergebende gleichrichterwirkung infolge der anwesenheit geradzahliger oberschwingungen", *Physikalische Zeitschrift*, **11** (1910) 413 - 417
134. Y. Kraftmakher, "Modulation calorimetry and related techniques", *Physics Reports*, **356** (2002) 1 – 117
135. E. Gmelin, "Classical temperature-modulated calorimetry: A review", *Thermochimica Acta*, **304/305** (1997) 1 – 26
136. B. Wünderlich, A. Androsch, M. Pyda, Y.K. Kwon, "Heat capacity by multi-frequencies sawtooth modulation", *Thermochimica Acta*, **348** (2000) 181 – 190
137. E.-Y. Ding, R.S. Cheng, "Theory of general temperature modulated differential scanning calorimetry", *Thermochimica Acta*, **378** (2001) 51 – 68
138. S.L. Simon, "Temperature-modulated differential scanning calorimetry: theory and application", *Thermochimica Acta*, **374** (2001) 55 – 71
139. G.W.H. Höhne, "Temperature modulated differential scanning calorimetry (TMDSC) in the region of phase transitions. Part 1: theoretical considerations", *Thermochimica Acta*, **330** (1999) 45 – 54
140. F. Cser, F. Rasoul, E. Kosior, "Modulated differential scanning calorimetry. The effect of experimental variables", *Journal of Thermal Analysis*, **50** (1997) 727 – 744
141. P.S. Gill, S.R. Saurbrunn, M. Reading, "Modulated differential scanning calorimetry", *Journal of Thermal Analysis*, **40** (1993) 931 – 939
142. J. Cao, "Mathematical studies of modulated differential scanning calorimetry I. Heat capacity measurements", *Thermochimica Acta*, **325** (1999) 101 – 109

143. J. Cao, "Mathematical studies of modulated differential scanning calorimetry II. Kinetic and non-kinetic components", *Thermochimica Acta*, **329** (1999) 89 – 95
144. K. Kanari, T. Ozawa, "Simulation of temperature modulated DSC of temperature dependent heat capacity", *Thermochimica Acta*, **304/305** (1997) 201 – 207
145. A.A. Lacey, C. Nikolopoulos, M. Reading, "A mathematical model for modulated differential scanning calorimetry", *Journal of Thermal Analysis*, **50** (1997) 279 – 333
146. B. Wünderlich, "Modelling the heat flow and heat capacity of modulated differential scanning calorimetry", *Journal of Thermal Analysis*, **48** (1997) 207 – 224
147. J.E.K. Schawe, "Principles for the interpretation of temperature – modulated DSC measurements. Part 2: A thermodynamic approach", *Thermochimica Acta*, **304/305** (1997) 111 – 119
148. K. Kanari, T. Ozawa, "Linearity and non – linearity in DSC: A critique on modulated DSC", *Thermochimica Acta*, **253** (1995) 183 – 188
149. M. Merzlyakov, C. Schick, "Optimization of experimental parameters in TMDSC. The influence of non – linear and non – stationary thermal response", *Journal of Thermal Analysis and Calorimetry*, **61** (2000) 649 – 659
150. C. Schick, M. Merzlyakov, A. Hensel, "Nonlinear thermal response at the glass transition", *Journal of Chemical Physics*, **111** (1999) 2695 – 2700
151. B. Wünderlich, A. Boller, I. Okazaki, S. Kreitmeier, "Linearity, steady state, and complex heat capacity in modulated differential scanning calorimetry", *Thermochimica Acta*, **282/283** (1996) 143 – 155
152. S.L. Simon, G.B. McKenna, "The effects of structural recovery and thermal lag in temperature – modulated DSC measurements", *Thermochimica Acta*, **307** (1997) 1 – 10
153. http://mathworld.wolfram.com/LissajousCurve.html, Eric Weinstein's World of Mathematics, Wolfram Research, accessed March 25th 2003
154. S. Weyer, M. Merzlyakov, C. Schick, "Application of an extended Tool – Narayanaswamy – Moynihan model Part 1. Description of vitrification and complex heat capacity measured by temperature – modulated DSC", *Thermochimica Acta*, **377** (2001) 85 – 96
155. S. Montserrat, F. Roman, P. Colomer, "Vitrification and dielectric relaxation during the isothermal curing of an epoxy – amine resin", *Polymer*, **44** (2003) 101 – 114

156. G. Van Assche, A. Van Hemelrijck, H. Rahier, B. Van Mele, "Modulated differential scanning calorimetry: Non – isothermal cure, vitrification, and devitrification of thermosetting systems", *Thermochimica Acta*, **286** (1996) 209 – 224
157. E. Girard-Reydet, H. Sautereau, J.P. Pascault, P. Keates, P. Navard, G. Thollet, G. Vigier, "Reaction-induced phase separation mechanisms in modified thermosets", *Polymer* **39** (1998) 2269 – 2280
158. M. Song, D.J. Hourston, H.M. Pollock, A. Hammiche, "Modulated differential scanning calorimetry: 14. Effect of molecular interactions on glass transition behaviour and increment of heat capacity in miscible polymer blends", *Polymer*, **40** (1999) 4763 – 4767
159. I. Alig, W. Jenninger, J.E.K. Schawe, "Curing kinetics of phase separating thermosets studied by DSC, TMDSC and dielectric relaxation spectroscopy", *Thermochimica Acta*, **330** (1999) 167 – 174
160. J.M. Barton, "The application of differential scanning calorimetry (DSC) to the study of epoxy resin curing reactions", *Advances in Polymer Science*, **72** (1985) 112 – 154
161. http://www.hexcelcomposites.com, official web site of Hexcel® Composites Company, accessed August 4th 2003
162. http://www.hexcelcomposites.com/NR/rdonlyres/eile3z2rtb5jmjjnu3uhdfmmzxwqxco4jco5ya4d3lvwqgz2mjpk7e7aocfdfckewcjaeqe3mre764nlpn5mwaajnff/RTM6_1.PDF, product data sheet for RTM6, accessed August 4th 2003
163. http://www.hexcelcomposites.com/NR/rdonlyres/eubq76hy47xiauxejdtq7d67xoteyyb57jzruu2lo4zhao72hihw6borljhyffeoondfgaragcmvjl/hexply%2b913.pdf, product data sheet for HexPly® 913 epoxy system, accessed August 4th 2003
164. http://link.springer.de/link/service/series/0284/index.htm , Landolt - Börnstein Numerical Data and Functional Relationships in Science and Technology, online database supplied by *Springer Science Online* (http://www.springer.de), accessed May 20th 2003
165. http://www.eurotherm.com/products/controllers/2200e.htm, Eurotherm 2200e temperature controllers series, accessed January 11th 2003
166. Solartron Analytical 1260 Impedance/Gain – Phase Analyzer, operating manual issued July 1993, part no: 1260012. The same information can also be found in the URL: http://www.solartronanalytical.com/fra/1260.html, accessed May 8th 2003

167. U. Bandara, "A systematic solution to the problem of sample background correction in DSC curves", *Journal of Thermal Analysis*, **31** (1986) 1063 – 1071
168. A.A. Skordos, "Modelling and monitoring of resin transfer moulding", *PhD Thesis*, Cranfield University, Cranfield 2000
169. S. Kahle, "Dielectric Spectroscopy", *IFF Ferienkurs*, **33** (2002) A3
170. V. Adamec, "Electrical properties of an epoxy resin during and after cure", *Journal of Polymer Science: Part A-1*, **10** (1972) 1277 – 1295
171. V. Adamec, J.H. Calderwood, "Electrode polarization in polymeric dielectrics", *IEEE Transactions on Electrical Insulation*, **24** (1989) 205 – 214
172. D.R. Day, T.J. Lewis, H.L. Lee, S.S. Senturia, "The role of boundary layer capacitance at blocking electrodes in the interpretation of dielectric cure data in adhesives", *Journal of Adhesion*, **18** (1985) 73 – 90
173. G. Gallone, G. Levita, J. Mijovic, S. Andjelic, P.A. Rolla, "Anomalous trends in conductivity during epoxy – amine reactions", *Polymer*, **39** (1998) 2095 – 2102
174. K.S. Cole, R.H. Cole, "Dispersion and absorption in dielectrics. I. Alternating current characteristics", *Journal of Chemical Physics*, **9** (1941) 341 – 351
175. D.W. Davidson, R.H. Cole, "Dielectric relaxation in glycerol, propylene glycol and n-propanol", *Journal of Chemical Physics*, **19** (1951) 1484 – 1490
176. S. Havriliak, S. Negami, "A complex plane representation of dielectric and mechanical relaxation processes in some polymers", *Polymer*, **8** (1967) 161 – 210
177. G. Williams, D.C. Watts, "Non – symmetrical dielectric relaxation behaviour arising from a simple empirical decay function", *Transactions of the Faraday Society*, **66** (1970) 80 – 85
178. R. Hilfer, "Analytical representations for relaxation functions of glasses", *Journal of Non – Crystalline Solids*, **305** (2002) 122 – 126
179. D.R. Paul, C.B. Bucknall, "Polymer Blends. Volume 1: Formulation", *John Wiley & Sons*, New York 2000, (ISBN: 0471248258)
180. D. Verchere, H. Sautereau, J.P. Pascault, S.M. Moschiar, C.C. Riccardi, R.J.J. Williams, "Rubber-Modified epoxies. I. Influence of carboxyl-terminated butadiene-acrylonitrile random copolymers (CTBN) on the polymerization and phase Separation Processes", *Journal of Applied Polymer Science*, **41** (1990) 467 – 485
181. D. Verchere, J.P. Pascault, H. Sautereau, S.M. Moschiar, C.C. Riccardi, R.J.J. Williams, "Rubber-Modified epoxies. II. Influence of the cure schedule and rubber

concentration on the generated morphology", Journal *of Applied Polymer Science*, **42** (1991) 701 – 716

182. S.M. Moschiar, C.C. Riccardi, R.J.J. Williams, D. Verchere, H. Sautereau, J.P. Pascault, "Rubber-Modified epoxies. III. Analysis of experimental trends through a phase separation model", *Journal of Applied Polymer Science*, **42** (1991) 717 – 735
183. I.K. Partridge, C.B. Bucknall, "Phase separation in epoxy resins containing polyethersulphone", *Polymer*, **24** (1983) 639 – 644
184. G.C. Psarras, E. Manolakaki, G.M. Tsangaris, "Electrical relaxations in polymeric particulate composites of epoxy resin and metal particles", *Composites Part A*, **33** (2002) 375 – 384
185. J.C. Maxwell, "A treatise on electricity and magnetism", 2nd ed., *Clarendon Press*, Oxford 1881, reprint by *Dover Publication Inc.* New York 1954, (ISBN: 486-60637-6)
186. K.W. Wagner, "Erklärung der dielektischen Nachwirkungsvorgänge auf grund Maxwellscher Vorstellungen", *Archiv für Electrotechnik*, **II** (1914) 371 – 387
187. W.R. Sillars, "The properties of a sielectric containing semiconducting particles of various shapes", *Journal of Institution of Electrical Engineers*, **80** (1937) 378 – 394
188. G.P. Johari, K. Pathmanathan, "The dipolar and conductivity relaxations in ionic conductors", *Physics and Chemistry of glasses*, **29** (1988) 219 – 224
189. Y. Feldman, E. Polygalov, I. Ermolina, Y. Polevaya, B. Tsentsiper, "Electrode polarization correction in time domain dielectric spectroscopy", **12** (2001) 1355 – 1364
190. C.H. Hsu, F. Mansfeld, "Concerning the conversion of the constant phase element parameter Y_o into a capacitance", *Corrosion*, **57** (2001) 747 – 748
191. W.H. Mulder, J.H. Sluyters, T. Pajkossy, L. Nyikos, "Tafel current at fractal electrodes. Connection with admittance spectra", *Journal of Electroanalytical Chemistry*, **285** (1990) 103 – 115
192. D.E. Goldberg, "Genetic Algorithms: In Search, Optimization and Machine Learning", *Addison-Wesley Publishing Company*, 1989, (ISBN: 0-201-15767-5)
193. M. Mitchell, "An introduction to genetic algorithms", *MIT Press*, New York 1999 (ISBN: 0-262-13316-4)
194. T.J. VanderNoot, I. Abrahams, "The use of genetic algorithms in the non-linear regression of immitance data", *Journal of Electroanalytical Chemistry*, **448** (1998) 17 – 23

195. M. Yang, X. Zhang, X. Li, X. Wu, "A hybrid genetic algorithm for the fitting of models to electrochemical impedance data", *Journal of Electroanalytical Chemistry*, **519** (2002) 1 – 8
196. J.R. Macdonald, "Analysis of impedance and admittance data for solids and liquids", *Journal of Electrochemical Society*, **124** (1977) 1022
197. J.R. Macdonald, "Exact and Approximate nonlinear least – square inversion of dielectric relaxation data", *Journal of Chemical Physics*, **102** (1995) 6241 – 6250
198. J.R. Macdonald, "Comparison and application of two methods for the least squares analysis of immitance data", *Solid State Ionics*, **58** (1992) 97 – 107
199. J.R. Macdonald, "Accurate fitting of immitance spectroscopy frequency response data using the stretched exponential model", *Journal of Non-Crystalline Solids*, **212** (1997) 95 – 116
200. J.R. Macdonald, "On relaxation-spectrum estimation for decades of data: accuracy and sampling-localization considerations", *Inverse Problems*, **16** (2000) 1561 – 1583
201. http://www.solartronanalytical.com/downloads/software.html , LEVM v7.11, accessed in February 21st 2003
202. http://www.itl.nist.gov/div898/handbook/, *NIST/SEMATECH e-Handbook of Statistical Methods*, section 4.1.4.3: Weighted least squares regression, accessed July 7th 2003
203. R. de L. Kronig, "On the theory of dispersion of X – Rays", *Journal of the Optical Society America*, **12** (1926) 547
204. H.A. Kramers, "Die Dispersion und Absorption von Röntgengebeit", *Physik. Z.*, **30** (1929) 522
205. A.Tarantola, "Inverse Problem Theory. Methods for data fitting and model parameter estimation", *Elsevier Science*, Amsterdam 1987, (ISBN: 0-444-42765-1)
206. M.E. Orazem, P. Agarwal, A.N. Jansen, P.T. Wojcik, L.H. Garcia – Rubio, "Development of physico – chemical models for electrochemical impedance spectroscopy", *Electrochimica Acta*, **38** (1993) 1903 – 1911
207. J.R. Dygas, M.W. Breiter, "Variance of errors and elimination of outliers in the least squares analysis of impedance spectra", *Electrochimica Acta*, **44** (1999) 4163 – 4174

208. A.N. Tikhonov, A.S. Leonov, A.G. Yagola, "Nonlinear Ill-Posed Problems", *Kluwer Academic Publishers*, New York 1997, (ISBN: 0-412-78660-5)*
209. G.H. Golub, P.C. Hansen, D.P. O'Leary, "Tikhonov regularization and total least squares", *SIAM Journal on Matrix Analysis and Applications*, **21** (2000) 185 – 194
210. J. Winterhalter, D.G. Ebling, D. Maier, J. Honerkamp, "An improved analysis of admittance data for high resistivity materials by a nonlinear regularization method", *Journal of Applied Physics*, **82** (1997) 5488 – 5495
211. A.A. Skordos, I.K. Partridge. "Impedance cure and flow monitoring in the processing of advanced composites", *International Conference for Manufacturing of Advanced Composites (ICMAC)*, conference organised by the Institute of Materials (IoM), September 2001, Belfast (pages 103 – 112 in the conference pre-prints, ISBN: 1-186125-153-X)
212. http://mathworld.wolfram.com/CubicEquation.html, Eric Weinstein's World of Mathematics, Wolfram Research, accessed March 28th 2003
213. G.O. Shonaike, S.G. Advani, "Advanced polymeric materials: structure property relationships", *CRC Press LLC*, New York 2003, (ISBN: 1-58716-047-1)
214. http://www.tainst.com/support/TA210.pdf, "Modulated DSC® compendium. Basic theory & experimental considerations", accessed September 1st 2003
215. A.V. Mamishev, Y. Du, B.C. Lesieutre, M. Zahn, "Development and applications of fringing electric field dielectrometry sensors and parameter estimation algorithms", *Journal of Electrostatics*, **46** (1999) 109 – 123
216. B.C. Lesieutre, A.V. Mamishev, Y. Du, E. Keskiner, M. Zahn, G.C. Verghese, "Forward and inverse parameter estimation algorithms of interdigital dielectrometry sensors", *IEEE Transactions on Dielectrics and Electrical Insulation*, **8** (2001) 577 – 588
217. http://www.cytec.com/business/EngineeredMaterials/Datasheets/CYCOM%20RTM%205250-4.pdf, product data sheet for Cycom® 5250-4 RTM, accessed 11st September 2003

* The book is also published by CRC press (ISBN: 0412759101)

Appendix A

In this appendix, the dependence of the real and imaginary components of the complex permittivity spectrum, ε' and ε'' respectively, on σ, ε_r and τ is briefly discussed.

For a system without any electrode polarisation ε' and ε'' are given by eqs. (4.14) – (4.15). Substitution from eqs. (4.5) – (4.8) gives the permittivity ε' and the dielectric loss ε'' in terms of σ, ε_r, ε_u and τ:

$$\varepsilon' = \varepsilon_u + \frac{\varepsilon_r - \varepsilon_u}{1 + \omega^2\tau^2} \tag{A1}$$

$$\varepsilon'' = \frac{(\varepsilon_r - \varepsilon_u)\omega\tau}{1 + \omega^2\tau^2} + \frac{\sigma}{\omega\varepsilon_0} \tag{A2}$$

The frequency dependence of ε' and ε'' is shown in Figure A1. In the permittivity spectrum the shoulder due to the relaxation of the permanent dipoles is observed. The low and high frequency values of ε' are defined by ε_r and ε_u respectively. The dielectric loss spectrum contains the dipolar relaxation peak and the conductivity contribution at low frequencies (second term in eq. (A2)).

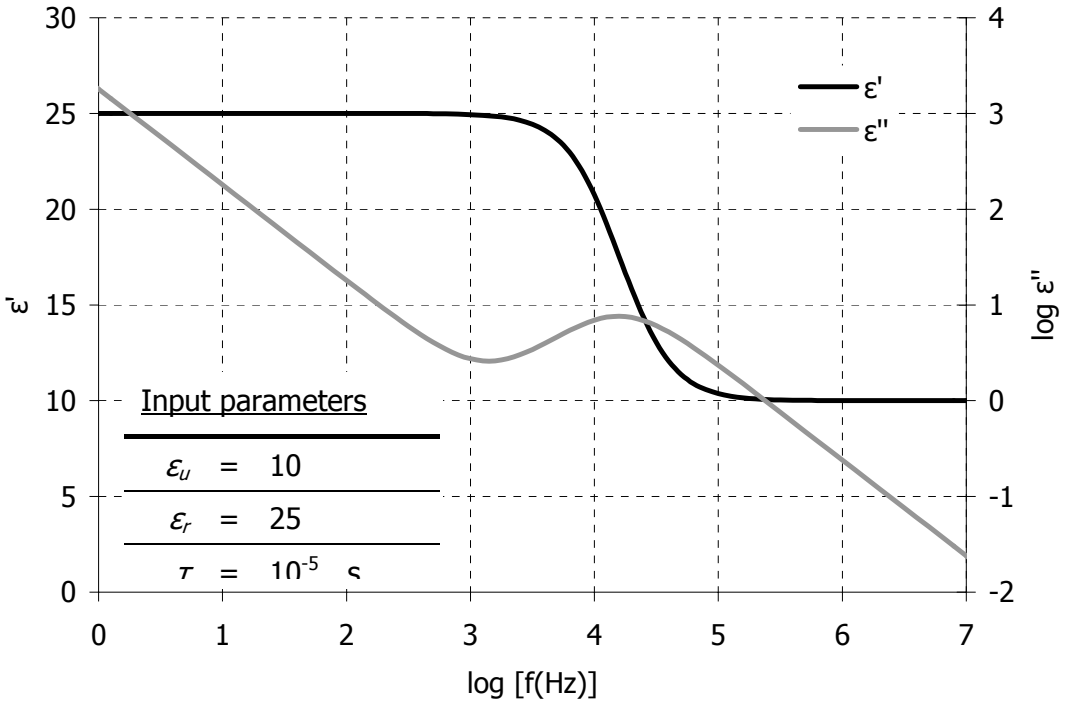

Figure A1 *Permittivity and dielectric loss spectra for a system containing migrating charges and permanent dipoles. The input parameters are given in the inset table.*

A1. Influence of the conductivity σ

A change in the conductivity value imposes changes in the low frequency side of the dielectric loss spectrum as pictured in Figure A2. Dielectric loss decreases as conductivity decreases. The permittivity spectrum is not affected by the conductivity changes (σ not present in eq. (A1)).

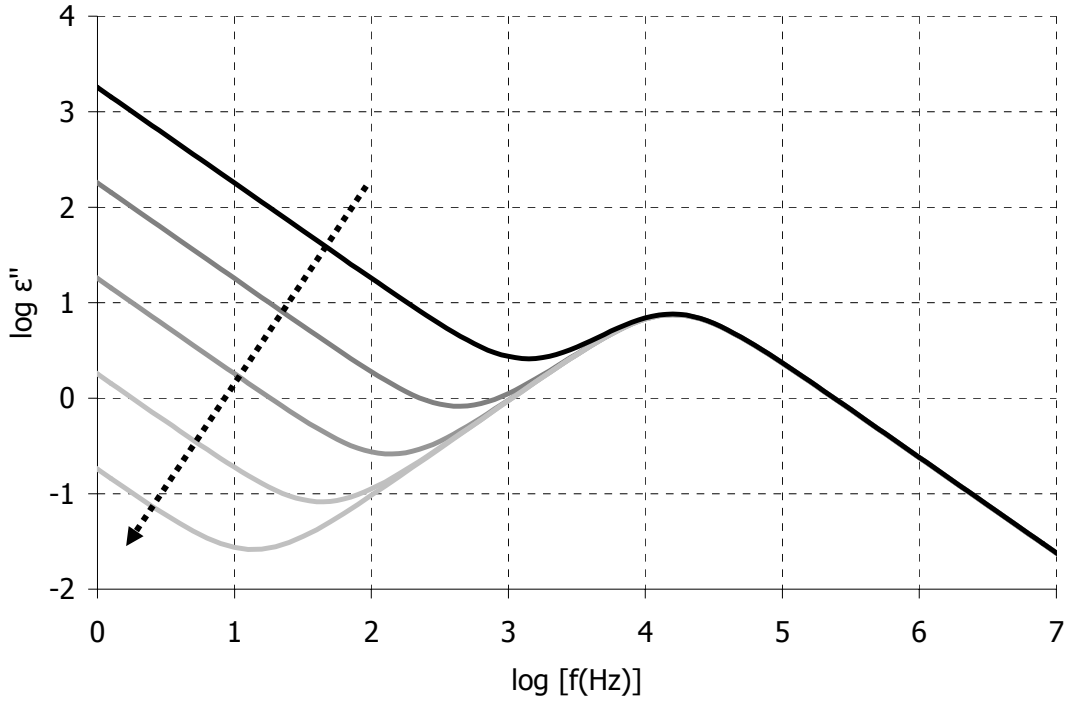

Figure A2 *Dielectric loss spectra for a system containing migrating charges and permanent dipoles. The input parameters are the same as in Figure A1. Conductivity varies from 10^{-7} S/m to 10^{-11} S/m (steps of one order of magnitude). The arrow shows the spectrum movement as conductivity decreases.*

A2. Influence of the relaxed permittivity ε_r

Changes in the relaxed permittivity value impose changes in the low frequency side of the permittivity spectrum as pictured in Figure A3. Permittivity values increase as ε_r increases.

The influence on the dielectric loss is given in Figure A4. Dielectric loss increases over the whole frequency range. The position of the peak moves to higher frequencies, although the shift is not significant in the logarithmic scale of the graph.

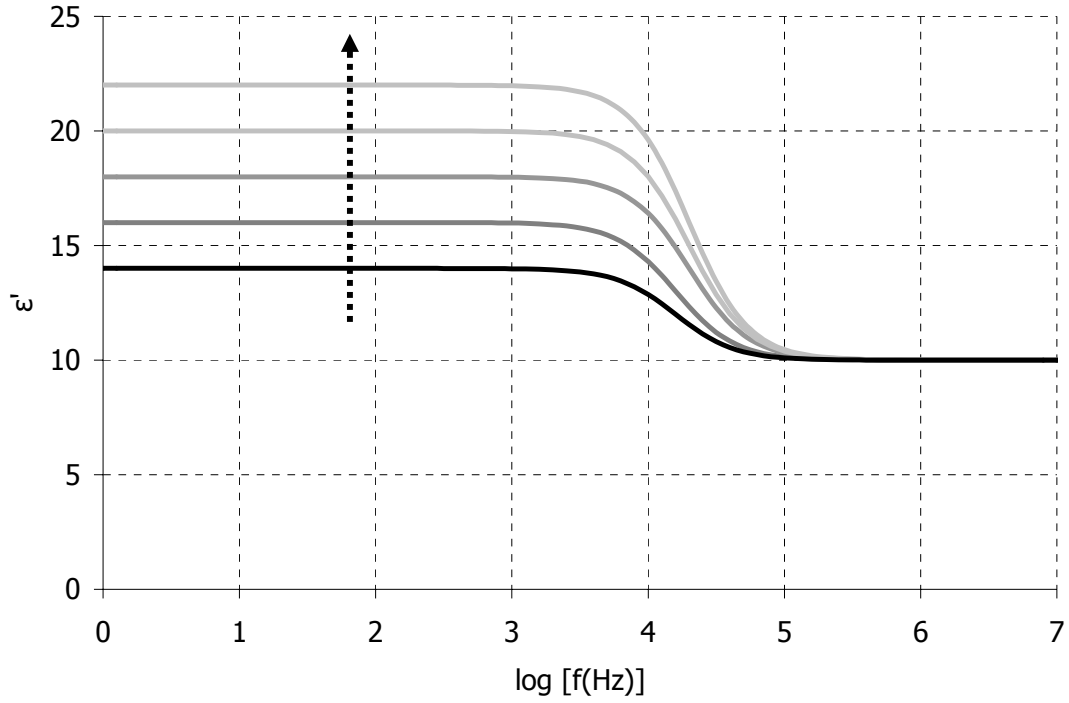

Figure A3 *Permittivity spectra changes when the relaxed permittivity varies from 14 to 22. The rest input parameters are the same as in Figure A1. The arrow shows the spectrum movement as ε_r increases.*

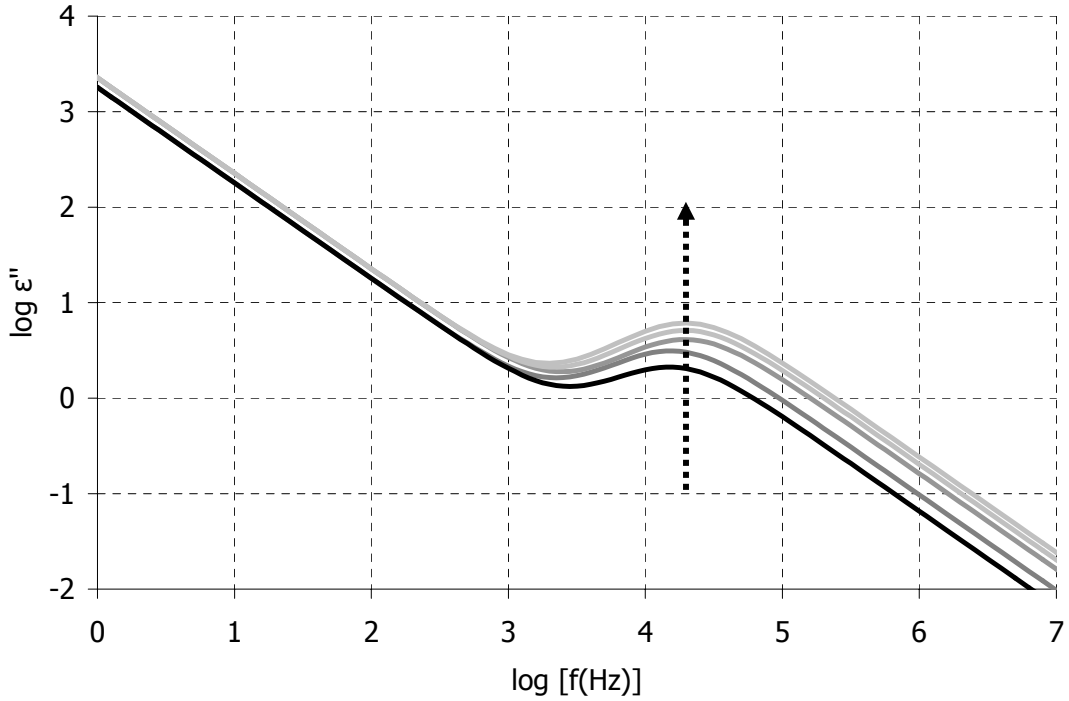

Figure A4 *Dielectric loss spectra changes when the relaxed permittivity varies from 14 to 22. The rest input parameters are the same as in Figure A1. The arrow shows the spectrum movement as ε_r increases.*

A3. Influence of the relaxation time τ

The relaxation time τ affects the frequency position of the permittivity shoulder and the dielectric loss peak as it is shown in Figures A5 and A6 respectively. The relaxation frequency moves to lower values as τ increases (see §4.2.3).

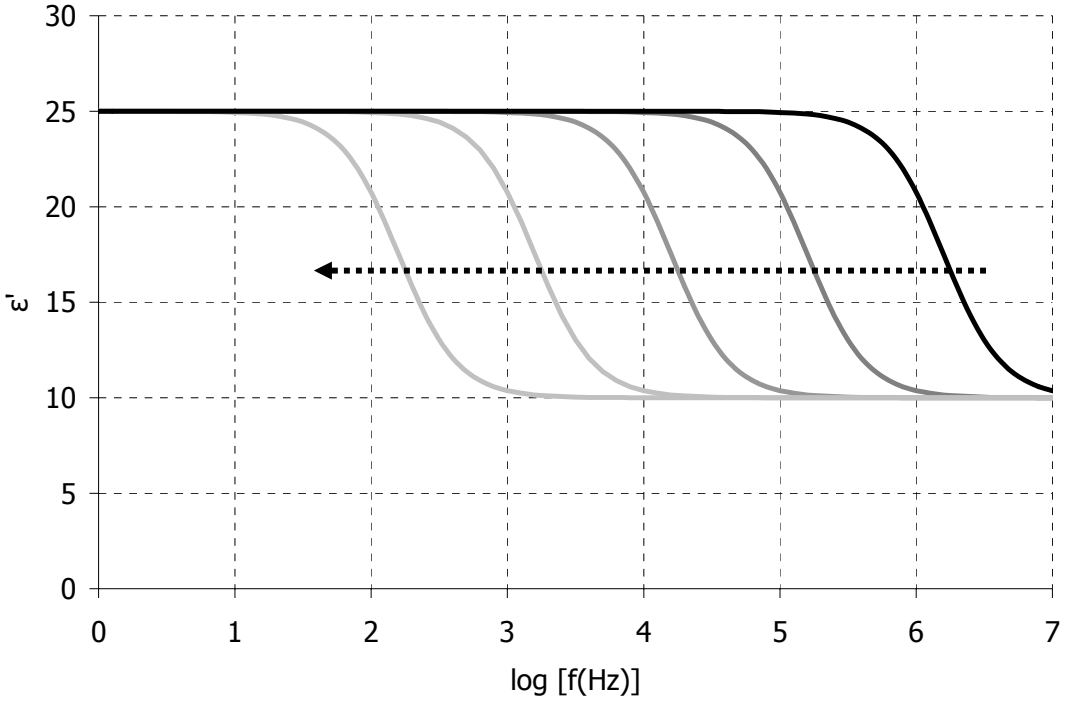

Figure A5 *Permittivity spectra for a system containing migrating charges and permanent dipoles. The input parameters are the same as in Figure A1. Relaxation time varies from 10^{-7} s to 10^{-3} s (steps of one order of magnitude). The arrow shows the spectrum movement as τ increases.*

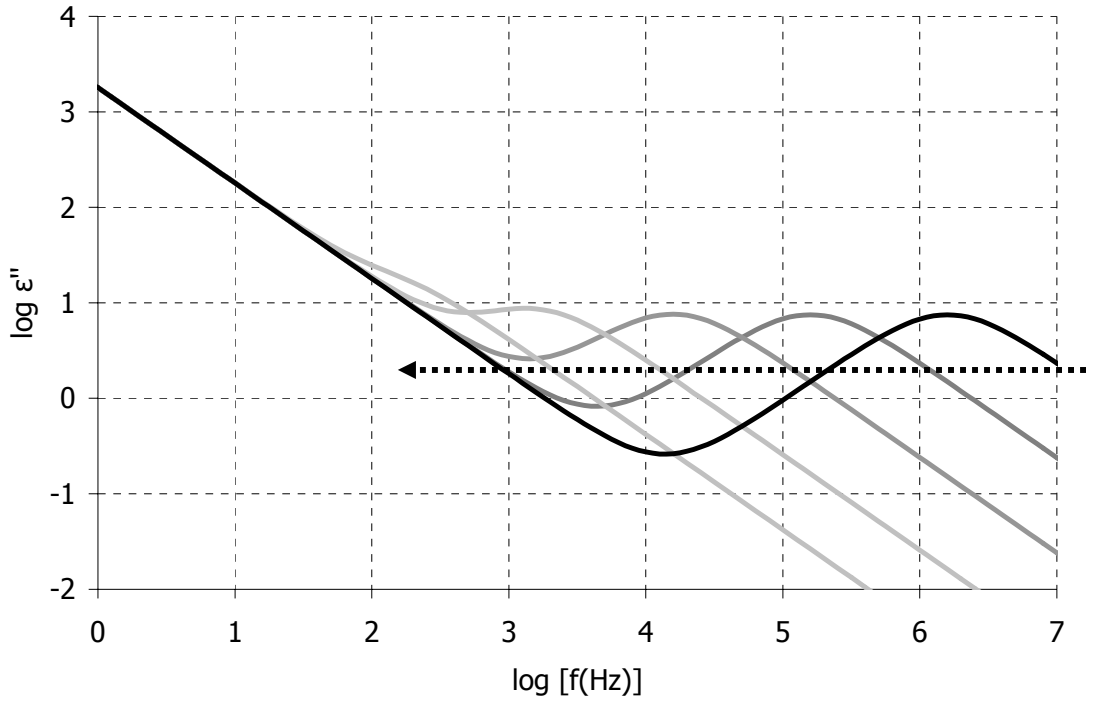

Figure A6 *Dielectric loss spectra for a system containing migrating charges and permanent dipoles. The input parameters are the same as in Figure A1. Relaxation time varies from 10^{-7} s to 10^{-3} s (steps of one order of magnitude). The arrow shows the spectrum movement as τ increases.*

Appendix B

Here, an investigation on the features of the real and imaginary impedance functions presented in § 4.3 is performed. The derivatives of eqs. (4.18) and (4.19) are evaluated. The conditions for the derivatives to be zero are outlined.

B1. Real Impedance Equation

The real impedance equation is:

$$Z' = \frac{\varepsilon_0}{C_O} \frac{\left(2\sigma\tau + \left(\varepsilon_r - \varepsilon_u\right)\varepsilon_0\right)\tau\omega^2 + 2\sigma}{\left(2\sigma\tau + \varepsilon_r\varepsilon_0\right)^2 \omega^2 + \left(\omega^2\tau\varepsilon_u\varepsilon_0 - 2\sigma\right)^2} \tag{B1}$$

The above equation is rewritten in the form:

$$f\left(\omega\right) = \frac{\varepsilon_0}{C_O} \frac{a_r\omega^2 + b_r}{c\omega^4 + d\omega^2 + e} \tag{B2}$$

where

$$a_r = \left(2\sigma\tau + \left(\varepsilon_r - \varepsilon_u\right)\varepsilon_0\right)\tau \tag{B3}$$

$$b_r = 2\sigma \tag{B4}$$

$$c = \left(\tau\varepsilon_u\varepsilon_0\right)^2 \tag{B5}$$

$$d = \left(2\sigma\tau + \varepsilon_r\varepsilon_0\right)^2 - 4\sigma\tau\varepsilon_u\varepsilon_0 \tag{B6}$$

$$e = 4\sigma^2 \tag{B7}$$

All the above parameters are positive. The number of optimum points of eq. (B2) (and hence (B1)) is found by taking the derivative of (B2):

$$\frac{d}{d\omega} f(\omega) = 0 \Rightarrow \cdots \Rightarrow \omega^4 + 2\frac{b_r}{a_r}\omega^2 - \frac{a_r e - b_r d}{a_r c} = 0 \tag{B8}$$

The final equation is quadratic in terms of ω^2. The discriminant is:

$$\begin{aligned} D &= 4\left(\frac{b_r^2}{a_r^2} - \frac{b_r d}{a_r c} + \frac{e}{c}\right) \Rightarrow \\ D &= \left(2\frac{b_r}{a_r} - \frac{d}{c}\left(1 + \sqrt{1 - 4\frac{ce}{d^2}}\right)\right)\left(2\frac{b_r}{a_r} - \frac{d}{c}\left(1 - \sqrt{1 - 4\frac{ce}{d^2}}\right)\right) \end{aligned} \tag{B9}$$

In order for the discriminant to be positive, both terms have to be either positive or negative.

The calculations for an analytic representation of the discriminant in terms of the initial parameters (ε_r, ε_u, τ and σ) is very tedious and complex. On the other hand is quite easy to investigate the discriminant sign numerically.

The extreme values of ε_r, ε_u, τ and σ are shown in Table B-1. The values are representative of thermoset cure (in fact they are stretched over the values normally found in literature).

Table B-1: *High and low limits for ε_r, ε_u, τ and σ*

	ε_r	ε_u	τ (s)	σ (S/m)
Upper limit	3	20	100	10^{-4}
Lower limit	1.5	4	10^{-9}	10^{-12}

Table B-2 contains the discriminant value for all combinations of the extreme values of ε_r, ε_u, τ and σ. We can see that in all cases the discriminant is negative. The relaxation time τ is the parameter that influences the discriminant the most.

Table B-2: *Discriminant values for extreme values of ε_r, ε_u, τ and σ*

ε_r	ε_u	τ (s)	σ (S/m)	D
1.5	4	10^{-9}	10^{-12}	-2.57×10^{27}
1.5	4	10^{-9}	10^{-4}	-2.55×10^{35}
1.5	4	10^{2}	10^{-12}	-1.13×10^{-6}
1.5	4	10^{2}	10^{-4}	-1.00×10^{2}
1.5	20	10^{-9}	10^{-12}	-8.68×10^{27}
1.5	20	10^{-9}	10^{-4}	-8.68×10^{35}
1.5	20	10^{2}	10^{-12}	-7.98×10^{-6}
1.5	20	10^{2}	10^{-4}	-7.43×10^{2}
3	4	10^{-9}	10^{-12}	-1.61×10^{27}
3	4	10^{-9}	10^{-4}	-1.55×10^{35}
3	4	10^{2}	10^{-12}	-1.28×10^{-7}
3	4	10^{2}	10^{-4}	-1.00×10^{1}
3	20	10^{-9}	10^{-12}	-2.36×10^{27}
3	20	10^{-9}	10^{-4}	-2.36×10^{35}
3	20	10^{2}	10^{-12}	-1.98×10^{-6}
3	20	10^{2}	10^{-4}	-1.71×10^{2}

B2. Imaginary Impedance Equation

The imaginary impedance equation is:

$$Z'' = \frac{\omega\varepsilon_0}{C_O}\frac{\varepsilon_u\varepsilon_0\tau^2\omega^2 + \varepsilon_r\varepsilon_0}{\left(2\sigma\tau + \varepsilon_r\varepsilon_0\right)^2\omega^2 + \left(\omega^2\tau\varepsilon_u\varepsilon_0 - 2\sigma\right)^2} \tag{B10}$$

The above equation is rewritten in the form:

$$f\left(\omega\right) = \frac{\varepsilon_0}{C_O}\frac{\left(a_i\omega^2 + b_i\right)\omega}{c\omega^4 + d\omega^2 + e} \tag{B11}$$

where

$$a_i = \varepsilon_u\varepsilon_0\tau^2 \tag{B12}$$

$$b_i = \varepsilon_r\varepsilon_0 \tag{B13}$$

and c, d, e are the same as in the real impedance case.

Similarly to the real impedance analysis we take the derivative of eq. (B11):

$$\frac{d}{d\omega}f\left(\omega\right) = 0 \Rightarrow \cdots \Rightarrow \omega^6 + \frac{3b_ic - a_id}{a_ic}\omega^4 + \frac{b_id - 3a_ie}{a_ic}\omega^2 - \frac{b_ie}{a_ic} = 0 \tag{B14}$$

The final equation is cubic in terms of ω^2. The cubic discriminant is (212):

$$D = Q^3 + R^2 \tag{B15}$$

where

$$Q = \frac{a_i c\left(b_i d - 3a_i c\right) - \left(3b_i c - a_i d\right)^2}{9a_i^2 c^2} \tag{B16}$$

$$R = \frac{9a_i c\left(b_i d - 3a_i c\right)\left(3b_i c - a_i d\right) - 27a_i^2 c^2 b_i e - 2\left(3b_i c - a_i d\right)^3}{54a_i^3 c^3} \tag{B17}$$

The cubic equation has three real roots when the discriminant is positive and one real root when it is negative. Table B-3 shows the discriminant values similarly to Table B-2:

Table B-3: *Discriminant values for extreme values of* ε_r, ε_u, τ and σ

ε_r	ε_u	τ (s)	σ (S/m)	Q	R	D
1.5	4	10^{-9}	10^{-12}	2.0×10^{36}	2.8×10^{54}	1.6×10^{109}
1.5	4	10^{-9}	10^{-4}	2.0×10^{36}	2.7×10^{54}	1.6×10^{109}
1.5	4	10^{-2}	10^{-12}	-3.3×10^{-1}	1.4×10^{-2}	-3.7×10^{-2}
1.5	4	10^{-2}	10^{-4}	-5.7×10^{27}	4.3×10^{41}	0
1.5	20	10^{-9}	10^{-12}	-1.9×10^{39}	4.2×10^{58}	-4.5×10^{117}
1.5	20	10^{-9}	10^{-4}	-1.9×10^{39}	4.3×10^{58}	-4.6×10^{117}
1.5	20	10^{-2}	10^{-12}	-3.3×10^{-1}	3.7×10^{-2}	-3.6×10^{-2}
1.5	20	10^{-2}	10^{-4}	-5.7×10^{27}	4.3×10^{41}	0
3	4	10^{-9}	10^{-12}	-2.9×10^{35}	4.7×10^{53}	2.0×10^{107}
3	4	10^{-9}	10^{-4}	-2.8×10^{35}	4.8×10^{53}	2.0×10^{107}
3	4	10^{-2}	10^{-12}	-3.3×10^{-1}	3.0×10^{-3}	-3.7×10^{-2}
3	4	10^{-2}	10^{-4}	-3.6×10^{26}	6.8×10^{39}	0
3	20	10^{-9}	10^{-12}	-3.4×10^{37}	-6.7×10^{56}	4.1×10^{113}
3	20	10^{-9}	10^{-4}	-3.4×10^{37}	-6.7×10^{56}	4.1×10^{113}
3	20	10^{-2}	10^{-12}	-3.3×10^{-1}	8.3×10^{-3}	-3.7×10^{-2}
3	20	10^{-2}	10^{-4}	-3.6×10^{26}	6.8×10^{39}	0

The discriminant takes positive and negative values. Consequently there are cases where it becomes zero. From the theory of cubic equations the sign of the discriminant determines the number of real solutions of eq. (B14). Table B-4 lists the possible cases:

Table B-4: *Number of real solutions of a cubic equation*

Discriminant sign	Number of real solutions
$D > 0$	1
$D < 0$	3
$D = 0$	3 (two of which are equal)

Therefore the imaginary impedance equation can exhibit one or three optimum points depending on the input parameters.

Eq. (B14) was solved numerically for different combinations of the input parameters ε_r, ε_u, τ and σ. The regions where eq. (B14) accepts one and three real solutions are shown in figure B1. In the space where eq. (B14) has three solutions the imaginary impedance spectrum exhibits two maxima and one minimum (between the maxima).

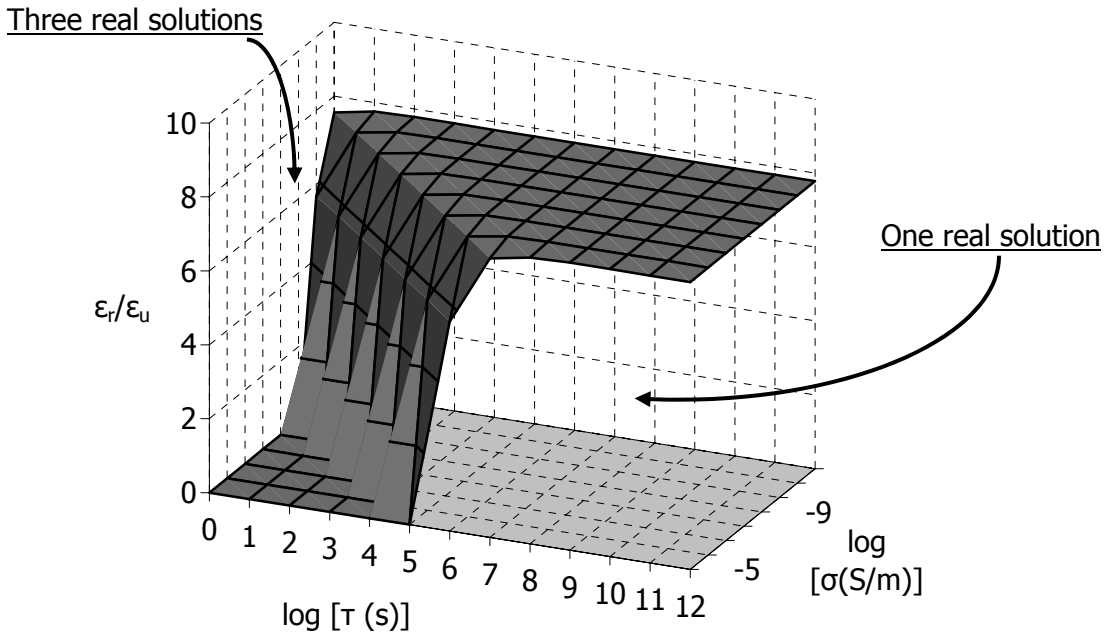

Figure B1 *Boundary surface which identifies the spaces where the imaginary impedance spectrum exhibits one or three optimum points. In the boundary two of the three solutions are equal. For the construction of the figure $\varepsilon_r = 2$.*

Appendix C

In this Appendix the interrelationships between the two circuits described in § 4.5.4 are calculated. For convenience, the circuits are reproduced here:

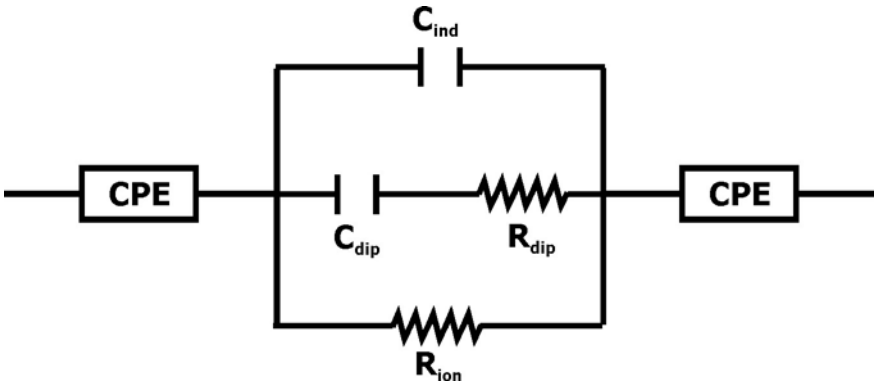

Figure C1 *Standard equivalent circuit*

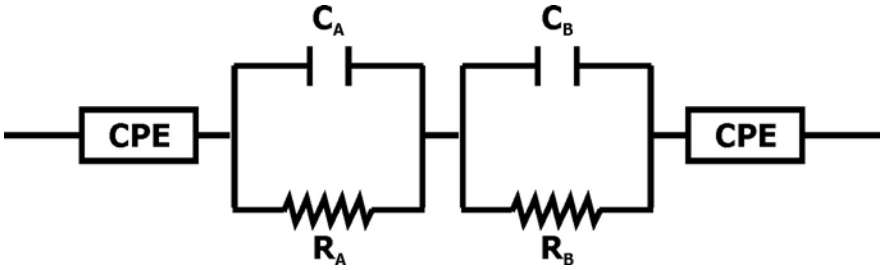

Figure C2 *Circuit that yields the same impedance with the standard circuit*

C1. Equations formulation

The real and imaginary impedance equations for the standard circuit (Figure C1) are:

$$Z' = \frac{R_{ion}\left[\omega^2\tau_3\left(\tau_3+\tau_2\right)+1\right]}{\omega^2\left(\tau_1+\tau_2+\tau_3\right)^2+\left(\omega^2\tau_1\tau_3-1\right)^2}+2A_{CPE}\frac{\cos\left(\frac{n\pi}{2}\right)}{\omega^n} \tag{C1}$$

$$Z' = \frac{\omega R_{ion}\left[\omega^2\tau_2\tau_3^2+\tau_1+\tau_2\right]}{\omega^2\left(\tau_1+\tau_2+\tau_3\right)^2+\left(\omega^2\tau_1\tau_3-1\right)^2}+2A_{CPE}\frac{\sin\left(\frac{n\pi}{2}\right)}{\omega^n} \tag{C2}$$

where

$$\tau_1 = R_{ion}C_{ind}$$
$$\tau_2 = R_{ion}C_{dip}$$
$$\tau_3 = R_{dip}C_{dip}$$
$$\tau_\Sigma = \tau_1+\tau_2+\tau_3$$
$$\tau_\Pi = \tau_1\tau_3$$

The impedance equations of the second equivalent circuit (Figure C2) are:

$$Z' = \frac{R_A}{1+\omega^2R_A^2C_A^2}+\frac{R_B}{1+\omega^2R_B^2C_B^2}+2A_{CPE}\frac{\cos\left(\frac{n\pi}{2}\right)}{\omega^n} \tag{C3}$$

$$Z'' = \frac{\omega R_A^2C_A}{1+\omega^2R_A^2C_A^2}+\frac{\omega R_B^2C_B}{1+\omega^2R_B^2C_B^2}+2A_{CPE}\frac{\sin\left(\frac{n\pi}{2}\right)}{\omega^n} \tag{C4}$$

Comparing eqs (C2) and (C4) results in the following correlations between the elements of the two circuits:

$$R_AC_AR_BC_B = \tau_\Pi = R_{ion}C_{ind}R_{dip}C_{dip} \tag{C5}$$

$$R_AR_B\left(C_A+C_B\right) = R_{ion}\tau_3 = R_{ion}R_{dip}C_{dip} \tag{C6}$$

$$R_A^2C_A+R_B^2C_B = R_{ion}\left(\tau_1+\tau_2\right) = R_{ion}^2\left(C_{ind}+C_{dip}\right) \tag{C7}$$

$$R_AC_A+R_BC_B = \tau_\Sigma = R_{ion}C_{ind}+R_{ion}C_{dip}+R_{dip}C_{dip} \tag{C8}$$

Similar analysis to the real impedance eqs (C1) and (C3) yields two more equations:

$$R_AR_B\left(R_BC_B^2+R_AC_A^2\right) = R_{ion}\left(\tau_3^2+\tau_2\tau_3\right) = R_{ion}C_{dip}^2R_{dip}\left(R_{dip}+R_{ion}\right) \tag{C9}$$

$$R_A+R_B = R_{ion} \tag{C10}$$

Dividing eq. (C8) with eq. (C5) gives:

$$\frac{R_A C_A + R_B C_B}{R_A C_A R_B C_B} = \frac{\tau_\Sigma}{\tau_\Pi} \longrightarrow$$

$$\frac{1}{R_B C_B} + \frac{1}{R_A C_A} = \frac{\tau_\Sigma}{\tau_\Pi} \xrightarrow{(B8)}$$

$$\frac{1}{\tau_\Sigma - R_A C_A} + \frac{1}{R_A C_A} = \frac{\tau_\Sigma}{\tau_\Pi} \longrightarrow$$

$$R_A C_A + \tau_\Sigma - R_A C_A = \frac{\tau_\Sigma}{\tau_\Pi}\left(\tau_\Sigma R_A C_A - R_A^2 C_A^2\right) \longrightarrow$$

$$R_A^2 C_A^2 - \tau_\Sigma R_A C_A + \tau_\Pi = 0$$

The solution of the final quadratic equation gives the following relationship:

$$R_A C_A = \frac{\tau_\Sigma \pm \sqrt{\tau_\Sigma^2 - 4\tau_\Pi}}{2} \tag{C11}$$

The algebraic expression under the square root is by definition positive. Substituting the last equation in eq. (C5) produces a relationship correlating the time constant $R_B C_B$ of the second equivalent circuit with elements of the initial circuit:

$$R_B C_B = \frac{\tau_\Sigma \mp \sqrt{\tau_\Sigma^2 - 4\tau_\Pi}}{2} \tag{C12}$$

It is obvious that eq. (C12) is the solution of the same quadratic equation that produces eq. (C11). Therefore, the signs of the last two equations can be arbitrarily chosen. In the present study, we take:

$$R_A C_A = \frac{\tau_\Sigma + \sqrt{\tau_\Sigma^2 - 4\tau_\Pi}}{2} \tag{C13}$$

and

$$R_B C_B = \frac{\tau_\Sigma - \sqrt{\tau_\Sigma^2 - 4\tau_\Pi}}{2} \tag{C14}$$

Substituting the last two equations in eq. (C7) yields:

$$\frac{\tau_\Sigma + \sqrt{\tau_\Sigma^2 - 4\tau_\Pi}}{2} R_A + \frac{\tau_\Sigma - \sqrt{\tau_\Sigma^2 - 4\tau_\Pi}}{2} R_B = R_{ion}\left(\tau_1 + \tau_2\right) \tag{C15}$$

Eq.s (C15) and (C10) form a 2x2 linear system. Its solution gives the values of the resistances of the equivalent circuit of Figure C2:

$$R_A = \frac{R_{ion}}{2}\left[1 + \frac{\tau_\Sigma - 2\tau_3}{\sqrt{\tau_\Sigma^2 - 4\tau_\Pi}}\right] = \frac{R_{ion}}{2}(1+k) \tag{C16}$$

$$R_B = \frac{R_{ion}}{2}\left[1 - \frac{\tau_\Sigma - 2\tau_3}{\sqrt{\tau_\Sigma^2 - 4\tau_\Pi}}\right] = \frac{R_{ion}}{2}(1-k) \tag{C17}$$

where

$$k = \frac{\tau_\Sigma - 2\tau_3}{\sqrt{\tau_\Sigma^2 - 4\tau_\Pi}} \tag{C18}$$

The capacitances are derived by eqs (C13) and (C12):

$$C_A = \frac{\tau_\Sigma + \sqrt{\tau_\Sigma^2 - 4\tau_\Pi}}{2R_A} \Rightarrow C_A = \frac{1}{k}\left(C_{ind} + C_{dip} + \frac{k-1}{k+1}\frac{R_{dip}C_{dip}}{R_{ion}}\right) \tag{C19}$$

$$C_B = \frac{\tau_\Sigma - \sqrt{\tau_\Sigma^2 - 4\tau_\Pi}}{2R_B} \Rightarrow C_B = \frac{1}{k}\left(\frac{k+1}{1-k}\frac{R_{dip}C_{dip}}{R_{ion}} - C_{ind} - C_{dip}\right) \tag{C20}$$

The extraction of the original parameters of the equivalent circuit from R_A, C_A, R_B and C_B is more straightforward. From eq. (C10) we have:

$$R_{ion} = R_A + R_B \tag{C21}$$

Eq. (C7) gives:

$$C_{ind} + C_{dip} = \frac{R_A^2 C_A + R_B^2 C_B}{(R_A + R_B)^2} \tag{C22}$$

Eq. (C6) gives:

$$R_{dip}C_{dip} = \frac{R_A R_B (C_A + C_B)}{R_A + R_B} \tag{C23}$$

Substituting eqs. (C10) and (C23) into eq. (C5) yields:

$$C_{ind} = \frac{C_A C_B}{C_A + C_B} \tag{C24}$$

Back substitution to eq. (C22) yields C_{dip}:

$$C_{dip} = \frac{(R_A C_A - R_B C_B)^2}{(R_A + R_B)^2 (C_A + C_B)} \tag{C25}$$

Finally, substitution of eq. (C25) into eq. (C23) gives R_{dip}:

$$R_{dip} = \frac{R_A R_B \left(R_A + R_B\right)\left(C_A + C_B\right)^2}{\left(R_A C_A - R_B C_B\right)^2} \tag{C26}$$

C2. Optima determination

The imaginary impedance equation, according to the circuit of Figure C2 has the form of eq. (C6). The first derivative of eq. (C6) will be:

$$\frac{dZ''}{d\omega} = \frac{R_A^2 C_A \left(1 - \omega^2 R_A^2 C_A^2\right)}{\left(1 + \omega^2 R_A^2 C_A^2\right)^2} + \frac{R_B^2 C_B \left(1 - \omega^2 R_B^2 C_B^2\right)}{\left(1 + \omega^2 R_B^2 C_B^2\right)^2} - n\frac{2A_{el} Sin\left(\frac{n\pi}{2}\right)}{\omega^{n+1}} \tag{C27}$$

The roots of the above equation provide the maximum and minimum points of the spectrum. For the maximum point we can exclude from the calculation the electrode polarization term, as its presence is only evident in the very low part of the spectrum. Eq. (C27) can therefore be written as follows for the maximum point determination:

$$\frac{R_A^2 C_A \left(1 - \omega_{\max}^2 R_A^2 C_A^2\right)}{\left(1 + \omega_{\max}^2 R_A^2 C_A^2\right)^2} + \frac{R_B^2 C_B \left(1 - \omega_{\max}^2 R_B^2 C_B^2\right)}{\left(1 + \omega_{\max}^2 R_B^2 C_B^2\right)^2} = 0 \tag{C28}$$

After some algebraic manipulation the above equation becomes:

$$\omega_{\max}^6 + c_2 \omega_{\max}^4 + c_1 \omega_{\max}^2 + c_0 = 0 \tag{C29}$$

where

$$c_2 = 2\frac{R_A^2 C_A + R_B^2 C_B}{R_A^2 C_A R_B^2 C_B \left(C_A + C_B\right)} - \frac{R_A^2 C_A^3 + R_B^2 C_B^3}{\left(R_A C_A R_B C_B\right)^2 \left(C_A + C_B\right)} \tag{C30}$$

$$c_1 = \frac{R_A^4 C_A^3 + R_B^4 C_B^3}{\left(R_A R_B C_A C_B\right)^3 R_A R_B \left(C_A + C_B\right)} - \frac{2}{\left(R_A R_B C_A C_B\right)^2} \tag{C31}$$

$$c_0 = -\frac{R_A^2 C_A + R_B^2 C_B}{\left(R_A R_B C_A C_B\right)^3 R_A R_B \left(C_A + C_B\right)} \tag{C32}$$

From a purely mathematical point of view, the above equation has six solutions and can be solved as a cubic equation (212). The discriminant of the cubic equation is:

$$D_\omega = \left(\frac{3c_1 - c_2^2}{9}\right)^3 + \left(\frac{9c_1 c_2 - 27c_0 - 2c_2^3}{54}\right)^2 \tag{C33}$$

The real solution which gives ω_{max} has the following form:

$$\omega_{\max}^2 = -\frac{c_2}{3} + \left(\frac{9c_1c_2 - 27c_0 - 2c_2^3}{54} + \sqrt{D_\omega} \right)^{\frac{1}{3}} + \left(\frac{9c_1c_2 - 27c_0 - 2c_2^3}{54} - \sqrt{D_\omega} \right)^{\frac{1}{3}} \quad \text{(C34)}$$

During the initial stages of an epoxy cure, the effect of circuit B in the overall signal is very small compared to the effect of circuit A, resulting to a *k* value close to unity. In this case, the term describing circuit B can be neglected. Furthermore, the influence of polarization effects reduces very fast with increasing frequency and its influence on the maximum value is several orders of magnitude smaller compared with circuit A. The above assumptions lead to a first approximation of the maximum point:

$$Z''_{\max} = \frac{R_A}{2} \Rightarrow Z''_{\max} = \frac{R_{ion}}{2} \quad \text{(C35)}$$

$$f_{\max} = \frac{1}{2\pi R_A C_A} \Rightarrow f_{\max} = \frac{1}{2\pi R_{ion}\left(C_{ind} + C_{dip}\right)} \quad \text{(C36)}$$

We can see that even when dipolar contribution is negligible, f_{max} is affected by C_{dip}.

The minimum value occurs in the area where the low frequency dependence of the A-circuit crosses the electrode polarization term. For that point eq. (C27) becomes:

$$\frac{dZ''}{d\omega} = R_A^2 C_A - \frac{2nA_{el}Sin\left(\frac{n\pi}{2}\right)}{\omega^{n+1}} \quad \text{(C37)}$$

Solving the above equation provides the minimum frequency and subsequently the imaginary impedance value at the minimum point:

$$f_{\min} = \frac{1}{2\pi}\left(\frac{2nA_{el}Sin\left(\frac{n\pi}{2}\right)}{R_A^2 C_A} \right)^{\frac{1}{n+1}} \Rightarrow f_{\min} = \frac{1}{2\pi}\left(\frac{2nA_{el}Sin\left(\frac{n\pi}{2}\right)}{R_{ion}^2\left(C_{ind} + C_{dip}\right)} \right)^{\frac{1}{n+1}} \quad \text{(C38)}$$

$$Z''_{\min} = \left(1 + \frac{1}{n}\right)\left(2A_{el}Sin\left(\frac{n\pi}{2}\right)\right)^{\frac{1}{n+1}}\left(R_{ion}^2\left(C_{ind} + C_{dip}\right)\right)^{\frac{n}{n+1}} \quad \text{(C39)}$$